ADVANCED STEEL CONSTRUCTION

An International Journal

Volume 16 Number 4

December 2020

CONTENTS

Technical Papers

Website: *http://www.hkisc.org*
ISSN 1816-112X
Science Citation Index Expanded, Materials Science Citation Index and ISI Alerting
Cover: MGM (Macau) Spectacle Roof, Designed by using Second-Order Direct Analysis
e-copy of IJASC is free to download at "www.ascjournal.com" in internet and mobile apps.

ADVANCED STEEL CONSTRUCTION

VOL.16, NO.4(2020)

ADVANCED STEEL CONSTRUCTION

an International Journal

ISSN 1816-112X

Volume 16 Number 4 *December 2020*

ISSN 1816-112X

Science Citation Index Expanded, Materials Science Citation Index and ISI Alerting

Advanced Steel Construction
an international journal

Cover: MGM (Macau) Spectacle Roof, Designed by using Second-Order Direct Analysis
e-copy of IJASC is free to download at "www.ascjournal.com" in internet and mobile apps.

General Information
Advanced Steel Construction, an international journal

Aims and scope

The International Journal of Advanced Steel Construction provides a platform for the publication and rapid dissemination of original and up-to-date research and technological developments in steel construction, design and analysis. Scope of research papers published in this journal includes but is not limited to theoretical and experimental research on elements, assemblages, systems, material, design philosophy and codification, standards, fabrication, projects of innovative nature and computer techniques. The journal is specifically tailored to channel the exchange of technological know-how between researchers and practitioners. Contributions from all aspects related to the recent developments of advanced steel construction are welcome.

Subscription inquiries and change of address. Address all subscription inquiries and correspondence to Member Records, IJASC. Notify an address change as soon as possible. All communications should include both old and new addresses with zip codes and be accompanied by a mailing label from a recent issue. Allow six weeks for all changes to become effective.

The Hong Kong Institute of Steel Construction
HKISC
c/o Department of Civil and Environmental Engineering,
The Hong Kong Polytechnic University,
Hunghom, Kowloon, Hong Kong, China.
Tel: 852- 2766 6047 Fax: 852- 2334 6389
Email: *ceslchan@polyu.edu.hk* Website: *http://www.hkisc.org/*
ISSN 1816-112X
Science Citation Index Expanded, Materials Science Citation Index and ISI Alerting

ISSN 1816-112X

Science Citation Index Expanded, Materials Science Citation Index and ISI Alerting

Advanced Steel Construction
an international journal

VOLUME 16 NUMBER 4 December 2020

Technical Papers

Advanced Steel Construction – Vol. 16 No. 4 (2020) 287–296
DOI:10.18057/IJASC.2020.16.4.1

EXPERIMENTAL AND THEORETICAL RESEARCH ON RCFT BEAM-COLUMNS FABRICATED WITH Q420B HIGH-STRENGTH STEEL SUBJECTED TO ECCENTRIC LOAD

Zhi-Hua Chen [1, 2], Rui Ma [2], Yan-Sheng Du [2, 3, *] and Ming Lian [4]

[1] *State Key Laboratory of Hydraulic Engineering Simulation and Safety, Tianjin, China*
[2] *School of Civil Engineering, Tianjin University, Tianjin, China*
[3] *State Key Laboratory of Green Building in Western China, Xi'an University of Architecture & Technology, Xi'an, China*
[4] *School of Civil Engineering, Xi'an University of Architecture and Technology, Xi'an,, China*
** (Corresponding author: E-mail: duys@tju.edu.cn)*

ABSTRACT

This study is motivated by the widespread use of concrete - filled tubular (CFT) columns and the increasing use of high - strength steel (HSS). However, due to limited research, HSS was not extensively utilized in rectangular concrete - filled tubular (RCFT) columns. In this paper, the behavior of RCFT columns manufactured with Q420B HSS subjected to eccentric load was studied through the method of experimental and finite element (FE) analysis. The eccentric compression test was conducted on seventeen specimens with different concrete strength, width - to - thickness ratio, aspect ratio, and excentricity ratio. It obtained and discussed failure modes, load-vertical displacement curves, load-lateral deflection curves, and variations in strain. ABAQUS software developed nonlinear FE models based on an experimental program. Several specifications, including EC4, AISC360, AIJ, GB 50936-2014, and DB 29-57 for predicting the ultimate capacities of RCFT columns under excentric loading, were discussed through comparison with experimental results. The proposed approaches were also verified to be reasonably conservative for practical design with the experimental results.

ARTICLE HISTORY

Received: 24 February 2020
Revised: 20 June 2020
Accepted: 22 June 2020

KEYWORDS

Rectangular concrete-filled tubular columns;
Experiment investigation;
Finite element analysis;
Design approach;
High-strength steel

1. Introduction

Concrete - filled steel tubular (CFT) columns have been extensively used in various structural engineering fields, such as high - rise buildings, bridges, residential structures, and so on[1-3]. Compared to square and circular columns of CFT[4], rectangular sections comprising steel and concrete are non-niform and more complex. Meanwhile the rectangular concrete - filled steel tubular (RCFT) column, as a kind of thin - walled component, is susceptible to local steel tube buckling. Hence, in recent years, the RCFT columns have attracted considerable attention. Some researchers (Du et al.[5], Hernán-dez-Figueirido et al.[6], Lai et al.[7], Lee et al.[8], Long et al.[9], Ding et al.[10], Wang et al.[11], Young et al.[12], and Du et al.[13]) used experimental and theoretical methods to study mechanical behavior in relation to normal RCFT columns.

High - strength steel (HSS) manufacturing and welding techniques have been developed rapidly over the past few years, making it possible to use HSS extensively in engineering construction. Several researchers performed experimental and theoretical studies on this kind of material to determine the mechanical performance of HSS in structure projects. Shi et al.[14] systematically explored the mechanical performance of HSS and offered some suggestions for design. Wang et al.[15] proposed a yield function and basically simulated HSS elastoplasty behavior in complex stress conditions. Li et al.[16] offered experimental and theoretical support to design and exploit members of the HSS. The findings suggest that initial imperfection should be considered during analyzes of finite elements. In China, CFT members with a mild carbon steel are the main objects of current CFT structure design specifications. CFT-focused component requirements and structures using HSS were not published. It would appear that further investigations are needed to determine if existing CFT structure codes could be extended to the designing of RCFT members and structures using HSS.

Some experimental and theoretical studies have been reported in recent years on the bearing capacities of CFT columns made from HSS, while most of them were under axial load. For example, Lue et al.[17], Liew etal.[18], Xiong et al.[19], and Lyu et al.[20] performed extensive experimental axial programs to reveal the actions of CFT columns composed of high - strength steel ($f_y = 379.8\text{MPa} \sim 780\text{MPa}$) and ultra – high - strength concrete ($f_c^{'} = 84\text{MPa} \sim 190\text{MPa}$), to extend the database of tests. Steel grade has a significant effect on the axial capacities of the RCFT columns, according to Du et al.[21]. Lee et al.[22] concentrated on evaluating the effect of slenderness on the mechanical performance of high - strength steel CFT columns (grade 800MPa). Ellobody and Young[23] developed a nonlinear finite element (FE) model with considerable accuracy of CFT columns with a square and rectangular hollow section to further understand the behavior of CFT columns under axial load. They carried out a parametric analysis to determine the effect of concrete strengths and cross -section geometries.

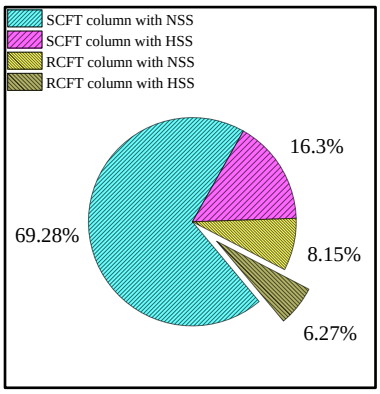

Fig. 1 Test database of square and RCFT beam-columns

To fully grasp the research status of CFT beam-columns under excentric loading, a database was developed and analyzed, as shown in Fig. 1, including 319 test results from previous literatures. Many test data came from square concrete-filled steel tubular (SCFT) columns made of normal strength steel (NSS), whereas just 6.27 percent were connected to RCFT columns with HSS, suggesting that there is still a shortage of experimental studies and theoretical study of the mechanical properties of excentric RCFT columns made of HSS. Reference [24] established the experimental system of sixteen stub columns and four slender CFT columns subjected to eccentric loading. The research findings showed the need for a revision of the application codes to design high - strength CFT columns. Choi et al.[25] studied the structural behavior of HSA800 high strength steel and SM490 mild steel hybrid RCFT columns subjected to weak axis bending, made of thick flanges and thin webs, respectively. The test results showed that using this type of section could dramatically reduce costs without degradation of the performance. Du et al.[26,27] investigated RCFT column output using Q460 grade steel under eccentric loads and suggested a new design approach. However, the approach considered backing plate resistance which is not common in RCFT columns.

Li et al.[28] experimentally studied 434MPa HSS concrete -filled square tube stub columns with different excentricity ratios. The effects of eccentricity ratio, concrete compressive, strength, steel yield strength and steel ratio were analyzed in detail but no consideration was given to the longitudinal effect. According to Li et al.[29], two important factors affecting bearing capacities are the steel ratio and the slenderness ratio. Earlier overall work did not conduct systematic column research using Q420 grade steel produced in China.

This paper presents further study of RCFT columns manufactured with Q420B HSS by conducting new experiments, setting numerical models and proposing theoretical formulae. The goal is to explore these component's mechanical behaviors under combined axial compression and bending. Firstly, an experimental program of 17 specimens is reported with different parameters. There are presented the modes of failure, load versus vertical displacement / lateral deflection, and load versus strain behaviors. The effects of concrete in-fill, the ratio of width to thickness and the ratio of eccentricity are discussed. The FE models are established and verified by experimental data for further analysis of the behavior of RCFT columns under loading process. By comparison with the experimental findings, predictions calculated using current design codes of different countries are discussed. It is also compared and tested that the proposed design approach based on the Chinese design code is relatively conservative for practical design. This research work may support the widespread use of Q420B high - resistance steel in practical CFT structural engineering.

2. Experimental program

2.1. Specimen details

Seventeen specimens were designed with different parameters, including three section forms (120×100 mm, 180×120 mm, 243×135 mm) with a different aspect ratio (h/b =1.2, 1.5, 1.8) and width-to-thickness ratio (h/t =15, 22.5, 30.5), three kinds of concrete condition (without concrete, C40, C50), and two nominal eccentricity ratios ($\eta = 2e_0/h$ =0.2, 0.4). All specimens were named by the form of "steel-concrete strength-tube section-eccentricity ratio", for instance, the first S in SC40SB-0.2 refers to Q420B high-strength steel, C40 represents C40 grade concrete, SB expresses section B (180×120mm), and 0.2 denotes that the nominal eccentricity ratio is 0.2. Detailed information about the specimens is listed in Table1. The symbols e_0 represents eccentric distance measured before the experiment, while α_s means the nominal proportion of load bore by steel tubes, which could be calculated through Eq. (1). The slenderness ratio about the principal x axis (λ) could be obtained through Eq. (2) and Eq. (3).

$$\alpha_s = \frac{f_y A_s}{f_y A_s + f_c A_c} \tag{1}$$

$$\lambda = l_{ox} / i_x \tag{2}$$

$$i_x = \sqrt{\frac{I_{sx} + I_{cx} E_c / E_s}{A_s + A_c f_c / f_y}} \tag{3}$$

In the equations, f_y and f_c refer to the yield strength of steel and compressive strength of concrete. While E_s and E_c represent Young's modulus; A_s and A_c refer to the cross-sectional areas where subscript s and c represent steel and concrete, respectively. l_{ox} is the effective length about the principal x axis; I_{sx} and I_{cx} are defined as the moment of inertia about principle x axis for the steel section and the concrete section, respectively.

To fabricate the columns, the steel tube of each specimen was assembled by welding four Q420B steel plates. Two cover plates were set onto the end of each steel tube after pouring concrete, as depicted in Fig.2.

Table 1
Detailed information about experimental specimens

Specimen No.	Steel material	Concrete material	λ	h(mm)	b(mm)	t(mm)	α_s	h/t	e_0 (mm)	N_u (kN)	M_u (kN·m)
SC40SA-0.2	Q420B	C40	22.50	123	101	8	0.77	15.0	14.00	1460	33.52
SC40SB-0.2	Q420B	C40	15.25	184	120	8	0.71	22.5	20.00	2375	76.67
SC40SE-0.2	Q420B	C40	11.45	244	134	8	0.67	30.4	24.50	3040	93.30
SC50SA-0.2	Q420B	C50	22.99	121	101	8	0.72	15.0	13.00	1590	36.00
SC50SB-0.2	Q420B	C50	15.63	180	121	8	0.65	22.5	20.00	2240	68.92
SC50SE-0.2	Q420B	C50	11.75	243	134	8	0.61	30.4	25.50	3260	102.53
SC40SA-0.4	Q420B	C40	22.50	121	100	8	0.77	15.0	25.50	1300	44.91
SC40SB-0.4	Q420B	C40	15.25	181	117	8	0.71	22.5	16.50	2500	59.90
SC40SE-0.4	Q420B	C40	11.45	244	135	8	0.67	30.4	49.75	2500	158.92
SC50SA-0.4	Q420B	C50	22.99	122	100	8	0.72	15.0	25.50	1230	42.98
SC50SB-0.4	Q420B	C50	15.63	181	120	8	0.65	22.5	36.00	1895	107.66
SC0SA-0.2	Q420B	-	21.47	121	99	8	1.00	30.4	11.50	1310	24.092
SC0SB-0.2	Q420B	-	14.61	181	120	8	1.00	15.0	17.00	1850	71.39
SC0SE-0.2	Q420B	-	11.04	243	133	8	1.00	22.5	29.50	2230	76.44
SC0SA-0.4	Q420B	-	21.47	120	100	8	1.00	30.4	23.00	1100	36.95
SC0SB-0.4	Q420B	-	14.61	180	121	8	1.00	15.0	13.50	1980	45.12
SC0SE-0.4	Q420B	-	11.04	245	135	8	1.00	22.5	50.50	1970	107.52

2.2. Material property test

The same batch of steel was used in this study and Ref.[18]; thus, the results of material property tests are the same as that in Ref[18], including the mean value of steel yield strength f_y=423.2MPa , tensile strength f_u=593.8MPa , elasticity modulus E_s=1.98GPa , yield ratio f_y/f_u=0.71 , percentage elongation after fracture Δ=27.18 and yield strain ε_y=2315 .

As for the concrete, six cubic blocks of C40 and C50 concrete were compared with that of experimental specimens after casting and curing in the same environment. The mean value of the cubic strength of concrete C40 and C50 is 43.2MPa and 55.3MPa.

2.3. Eccentric compression experiment equipment

As seen in Fig. 2(a)-(b), two steel bars were welded onto each cover plate to locate the loading line, which is the middle line between these two steel bars. The eccentric distance e_0 equals to the distance between the middle line of the specimen section and the loading line. Knife-edges could be stuck between the two steel bars; therefore, different eccentricity could be applied through the various locations of knife-edge, as shown in Fig. 3.

A NYL-500 5000kN long-column hydraulic compression machine was employed to apply compression loads. Pin constraints were simulated by the knife-edge supports set on both sides of the specimens, as demonstrated in Fig. 3. The arrangement of measurement equipment is presented in Fig. 4. Five

linear variable displacement transducers (LVDT1-LVDT5) were installed along the column to measure the lateral deflections, while the other four (LVDT6-LVDT9) were used to test the axial displacement. The total of twelve strain gauges at the mid-height cross-section of each specimen were utilized to monitor the longitudinal and lateral strains, four of which were respectively set on flange B and flange D, six were set on the web A and two were attached to web C.

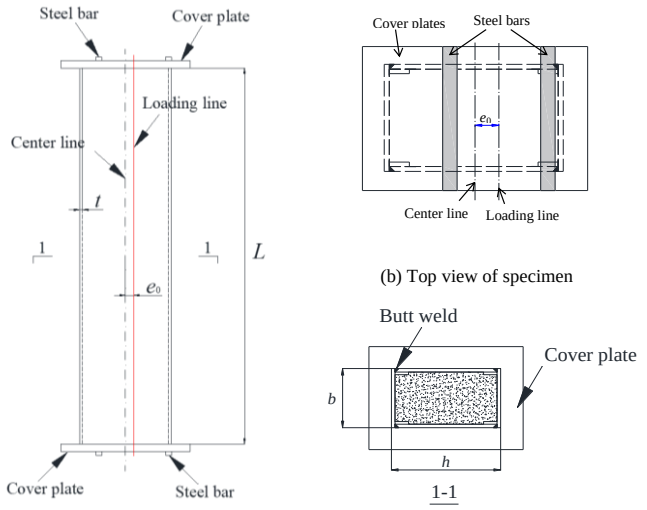

Fig. 2 Illustration of experimental specimen

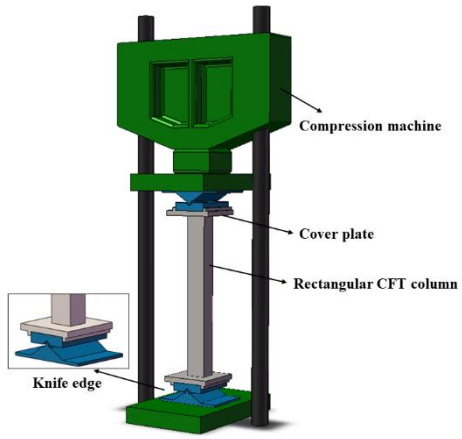

Fig. 3 Experimental apparatus

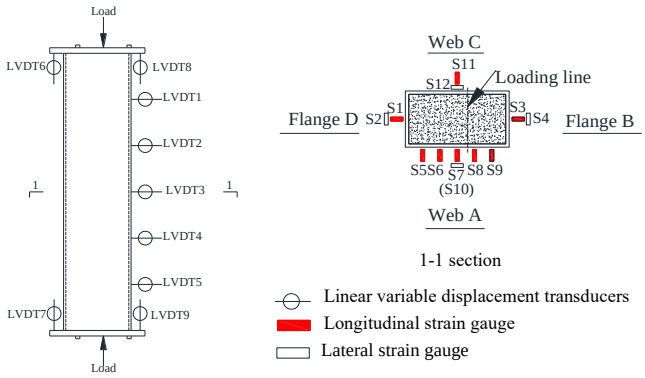

Fig. 4 Arrangement of measurement equipment

The multi-stage loading method, with the meaning of applying load at 50kN intervals, was adopted to record experimental data including the load, strain, and displacement during the experimental process. Besides, both buckling and fracture of steel tubes were observed and recorded.

3. Experimental results

3.1. Failure modes

As shown in Fig.5, all specimens experienced lateral bending failure. This confirms that both local buckling and steel tube fracture occurred with concrete crushing of specimens with SB and SE parts at the same location. Presenting a significant correlation with initial imperfection, in the center of tubes the local buckling did not occur all the time. In general, fracture occurred at the corner, which due to welding is close to the heat - affected zone. It is known that not only outward buckling but inward buckling occurred in the hollow steel columns, which showed that concrete increases the ability of resistance by preventing local steel tube buckling. Typical phenomena, including local steel web and flange buckling, concrete crushing (concrete approaches fault strain), and steel tube fracturing, are described in load - vertical displacement curves, as shown in Fig. 6.

Fig. 5 Failure of the specimens

3.2. Load versus axial shortening behaviors and load versus lateral deformation behaviors

The curves of load-vertical displacement and load-lateral deflection curves are shown in the Fig. 6 and Fig.7, respectively. These figures indicate that the RCFT columns under eccentric loads have three working stages, namely the elastic linear stage, the elasto - plastic stage, and the post - peak recession phase. Curves through Fig. 6 prove that with section dimension growth, initial axial stiffness and ultimate axial load generally increase signif-

icantly. The eccentric distance between SC40SB-0.4 and SC0SB-0.4 is smaller than the intended value due to fabrication error. Therefore, the ultimate axial loads of specimens with the SB section are identical to those of specimens with 0.4 eccentricity ratio in the SE section. As shown in Fig.7, the slope of the curves in the elastic stage of all specimens remains basically unchanged. Due to the higher aspect ratio, specimens in SE parts have greater flexural stiffness. Specimens with smaller sections show better ductility, due to the higher slenderness ratio.

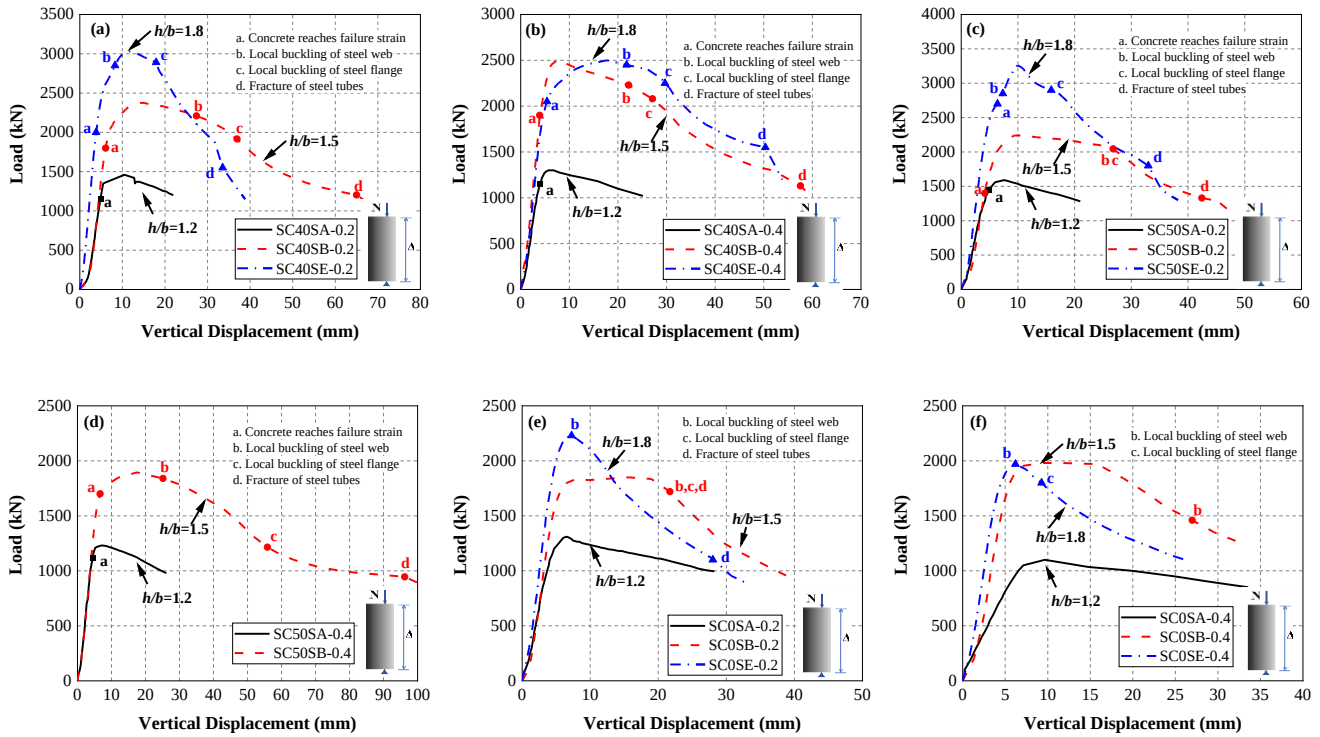

Fig. 6 Load-vertical displacement relationship of specimens

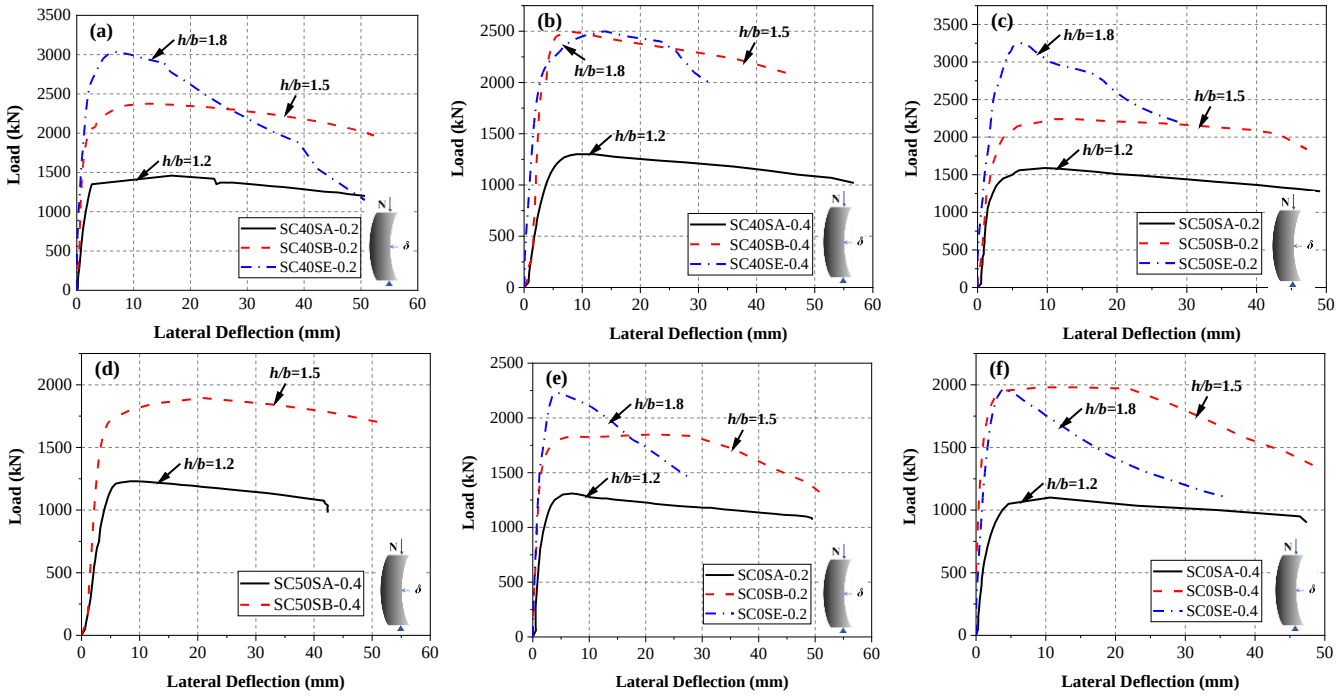

Fig. 7 Load-lateral deflection variations of specimens

3.3. Load versus strain behaviors

Typical flange and web A load-strain relationships of the specimens SC40SA-0.2, SC40SB-0.2, SC40SE-0.2, SC40SA-0.4, SC0SA-0.2, and SC50SA-0.2 are shown in Fig.8 and Fig.9 respectively. Those six specimens included all the variables, namely the different sections, the eccentricity ratios and the strength of concrete. Other specimens produced similar load-strain rela-tionships; thus, they weren't shown here. The flange D of all specimens is under stress before reaching the ultimate condition which could be obtained from the variation of the longitudinal strain S1, as shown in Fig.8. The value of S1 dropped rapidly after attaining the ultimate load. Before the ultimate load for SC40SA-0.4, the S1 strain approximates to zero, which means that S1 is located near neutral axis. The S3 variance shows that flange B has approached yield before the final state.

As presented in Fig.9, the strains of web A developed yielding after 0.6 N_u for most specimens, while the web A was in the elastic stage before 0.8 N_u for SC40SA-0.4. The strains measured by S5-S9 show a linear relationship before yielding. The trend of strains changed at N_u because of the occurrence of local buckling.

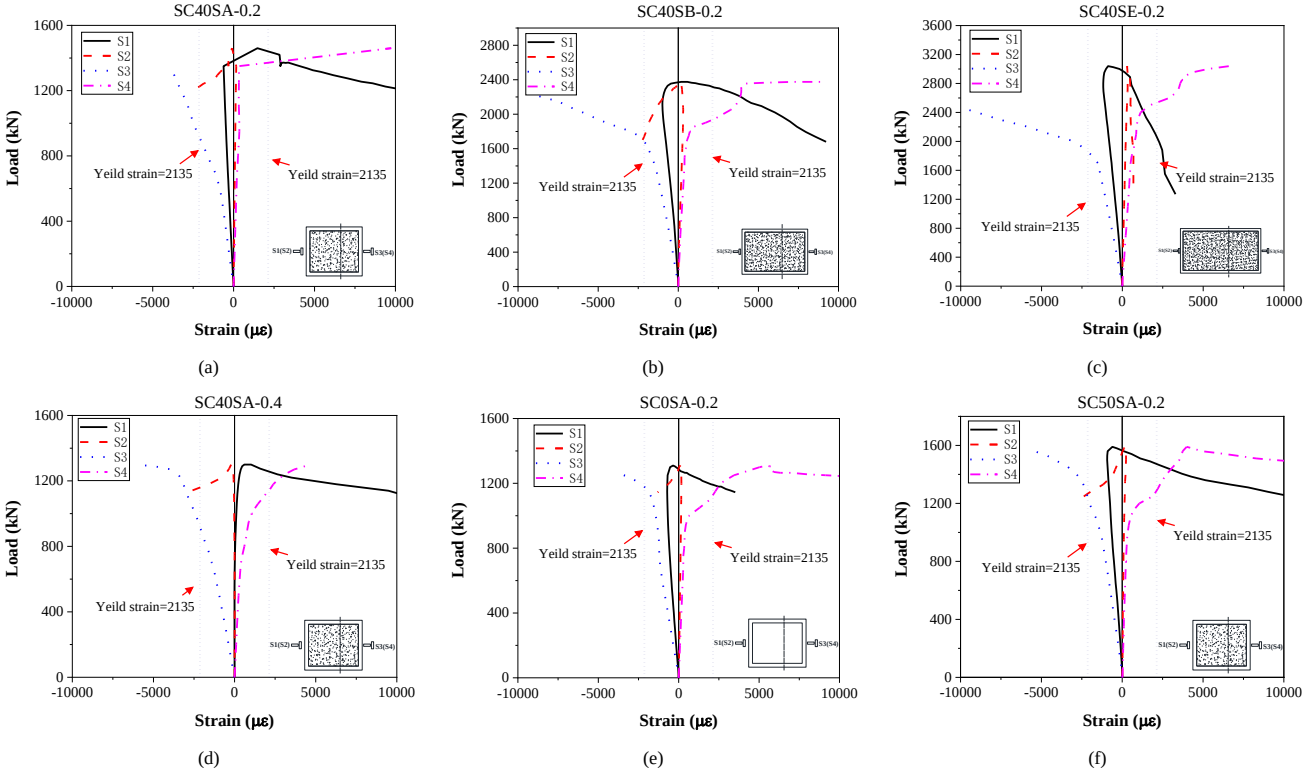

Fig. 8 Variations of strains on the flanges (S1–S4)

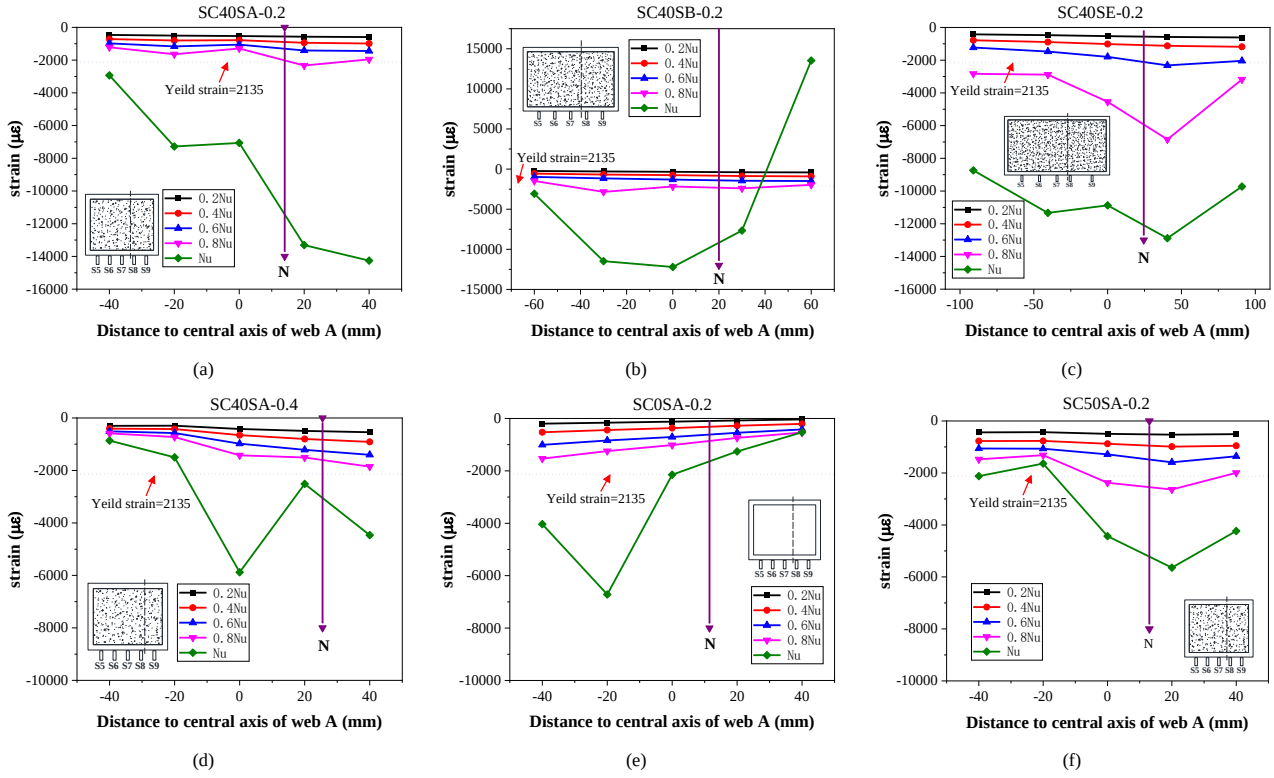

Note: the arrows refer to the actual eccentricity location of the load N

Fig. 9 Variations of longitudinal strains on the web A (S5-S9)

3.4. Ultimate resistance

Test ultimate compressive resistance, including ultimate axial load N_u and ultimate bending moment M_u, is listed in Table 1. The value N_u is directly obtained from experimental data, whereas M_u the sum of the moment and secondary moment is calculated through equation (4), where δ refers to the max lateral deflection recorded by LVDT1 to LVDT5.

$$M_u = N_u e_0 + N_u \delta \quad (4)$$

3.5. Discussions

3.5.1. Effect of in-fill concrete

The in-fill concrete strength influences not only the failure modes but also

the ultimate specimen capacity, as seen in Fig.5 and Fig.10. Comparing hollow steel tube column failure modes with those of CFT columns, it can be found that in-fill concrete could increase resistance ability to local buckling of steel tubes. The ultimate axial load N_u of SC40SA-0.2, SC40SB-0.2, and SC40SE-0.2 increase 11.5%, 28.4%, and 36.3%, respectively, compared with SC0SA-0.2, SC0SB-0.2, and SC0SE-0.2, which indicated that in-fill concrete improves the bearing capacity of columns remarkably in higher h/b and h/t. However, there were few changes in the bearing capacity when the grade of concrete increases from C40 to C50. From Fig.10(a) and Fig.10(b), it is worth noting that the percentage of bearing capacity raise become smaller as η changes from 0.2 to 0.4.

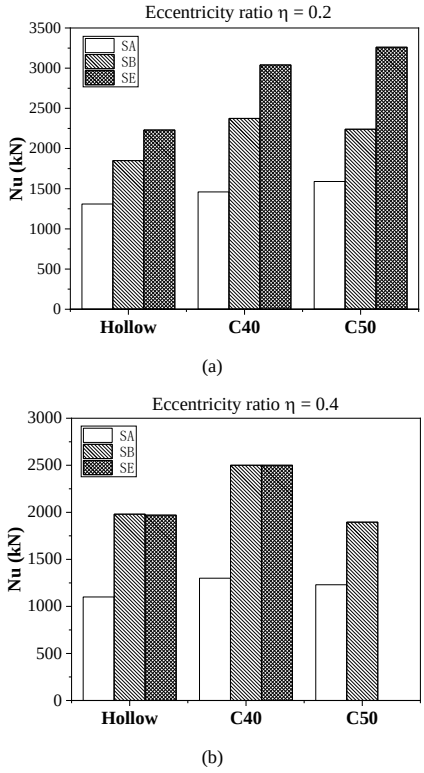

Fig. 10 Effect of in-fill concrete

3.5.2. Effect of width-to-thickness ratio h/b

Normalized ratios M_u/M_c and N_u/N_c are calculated to analyze the effect of width-to-thickness ratio h/b, where M_c and N_c refer to the bending moment and design axial load calculated by one of Chinese codes DB 29-57[30], respectively. All normalized ratios are larger than one, which indicated that using DB 29-57 to design RCFT columns fabricated with Q420 HSS will get a safer result. As presented in Fig. 11(a) and (b), when $\eta = 0.2$, with the growth in h/b, the value of N_u/N_c increased from 1.25 to 1.4 and the value of M_u/M_c undergone an approximate process of linear decline. Figure. 11(c) and (d) show that the value of N_u/N_c and M_u/M_c changed little with the improvement of h/b on the columns when $\eta = 0.4$. It indicates in the study that h/b has a little influence on N_u/N_c when it is smaller than 30.5. Thus, DB 29-57 tends to be less conservative with higher h/b according to the variation trends of M_u/M_c as displayed in Fig. 11(b).

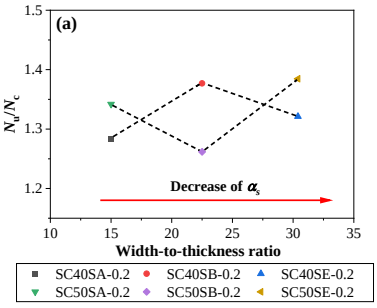

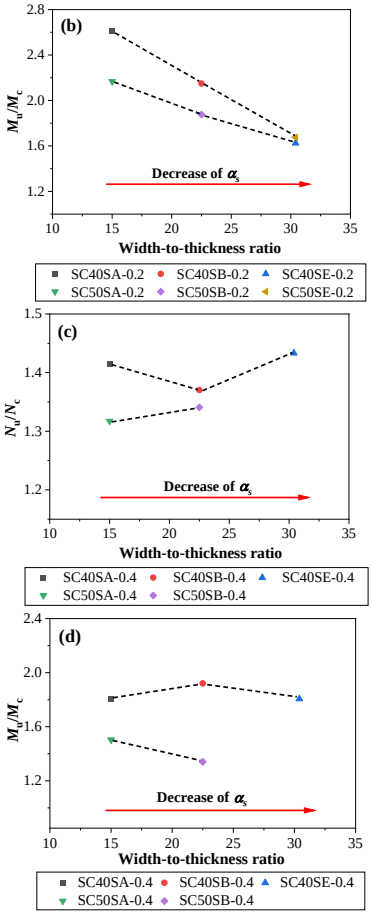

Fig. 11 Influence of width-to-thickness ratio

3.5.3. Effect of eccentricity ratio η

The effect of the eccentricity ratio η on the behaviors is estimated by analyzing the comparison result of SC40SB-0.2 with SC40SB-0.4. Figure 12 depicts the load versus vertical displacement curves. With η increasing from 0.2 to 0.4, the value of N_u dropped 160 kN, while M_u increased 0.15 kN·m. The load dropped slower after the ultimate state for the columns with a relatively higher eccentricity ratio. According to this, the ductility of RCFT columns may be improved when undergoing a higher eccentricity ratio.

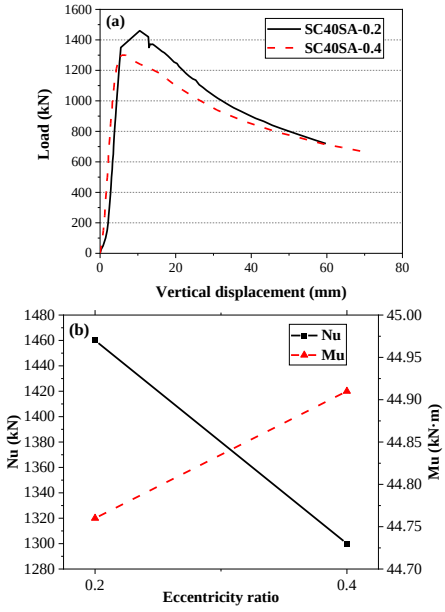

Fig. 12 Effect of eccentricity ratio

4. Finite element analysis

4.1. Analytic model

ABAQUS software was utilized to establish the FE models for the aim of analyzing the behavior of RCFT columns during the eccentric loading process. The entire specimen was simulated, including the cover plate and the knife-edge, and the general view of a model is depicted in Fig.13(a). Eight-node reduced integration brick element (C3D8R), and four-node thick reduced integration shell element (S4R) were chosen to model in-fill concrete and steel tubes respectively, as shown in Fig.13(b). A mesh size of $h/10$ can achieve relatively precise results with the minimum computational cost for most of the specimens according to mesh sensitive analysis result. Loading lines on the top and bottom were coupled to two reference points, respectively, as seen from Fig.13(c). All degrees of freedom of RP1 and RP2 were restrained except rotation around the Y axis and displacement in the Z direction of RP1.

Regarding the Q420B steel material stress - strain model, the simpler bilinear model, regardless of strain-hardening, was adopted according to Ref[28]. Elasticity modulus E_s and yield strength f_y values were set in accordance with the tested values in Section 2.2. As for in-fill concrete in this study, the stress-strain model proposed by Han [31] and the damaged plastic model were adopted into the simulation. The values of key parameters in damaged plastic model are listed in Table 2.

Table 2
Key parameters value in damaged plastic model

Parameter	Value
Dilation angle (ψ)	20°
Flow potential eccentricity (e_f)	0.1
Biaxial compression strength to uniaxial compression strength of concrete (f_{b0}/f_{c0})	1.13 for C40 1.11 for C50
Ratio of the second stress invariant on the tensile meridian to that on the compressive meridian (K)	0.719 for C40 0.714 for C50
Viscosity parameter (ν)	0

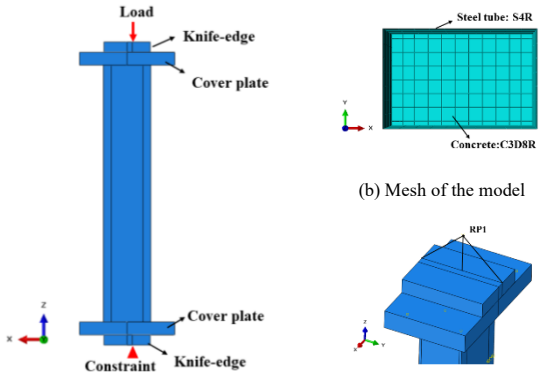

(a) General view of FE model (b) Mesh of the model (c) Reference point

Fig. 13 FE model of the specimen

The interface of concrete and steel tube was set as surface-to-surface contact. A "hard contact" was used in the normal direction, which permits separation in tension together with nonpenetration in compression. In contrast, in the tangential direction, Coulomb friction was applied with friction factor 0.25, according to Ellobody and Young[23]. In order to consider the influence of initial imperfection, an initial imperfection with the value of L/1000 is applied for all specimens. The shape of imperfection was regarded as the first mode acquired by an eigenvalue buckling analysis, which contains both global and local buckling.

4.2. Validations

The mode of failure of the whole columns is similar to that of experimental results. Figure 14 presents a comparison of typical failure mode between the FE analysis and the experiment for the specimen SC40SB-0.2. The FE predicted ultimate axial load N_{FE}, the corresponding ultimate moment M_{FE}, calculated value N_u/N_{FE} and M_u/M_{FE} are given in Table 3. FE analysis results match well with experimental data, where the mean value and standard deviation N_u/N_{FE} and M_u/M_{FE} are 0.999, 0.936, 0.041, and 0.032, respectively.

The FE predicted load-vertical displacement curves and load-lateral deflection curves compared to the experimental curves of SC40SA-0.2, SC40SB-0.2, SC40SE-0.2, SC40SA-0.4, SC0SA-0.2, and SC50SA-0.2 are presented in Fig.15 and Fig.16. All curves obtained through FE analysis show good agreement with that from the experiment before the failure, which indicates that the FE models proposed in this study could be utilized to simulate the rectangular columns with Q420B high-strength steel tubes.

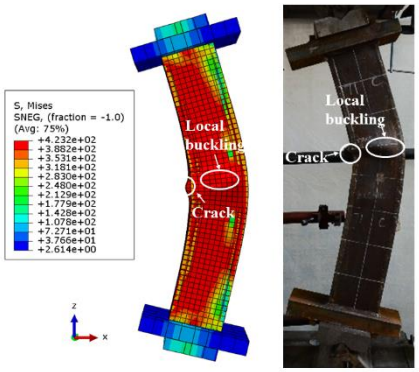

Fig. 14 Failure mode comparisons between FE analysis and experiment of SC40SB-0.2

Table 3
FE analysis results and the comparison with the experimental results

Specimen No.	N_{FE}/kN	M_{FE}/(kN·m)	N_{FE}/N_u	M_{FE}/M_u
SC40SA-0.2	1545.515	30.254	1.058	0.903
SC40SB-0.2	2392.000	70.266	1.007	0.917
SC40SE-0.2	3017.030	90.430	0.992	0.969
SC50SA-0.2	1621.261	32.245	1.020	0.900
SC50SB-0.2	2451.37	63.370	1.094	0.919
SC50SE-0.2	3174.300	93.891	0.974	0.916
SC40SA-0.4	1277.542	43.743	0.983	0.974
SC40SB-0.4	2482.421	56.430	0.993	0.942
SC40SE-0.4	2409.730	143.159	0.964	0.901
SC50SA-0.4	1327.032	43.578	1.079	1.014
SC50SB-0.4	1879.782	98.856	0.992	0.918
SC0SA-0.2	1291.244	22.683	0.986	0.942
SC0SB-0.2	1765.331	64.612	0.954	0.905
SC0SE-0.2	2170.81	70.268	0.973	0.919
SC0SA-0.4	1118.162	34.239	1.007	0.926
SC0SB-0.4	1849.750	43.104	0.934	0.955
SC0SE-0.4	1929.465	105.978	0.979	0.986
Mean value			0.999	0.936
Standard deviation			0.041	0.032

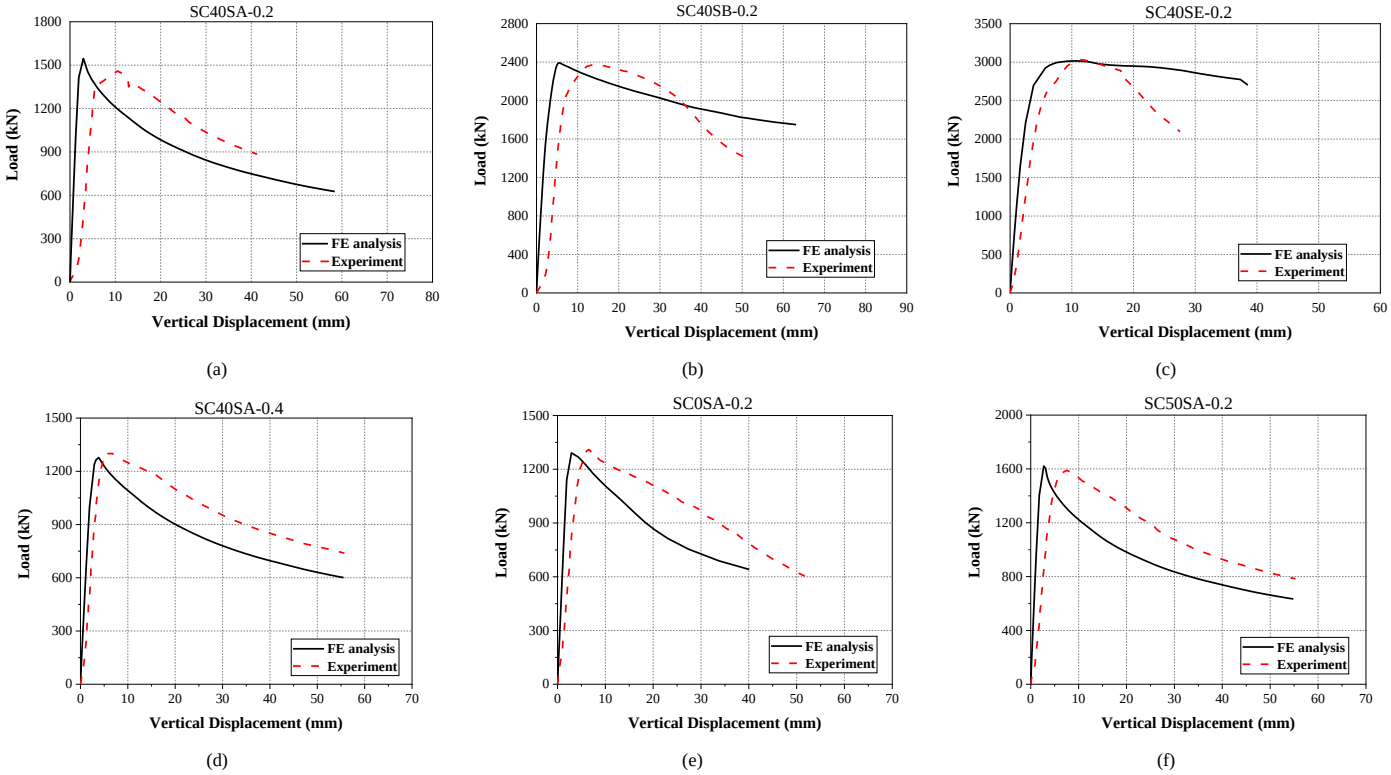

Fig. 15 Comparison between experiment and FE predicted result in load-vertical displacement curves

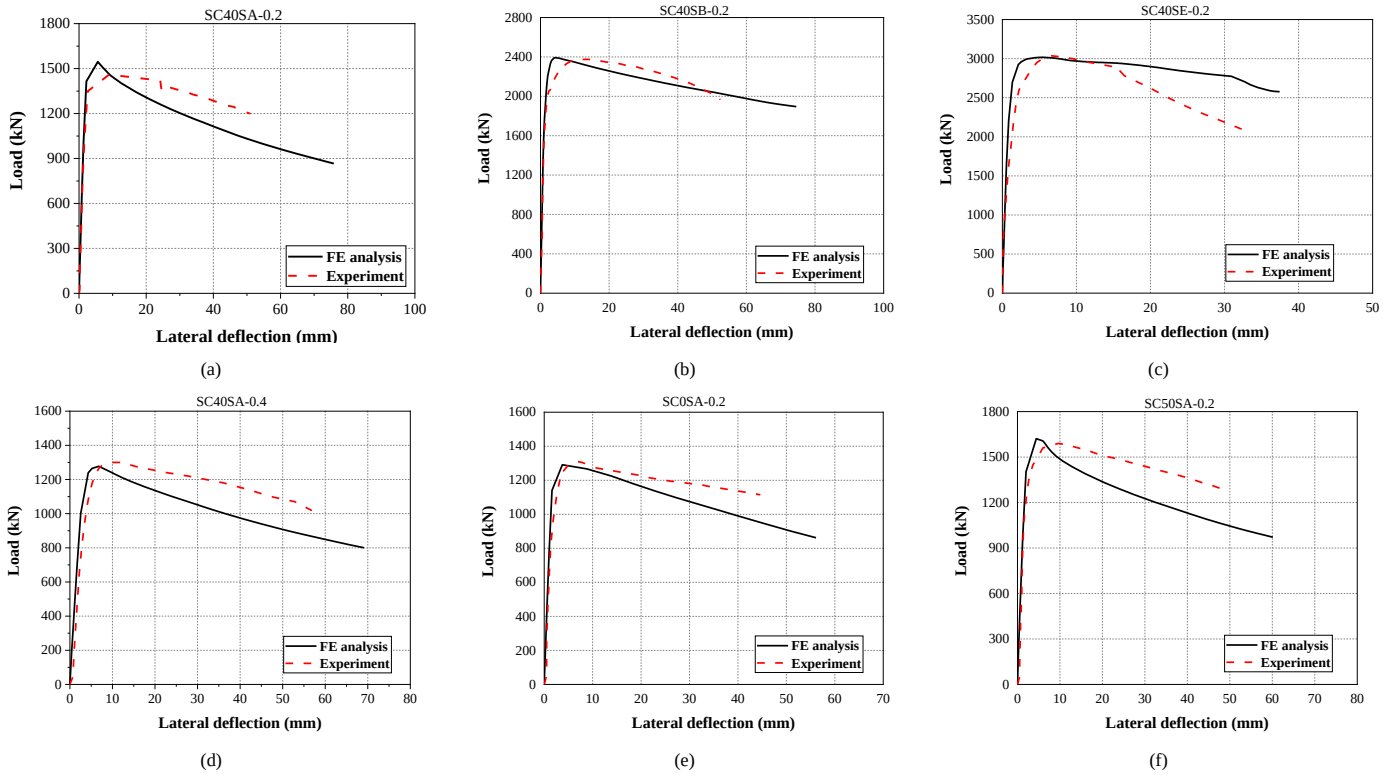

Fig. 16 Comparison between experiment and FE predicted load-lateral deformation curves

5. Evaluation of design codes and proposed design approach

5.1. Evaluation of the current design codes

At present, a series of design specifications about composite structures have been widely used in different countries, for instance, European code (EC4[32]), Specification for Structural Steel Buildings in America (AISC360[33]), AIJ[34] in Japan, GB 50936-2014[35] and DB 29-57[30] in China, et al. In the above-mentioned codes, which are based on the resistance interaction curves, namely N-M interaction curves, the method of calculating bearing capacity of RCFT beam - columns under compression and bending was stipulated. In order to verify the applicability of these codes, the N-M interaction curves determined by design equations were compared to the experimental results which can be seen in Fig.17. The green points represent the bearing capacities of the specimens with the meaning of the ultimate axial loads and the corresponding bending moments.

As shown in Fig.17, all the abovementioned codes are conservative in predicting the bearing capacities of RCFT columns fabricated with Q420B HSS in this paper. The results calculated by EC4, AISC360, and AIJ are close to each other, while the results from GB 50936 and DB 29-57 are much more conservative, especially GB 50936 provides the most conservative results for the columns with $h/t=1.2$ and $h/b=15$. With the raising of h/b, h/t and concrete strength, the results obtained from experiments are closer to but consistently higher than the predicted results from design codes. Too con-

servative design leads to a waste of building materials and an increase in the project costs. Thus it is necessary to propose more accurate approaches and revise the design codes in China for designing RCFT columns incorporating HSS.

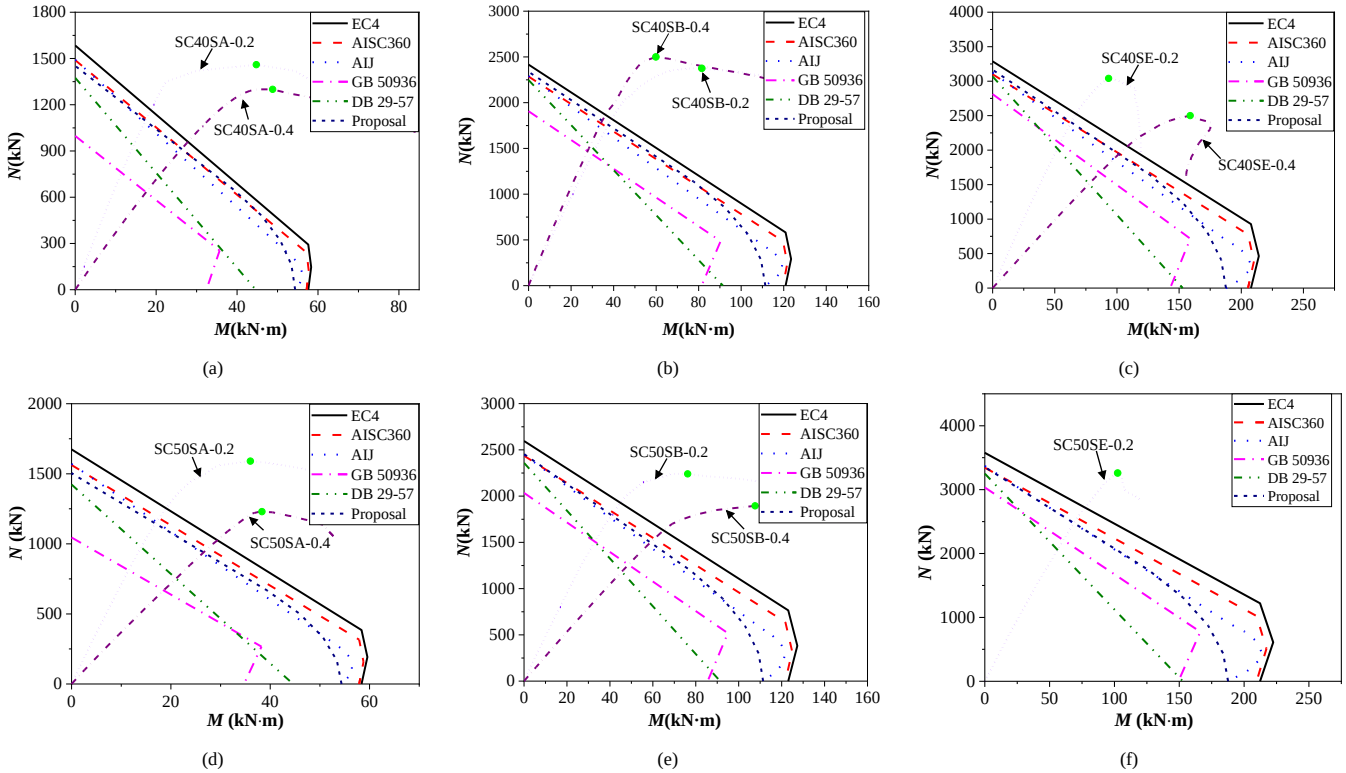

Fig. 17 Comparison of N-M interaction curves

5.2. Proposed design approach and validation

As quantitatively analyzed in Ref [27], the steel tubes in RCFT columns fabricated with HSS undertake most load because of higher steel strength and higher steel ratio. Chinese design code DB 29-57 assumes that part of axial loads and all bending moments are bored by the steel tubes, while the concrete bears only part of axial loads. The above assumptions are particularly suited for designing RCFT columns fabricated with HSS. The test results show that majority of steel webs could develop yielding before buckling when approaching the ultimate load; hence, the fully-plastic state could be assumed as the ultimate state of the CFT columns, as shown in Fig.18.

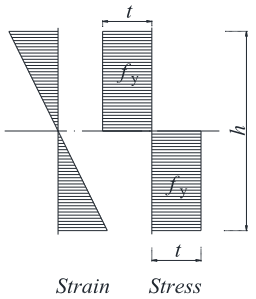

Fig. 18 Fully-plastic state of steel web

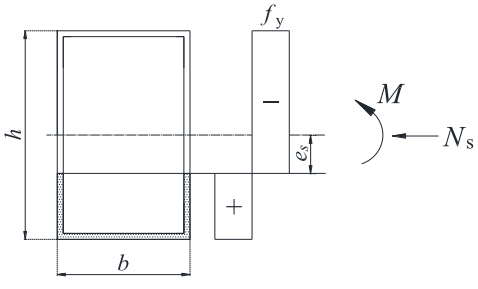

(a) $0 \le e_s < h/2-t$

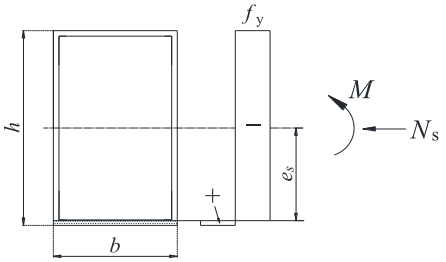

(b) $h/2-t \le e_s \le h/2$

Fig. 19 Stress blocks of steel tubes

The stress blocks to calculate the ultimate capacity were illustrated in Fig.19. The total bearing capacity could be obtained using the factor α_s defined in Eq. (1) as specified in DB 29-57; thus, only the stress of steel tubes was calculated in this study. e_s refers to the distance from the centerline to the neutral axis of the cross-section. The stress blocks in Fig.19 are more universal than those presented in Ref [26], which accounts for the influence of the steel backing plates.

The load sustained by the steel (N_s) could be obtained through the integration of the axial stress of the steel. The total axial capacity N could be calculated by the equation $N_s = \alpha_s \cdot N$. The bending moment M could be obtained in the stress blocks of the steel section, which is around the principal axis. As presented in Fig.19, when $0 \le e_s < h/2-t$ the axial capacity N and the corresponding moment M can be calculated according to Eq. (5)-(7):

$$N_s = 4 f_y e_s t \tag{5}$$

$$N = \frac{4 f_y e_s t}{\alpha_s} \tag{6}$$

$$M = 2 f_y t \left[b(h-t)/2 + (h/2-t)^2 - e_s^2 \right] \tag{7}$$

When $h/2-t \le e_s < h/2$, N, and M can be calculated by Eq. (8)-(10):

$$N_s = f_y\left[2(h+b)t - 4t^2 - b(h-2e_s)\right] \quad (8)$$

$$N = \frac{f_y\left[2(h+b)t - 4t^2 - b(h-2e_s)\right]}{\alpha_s} \quad (9)$$

$$M = f_y b(h^2/4 - e_s^2) \quad (10)$$

The N-M curves were determined through the corresponding moment M and axial force N when e_s changes from h/2 to zero. Besides, the reduction factor φ_x stipulated in DB 29-57 was also introduced in the equations to reflect the influence of the length effect.

A comparison between the experimental results and predictions calculated by the proposed approach is presented in Fig.17. Comparing with the experimental results, the results obtained from the above-proposed N-M design curves are relatively conservative and more precise than GB 50936-2014 and DB 29-57 used in China, but close to the results of EC4, ASIC 360 and AIJ.

6. Conclusions

This paper presents a systematic examination to reveal the mechanical behaviors of RCFT columns manufactured with Q420B HSS under excentric load, including experiments, numerical simulation, and theoretical analysis. Seventeen specimens were designed and tested taking into account the impact of concrete strength, cross - section aspect ratios, width to thickness ratios , and eccentricity ratios. In order to reveal the behavior of RCFT columns during the eccentric loading process, nonlinear FE analysis was performed. Comparing experimental results, the criteria GB 50936, DB 29-57, EC4, AISC 360, AIJ and the proposed approach have been evaluated. The key findings are categorized as follows:

(1) By delaying the occurrence of local buckling of steel tubes, in-fill concrete could effectively enhance the ultimate capacity of columns. Considerable difference could be observed between the columns with and without concrete - filling , whereas the concrete grade has a marginal influence , particularly on the one with a larger aspect ratio.

(2) Based on the results of this study, the width-to-thickness ratio has little influence on the ultimate capacity N_u to design axial load N_c calculated through Chinese code DB 29-57 when the value is below 30.5. However, a higher width-to-thickness ratio has disadvantageous effects on the bearing moment M_u.

(3) The proposed FE models had a reasonable accuracy in predicting the ultimate capacities of RCFT columns made of Q420B HSS. Not only failure modes but load-vertical displacement curves and load-lateral deflection curves also matched the experimental results.

(4) All design codes, including EC4, AISC360, AIJ, GB 50936-2014, and DB 29-57, are conservative when calculating the ultimate capacities of RCFT columns fabricated with Q420B HSS under eccentric loads. GB 50936 and DB 29-57 obtain the most conservative results, while EC4 is relatively the least conservative one. Compared with the current design codes used in China, the calculation method of N-M interaction curves proposed in this paper could obtain much more precise ultimate capacities. Therefore, the proposed approach is recommended to be a reference for future practice.

Acknowledgements

This work is sponsored by the National Natural Science Foundation of China (Grant No. 51808182) and the National Key Research and Development Project (Grant No. 2019YFD1101002). The authors also appreciate the financial support provided by The Opening Fund of State Key Laboratory of Green Building in Western China (Grant No. LSKF202005). This work was also supported by the China Postdoctoral Science Foundation (Grant No. 2020M670680).

References

[1] Han L-H, Li W, Bjorhovde R., Developments and advanced applications of concrete-filled steel tubular (CFST) structures: Members, Journal of Constructional Steel Research, 100, 211-228, 2014.
[2] Uy B., Static long-term effects in short concrete-filled steel box columns under sustained loading, ACI Structural Journal, 98(1), 96-104, 2001.
[3] Sakino K, Nakahara H, Morino S, Nishiyama I., Behavior of centrally loaded concrete-filled steel-tube short columns, Journal of Structural Engineering. 130(2), 180-188, 2004.
[4] Guler S, Copur A, Aydogan M., A Comparative Study on Square and Circular High Strength Concrete-Filled Steel Tube Columns, Advanced Steel Construction, 10(2), 234-47, 2014.
[5] Du Y, Chen Z, Xiong M., Experimental behavior and design method of rectangular concrete-filled tubular columns using Q460 high-strength steel, Construction and Building Materials, 125, 856-872, 2016.
[6] Hernández-Figueirido D, Romero ML, Bonet JL, Montalvá JM., Ultimate capacity of rectangular concrete-filled steel tubular columns under unequal load eccentricities, Journal of Constructional Steel Research, 68(1), 107-117 2012.
[7] Lai Z, Varma AH, Zhang K., Noncompact and slender rectangular CFT members: Experimental database, analysis, and design. Journal of Constructional Steel Research, 101,455-468, 2014.
[8] Lee C, Kang THK, Kim S, Kang K., Strain compatibility method for the design of short rectangular concrete-filled tube columns under eccentric axial loads, Construction and Building Materials, 121, 143-153, 2016.
[9] Long Y, Wan J, Cai J., Theoretical study on local buckling of rectangular CFT columns under eccentric compression, Journal of Constructional Steel Research, 120, 70-80, 2016.
[10] Ding F, Luo L, Zhu J, Wang L, Yu Z., Mechanical behavior of stirrup-confined rectangular CFT stub columns under axial compression, Thin-Walled Structures, 124, 136-150, 2018.
[11] Wang R, Han LH, Nie JG, Zhao XL., Flexural performance of rectangular CFST members, Thin-Walled Structures, 79, 154-65, 2014.
[12] Bong Kwon Y, Kyu Jeong I., Resistance of rectangular concrete-filled tubular (CFT) sections to the axial load and combined axial compression and bending, Thin-Walled Structures, 79, 178-186, 2014.
[13] Du Z, Liu Y, He J, Chan S., Direct analysis method for noncompact and slender concrete-filled steel tube members, Thin-Walled Structures, 135, 173-184, 2019.
[14] Shi G, Zhu X, Ban H., Material properties and partial factors for resistance of high-strength steels in China, Journal of Constructional Steel Research, 121, 65-79, 2016.
[15] Wang YB, Lyu YF, Wang YZ, Li GQ, Richard Liew JY., A reexamination of high strength steel yield criterion, Construction and Building Materials, 230, 2020.
[16] Li G, Wang Y, Chen S., Experimental study on ultimate bearing capacity of axially compressed high strength steel columns, Jianzhu Jiegou Xuebao/Journal of Building Structures, 33(3), 8-14, 2012. (in Chinese).
[17] Lue DM, Liu J, Yen T., Experimental study on rectangular CFT columns with high-strength concrete, Journal of Constructional Steel Research, 63(1), 37-44, 2007.
[18] Liew JYR, Xiong M, Xiong D., Design of Concrete Filled Tubular Beam-columns with High Strength Steel and Concrete, Structures, 8, 213-26 2016.
[19] Xiong M, Xiong D, Liew JYR., Axial performance of short concrete filled steel tubes with high- and ultra-high- strength materials, Engineering Structures. 136, 494-510, 2017.
[20] Lyu X, Shu GP, Liew JYR, Du E., Fire Resistance of Steel Tubular Columns Infilled with Ultra-High Strength Concrete. Advanced Steel Construction. 14(3), 438-460, 2018.
[21] Du Y, Chen Z, Yu Y., Behavior of rectangular concrete-filled high-strength steel tubular columns with different aspect ratio, Thin-Walled Structures, 109, 304-318, 2016.
[22] Lee H, Park H, Choi I., Compression loading test for concrete-filled tubular columns with high-strength steel slender section, Journal of Constructional Steel Research, 159, 507-520, 2019.
[23] Ellobody E, Young B., Nonlinear analysis of concrete-filled steel SHS and RHS columns, Thin-Walled Structures, 44(8), 919-930, 2006.
[24] Liu D., Behaviour of eccentrically loaded high-strength rectangular concrete-filled steel tubular columns, Journal of Constructional Steel Research, 62(8), 839-846, 2006.
[25] Choi I, Chung K, Kim C., Experimental study on rectangular CFT columns with different steel grades and thicknesses, Journal of Constructional Steel Research, 130, 109-119, 2017.
[26] Du Y, Chen Z, Richard Liew JY, Xiong M., Rectangular concrete-filled steel tubular beam-columns using high-strength steel: Experiments and design, Journal of Constructional Steel Research, 131, 1-18, 2017.
[27] Du Y, Chen Z, Wang Y, Richard Liew JY., Ultimate resistance behavior of rectangular concrete-filled tubular beam-columns made of high-strength steel, Journal of Constructional Steel Research, 133, 418-433, 2017.
[28] Li G, Chen B, Yang Z, Feng Y., Experimental and numerical behaviour of eccentrically loaded high strength concrete filled high strength square steel tube stub columns, Thin-Walled Structures, 127: 483-499, 2018.
[29] Li G, Yang Z, Lang Y., Experimental Behavior of High Strength Concrete-Filled Square Steel Tube under Bi-Axial Eccentric Loading, Advanced Steel Construction, 6(4), 963-975, 2010.
[30] DB 29-57. Technical Specification for Design of Steel Structure Dwelling Houses, Tianjin Urban Rural Construction Commission, Tianjin, China, 2003.(in Chinese)
[31] Han L, Yao G, Tao Z. Performance of concrete-filled thin-walled steel tubes under pure torsion. Thin-Walled Structures, 45(1): 24-36, 2007
[32] Eurocode 4, EN 1994-1-1 Design of composite steel and concrete structures, Part 1.1. General rules and rules for buildings, British Standards Institution, 2004.
[33] ANSI/AISC 360-16, Specification for Structural Steel Buildings. American Institute of Steel Construction, Chicago, USA, 2010.
[34] AIJ. Recommendations for design and construction of concrete filled steel tubular structures. Architectural Institute of Japan , Japan, 2008.
[35] GB50936-2014, Technical code for concrete filled steel tubular structures. Standard Press of China, Beijing, China, 2014.(in Chinese)

Advanced Steel Construction – Vol. 16 No. 4 (2020) 297–309
DOI: 10.18057/IJASC.2020.16.4.2

EXPERIMENTAL AND NUMERICAL STUDY OF MECHANICAL PROPERTIES FOR THE DOUBLE-RIBBED REINFORCED BEAM-COLUMN CONNECTION

Hong-Wei Ma [1], Hao Zheng [1], Wei Zhang [1, 2 *] and Zhan-zhan Tang [1, 2]

[1] *College of Civil Science and Engineering, Yangzhou University, Yangzhou, China*
[2] *Institute of Theoretical and Applied Mechanics, Czech Academy of Sciences, Prague, Czech Republic*
**(Corresponding author: E-mail: zhangwei621@gmail.com)*

A B S T R A C T

This paper investigates the hysteretic behavior of steel reinforced beam-column connections with or without double-ribs and optimizes the reinforced ribs of these connections under cyclic loading. The objective is to give a reasonable range of double-ribs' size and fracture behavior of the weld at beam-column connections. Two specimens (the conventional beam-column connection and the double-ribbed reinforced beam-column connection) are designed and tested under cyclic loads. Meanwhile, the finite element models of these two kinds of connections are established. The hysteretic performance and damage evolution of the connections, such as the failure modes, hysteretic curves, skeleton curves, stiffness degradations, ductility, and energy dissipation capacities, are analyzed and verified. Moreover, fifteen numerical models with different lengths of the line (l_a), the width (b), and the thickness (t_s) of reinforced ribs are established for parametric study. The results show that double-ribs can improve the strength and ductility of the connection. And the FE predictions agree well with the experimental results. The reasonable parameters of reinforced ribs of double-ribbed reinforced beam-column connection are proposed.

ARTICLE HISTORY

Received: 21 March 2020
Revised: 31 May 2020
Accepted: 22 June 2020

KE Y W O R D S

Double-ribbed;
Beam-column connections;
Steel;
Hysteretic behavior

1. Introduction

The lateral stiffness of a steel frame depends on the strength and ductility of beams, columns, and beam-column connections. Therefore, these connections should be rigid connections [1]. It has been reported in some literature that during the Northridge earthquake in the United States in 1994 and the Kobe earthquake in Japan in 1995, brittle damage occurred in many rigid beam-column connections of steel moment frames [2-4]. To avoid the seismic vulnerability of steel beam-column connections, the seismic design principle of "strong column weak beam and strong connection weak member" [5-6] in the Chinese code is proposed.

Based on the above seismic design principle, the solution of moving the beam plastic hinge away from the column is proposed by weakening or reinforcing the connections. Over the years, numerous studies on the mechanical performance of steel beam-column connections with reduced beam sections have been carried out in the references [7-14]. In comparison, relatively few studies [15-21] on the mechanical properties of beam-column connections with the reinforcement of steel frames have been performed, and there are especially few results concerning double-ribbed reinforced beam-column connections. Besides, those studies mainly focused on the mechanical performance of the connections themselves without considering the difference in rib size, which may affect the fracture behavior of the connections. As a result, the major objective of this study is to build and verify the finite element (FE) models of double-ribbed reinforced beam-column connections by comparing the experimental and numerical results and to optimize the parameters of reinforced ribs by analyzing the stress triaxiality index (R_σ), equivalent plastic strain index (*P.I.*) [22], cracking index (*R.I.*) [23], and cracking development of these connections [24].

To achieve a deep understanding of the hysteretic behavior and the reasonable parameters of the ribs of double-ribbed reinforced connections, two full-scale connection specimens are designed and fabricated, which are assembled and tested under cyclic loads. Of the two specimens, one has two reinforced ribs, and the other is a conventional connection. Meanwhile, two FE models are established for the above two specimens. These specimens and numerical models are used to study the hysteretic behavior, such as the plastic hinge positions, hysteresis curves, failure modes, load-bearing capacities, ductility capacities, stiffness degradations, coefficient curves, and damage curves. They are also used to verify the FE models by comparing with each other.

Furthermore, fifteen FE models with different rib sizes are established and analyzed to discuss the stress triaxiality ratio (R_σ), plastic equivalent strain index (*P.I.*), and cracking index (*R.I.*). Based on the benefits or accelerated failure found through analyzing the fracture behavior, the parameters of these connections are optimized. The results can provide supportive data and a theoretical basis for the design of symmetric double-ribbed reinforced connections.

2. Experimental program

2.1. Specimen Design

Two specimens of beam-column connections of a steel frame are designed, including one normal beam-column connection (NBN) for experimental verification and one double-ribbed reinforced beam-column connection (RRN).They are fabricated using Q345B structural steel. The beam, column, and stiffener are welded with an E5015 electrode and full penetration groove welding, while the shear plate and beam web are connected by 4-M20 high strength bolts (the performance grade of these bolts is 8.8). The section dimensions of the beam and column are HN 248 mm × 124 mm × 5 mm × 8 mm and HW 250 mm × 250 mm × 9 mm ×14 mm, respectively, and the shear plate is 170 mm × 170 mm × 5 mm. The lengths of the beam and the column of these connections are 1400 mm and 1450 mm, respectively, and the beam-column section stiffness ratio is 0.32. According to the American code [25], the structural size of the reinforcing rib should meet the following requirements: the length of a = (0.6-0.7) h_b, which is the beam section height, and the width of b = (0.45-0.55) a, $a' \approx 0.2a$, $b' \approx 0.2b$, and the thickness is $t_s \geqslant 1.5t_f$, which is the beam flange thickness. The details of the beam and column are shown in Table 1. According to the above rules, the length a =160 mm, the width b=80 mm, a' = 35 mm, b' = 20 mm, and the thickness t_s = 2 × 6 mm, are used in this study. The details of these two specimens and the model parameters are shown in Fig. 1.

Table 1
Parameters of Specimens

Specimen number	Beam section (mm)	Column section (mm)	Parameters of ribs (mm)				
			a	*b*	*a'*	*b'*	t_s
NBN	HN 248×24×5×8	HW 250×250×9×14	/	/	/	/	/
RRN	HN 248×124×5×8	HW 250×250×9×14	160	80	35	20	12

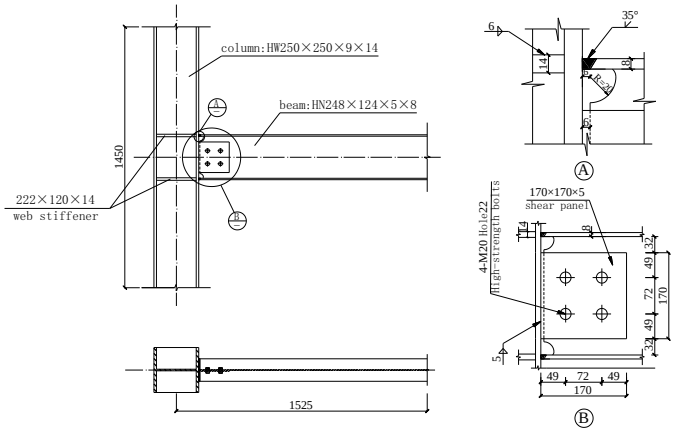

(a) Normal beam-column connection (NBN)

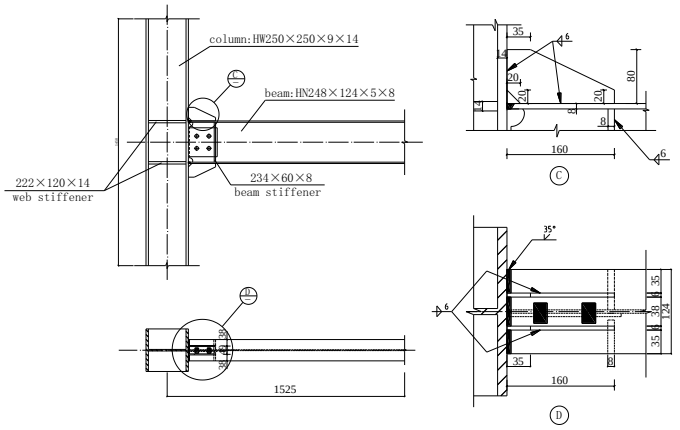

(b) Double-ribbed reinforced beam-column connection (RRN)

Fig. 1 Details of specimens

2.2. Mechanical properties of the material

Five plate samples (thicknesses of 5 mm, 6 mm, 8 mm, 9 mm and 14 mm) are taken from the shear plate, ribs, webs, and flanges of the beam and column in accordance with relevant codes [26,27], and three groups of tensile testing specimens are prepared for each sample type. The detailed dimensions of the samples are shown in Fig. 2(a). The samples are subjected to uniaxial tensile loads by a WDW-300 microcomputer controlled electronic universal testing machine (the test setup and the failure mode of the specimens are shown in Fig. 2(b)).The Young's modulus, yield strength, tensile strength, and elongation are obtained. Table 2 shows the tested material properties, and the deviations between the material performance data and the theoretical values of the Q345B plate.

Table 2
Material properties of the plate samples

Specimen No.	Section area A_1 / mm2	Yield strength f_{y1} / MPa	Tensile strength f_{u1} / MPa	Elastic modulus E_1 / MPa	Elongation d / %
A-1	72.81	358.85	590.53	202860	9.82
A-2	72.77	339.41	582.59	203325	8.64
A-3	73.85	360.52	595.39	206894	9.66
B-1	83.01	340.84	572.26	205687	10.13
B-2	86.45	380.26	606.23	203346	9.20
B-3	87.35	366.22	590.16	198892	9.92
C-1	118.88	342.15	585.69	197961	11.58
C-2	117.36	378.94	608.57	201238	11.12
C-3	116.38	362.59	585.58	205897	11.88
D-1	128.52	353.68	588.41	206502	11.90
D-2	131.47	362.15	589.63	198592	11.62
D-3	130.70	349.86	580.22	198950	12.14
E-1	206.88	351.63	573.86	206253	15.56
E-2	205.53	364.12	585.58	205682	15.81
E-3	206.31	372.59	600.26	203960	15.06
Average value		358.92	589	203069	11.60
Deviation from theoretic value (%)		4.04	6.13	-0.94	/

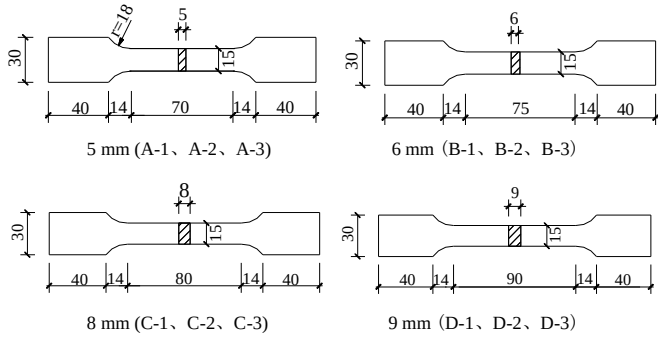

(a) Plate samples

(b) Test setup and failure mode

Fig. 2 Details of plate samples

2.3. Instrumentation

The displacement is measured with the YHD-50 high-precision displacement meters, whereas the strain acquisition is performed with a DH3816N static strain test system. The following measurements are acquired: (1) the load-displacement curve, (2) the strain in the upper/lower flanges and the web of beam, (3) the strain in two reinforced ribs, (4) the relative displacement of two diagonal points in the node domain, (5) the horizontal displacement of the flange at the beam end and the vertical displacement of the column corner. The locations of the strain gauges and displacement meters are shown in Fig. 3.

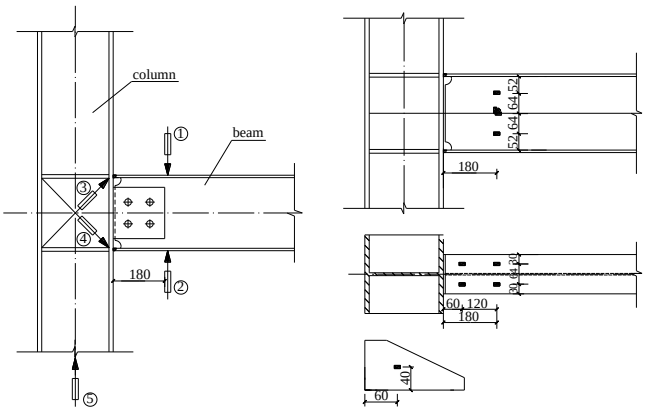

(a) Arrangement of displacement meter (b) Strain gauge arrangement

Fig. 3 Instrumentation (Unit: mm)

2.4. Loading protocol

According to the Chinese code [28], when the resistance of the connection reaches the peak value and then drops to 85% of the ultimate load, the failure state is reached. When the maximum load reaches the ultimate capacity of the loading equipment, the loading should be stopped. The loading method is shown in Fig. 4 and Table 3.

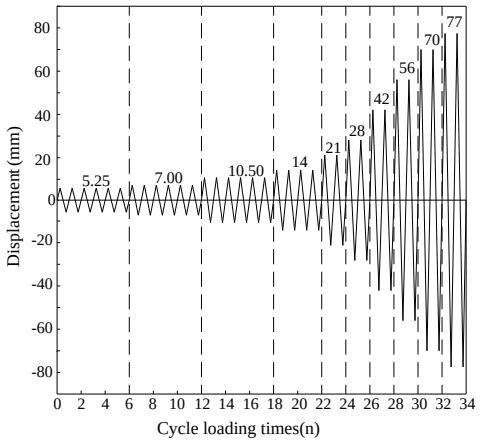

Fig. 4 Loading method

Table 3
Loading scheme

Loading level	Displacement amplitude (mm)	Interlayer displacement angle(rad)	Loading step
1	5.25	0.003 75	6
2	7.00	0.005 00	6
3	10.50	0.007 50	6
4	14.00	0.010 00	4
5	21.00	0.015 00	2
6	28.00	0.020 00	2
7	42.00	0.030 00	2
8	56.00	0.040 00	2
9	70.00	0.050 00	2
10	77.00	0.055 00	2

2.5. Experimental setup

The column is horizontally placed on the hinged supports with a height of 60 mm, which is reliably connected to the rigid ground by anchors. A thrust collar is used to prevent horizontal slip so that the articulated boundary conditions of the column are ensured. The tensile or compressive loads are applied by a 50T-MTS hydraulic servo actuator, which is horizontally fixed on the reaction wall. Moreover, the computer simultaneously collects load, displacement, and strain data. The experimental setup is shown in Fig. 5.

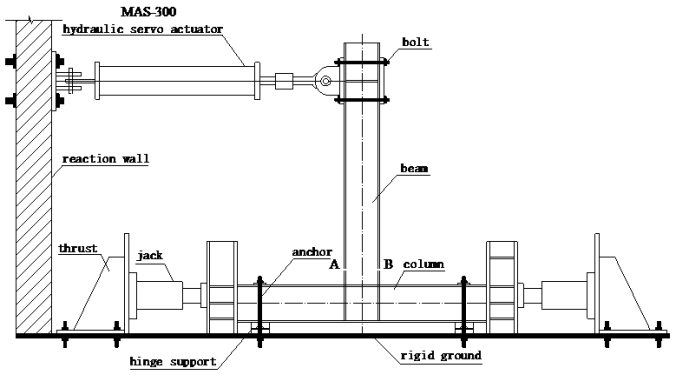

(a) Schematic diagram

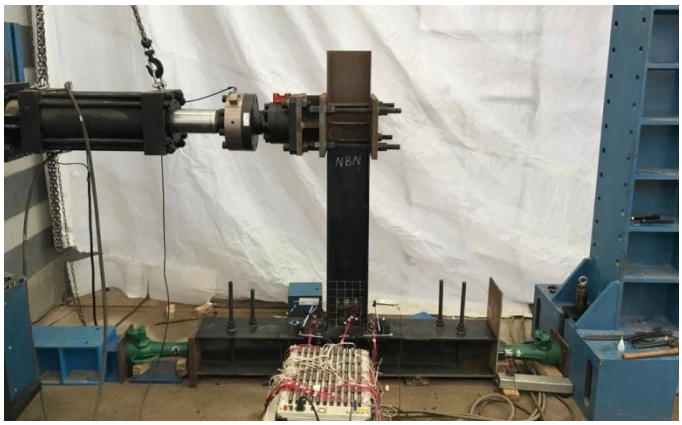

(b) Actual loading device

Fig. 5 Testing setup

3. Numerical simulation

The normal beam-column connection (NBN) and the double-ribbed reinforced beam-column connection are analyzed by ABAQUS software [29, 30].

3.1. Constitutive model of the materials

The constitutive relations of the Q345B steel, E5015 weld, and bolts (all three materials adopt three-fold line models (Song [31])) are shown in Fig. 6. The material parameters of the Q345B steel, E5015 weld and bolts are listed in Table 4, where E is the Young's modulus, f_y is the yield strength, ε_y is the yield strain corresponding to the yield strength, f_u is the ultimate strength, and ε_u is the ultimate strain corresponding to the ultimate strength. The parameters of the connections, such as the geometric nonlinearity, material nonlinearity and the Bauschinger effect [32], and the effects of welding defects are taken into consideration, while the residual stresses caused by welding are not considered.

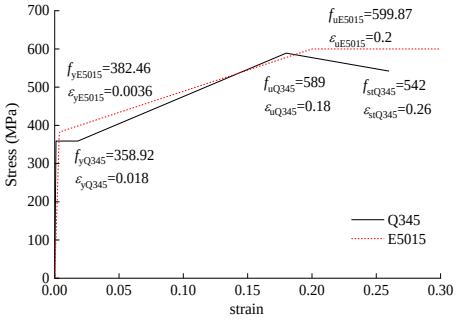

(a) Steel and weld

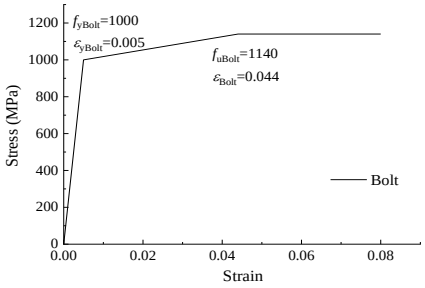

(b) Bolt

Fig. 6 Material constitutive model

Table 4
Constitutive parameters of the materials

Material	E (GPa)	f_y (MPa)	ε_y	f_u (MPa)	ε_u	v
Q345B	203.069	358.92	0.0018	589.0	0.18	0.3
E5015	204.720	382.46	0.0036	599.9	0.20	0.3
Bolt	206.00	1000.0	0.0050	1140.0	0.044	0.3

3.2. Mesh and boundary conditions

The solid eight-node hexahedral linear reduced integral element (C3D8R), which has the advantages of high accuracy, low computational cost, and better ability to withstand buckling deformation [33], is selected to mesh the beam, column, shear plate, bolts, ribs, column stiffeners, and welds. For most parts of the beam and the column, the mesh size is approximately 30 mm. The mesh size at the beam-column connection and the beam within a length of 180 mm from the beam end, rib plate, shear plate, and bolts is approximately 10 mm, and the mesh size at the welds is approximately 2 mm. The whole structure is divided into 15,916 elements, and the FE model is shown in Fig. 7. Face-to-face contact is adopted between the bolt and steel. The Coulomb friction "penalty" function is adopted for the tangent friction of the contact surfaces, and the friction coefficient is 0.3 (no friction is set between the screw and wall hole).In the normal direction, a “hard” contact is used. In the load interface, the displacement and rotation angle of the two ends of the column in the X, Y, and Z directions are constrained first, and the displacement is controlled at the coupling point. The loading system is consistent with that of the test.

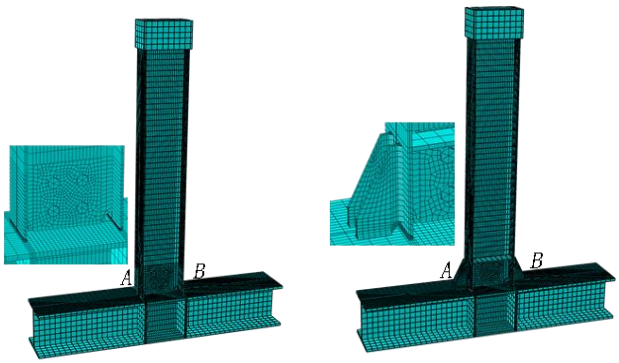

(a) NBN (b) RRN

Fig. 7 Finite element models

3.3. Hysteretic behavior

3.3.1. Specimen deformation

(1) Normal beam-column connection (NBN)

Fig. 8 presents the deformed diagram of the test and numerical simulation of the common connections (NBN) at different loading levels. The highest value is set to 600 MPa since the average experimental ultimate tensile strength of Q345B steel is 589 MPa, and the maximum experimental value is 608 MPa from Table 2. If the stress of any part exceeds the highest value, these parts turn gray. Then, they will be regarded as failed or damaged. The results show that the numerical results and test results for the plastic hinge position and the deformation are basically the same. The whole connection is still in the elastic stage at the fourth loading level, and the stress at the beam end is the largest from the simulation results. The test and numerical results show that the beam experiences severe buckling at 80 mm, and a plastic hinge begins to appear at the seventh loading level, but the deformation in the finite element analysis is more obvious than that in the actual test because the whole analysis process is ideal. The welds of sides A and B are damaged to varying degrees at the ninth loading level in the theoretical results. However, damage to the weld occurs at the eighth level, and the damage is severe.

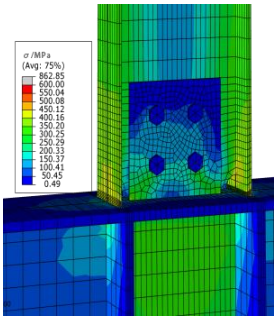

(a) Stress cloud diagram at level 4 loading

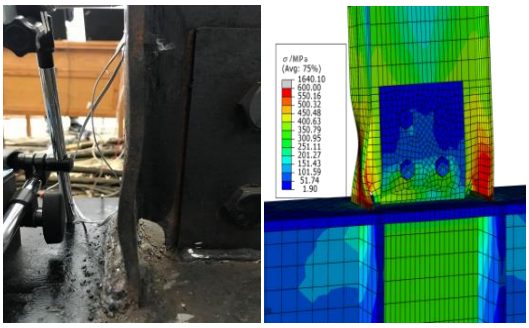

(b) Plastic hinge change at level 7 loading

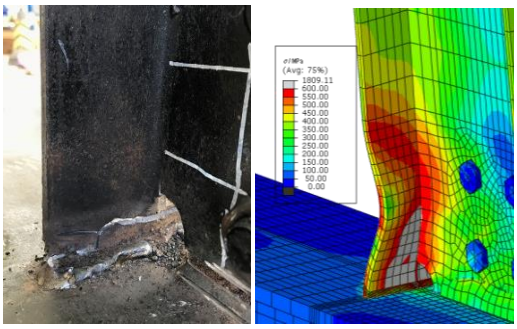

(c) Failure of A-side flange at level 9 loading

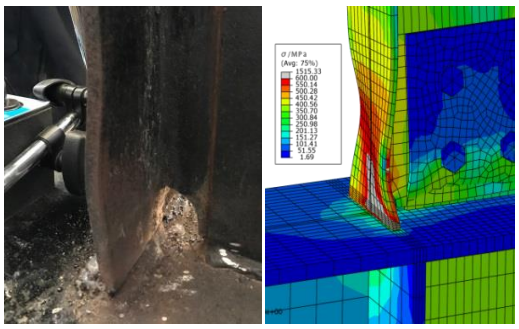

(d) Failure of B-side flange at level 9 loading

Fig. 8 Comparison of deformation of specimen NBN

(2) Double-ribbed reinforced beam-column connection (RRN)

In the same way, the deformed diagram for the test and numerical simulation of the double-ribbed reinforced connections (RRN) at different loading levels are presented in Fig. 9. The results show that both the numerical and tested results at the plastic hinge position and the deformation size are not the same as that of the NBN because of the existence of strengthened ribs. The whole connection is also in the elastic range at the fourth loading level, but the largest stress from the simulation results is at the ribs and beam flanges near the ends of the ribs and the strengthened web plate. The test and numerical results showed that the beams buckled slightly in the two above parts and the weld that connects the beam and the column at the ninth loading level. The welds of the rib of side A and that of the beam flange of side B crack at the tenth loading level during the structural test, but the damage of side A and side B is symmetrical. The damage of the welds of side

A and side B occurs at different parts during the test because the quality of the welds is inconsistent due to manual welding.

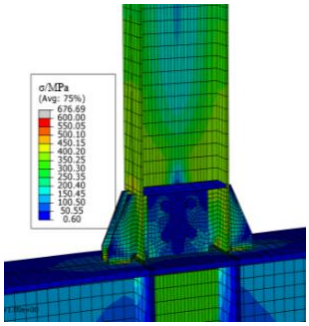

(a) Stress cloud diagram at 4 level loading

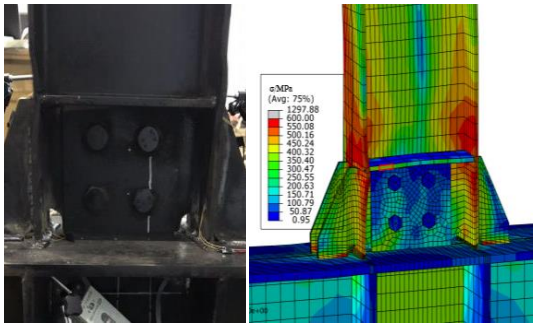

(b) Plastic hinge change at 8 level loading

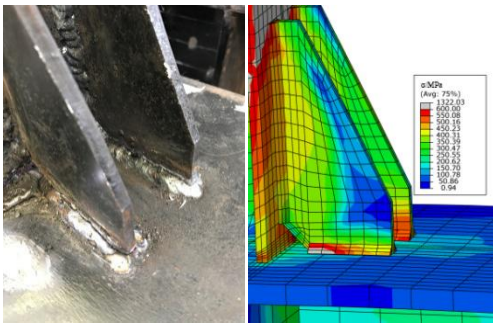

(c) Failure of A-side rib at 9 level loading

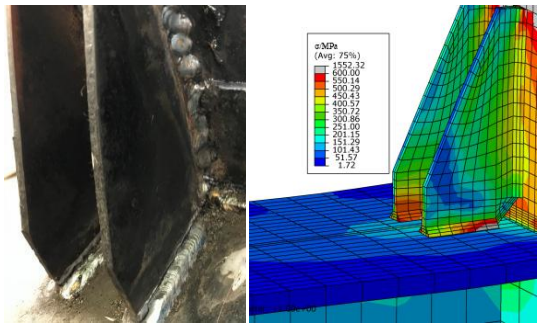

(d) Failure of B-side rib at 9 level loading

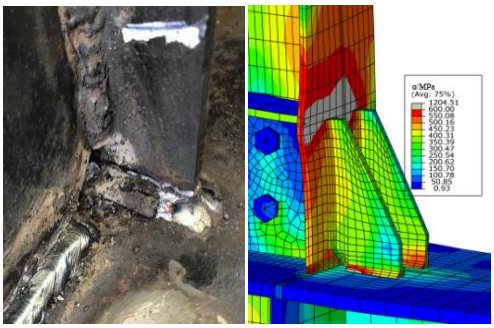

(e) Failure of A-side flange at 10 level loading

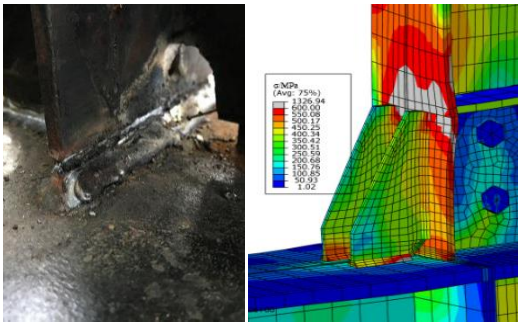

(f) Failure of B-side flange at 10 level loading

Fig. 9 Comparison of deformation of specimen RRN

3.3.2. Hysteretic curve

Fig. 10 shows the comparison of the hysteresis curves obtained by the test and the numerical results. All of the curves exhibit spindle shapes. However, the stress values from the test are slightly smaller than those from the FE results; moreover, rheostriction is observed in the middle of the test curves. It is determined that there is a small level of slippage during the test. The results also show that both hysteresis curves obtained from the test and the finite element calculation are basically consistent at the initial loading stage. After reaching the peak load, the hysteresis curves of the specimen in the test are not full enough because specimens had defects in the welds, and there were some unstable factors, such as the stress concentration caused by the weld, processing errors, and uneven material properties in the test. Comparing the hysteresis curves of the two connections proves that the double-ribbed reinforced beam-column connection has better seismic performance than the other connection because it is fuller and exhibits a higher bearing capacity.

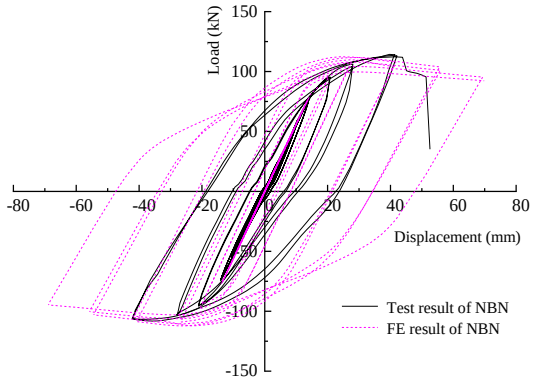

(a) NBN

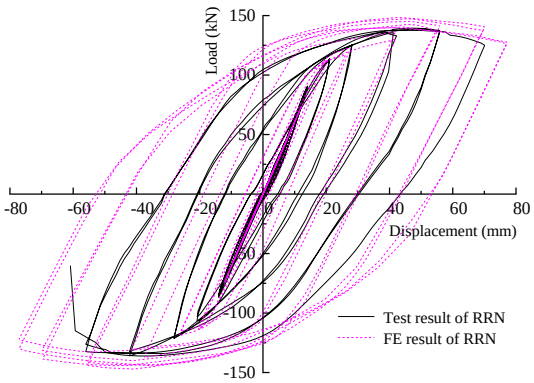

(b) RRN

Fig. 10 Comparison of hysteretic curves

3.3.3. Skeleton curve and stiffness degradation curves

The skeleton curve can reflect the relationship between the strength and deformation of a component. Fig. 11 presents four skeleton curves of the NBN and RRN from the tests and numerical simulations. This figure shows that the skeleton curves of each specimen are linear before yielding, while they are nonlinear after yielding. Besides, the skeleton curves of the experiment and

simulation basically coincide with each other before yielding. Upon reaching the ultimate load, the decline slope of the RRN curves is less than that of the NBN curves, which indicates that there is a larger plastic deformation at the strength node, and the plasticity of the steel beam-column connection always plays an important role. However, after exceeding the peak point, the test and simulation curves begin to separate. The decrease in the skeleton curve of the simulation is relatively smaller than that of the test because the material of the finite element model is relatively ideal. Meanwhile, it could be concluded from these curves that the double-ribbed reinforced beam-column connection has a higher bearing capacity than the other connections.

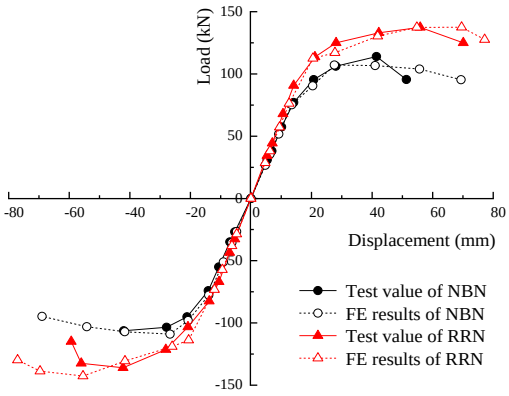

Fig. 11 Comparison of skeleton curves

Additionally, stiffness degradation refers to the phenomenon that the stiffness of the secant at each point on the skeleton curve gradually decreases after the specimen enters the plastic stage. The degree of degradation can be measured by the stiffness degradation coefficient β, which refers to the stiffness of the loaded secant position and the stiffness at the initial elastic stage ratio. According to the coordinates of each point on the skeleton curve, the coefficient of stiffness degradation corresponding to each stage of loading is calculated and drawn into a curve, as shown in Fig. 12. Before reaching the fifth loading level, the stiffness of the two connections barely decreases. After entering the yield stage, the test values of the NBN are highly coincident with those of the simulation, but the test results of the RRN are generally lower than those of the simulation. The development of the plastic hinge and failure mode of the numerical simulation and test of the NBN are consistent, as seen from the comparison with the displacement in the whole loading process. However, after the plastic hinges appear at the beam end of the RRN, with the increase in the loading grade, the buckling of the beam flange in the test or simulation is intensified in the same position, but the change in the test is not obvious.

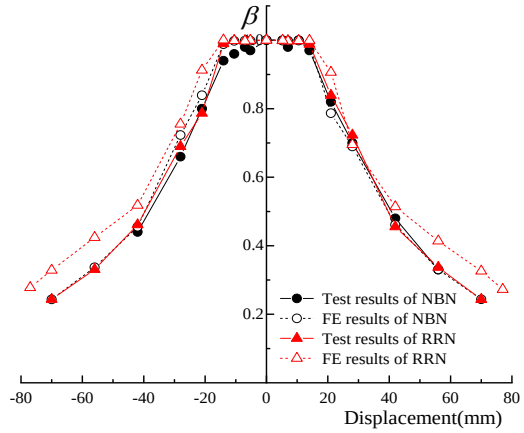

Fig. 12 Comparison of stiffness degradation curves

3.3.4. Ductility and energy dissipation coefficient

The ductility is an important index for evaluating the seismic resistance of connection specimens, which is defined as the ratio of the ultimate displacement Δ_u to the yield displacement Δ_y. The ductility coefficients of the NBN and RRN are shown in Table 5. In terms of μ, the positive and negative ductility coefficients of the same specimen have little difference, but the average value of the ductility coefficient of the RRN is 38.3%, which is higher than that of the NBN. Meanwhile, the ductility coefficients of the RRN are larger than those of the NBN. This means that reinforcing the beam with ribs can significantly improve the ductility of the beam-column connection.

Table 5
Load and displacement at characteristic points and ductility factor

Specimen	Force direction	D_y (mm)	P_y (kN)	D_u (mm)	P_u (kN)	μ	$\bar{\mu}$
NBN	Positive	20.64	88.56	51.33	114.00	2.48	2.30
	negative	19.85	89.98	42.02	106.30	2.12	
RRN	Positive	20.66	112.20	70.10	137.42	3.39	3.18
	negative	20.06	100.62	59.36	136.15	2.96	

In general, the equivalent adhesive damper coefficient h_e [21] can measure the energy dissipation capacity of a beam-column connection. Comparing the equivalent adhesive damping coefficients of the two types of beam-column connections (which are shown in Table 6), these values for the RRN are still larger than that for the NBN, which shows that the reinforced ribs of the beam have some effect on the value of E_h in each model, and the reinforcing ribs will increase the energy dissipation coefficient of the connections.

Table 6
Comparison of equivalent adhesive damper coefficients

Specimen	Test value	Theoretical value	Error/%
NBN	0.290	0.322	11.03
RRN	0.345	0.368	6.67

3.3.5. Damage curve

Corresponding to the hysteretic curves of both beam-column connections, the damage curves are fitted by a power function, which is shown in Fig. 13, where the damage modulus is calculated by the energy model [34], and the curves of both specimens are highly consistent with the damage value. The cumulative plastic damage values of both connections are relatively large because the simulation displacement results are large. Besides, the slope of these curves has gone through the same process from small to large, which proves that the damage degradation of both connections is accelerated. The final damage value of the simulation of the NBN is higher than that of the test, and the difference between the final damage value and the fitting formula of the RRN is small. Moreover, the final damage value of the RRN is still higher than that of the NBN, and the energy dissipation time of the RRN is longer than that of the NBN. This result is consistent with the conclusion from the experimental results.

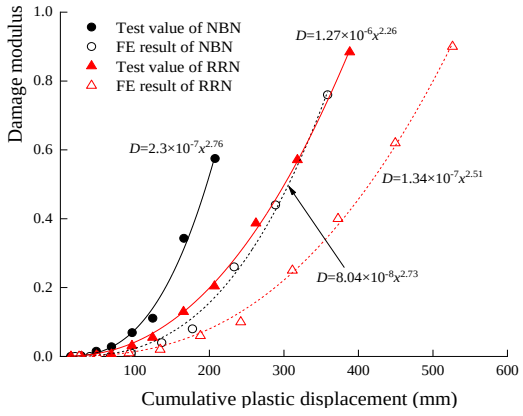

Fig. 13 Comparison of fitting curves of damage degradation

From the above seismic performance analysis, it is recommended that the double-ribbed reinforced beam-column connection is adopted for a steel frame in practical engineering applications, but the optimal range of the ribs cannot be obtained by only one length.

4. Parameter analysis with reinforced ribs

4.1. FE model analysis

From the evolution of fracture theory, if double-ribbed reinforced beam-column connections are to fully realize the purpose of fracture resistance under earthquake loads, it is also necessary to study the brittle fracture of steel connections with expanded flanges. According to the experimental and simulated failure modes of the RRN, the flange weld between the beam and column and the plastic hinge belong to the key failure zone. Based on the results of the above test and numerical simulation, the parameters of the finite element model of the RRN are consistent with those of the above specimens. To distinguish the influence of ribs of different sizes on the fracture performance of these connections, the ranges of the parameters of the reinforced ribs of the RRN are expanded as length l_a = (0.55~0.75)h_b, width b = (0.4~0.6)a, thickness t_s = (1.4~1.8)t_f, a'=35 mm and b' = 20 mm. The dimensions and key analysis parts of the ribbed plate are shown in Fig. 14. These models are divided into three group models (RRN-A, RRN-B, and RRN-C) in accordance with the three indexes of the rib length, width, and thickness. Every index of the rib in each group of models has five different parameters, which are shown in Table 7, Table 8, and Table 9.

Table 7
Parameters of ribbed plate of RRN-A group model

Model number	a (mm)	a/h_b	b (mm)	b/a	t_s(mm)	t_s/t_f
RRN-A1	137.5	0.55	69	0.5	12	1.5
RRN-A2	150	0.6	75	0.5	12	1.5
RRN-A3	162.5	0.65	81	0.5	12	1.5
RRN-A4	175	0.7	88	0.5	12	1.5
RRN-A5	187.5	0.75	94	0.5	12	1.5

Table 8
Parameters of ribbed plate of RRN-B group model

Model number	a (mm)	a/h_b	b (mm)	b/a	t_s(mm)	t_s/t_f
RRN-B1	160	0.645	64	0.4	12	1.5
RRN-B2	160	0.645	72	0.45	12	1.5
RRN-B3	160	0.645	80	0.5	12	1.5
RRN-B4	160	0.645	88	0.55	12	1.5
RRN-B5	160	0.645	96	0.6	12	1.5

Table 9
Parameters of ribbed plate of RRN-C group model

Model number	a (mm)	a/h_b	b (mm)	b/a	t_s(mm)	t_s/t_f
RRN-C1	160	0.645	80	0.5	11.2	1.4
RRN-C2	160	0.645	80	0.5	12	1.5
RRN-C3	160	0.645	80	0.5	12.8	1.6
RRN-C4	160	0.645	80	0.5	13.6	1.7
RRN-C5	160	0.645	80	0.5	14.4	1.8

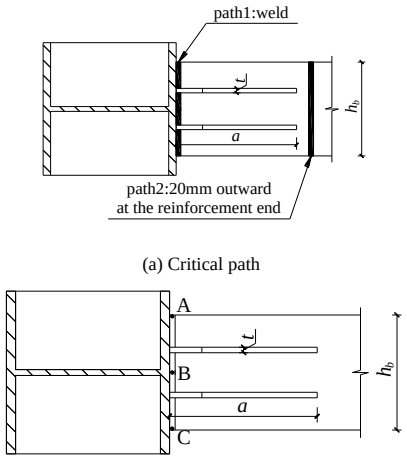

(a) Critical path

(b) Key point

Fig. 14 Key paths and key points

4.2. Fracture analysis indexes

Using the indexes (stress triaxiality ratio (R_σ), plastic equivalent strain index (*P.I.*), and cracking index (*R.I.*)), the possibility of brittle fracture of the RRN is analyzed, and the fracture characteristics of these connections are studied and evaluated. Furthermore, the influence of ribs of different sizes on the fracture performance of these connections is comprehensively analyzed.

The stress triaxiality ratio can effectively reflect the plastic deformation and stress concentration in the material (Schafer B. W. et al. [35]). The larger the Rσ value is, the larger the volumetric deformation. The greater the stress concentration, the more elastic strain energy is released, and the easier it is for cracks to occur. The specific calculation is as follows:

$$R_\sigma = \frac{\sqrt{2}(\sigma_1+\sigma_2+\sigma_3)}{3\sqrt{(\sigma_1-\sigma_2)^2+(\sigma_2-\sigma_3)^2+(\sigma_3-\sigma_1)^2}} \tag{1}$$

where σ_1, σ_2, and σ_3 are the principal stresses.

EI-Tawil [36] proposed the equivalent plastic strain index, which is equal to the ratio between the equivalent plastic strain and the yield strain. The equivalent plastic strain index can reflect the local ductility and fracture tendency of the material. The larger the value of *P.I.* is, the greater the plastic deformation at that point, and the greater the possibility of ductile cracking of the material, which is defined as follows:

$$PI = \frac{\sqrt{\frac{2}{3}\varepsilon_{ij}\varepsilon_{ij}}}{\varepsilon_y} \tag{2}$$

where ε_y is the yield strain at the calculation point and ε_{ij} is the equivalent plastic strain component.

Haneock [37] and Mao [39] proposed using the stress triaxiality ratio Rσ and the equivalent plastic strain index *P.I.* to define the cracking index R.I. when studying the brittle fracture of metal materials. The cracking index is equal to the ratio between the average stress and the equivalent stress. The higher the R.I. value is, the greater the possibility of cracking, and the larger the joint damage. The calculation formula is as follows:

$$RI = \frac{PI}{\exp[-3(\sigma_1+\sigma_2+\sigma_3)/4\sigma_e]} \tag{3}$$

where σ_e is the von Mises stress.

4.3. Influence of l_a

The elastic-plastic fracture indexes (R_σ, *PI*, and *R.I.*) of path 1, path 2, and three key points of RRN-A derived from ABAQUS are shown in Figs. 15-17, respectively.

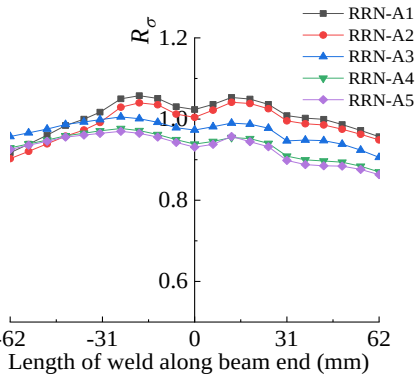

(a) Stress triaxiality ratio

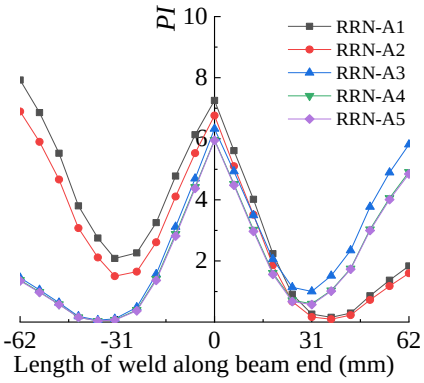

(b) Equivalent plastic strain index

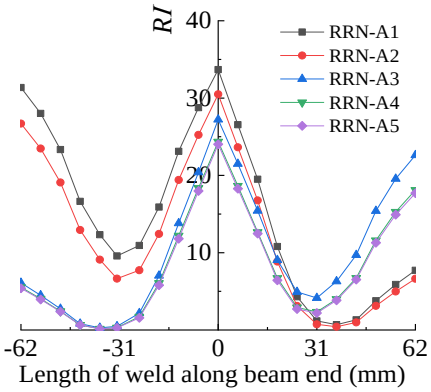

(c) Cracking index

Fig. 15 Fracture assessment parameters in path 1 of the RRN-A

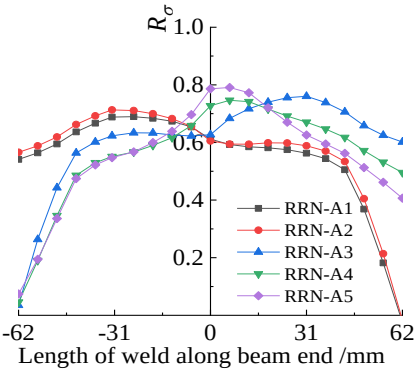

(a) Stress triaxiality ratio

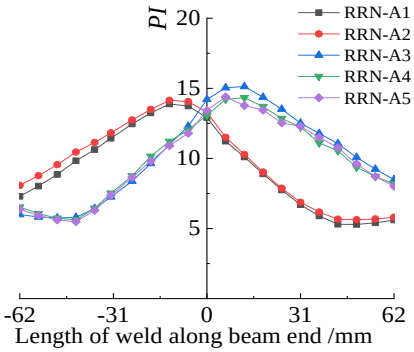

(b) Equivalent plastic strain index

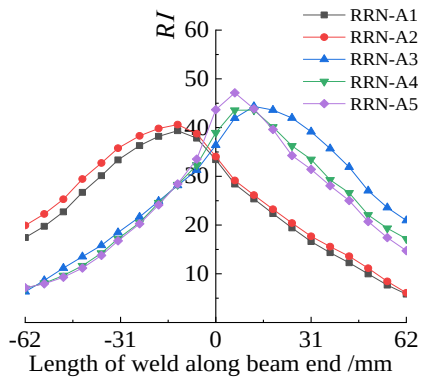

(c) Cracking index

Fig. 16 Fracture assessment parameters in path 2 of RRN-A

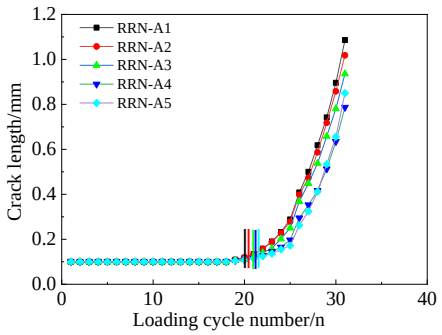

(a) point A

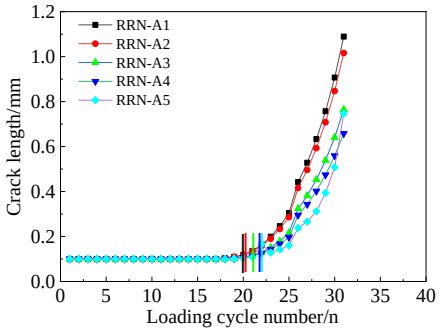

(b) point B

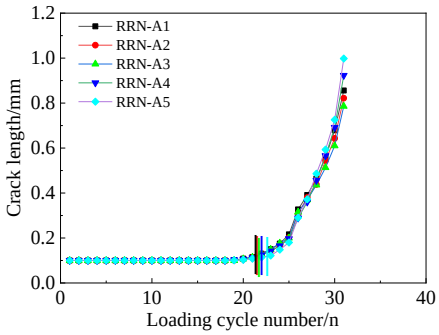

(c) point C

Fig. 17 Crack development at key points in RRN-A

The stress triaxiality curves of RRN-A in path 1 have an “M” fluctuation along the length of the weld, which indicates that there is a high possibility of brittle fracture near the rib between the reinforced ribs. The maximum value (1.06) of RRN-A1 is slightly higher than that of the other four values. The values of R_σ decrease with increasing rib length. However, the decrease in the three indexes is not obvious when the rib length increased to 175 mm. Compared with the stress triaxiality curves for path 1, the “M” fluctuation

along the beam end of the stress triaxiality curves in path 2 is more complex. The maximum value of R_σ is at one side of the rib of RRN-A5, which is 0.79 and is near the mid-beam point. The maximum value of the equivalent plastic strain index curves in path 1 is larger than that in path 2, which indicates that the middle of path 1 has a greater possibility of brittle cracking. Therefore, a reasonable length of the reinforced rib is 0.60 ~ 0.70 h_b.

The equivalent plastic strain index curves of RRN-A in path 1 show a "W" shape along the length of the weld, which means that the weld at both ends of the weld and in the middle of the weld has a great possibility of cracking. The value of RRN-A1 is mostly higher than that of the other four values, especially the maximum value (7.92), which is close to the right end of the beam. Besides, the maximum value of the middle weld is between 5.95 and 7.26, indicating that the cracking possibility of the right end of the weld is the highest. The equivalent plastic strain index curves of RRN-A in path 2 have an inverted "V" fluctuation along the beam. Unlike that in path 1, the maximum value is in RRN-A5 not in RRN-A1, which is 15.13. Besides, the value of the equivalent plastic strain index in the middle of the beam is higher than that of the other parts. Furthermore, the maximum value of the equivalent plastic strain index curves in path 2 is larger than that in path 1, which indicates that the close-middle in path 2 has a greater possibility of cracking. Thus, a reasonable length of the reinforced rib is 0.60 ~ 0.70 h_b.

The cracking index curves of RRN-A in path one also show a "W" shape along the length of the weld, which means that the weld at both ends of the weld or in the middle of the weld has a great possibility of cracking. Through analyzing the values of RRN-A in path 1, the crack probability in the middle of the weld is higher than that of the others because the maximum value (33.69) of RRN-A1 is higher than that (30.50) of RRN-A2. The cracking index curves of RRN-A in path 2 show an inverted "V" shape along the beam width. The maximum value (47.13) is in RRN-A5, which is close to the mid-beam point. Comparing the maximum value of the two diagrams, the cracking possibility at the mid-beam point in RRN-5 is largest because its maximum value is larger than that of RRN-A1. Therefore, a reasonable length of the reinforced rib is 0.60 ~ 0.70 h_b.

Fig. 17 shows the crack length development curves of three key points of RRN-A. With increasing reinforced rib length, the cracking time is gradually delayed, but the crack length increases. After entering the fifth stage of loading (the 22nd circle), the slope of each crack length development curve at points A and B rises rapidly, but the curves at point C rise slowly. The longest crack lengths at points A, B, and C are 1.07, 1.09, and 1.02, respectively. The crack length at point A and point B of RRN-A1 is the longest and that of RRN-A2 is the second longest, but the crack length at point C of RRN-A5 is the longer than that of RRN-A2. According to the above analysis of the cracking index, the crack probability of the weld at point B is highest. The final crack lengths of RRN-A1, RRN-A2, RRN-A3, RRN-A4, and RRN-A5 at point B are 1.09 mm, 1.02 mm, 0.77 mm, 0.66 mm, and 0.75 mm, respectively. The cracking times of RRN-A3, RRN-A4, and RRN-A5 are later than those of the other two. Consequently, a reasonable length of the reinforced rib is 0.60~0.75 h_b.

In summary, a reasonable length of the reinforced rib of the double-ribbed reinforced beam-column connections of 0.60 ~ 0.70 h_b was determined through studying the stress triaxiality ratio (R_σ), plastic equivalent strain index (*P.I.*), cracking index (*R.I.*), and crack development at three key points.

4.4. Influence of b

Similar to the analysis of la, the elastic-plastic fracture indexes (R_σ, *PI*, and *R.I.*) of RRN-B derived from ABAQUS are shown in Fig. 18, Fig. 19, and Fig. 20, respectively. Compared with the R_σ curves of RRN-A, the curves of the stress triaxiality ratio of RRN-B in Fig. 18 and Fig. 19 are similar to those of RRN-A. The stress triaxiality curves of RRN-B in path one also have an "M" fluctuation along the length of the weld, which indicates that the possibility of brittle cracking of the weld near the rib between the two ribs is high. Although the maximum value (1.02) is in RRN-B5, the maximum values of these five curves are very close (the error is within 5%). Similar to the stress triaxiality curves of RRN-A in path 2, the shape of the "M" fluctuation along the beam end is slanted. Similarly, the maximum value (0.74) is in RRN-B5, but the maximum value of these five curves is still very close (the error is within 5%). Therefore, it is difficult to analyze the influence of *b* by discussing the stress triaxiality ratio.

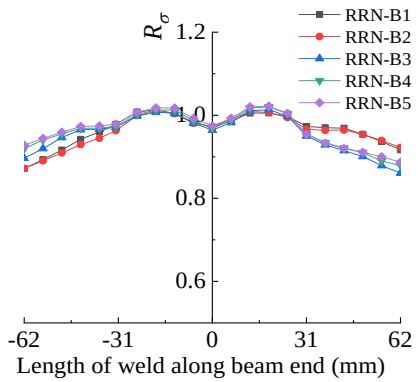

(a) Stress triaxiality ratio

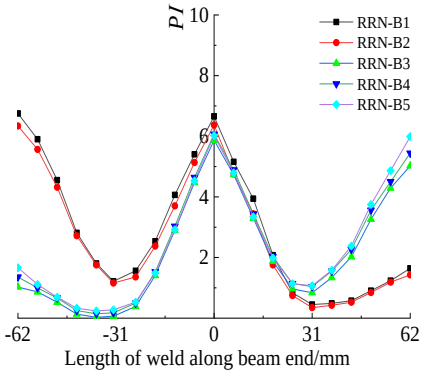

(b) Equivalent plastic strain index

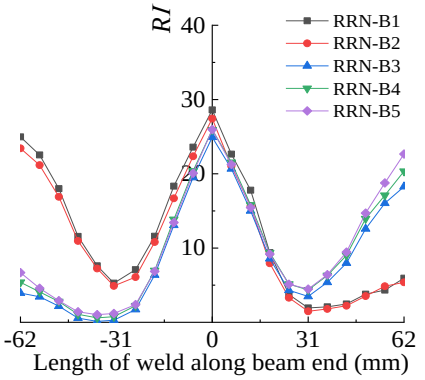

(c) Cracking index

Fig. 18 Parameters about fracture assessment in path 1 of RRN-B

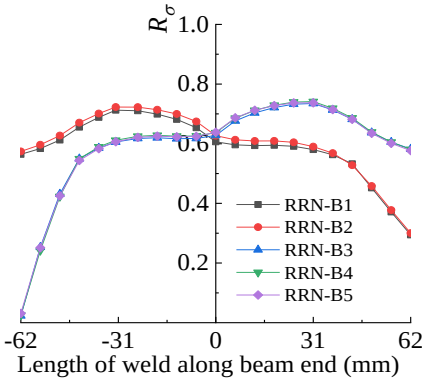

(a) Stress triaxiality ratio

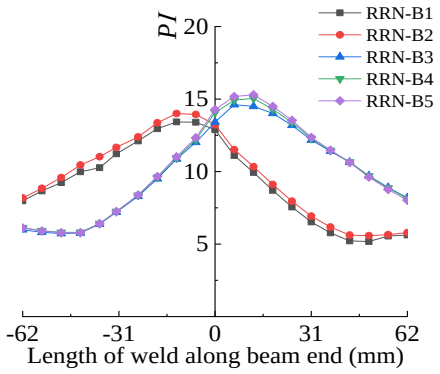

(b) Equivalent plastic strain index

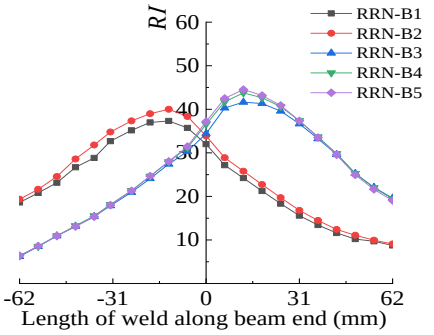

(c) Cracking index

Fig. 19 Parameters about fracture assessment in path 2 of RRN-B

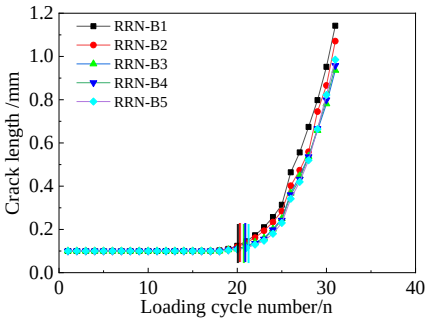

(a) point A

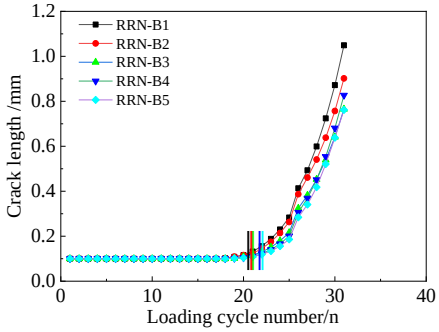

(b) point B

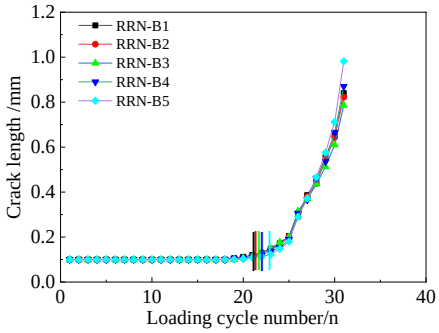

(c) point C

Fig. 20 Crack development at key points in RRN-B

In the same way, the equivalent plastic strain index curves of RRN-B in path one also show a “W” fluctuation along the length of the weld. The value of RRN-B1 is mostly higher than that of the other four values, and the maximum value is 6.75. Besides, the value of the *P.I.* in the middle part of the weld is between 5.87 and 6.67, indicating that the change in the rib width has some influence on the cracking condition of path 1. Regarding the equivalent plastic strain index curves of RRN-B in path 2, the shape of these curves along the beam is similar to that of RRN-A in path 1. The maximum value (15.30) is in RRN-A5, which is close to the midpoint of the beam. Meanwhile, the error among RRN-B3, RRN-B4, and RRN-B5 is small, and the maximum value of these three curves is also higher than that of the other two curves. Compared with the maximum value of the equivalent plastic strain index curves in the path, the maximum value of the equivalent plastic strain index curves in path 2 is larger, which means that the near-middle in path 2 has a greater possibility of cracking. Therefore, a reasonable width of the double ribs is 0.50 ~ 0.60 *a*.

Similarly, the cracking index curves of RRN-A in path one also show a “W” shape along the length of the weld, which means that the weld at both ends of the weld or in the middle of the weld has a great possibility of cracking. Through analyzing the values of RRN-B in path 1, the crack probability in the middle of the weld is higher than that of the others because the maximum value (28.60) of RRN-B1 is higher than that of the others. The cracking index curves of RRN-A in path 2 show an inverted “V” shape along the beam width. The maximum value (44.54) is in RRN-B5, which is close to the mid-beam point. Comparing the maximum value of the two diagrams, the cracking possibility at the mid-beam point in RRN-5 is largest because its maximum value is larger than that of RRN-A1. Therefore, a reasonable length of the reinforced rib is 0.45 ~ 0.55 *a*.

The crack length development curves of three key points of RRN-B are shown in Fig. 20, which have the same trend as that of RRN-A. After entering the fifth stage of loading (the 20th cycle), the slope of each crack length development curve at point A rises rapidly, but the curves at points B and C rise slightly later, and the longest crack lengths at points A, B, and C are 1.12 mm (RRN-B1), 1.05 mm (RRN-B1) and 0.91 mm (RRN-B5), respectively. According to the above analysis of the cracking index, the crack probability of the weld at point A is the highest. The final crack lengths of RRN-B1, RRN-B2, RRN-B3, RRN-B4, and RRN-B5 at point B are 1.12 mm, 1.05 mm, 0.93 mm, 0.94 mm, and 0.98 mm, respectively. Besides, the cracking times of RRN-B3, RRN-B4, and RRN-B5 are later than those of the other two. As a result, a reasonable width of the reinforced rib is 0.50 ~ 0.60 *a*.

In summary, a reasonable length of the reinforced rib of the double-ribbed reinforced beam-column connections is difficult to obtain by studying the stress triaxiality ratio (R_σ) because the error between the values of the five models is very small. However, a reasonable length of the reinforced rib of the double-ribbed reinforced beam-column connections is 0.50 ~ 0.55 *a*, which is determined by studying the plastic equivalent strain index (*P.I.*), cracking index (*R.I.*), and crack development at three key points.

4.5. Influence of t_s

The curves of the elastic-plastic fracture indexes (R_σ, *PI*, and *R.I.*) of the RRN-C group model are presented in Figs. 21-23, respectively. Compared with the R_σ curves of RRN-A and RRN-B, the curves of the stress triaxiality ratio of RRN-C in Fig. 21 and Fig. 22 are more regular than those of the other two, and the shape of the curves looks like a wave along the length of the weld. The values of all stress triaxiality curves of RRN-Care between 0.87 and 1.04, and the maximum value (1.04)is in RRN-C1 near the reinforced rib, which indicates that the possibility of brittle cracking of the weld near the rib

is high. The values of RRN-C3, RRN-C4, and RRN-C5 are relatively smaller than those of RRN-C1 and RRN-C2, which indicates that the crack probability of RRN-C1 is highest among these five models. Concerning the curves of the stress triaxiality ratio in path 2, these curves also show an “M” fluctuation along the width of the beam, but they tilt left. The maximum value (0.81) near the right rib is in RRN-C5, and the values of RRN-C5 are significantly higher than those of the other four values, which means that the crack probability near the right reinforced rib of RRN-C5 is the highest among these five models. As a result, the reasonable thickness ts of the double ribs is 1.50 ~ 1.60 t_f by discussing the stress triaxiality ratio (R_σ).

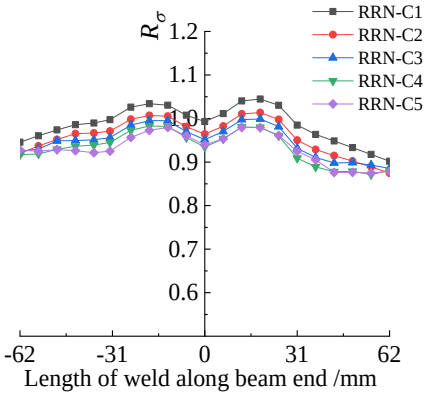

(a) Stress triaxiality ratio

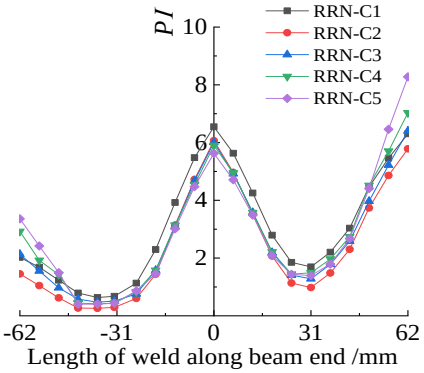

(b) Equivalent plastic strain index

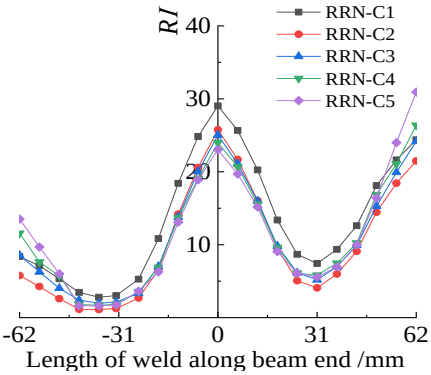

(c) Cracking index

Fig. 21 Fracture assessment parameters in path 1 of RRN-C

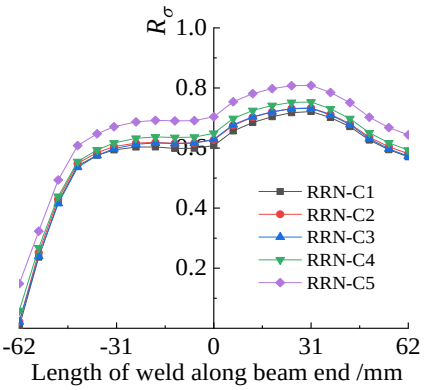

(a) Stress triaxiality ratio

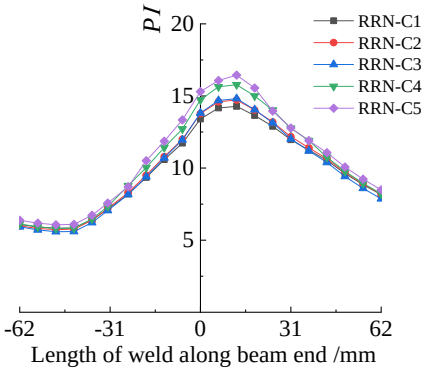

(b) Equivalent plastic strain index

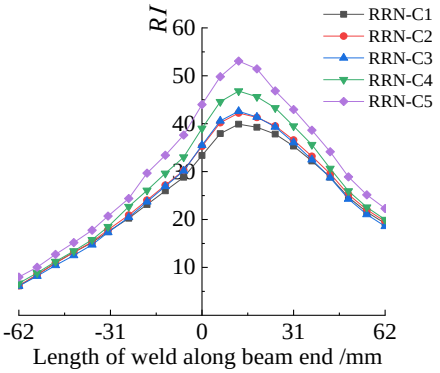

(c) Cracking index

Fig. 22 Parameters of fracture assessment in path 2 of RRN-C

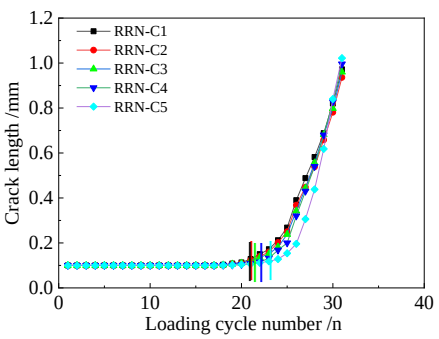

(a) point A

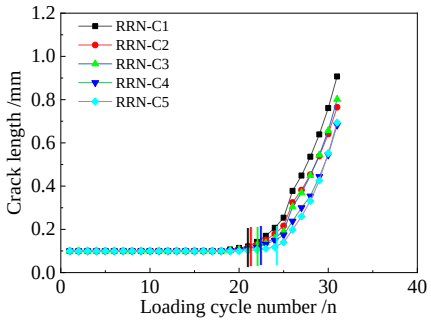

(b) point B

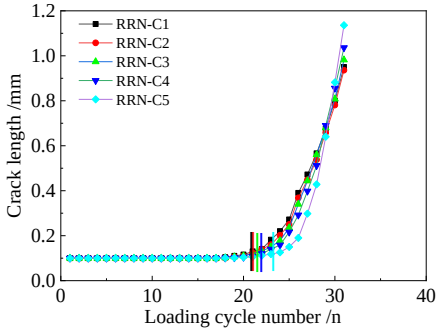

(c) point C

Fig. 23 Development of crack at key points in RRN-C

In Fig. 21(b), the curves of the equivalent plastic strain index of the RRN-C in path one also show a "W" fluctuation with low left and high right along the length of the weld. The value of RRN-C1 is partly higher than that of the other four values, but the maximum value (8.28) at the right end of the weld is in RRN-C4. This indicates that the crack probability of the right end of the weld is the highest. However, the shape of the equivalent plastic strain index curves of RRN-B in path 2 is different from that of RRN-C in path 1, and they are similar to those of RRN-A and RRN-B in path 2. The maximum value (16.45) is in RRN-C5, which is close to the midpoint of the beam, followed by RRN-C4 (15.78). Meanwhile, the error among RRN-B3, RRN-B4, and RRN-B5 is small, and the maximum value of these three curves is also lower than that of the other two curves. Therefore, a reasonable thickness t_s of the double ribs is 1.40 ~ 1.60 t_f, determined by discussing the equivalent plastic strain index.

The curves of the cracking index (*R.I.*) in path 1 of RRN-C in Figs. 21(c) and 22(c) are similar to those of RRN-A and RRN-B, respectively. From Fig. 21(c), the crack probability of the right end of the weld is higher than that of the mid-weld because the maximum value (30.92) of RRN-C5 is higher than that (28.8) of RRN-C4. The error among the other three models is relatively small. Similarly, in Fig. 22, the maximum value (53.08) is in RRN-C5, and the second largest value (46.81) is in RRN-C4. Therefore, a reasonable thickness t_s of the double ribs is 1.40 ~ 1.70 t_f based on the cracking index.

The crack length development curves of the three key points of RRN-C are shown in Fig. 23, which have the same trend as those of RRN-A and RRN-B. After entering the fifth stage of loading (the 21st circle), the slope of each crack length development curve at three points rises rapidly. The shape of the curves at point C is the largest and that of the curves at point B is the smallest. Besides, the longest crack lengths at points A, B, and C are 1.06 mm (RRN-C5), 0.92 mm (RRN-C1), and 1.15 mm (RRN-C5), respectively. However, the time to start cracking of RRN-C5 at the three points is later than that of the other models and that of RRN-C1 at the three points is the earliest. According to the above analysis of the cracking index, point C is the most dangerous among the three points, which means that RRN-C2, RRN-C3, and RRN-C4 are relatively safe. The final crack lengths of RRN-C1, RRN-C2, RRN-C3, RRN-C4, and RRN-C5 at point B are 0.93 mm, 0.92 mm, 0.98 mm, 1.02 mm, and 1.15 mm, respectively. Thus, a reasonable thickness of the reinforced rib is 1.40 ~ 1.60 t_f.

In summary, a reasonable thickness of the reinforced rib of the double-ribbed reinforced beam-column connections is 1.50 ~ 1.60 t_f, which is determined by studying the stress triaxiality ratio (R_σ), plastic equivalent strain index (*P.I.*), cracking index (*R.I.*) and crack development at three key points.

5. Conclusions

Based on the experimental and numerical analytical results, the FE model of a double-ribbed reinforced beam-column connection is verified. Using the stress triaxiality ratio (R_σ), the plastic equivalent strain index (*P.I.*), cracking index (*R.I.*), and crack development at three key points, reasonable parameters of the reinforced ribs of the double-ribbed reinforced beam-column connections are suggested. The following conclusions are drawn:

(1) Compared to conventional connections, double-ribbed reinforced beam-column connections have a higher damage modulus and ultimate bearing capacity with increasing cumulative displacement, and the reinforced ribs can effectively move the plastic hinge away from the beam end.

(2) For the hysteretic behavior, the hysteresis curves of the two specimens and the two finite element models are basically consistent at the initial loading stage and gradually become different due to the existence of stress concentrations, processing errors, and uneven material in the specimens. Due to the existence of the reinforced ribs, the average value of the ductility coefficient of the RRN is higher than that of the NBN, and the energy dissipation coefficient of the RRN is higher than that of the NBN.

(3) From the comprehensive analysis of the stress triaxiality ratio (R_σ), equivalent plastic strain index (*P.I.*), cracking index (*R.I.*), and crack development at three key points, reasonable parameters for the ribs of the double-ribbed reinforced connections are given as follows: l_a=0.60 ~ 0.70 h_b; b = 0.50 ~ 0.55 a; and t_s = 1.50 ~ 1.60 t_f.

6. Acknowledgments

The authors appreciate the support of the National Science Foundation of China (51708485, 51878589 and 51878590), the Natural Science Foundation of Jiangsu Province (BK20191441), the Jiangsu Planned Projects for Postdoctoral Research Funds (1701191B), the Science and Technology projects of Ministry of Housing and Urban-rural Development (2014-K2-045 and 2014-K2-022), the China Postdoctoral Science Foundation (2017M611925), the Talent Plan of Innovate and Entrepreneurship in Jiangsu Province and the Talent Plan of Yangzhou City.

References

[1] Shen Z., Chen Y., Chen Y. and Zhao X., "Basic principle of steel structure," China Architecture &Building Press, 2018.
[2] White D. W. and Chen W. F., "Organization and summary of discussions at the US-Japan seminar on innovations in stability concepts and methods for seismic design in structural steel," Engineering Strutures, 20(4-6), 242-248, 1998.
[3] Miller D. K., "Lessons learned from the Northridge earthquake," Engineering Strutures, 20(4-6), 249-260, 1998.
[4] Saher E. K., Sakr M. A., Khalifa T. M. and Eladly, M.M., "Modelling and behavior of beam-to-column connections under axial force and cyclic bending," Journal of Constructional Steel Research, 129, 171-184, 2017.
[5] GB50017-2017, Standard for the design of steel structures, China Construction Industry Press, 2017.
[6] Guo B., Gu Q. and Liu F., "Experiment behavior of stiffened and unstiffened end-plate connections under cyclic loading," Journal of Structural Engineering, 132(9), 1352-1357, 2006.
[7] Pachoumis D. T, Galoussis E. G., Kalfas C. N. and Christitsas A. D., "Reduced beam section moment connections subjected to cyclic loading: Experimental analysis and FEM simulation," Engineering Strutures, 31(1), 216-223, 2009.
[8] Sophianopoulos D. S. and Deri, A. E., "Parameters affecting response and design of steel moment frame reduced beam section connections: An overview," International Journal of Steel Structures., 11(2), 133-144, 2011.
[9] Han S. W., Moon K. H., Hwang S. H. and Stojadinovic B., "Rotation capacities of reduced beam section with bolted web (RBS-B) connections," Journal of Constructional Steel Research, 70, 256-263, 2012.
[10] Swati A. K. and Vesmawal G., "Study of steel moment connection with and without reduced beam section," Case Studies in Engineering Structures, 1, 26-31, 2014.
[11] Oh K. Y., Lee K. M., Chen L. Y., Hong S. B. and Yang Y., "Seismic performance evaluation of weak axis column-tree moment connections with reduced beam section," Journal of Constructional Steel Research, 105, 28-38, 2015.
[12] Rahnavard R., Hassanipour A. and Siahpolo N., "Analytical study on new types of reduced beam section moment connections affecting cyclic behavior," Case Studies in Structural Engineering, 3, 33-51, 2015.
[13] Soliman A. A., Ibrahim O. A. and Ibrahim A. M., "Effect of panel zone strength ratio on reduced beam section steel moment frame connections," Alexandria Engineering Journal, 57, 3523-3533, 2018.
[14] Nia M. M. and Moradi S., "Effects of design factors on the cyclic response of shaped RBS moment connections," Engineering Structures, 207, 1-16, 2020.
[15] Engelhardt M. D. and Sabol T. A., "Reinforcing of steel moment connections with cover plates: benefits and limitations," Engineering Structures, 20(4-6), 510-520, 1998.
[16] Chen C. C., Lin C. C. and Tsai C. L., "Evaluation of reinforced connections between steel beams and box columns," Engineering Structures, 26(13), 1889-1904, 2004.
[17] Ghobadi M. S., Mazroi A. and Ghassemieh M., "Cyclic response characteristics of retrofitted moment-resisting connections", Journal of Constructional Steel Research, 65, 586-598, 2009.
[18] Erfani S., Asnafi A. A. and Goudarzi A., "Connection of I-beam to box-column by a short stub beam," Journal of Constructional Steel Research, 127, 136-150, 2016.
[19] Yang L. and Chen H., "Mechanical performance of beam-column joint with widened beam

flange," Journal Shenyang University of Technology, 39(4), 459-463, 2017 (in Chinese).
[20] Tian Y., Liu M., Jia Z. and Dai Y., "Study on mechanical behavior and optimization of prefabricated square column H-beam outer-shell joint," Mechanics of Advanced Materials and Structures, 27, 409-416, 2019.
[21] Ma H. W., Wang J. W., Lui E. M., Wang K. and Wan Z. Q., "Experimental study of the behavior of beam-column connections with expanded beam flanges," Steel and Composite Structures, 31, 319-327, 2019.
[22] Wang Z. X. and Shi H. J., "Effect of the stress triaxiality on the ductile fracture," Chinese Journal of Materials Research, 21, 170-176, 2007.
[23] Shi Y., Shi G., Wang Y. and Chen H., "Beam-column joints of multi high rise steel frame -- Theory and design," China Architecture & Building Press, 2014.
[24] Wang Y., "A seismic design theory and application of new ductility joint of steel structure," China Science Publishing Media Ltd, 2012.
[25] Hamburger R. O., Hooper J. D., Sabol T., et al., "FEMA-350 recommended seismic design criteria for new steel moment-frame buildings", Washington D. C.: The Federal Emergency Management Agency, 2000.
[26] Steel and Steel Products Location and Preparation of Test Pieces for Mechanical Testing 2017, China Architecture & Building Press, Beijing, China, 2017.
[27] Metallic Materials Tensile Testing 2010. China Architecture & Building Press, Beijing, China, 2010.
[28] Specification for Seismic Test of Buildings 2015. China Architecture & Building Press, Beijing, China, 2015.
[29] ABAQUS/Standard User Subroutines Reference Manual 1998. The Pennsylvania State University, USA, 1998.
[30] Amar K., "Introduction to finite element analysis using MATLAB and ABAQUS," Taylor & Francis Group, 2013.
[31] Song Z., "Cumulative Damage Failure Mechanism and Seismic Design Countermeasures for Rigid Beam-column Connections in Steel Frames under Earthquake Action," Xi'an University of Architecture and Technology, Xi'an, China, 2001.
[32] Narita S., Hyakawa K., Uenori T. and Kubota Y., "Evaluation of strength of stainless steel bolt without heat treatment considering Bauschinger effect during the manufacturing process", Journal of Materials Processing Technology, 278, 116481, 2020.
[33] Ma H. W., Zhao Y., Wang Z. J. and Chen Y. K., "Hysteretic behavior analysis of new beam-column connections with the expanded flange of the steel frame," Journal of Yangzhou University, 20(4-6), 242-248, 2018.
[34] Kumar S. and Usami T. "A note on the evaluation of damage in steel structures under cyclic loading", Journal of Structural Engineering, 40, 177-178, 1998.
[35] Schafer B. W., Ojdrovic R. P. and Zarghamee M. S., "Triaxiality and fracture of steel moment connections," Journal of Structural Engineering, 126, 1131-1139, 2000.
[36] El-Tawil S., Mikesell T. and Kunnath S. K., "Effect of local details and yield ratio on the behavior of FR steel connections," Engineering Structures, 126(11), 79-87, 2000.
[37] Hancock J. W. and MacKenzie A. C. "On the mechanisms of ductile failure in high strength steel subject to multi-axial stress-states." Journal of the Mechanics and Physics of Solids, 24, 147-169, 1976.
[38] Mao C., Ricles J., Lu L. and Fisher J., "Effect of local details on the ductility of welded moment connections," Journal of Structural Engineering, 127, 1036-1044, 2001.

Advanced Steel Construction – Vol. 16 No. 04 (2020) 310–320
DOI:10.18057/IJASC.2020.16.4.3

EFFECT OF CIRCULAR OPENINGS ON WEB CRIPPLING OF UNLIPPED CHANNEL SECTIONS UNDER END-TWO-FLANGE LOAD CASE

Elilarasi. K, Kasthuri. S and Janarthanan. B *

Department of Civil Engineering, Faculty of Engineering, University of Jaffna, Sri Lanka
** (Corresponding author: E-mail: Jana151188@eng.jfn.ac.lk)*

ABSTRACT

Cold-formed steel unlipped channels with web openings increasingly employed as bearers and joists in the floor systems to embed the building services to maintain adequate clear storey-height and aesthetic appearance. The use of thin-unlipped channels is limited in the past due to flange buckling and mostly web crippling behaviour of lipped channels with web openings was investigated. However, with the thickness increment, the flange buckling of unlipped channels is limited, and these sections are used widely in construction. The major drawback with these cold-formed steel profiles is web crippling, localized failure due to higher web slenderness ratio. Web openings reduce the carrying web area of the sections, hence makes the unlipped channels more vulnerable to web crippling. Currently, unlipped channels with web openings are increasingly employed, although no proper guidelines are available to determine the capacity reductions due to the introduction of web openings. The main cold-formed steel specifications such as North American Specification (AISI S100) and Australian/ New Zealand standard (AS/NZS 4600) employ the unified design equation with different coefficients for all four load cases while Eurocode 3 Part 1-3 (ECS) employs different equations for each load case. In these specifications, design guidelines are available only for offset web openings for unlipped channels under one-flange load cases. This study investigates the effects of circular centred beneath and offset web openings on the capacity reduction of unfastened support unlipped channels subject to web crippling under end two flange load cases. The suitable reduction factor equations have been proposed for circular web openings of unlipped channels located directly underneath and away for the bearing plate using the outcome form the numerical study.

ARTICLE HISTORY

Received: 6 March 2020
Revised: 23 June 2020
Accepted: 27 July 2020

KEYWORDS

Web crippling,
Cold-formed steel,
Unlipped channels,
Finite element analysis,
End-Two-Flange (ETF),
Web openings.

1. Introduction

Cold-formed steel portrays benefits such as the enhanced strength to weight ratio, fabrication easy and accurate in dimensions, compared to hot-rolled steel. The thickness of cold-formed steel profiles has been limited to 3.00 mm due to limitations in manufacturing technology in the past. Channel profiles such as lipped and unlipped are commonly employed in the building industry among different available shapes of cold-formed steel profiles. The lipped channels are more employed as joists and bearers in the typical floor systems due to their better performance under flexure compared to unlipped channels, where later may experience the buckling at compression flange under flexure. The thickness of cold-formed steel profiles is improved up to 8.00 mm due to advancement in the manufacturing technology. The thickness improvement reduces the possibilities of flange buckling of unlipped channels, and hence the usage of unlipped channels also increased similar to lipped channel profiles. Web crippling is a crucial localised problem, especially at the point loads and reactions in this cold-formed steel profiles because of higher web slenderness ratios due to small thicknesses. New building constructions employ these unlipped steel channels with circular openings at their webs to accommodate building services within the floor system to ensure aesthetic appearance and to maintain the clearance storey-height. However, the removal of the circular web part from the unlipped channel reduces the carrying area of the point loads and reactions and makes the profile more critical under web crippling. The behaviour of lipped channels under web crippling has been investigated without [1-5] and with the opening [6-17] at its webs, which is different from the performance of unlipped channels. However, the behaviour of unlipped channels with an opening has not explored in the past. Therefore, the web crippling performance of unlipped channels with circular openings at the web should be investigated thoroughly due to its increase in usage.

In addition to the conventional parameters such as different load cases, steel profiles and support conditions, the ultimate failure load of steel profiles with web opening depends on types and diameter of the web opening. As per existing cold-formed steel codes such as North American Specification (AISI S100) [18], Australian/ New Zealand Standard (AS/NZS 4600) [19] and Eurocode 3 Part 1-3 (ECS) [20] classified the practical failure modes into four as shown in Fig. 1 such as (i) End-One-Flange (EOF) (ii) End-Two-Flange (ETF) (iii) Interior-One-Flange (IOF) and (iv) Interior-Two-Flange (ITF) load cases based on their distances between loading and support reactions and failure locations while support conditions are unfastened and fastened conditions. Openings at the webs of the profiles are also commonly classified into two groups in the past studies as shown in Fig. 2 such as (i) centred beneath web opening, where the opening is located directly underneath the loading plate (ii) offset web opening where the opening is placed away from the bearing plate. Usually, the performance of cold-formed steel under web crippling is being investigated experimentally due to complexities involved in the theoretical methods. However, experimental studies are expensive and require more material. Hence the new approach of using numerical analysis which was introduced by Sivakumarn [22] with proper validations, is followed in this study. Finally, this study carefully investigates the reduction in the failure capacity of unlipped channels with a circular opening at the web of the profiles under web crippling with unfastened supports under ETF load case based on adequately developed and validated numerical models.

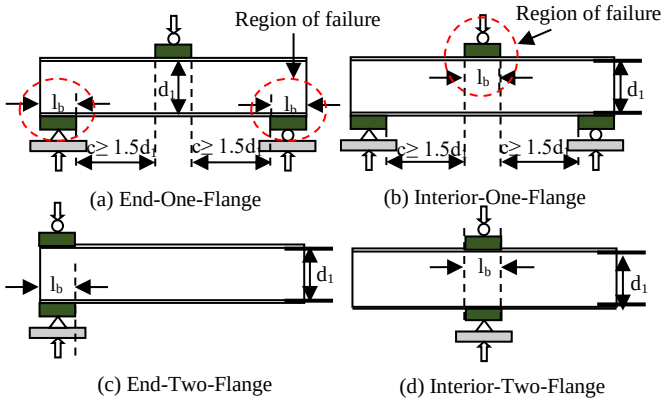

Fig. 1 Web crippling load cases [21]

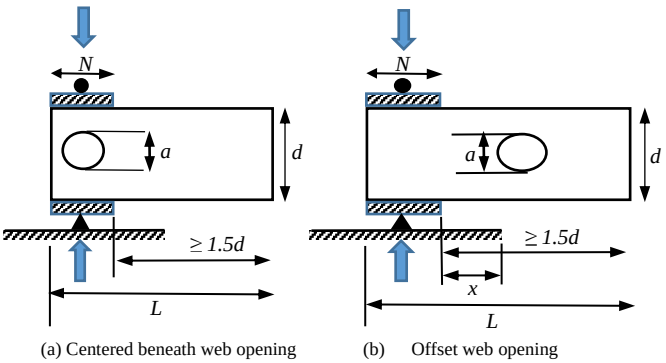

Fig. 2 ETF loading condition with centred beneath and offset web opening

Among available primary three cold-formed steel standards, AISI S100 [18] and AS/NZS 4600 [19] employ the unified web crippling design equation which is shown by Equation 1 to determine ultimate failure loads of various steel profiles subjected to web crippling. As shown, the particular equation is developed based on different ratios such as: bearing length to thickness (l_b/t),

web slenderness (d_1/t) and inside bent to thickness (r_i/t) in addition to material yield strength (f_y) and section thickness (t). Particular equation covered all four load cases and fastened/unfastened supports with only differing values of four coefficients. Eurocode 3 Part 1 [20], totally different from the two standards mentioned above, employs different equations for each load case without separating support conditions, as shown in Equations 2 & 3.

$$R_b = Ct^2 f_y \sin\theta \left(1-C_r\sqrt{\frac{r_i}{t}}\right)\left(1+C_1\sqrt{\frac{l_b}{t}}\right)\left(1-C_w\sqrt{\frac{d_1}{t}}\right) \quad (1)$$

For the ETF load case:

$$R_b = k_1 k_2 k_3 \left[6.66-\frac{h_w}{64t}\right]\left[1+0.01\frac{l_b}{t}\right]t^2 f_y/\gamma_{M1} \quad (2)$$

For the ITF load case:

$$R_b = k_3 k_4 k_5 \left[21.0-\frac{h_w}{16.3t}\right]\left[1+0.0013\frac{l_b}{t}\right]t^2 f_y/\gamma_{M1} \quad (3)$$

where: k_1, k_4 : coefficients for the strength of the material, k_2, k_5 : coefficients for the inside bend radius to the thickness ratio, k_3: coefficients for the angle between the flange and web, h_w : web height between flange mid-lines,γ_{M1}: partial safety factor. Other notations are similar to Equation 1.

Although steel profiles with web openings used in building construction, there are only a few guidelines available in main cold-formed steel specifications such as AISI S100 [18] and AS/NZS 4600 [19] to calculate the capacity reduction of web crippling due to web openings. The available guideline is also limited to offset web openings for unlipped channels subject to interior one flange load cases as shown by Equations (4a) and (4b), where *d*, *h*, and *x* are the diameter of the web opening, depth of a straight portion of the web of unlipped channels and closest distance to web opening from the bearing plate. Unlipped channels with higher thicknesses are used in floor systems as bearers with web openings nowadays more often, especially with circular web openings. However, there have been no investigations performed to determine the reduction of the web crippling of unlipped channels with circular web openings. Hence, it is addressed in this study by numerical analysis. The effects of both types of web openings such as centred beneath and offset have been investigated for unlipped channels with unfastened supports under the load case of End-Two-Flange.

$$R = 1.01 - 0.325 d/h + 0.083 x/h \le 1.0 \quad (4a)$$

$$R = 0.90 - 0.047 d/h + 0.053 x/h \le 1.0 \quad (4b)$$

2. Literature review

The behaviour of cold-formed steel profiles subjected to web crippling failure have been investigated since the 1940s with the experimental studies performed by Winter and Pian [23], hence have a long history. These past studies have been critically analysed and discussed in this section into mainly two groups such as (i) experimental investigations of steel profiles without and with the presence of web openings and then (ii) numerical studies of steel profiles without and with the presence web openings.

1a: Firstly, web crippling performance of cold-formed I-sections were explored by Winter and Pian [23] using 136 tests and empirical design equations were developed. Hetrakul and Yu [1] investigated the performance of lipped and unlipped channels subjected to web crippling, and they noticed the capacity is slightly higher (about 10%) for lipped channels compared to similar unlipped channels. However, they did not consider this capacity enhancement and proposed design equation commonly for channel profiles. Gerges and Schuster [2] explored the performance of lipped channels with the ratio large inside bent radius changing from 5 to 10, subjected to web crippling with fastened supports. Beshara and Schuster [3] reported that the ultimate capacity of cold-formed steel profiles under web crippling depends on the specimen length, 50% and 5% higher for ITF and ETF load cases for long specimen compared to short lengths, based on a pilot study, respectively. The above-researchers [3] proposed standard specimen lengths such as 3*d* and 5*d*, respectively for ETF and ITF load cases, where *d* is the straight web portion of the profiles. The suggestion by the above researchers has been included in the guidelines of AISI web crippling test method [21]. Research studies mentioned above targeted the behaviour of lipped channels under web crippling while recently only, more research studies have been performed to investigate the behaviour of unlipped channels. Young and Hancock [24] and Gunalan and Mahendran [25, 26] investigated the performance of unlipped channels with unfastened supports subjected to web crippling under all four load cases. Based on their study above researcher [24-26] informed that predicted values of unified design equation with existing coefficients were unconservative for unlipped channels with unfastened support condition. Therefore Young and Hancock [24] developed a design equation which is partly based on the theoretical background, yield line theory, only applicable for thick (stocky) unlipped channels for all load cases. Gunalan and Mahendran [25, 26] stayed with the unified design equation format but with new proposed coefficients by them for all load cases. Sundararajah et al. [5, 27] proved that the structural performance of lipped and unlipped channels are different, and they separately proposed coefficients to the unified design equation as listed in Table 1. Janarthanan et al. [28-31] identified that AISI S100 [18] still have shortcomings, such as no coefficients available to determine the web crippling capacity of unlipped channels with fastened supports under one flange load cases. They have proposed coefficients to the unified design equation based on experimental and numerical investigations. These show there are certain shortcomings in the current North American Specification (AISI S100) [18] and Australian/New Zealand standard (AS/NZS 4600) [19].

Table 1
Proposed coefficients to web crippling unified design equation [5, 27]

Equation	Load case	C	C_r	C_l	C_w
Proposed for Lipped channels	ETF	5.35	0.22	0.23	0.06
	ITF	17.0	0.19	0.05	0.03
	EOF	6.3	0.1	0.10	0.02
	IOF	4.9	0.01	0.38	0.03
Proposed for Unlipped channels	ETF	3.60	0.15	0.15	0.05
	ITF	15.6	0.25	0.01	0.001
	EOF	9.0	0.30	0.20	0.05
	IOF	14.7	0.18	0.05	0.01

Note: EOF, IOF, ETF and ITF: End-One, Interior-One, End-Two and Interior-Two-Flange load cases, C_r, C_l, C_w – coefficient values ratios for the corner radius to thickness, bearing length to thickness, web slenderness and C is a general coefficient

1b: The cost-effective way of investigating the behaviour of cod-formed steel subject to web crippling is using numerical analysis. Lots of finite element software are available nowadays, among that commonly used software in the investigation of web crippling are ANSYS, ABAQUS and ADINA. These softwares mentioned above are used for parametric study and to enhance the data strength after proper model validation. Considering recent numerical studies, McDonald et al. [4] developed numerical models for lipped channels using ANSYS for all four load cases and validated the developed models using their test results. Ren et al. [32] also used ANSYS and validated their developed FE models using already existed test data of web crippling of Young and Hancock [24]. Similarly, Natario et al. [33], Sundararajah et al. [5], and Janarthanan et al. [29, 31] developed FE models in ABAQUS and validated their FE models using quasi-static analysis by explicit analysis. As discussed above, the crucial part of finite element analysis is accurate validation.

2a: Similar to steel profiles without web opening, the effect of web openings on the web crippling capacity of the lipped channel is investigated mostly in the past, compared to unlipped channels. In all past studies [7-9], the web openings are classified into main two types such as (i) centred beneath and (ii) offset web openings as shown in Fig. 2, wherein the first type, the web opening is directly placed underneath the bearing plate while in the second type, the web opening is placed away from the bearing plate. First, Yu and Davis [6] investigated the performance of lipped channels under web crippling with two different opening shapes such as (i) circular and (ii) square, located directly underneath the bearing plate under IOF load case based on 20 results. Sivakumaran and Zielonka [7] performed an experimental study to find the effect of different shapes of web openings on the web crippling capacity of lipped channels with unfastened supports using 103 test results. The above researchers [7] observed that then design equations were unconservative for lipped channels with web openings. Hence they proposed a reduction factor equation for lipped channels using two ratios such as (i) opening height to a depth of a straight portion of the web (a/h) and (ii) opening width to effective bearing length (b/n_1). Langan et al. [8] explored web crippling behaviour of lipped channels with a rectangular opening under one flange load cases (both EOF and IOF) using 78 and 90 tests, respectively and they proposed reduction

factors separately for load cases.

LaBoube et al. [9] explored the behaviour of lipped channels with circular web openings subjected to web crippling for EOF and IOF load case based on their 56 and 52 tests, respectively. They developed an equation for capacity reduction for lipped channels based on two ratios such as the ratio of web opening distance from the edge of the bearing plate (x/h) and bearing length to the height of the straight portion of the web (N/h). However, the critical limitation in the outcome of the study is that the thicknesses of the profiles used ranged between 0.83 mm to 1.42 mm. These developed equations by LaBoube et al. [9] are included in AISI S100 [18] and AS/NZS 4600 [19] standards and still used to calculate the web crippling capacities of lipped channels with web openings. As mentioned above, the limitation raises the question of the applicability of these equations to thick-lipped channels, which are mostly used in current building construction. There are no other design guidelines available in any cold-formed steel specifications to determine web crippling failure loads of cold-formed steel profiles with web openings.

2b: Recently Uzzaman et al. [10-13] investigated the performance of lipped channels with circular web openings (i) located directly underneath and (ii) located away from the bearing plates, subjected to web crippling for two-flange load cases using experimentally and numerically. They have only modelled half of the profiles considering symmetric boundary conditions shown in Fig. 3 in ANSYS software to make their FE models time effective. Boundary conditions were only applied to the modelled loading plates and then transferred to flanges of the beam via contacts. Two support conditions, such as unfastened and fastened, were considered during their investigation. After proper validation and then parametric studies, they identified two critical ratios affects the web crippling capacity of lipped channels with web openings placed directly beneath the bearing plate such as the ratio of the diameter of the web opening to the straight portion of the web (a/h) and the ratio of bearing length to the height of the straight part of the web (N/h). Similarly, another two critical ratios were identified for web openings placed away from the bearing plate such as the ratio of the web opening distance from the bearing plate to the height of the straight portion of the web (x/h) and bearing length to the height of the straight portion of the web (N/h). The two separate reduction factor equations were proposed for unlipped channels with web openings located directly underneath and away from bearing plates using above-identified critical ratios. Based on their observation, the capacity reduction percentages improved from 40 to 35 and 50 to 40 for lipped channels with the circular centred beneath web opening with its size equal to 0.8 times the height of straight part of the web, under ITF and ETF load cases, respectively when supports were converted to fastened from the unfasted condition. Similarly, the capacity increased from 20 to 25 and 30 to 35 percentage for unlipped channels with web openings located away from the bearing plate for ITF and ETF load cases, respectively for the web openings placed with the distance of 0.8 times the height of the straight part of the web when supports were changed to a fastened case from unfastened supports.

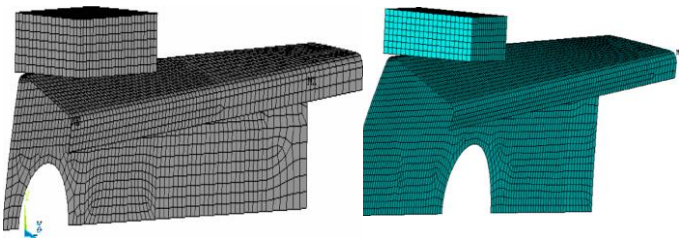

(a) Centered beneath web hole (b) Offset web hole

Fig. 3 Half FE models in ANSYS [10- 13]

Lian et al. [14-17] investigated the effect of both types of circular web openings, openings located underneath and away from the bearing plates on the capacity of unlipped channels subject to web crippling under one flange load cases. They first performed a limited number of experimental studies then performed numerical analysis using ABAQUS/CAE software. Above researchers [14-17] reported that the capacity reduction of unfastened support lipped channels with circular web opening placed directly underneath the bearing plate is about 10 and 12 percentages for EOF and IOF load cases when the ratio of the diameter of the web opening to the height of straight part of the web (a/h) is varied from 0 to 0.6. However, capacity reduction percentages are less than 5% for unlipped channels with web openings with fastened supports for both EOF and IOF load cases for the above-mention ratio with the same value range. The comparison of Uzzaman et al. [10-13] and Lian et al. [14-17] showed that the capacity reduction is more significant for lipped channels subjected to web crippling under two flange load case compared to one flange load case. Therefore, the behaviour of unlipped channel profiles under two-flange load cases also should be investigated for conservative design. Recently, Elilarasi and Janarthanan [34] investigated the behaviour of unfastened supports rectangular hollow flange beams (LSBs) with a circular web centred beneath and offset openings subject to web crippling using numerical analysis in ANSYS after accurate validation. They proposed two separate capacity reduction factor equations for LSBs with web openings located directly underneath and away from the bearing plates, respectively, after identifying the critical ratios.

In past experimental investigations, the different test set-ups and specimen lengths were used and created inconsistent between investigations. Three different test specimen arrangements such as (i) two mono-symmetric profiles facing each other to form a box arrangement [1, 25-28] (ii) two mono-symmetric profiles placed back to back [24] and (iii) single section only [4] for one flange load cases were employed. In addition, different specimen lengths were used especially under two flange load case such as (i) 1.5 times the height of the straight part of the web plus bearing length [24], (ii) 400 and 600 mm specimen lengths for ETF and ITF respectively [4] and (iii) three and five times overall depth of the sections for ETF and ITF respectively [3, 25-27]. AISI web crippling standard test method [21] is updated, which gives the proper guidelines about the specimen lengths and test set-up arrangement, should be followed in all experimental and numerical investigations about web crippling to prevent discrepancies in the selection of specimen lengths and test set-ups.

The discussion in the above section indicates that the structural performance of lipped and unlipped channels subject to web crippling is different under all four load cases. The recent research studies proposed new coefficients to the unified design equation to predict the capacity of unlipped channels subject to web crippling with fastened and unfastened supports. However, the main research gap is, although these steel profiles are increasingly used with web openings in the floor system, still, there have been no research studies performed to investigate the capacity reduction due to web openings on the web crippling capacity of unfastened unlipped channels under all four load cases. The effective approach to investigate this problem is utilizing the advancement in the computer technology, accurate finite element model development with the help of existing experimental data and then use the develop numerical models to investigate the capacity reduction of unlipped channels with web openings under web crippling. This journal paper addresses the reduction in the web crippling capacity of unlipped channel sections with unfastened supports due to the centred beneath and offset web openings under End-Two-Flange load case.

3. Research approach

The capacity reduction of unfastened support unlipped channels with web openings subject to web crippling under ETF load case is investigated using numerical analysis based on the given research approach as shown in Fig. 4 in this study. Five different existing web crippling data such as Sundararajah et al. [5, 27], Young and Hancock [24] and Uzzaman et al. [11-13] were used for this validation purpose.

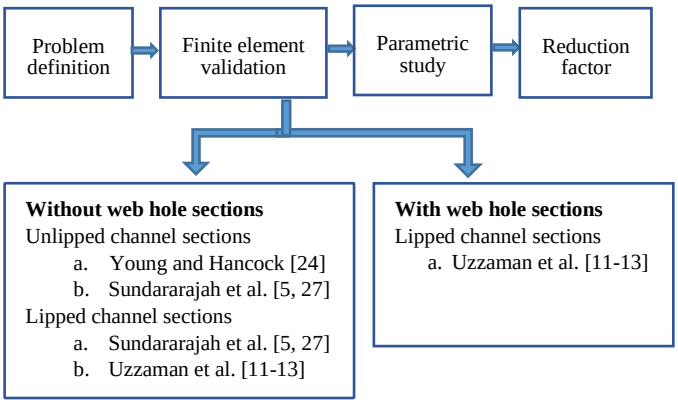

Fig. 4 Research approach

In the above studies, Sundararajah et al. [5, 27] explored the behaviour of thin-lipped and unlipped channels under web crippling where the overall depth of considered steel profiles varied from 100 to 200 mm while their thicknesses varied from 1.0 mm to 2.4 mm. Their specimen length is 3d, where d is the

height of straight part of the web of the sections, and three bearing lengths were used in their studies. Since Sundararajah et al. [5, 27] experimental study was limited to thin-sections, Young and Hancock [24] test results also used to validate the developed FE models to ensure the accuracy of models for both thin and thick steel profiles. Young and Hancock's [24] tests used thick unlipped channels with an overall depth of 75 to 300 mm while the thicknesses varied from 3.8 to 6.0. Their specimen lengths are equal to 1.5 times overall height of unlipped channel sections plus bearing length, and their bearing lengths were chosen equal to half and the full width of flanges. Uzzaman et al. [11-13] investigated the effect of web openings, both placed underneath and away from the bearing plates on the web crippling capacity of lipped channels using experimentally and numerically for two flange load cases. The overall depth varied from 142 to 302 mm while thicknesses ranged from 1.3 to 2.0 mm. They used three bearing lengths such as 90, 120 and 150 mm while the ratio of the diameter of circular web opening to the height of the straight part of the web is varied from 0 to 0.8 for centred beneath web openings. Their specimen length is similar to Young and Hancock [24]. The specimen lengths used by Young and Hancock [24] and Uzzaman et al. [11-13] are different compared to guidelines given in the recently updated AISI web crippling standard test method [21] while Sundararajah et al. [5, 27]'s specimen lengths are agreeing with the guidelines, which suggested to use three times the straight portion of web height of the channel sections. Although specimen length varied in above mentioned all three studies, the boundary and loadig conditions of loading and supporting plates are similar in all three tests and hence used for the validation purpose.

After accurate validation, the developed numerical model is used to enhance the data strength of unlipped channels subject to web crippling and to identify the critical parameters affecting the reduction of unlipped channels subject to web crippling. The comparison of FE capacities of unlipped channels without and with web openings are used to determine the effects of the critical parameters on the capacity reduction and to propose reduction factor equation.

4. Numerical analysis

Cold-formed steel profiles are thin with a thickness of less than 8.0 mm. Hence thickness can be neglected compared to the other two dimensions. Therefore, cold-formed steel profiles, both lipped and unlipped, are simulated in ANSYS [35] as shell element models. The FE models are generated according to the measured centre line dimensions, and measured thickness is assigned to them. The prediction accuracy of finite element models depends on several factors such as (i) element type (ii) mesh size (iii) material models (iv) boundary conditions (v) contact formulation and (vi) analysis type, and importance of each factor are discussed below.

a) Element type: ANSYS [35] has different elements types such as plane, shell and solid. The behaviour of cold-formed steel profiles under web crippling can be accurately simulated using three-dimensional shell elements such as SHELL43, SHELL63, SHELL93, SHELL181 and SHELL281. In above-mentioned shell elements, the first four elements are four-node elements while SHELL 281 is an eight-node element, where each node of the elements above-mentioned has six degrees of freedom. However, SHELL43 is used for plastic strain, while SHELL63 and SHELL93 are used for elastic strain only. SHELL181 and SHELL281 are finite strain elements and suitable to be used in web crippling problems. The predictions of web crippling finite element models using SHELL181 and SHELL281 are the same based on the preliminary investigations. However, the FE models with SHELL281 required more computational time and resources due to its eight nodes compared to FE models with SHELL181. Therefore, SHELL181 elements were employed to model the deformable beam in the developed FE models, similar to Ren et al.'s [32] and MacDonald et al.'s [4] studies. Bearing and loading plates are also modelled using SHELL181 elements and then converted to rigid elements using rigid elements.

b) Mesh size: Mesh sizes also equally impact the prediction accuracy of web crippling capacity of generated FE models. In FE models, 3 mm × 3 mm square meshes were employed for all channel sections except at the corners while fine meshes 3 mm × 1 mm were employed at the corners of unlipped channel profile to ensure proper load transfer from flanges to webs of the sections.

c) Mechanical properties: Since web crippling failure occurs at a yield strength of the steel, Young's modulus and material yield strengths are two material properties influence the web crippling capacity of cold-formed steel profiles. In these models, Young's modulus value of 203 GPa with measured material yield strengths were inserted into ANSYS software. Material yield strength can be defined using two methods such as (i) engineering stress vs engineering strain and (ii) true stress vs true strain values, where the later method considers the strain hardening effects of tensile coupon specimen. The measured engineering stress-strain values can be converted to true stress-strain using the below equations (Equations. 5a and 5b). Web crippling happens at the material yield strength, not at tensile strength. Hence the impact of strain hardening effects on the web crippling failure load is minimal (maximum of 2%) and can be neglected. Janarthanan et al. [29, 31] also reported that strain hardening effects on the web crippling are small. Hence, the bi-linear material model can be used in web crippling FE models.

$$\sigma_{true}=\sigma(1+\varepsilon) \tag{5a}$$

$$\varepsilon_{true} = \ln(1+\varepsilon) \tag{5b}$$

d) Loading and boundary conditions: In the developed FE models, loading and boundary conditions are only applied to the pilot node of bearing plates and then passed to the flanges of the cold-formed steel channels using interaction/ contacts only. Hence, contact/ interaction behaviour also equally contribute to the accuracy of FE models similar to boundary conditions. Contact formulation in FE models automatically considers the thickness of deformable shell elements. In the web crippling model, specimens were created using centre line dimensions. Therefore, the gap between the loading and support plates and deformable shell beams should be equal to half of the specimen thickness. Three types of contact generations are available such as pair-based contact, general contact and node to node contact. Both pair-based and general contact use surfaces to define contact and suitable for solving small or large sliding problems while node to node contact used in well-known contact locations and suitable for small sliding problems. In the developed FE models, the pair-based surface to surface contact option was used to form a contact between bearing plates and cold-formed steel sections. The penetration behaviour between rigid plates and cold-formed steel profile is decided by pressure-over closure relationship. There are two types available such as hard contact and soft contact. In these FE models, hard contact was employed in which infinity pressure is applied when both surfaces come in to contact.

The pilot node is created at mid-point of the bearing length and connected to mid-line of support and loading plates using TARGET170 element, which constraints all six degrees of freedom (three translational and three rotational degrees about x, y and z axes). The boundary and loading conditions are applied to the pilot node, as displayed in Fig. 5, which is located in the centre line of the bearing plate. Two translation degrees of freedom (UX and UZ) and two rotational degrees of freedom (ROTY and ROTZ) were fixed for support and loading plates. The vertical translation was fixed (UY) for support plates, while the displacement value of -40 mm was assigned to the loading plate. The loading rate was carefully controlled using a displacement controlled method. ROTX was allowed for both loading and support plates to simulate hinge supports similar to web crippling test set-up.

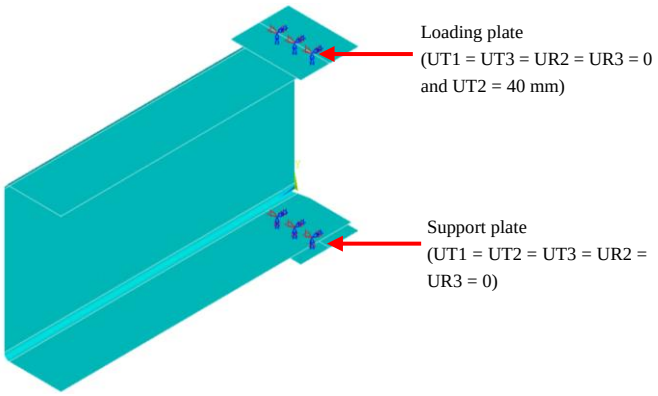

Fig. 5 Stimulation of the boundary condition

UT-Translation, UR-Rotation and 1, 2 and 3 denote the global axes x, y and z respectively.

e) Analysis method: In web crippling tests, displacement control method with the displacement rate of 1mm/minute was used to apply load. Hence this is a static problem. Among various analysis methods available in ANSYS [35], the static analysis was chosen in the FE study, which is related to time. The static analysis classifies large strain and small strain options. Cold-formed steel profiles experienced large strains when they were subjected to web crippling.

Addition to that, the web crippling strength of the channels were underestimated slightly by using small strain analysis and the large strain analysis provided a better prediction. So, large displacement static was used in this study.

5. Finite element validation & Parametric study

Five experimental datasets of web crippling performed by different researchers were used for the accurate FE validation purpose, as shown in Fig. 4. First, (i) Sundararajah et al. [5, 27], (ii) Young and Hancock [24] and (iii) Uzzaman et al. [11-13] test datasets were used to validate the developed FE models of channel sections, both lipped and unlipped profiles in the absence of web openings. For the validation purpose, the ultimate failure loads and failure modes obtained from numerical analysis were compared with test results. Figs. 6 and 7 show the comparison of ultimate failure loads obtained from FE models with Sundararajah et al.'s [5, 27] experimental results of lipped and unlipped channels, respectively. The comparison showed that the developed FE models of lipped and unlipped channels predicted web crippling capacities of the tested specimens accurately with the mean values of ratios of Sundararajah et al.'s [5, 27] tests to FEA predictions are 1.00 and 0.98, respectively while corresponding COV values of 0.09 and 0.03. In addition to web crippling capacity, web crippling failure mode of FE model is also compared with their experimental failure mode, as shown in Fig. 8. It can be seen that the FE model predicted the experimental failure mode accurately. However, Sundararajah et al.'s [5, 27] test data are only for thin channel sections. Hence, the developed FE models were again validated using Young and Hancock's [24] test data to ensure accurate predictions for thick channel sections. The comparison showed that the mean value of ratios of Young and Hancock's [24] tests to FEA predictions is 0.97, with COV value of 0.06, as shown in Table 2.

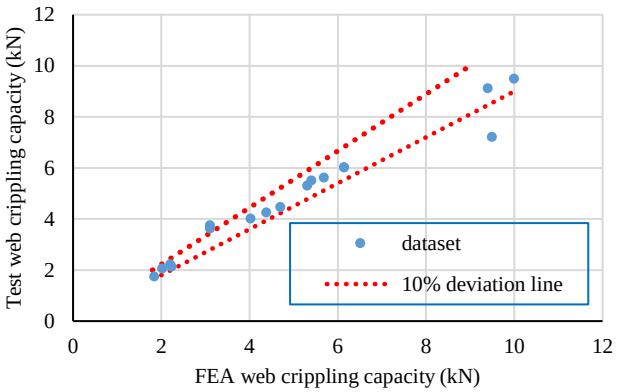

Fig. 6 Validation of lipped channel sections [5, 26]

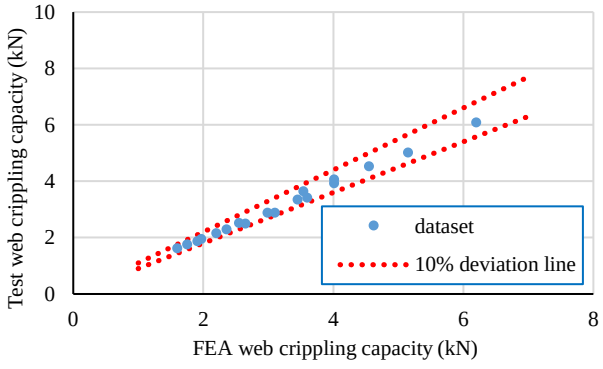

Fig. 7 Validation of unlipped channel sections [5, 27]

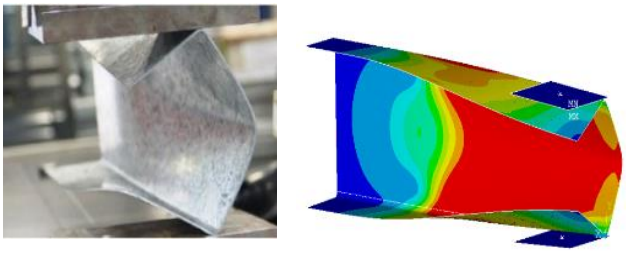

(a) Test [5] (b) FEA

Fig. 8 Failure mode comparison for without hole section

Finally, the developed FE models of lipped channels without and with web openings were validated using Uzzaman et al.'s [11-13]'s test data. Table 3 shows the comparison of Uzzaman et al.'s [11-13] test data to FEA predictions without web openings. The comparison showed that the mean value of ratios of the test to FEA predictions of lipped channels without web opening are 1.01 with COV value of 0.04.

Table 2
Validation of Young and Hancock's [24] test data

Unlipped channel section	*N* (mm)	*L* (mm)	FEA value (kN)	Test/FEA
75-40-4	20.0	113.6	19.8	0.92
75-40-4	40.0	152.0	23.8	0.93
100-50-4	25.0	175.0	21.5	1.05
100-50-4	50.0	200.2	25.6	0.97
125-65-4	32.5	219.8	22.6	1.04
125-65-4	65.0	252.5	27.5	1.03
200-75-5	37.5	336.9	33.5	0.93
200-75-5	75.0	375.3	38.9	1.03
250-90-6	45.0	421.0	51.0	0.92
250-90-6	90.0	465.1	55.0	0.92
300-90-6	45.0	495.2	44.7	1.02
300-90-6	90.0	539.6	54.5	0.91
	Mean			0.97
	COV			0.06

Table 3
Validation of Uzzaman et al.'s [11-13] test data

Lipped channel section	N (mm)	*L* (mm)	FEA value (kN)	Test/FEA
142-60-13	90	337.5	2.20	1.00
142-60-13	120	350.0	2.50	0.94
172-65-13	120	400.0	2.31	1.03
202-65-13	100	410.0	2.78	1.04
202-65-13	120	425.0	2.60	1.04
202-65-13	150	450.0	2.74	1.04
202-65-14	150	460.0	3.10	1.03
202-65-15	200	510.0	3.78	1.03
262-65-13	120	525.0	2.71	0.94
262-65-13	150	550.0	2.89	0.98
	Mean			1.01
	COV			0.04

Note: *N*- bearing length, *L*- specimen length

Figs. 9 and 10 show the comparison of FE results of lipped channels with centred beneath and offset web openings, respectively, with Uzzaman et al.[11-13]'s experimental studies. The comparison showed that mean values of ratios of the tests to FEA predictions of lipped channel sections with centred beneath and offset web openings are 0.97 and 1.10, respectively with corresponding COV values of 0.03 and 0.06. Failure modes obtained from FE models are agreed with Uzzaman et al.'s [11-13] experimental failure modes with increasing *a*/*h* ratio from 0 to 0.6, as shown in Fig. 11. Table 4 shows a summary of finite element validation. This validation procedure showed that the developed web crippling FE models without and with web opening under ETF load case predicted test web crippling capacities accurately. Therefore, these FE models can be used for parametric study confidently.

A detailed parametric study is undertaken using validated FE models to improve understanding of the web crippling behaviour of unlipped channels without and with web openings under ETF load case. The parametric study considers the effects of different parameters such as section thickness, material strength, web slenderness ratio and bearing length on the web crippling of unlipped chan-

nels without web openings. Additionally, the effect of centred beneath and offset web opening was investigated by varying the ratios of the diameter of web opening to a height of straight part of the web of the section (*a*/*h*) and distance from bearing plate to clear height of the web (*x*/*h*). Totally 186 FE models with centred beneath web openings, 540 offset web openings, and 72 FE models without web opening were developed and analysed in this parametric study. The predictions of existing web crippling design equations for unlipped channel sections without web opening were checked, and new reduction factor equation is proposed based on the obtained web crippling data.

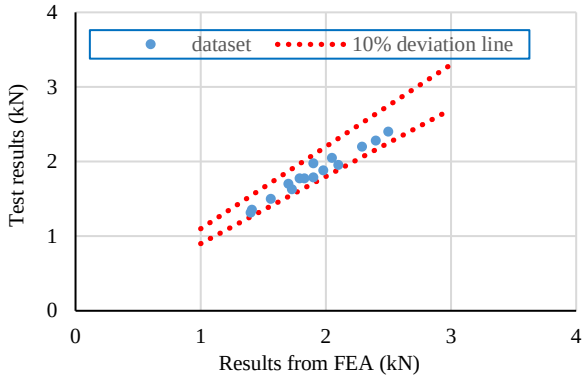

Fig. 9 Validation results of Uzzaman et al.'s [11-13] test with openings

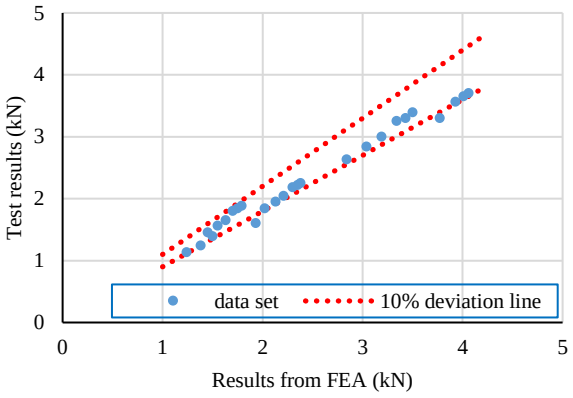

Fig. 10 Validation results of Uzzaman et al.'s [12,13] with offset hole sections

Table 4
Summary of past research studies validations

Section	Researcher	No of models	Mean	COV
Without web opening				
Unlipped channel	Young and Hancock [24]	12	0.97	0.06
	Sundararajah et al. [5, 27]	18	0.98	0.03
Lipped channel	Uzzaman et al. [11-13]	10	1.01	0.04
	Sundararajah et al. [5, 27]	18	1.00	0.09
With web opening				
Lipped channel-centred beneath	Uzzaman et al. [11-13]	15	0.97	0.03
Lipped channel-offset	Uzzaman et al. [11-13]	26	1.1	0.06
	Overall	99	1.01	0.05

6. Results and discussion

6.1. Predictions compared with existing design equations

The capacities of unlipped channels with web openings under ETF load case obtained from parametric numerical studies were compared with the available design equation for web crippling such as (i) unified design equation with coefficients of AISI S100 [18] and AS/NZS 4600 [19], the same above mentioned equation but with modified coefficients suggested by Gunalan and Mahendran [25, 26] and semi-empirical equation proposed by Young and Hancock [24].

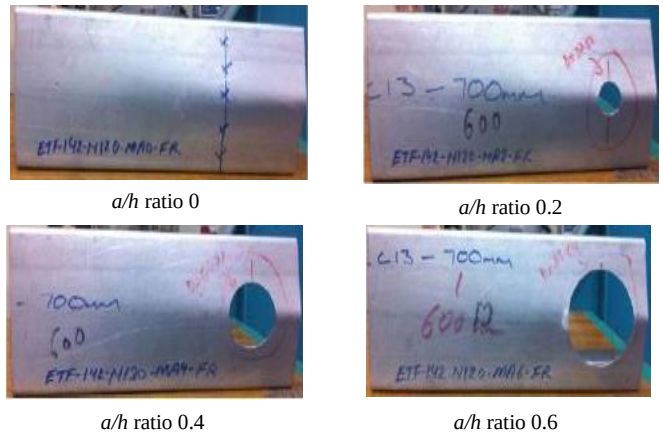

(a) Uzzaman et al.'s [11-13] test failure

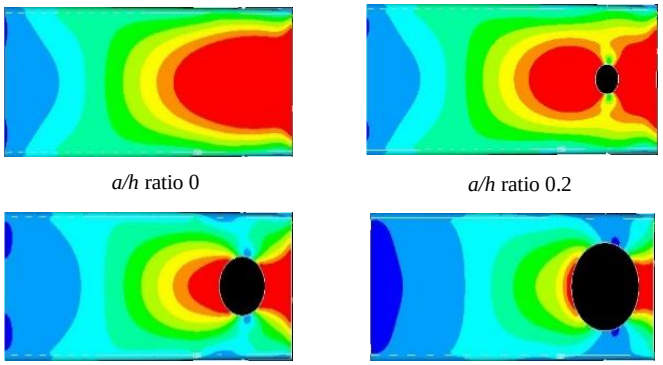

(b) FEA failure modes

Fig. 11 Failure mode comparisons of with and without web opening sections

(i) Fig. 12 compared the capacity predictions of unlipped channels using numerical models under web crippling without web-openings with estimated web crippling capacities based on unified design equation (Equation 1) with available coefficients in AISI S100 [18] and AS/NZS 4600 [19]. The comparison indicated that the mean value of the ratio of predictions from FE models to unified design equation with coefficients available in AISI S100 [18] and AS/NZS 4600 [19] is 0.91 while the COV of the comparison is 0.22 for unlipped channels with unfastened supports under ETF load case. The comparison showed that the predictions of the unified design equation with current existing coefficients are slightly conservative.

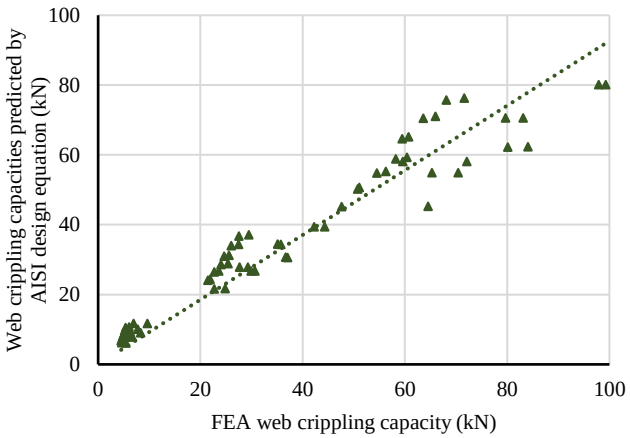

Fig. 12 Comparison of FEA results with predictions using unified web crippling equation based on AISI S100 [18] coefficients

(ii) Gunalan and Mahendran [25] also reported that capacity predictions of

current design equations with available coefficients in AISI S100 [18] and AS/NZS 4600 [19] for unfastened support unlipped channels under all four load cases are unconservative. The observation mentioned above is similar to Fig. 13. Therefore, they proposed new coefficients only to the current unified design equation (Equation 1) as listed in Table 5. In this study, the FEA capacity predictions of unlipped channels observed from numerical models were compared with the capacity estimation of unified design equation using the proposed coefficients by Gunalan and Mahendran [25]. The comparison indicated that the mean value of the ratio of predictions from FE models to unified design equation with coefficients proposed by Gunalan and Mahendran [25] is 1.17 while the COV of the comparison is 0.12 for unlipped channels with unfastened supports under ETF load case. This comparison showed that the capacity predictions of the unified design equation with proposed coefficient by Gunalan and Mahendran [25] is conservative for unlipped channels without web openings under ETF load case. Hence these coefficients can be used with the unified design equation to estimate web crippling capacity of unlipped channels under ETF loading. However, the new coefficients can be proposed to improve the prediction accuracy further.

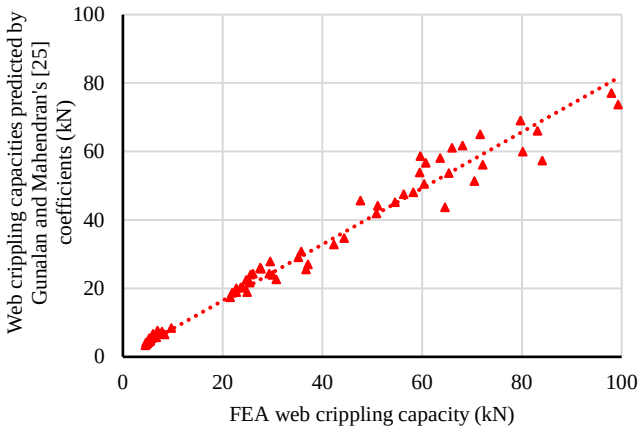

Fig. 13 Comparison of FEA results with predictions using unified web crippling equation based on Gunalan and Mahendran's [25] coefficients

Table 5
Proposed web crippling coefficient for unlipped channels

Equation	C	C_r	C_l	C_w	Mean	COV
AS/NZS 4600 [19]	2.00	0.11	0.37	0.01	0.91	0.22
Gunalan and Mahendren [25]	3.05	0.19	0.26	0.05	1.17	0.12
Proposed	3.50	0.19	0.27	0.05	1.00	0.10

(iii) Young and Hancock [24] developed a semi-empirical equation as shown in Equations 6a to 6e, to predict the web crippling capacities of unlipped channels without web-openings under ETF load case. This equation was developed using a combination of theoretical and empirical analysis and had a critical limitation which is only applicable to stocky unlipped channels, where slenderness of the web is less than 45.

$$P_{pm}=\frac{M_p N_m}{r}\left[1.44-0.0133\left(\frac{h}{t}\right)\right] \quad (6a)$$

$$M_p=\frac{f_y t^2}{4} \quad (6b)$$

$$r=r_i+\frac{t}{2} \quad (6c)$$

$$N_m=N+0.5d\ ,\quad N+0.3d \quad \text{for EOF and ETF load case} \quad (6d)$$

$$N_m=N+1.3d\ ,\quad N+1.40d \quad \text{for IOF and ITF load case} \quad (6e)$$

Where P_{pm} is the capacity prediction of web crippling based on plastic mechanism model, M_p - plastic moment per unit length, r and r_i are bent radii about centreline and internal dimensions, respectively, h - the height of the straight portion of the web of unlipped channels, d- web overall depth, N - the bearing length

Fig. 14 compared the capacity predictions of unlipped channels using numerical models under web crippling without web-openings with estimated capacity values using the equation proposed by Young and Hancock [24]. The comparison indicated that the mean value of the ratio of predictions from FE models to the capacity estimation by Young and Hancock's [24] semi-empirical equation is 1.00 while the COV of the comparison is 0.14 for unlipped channels with unfastened supports under ETF load case. The comparison mentioned above showed that the proposed equation by Young and Hancock [24] can be still used to estimate the web crippling capacities of unlipped channels without web openings under ETF load case.

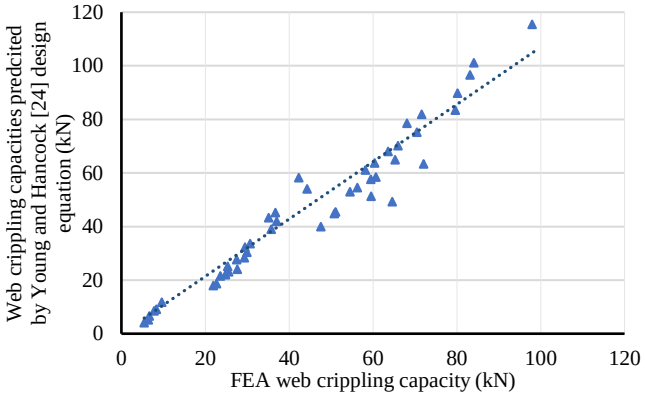

Fig. 14 Comparison of FEA results with predictions using Young and Hancock's [24] design equation

6.2. Improved design equation

As discussed in the above section (Section 6.1), currently available coefficients with unified design equation (Equation 1) predicted the capacities of unlipped channels without web-openings under web crippling for ETF load case unconservatively. Therefore, these currently available coefficients cannot be used to estimate failure loads of unlipped channels when they used as bearers and joists in construction. Although predicted capacities using the semi-empirical equation by Young and Hancock [24] agreed with predictions by FEA predicted capacities, their equation has a significant limitation, which restricts the applicability of their equation only to stocky unlipped channels, where the slenderness of the web is less than 45. The unified design equation (equation 1) with proposed improved coefficients by Gunalan and Mahendarn [25] predicted the capacities of unlipped channels without web-openings under ETF load case, conservatively. However, their coefficients were proposed based on 28 test results, and hence the proposed coefficients by them have fine-tuned form this study and given in Table 5. Fig. 15 compared the capacity predictions of unlipped channels using numerical models under web crippling without web-openings with estimated capacity values using the unified design equation with proposed coefficients as listed in Table 5. The comparison indicated that the mean value of the ratio of predictions from FE models to unified design equation with coefficients proposed from this study is 1.00 while the COV of the comparison is 0.10 for unlipped channels with unfastened supports under ETF load case. It is shown that the proposed coefficients agree well with the numerical results. The coefficient only applies for $h/t \le 115$, $N/t \le 75$, $N/h \le 1.9$, $a/h \le 0.8$ and $\Theta = 90$.

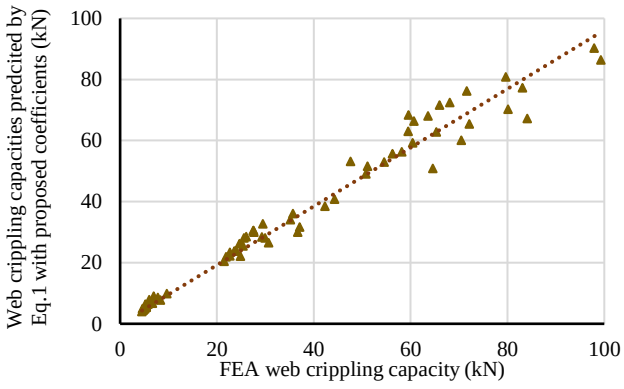

Fig. 15 Comparison of FEA results with predictions using unified web crippling equation based on Authors proposed coefficients

6.3. Capacity reduction due to web opening

As discussed earlier, the introduction of the openings at the web of unlipped channels reduces the resisting area of the concentrated loads and hence vulnerability chances of web crippling increase further for unlipped channels under concentrated loads. Typically, web crippling failure initiates at the free edges of channel sections under ETF load cases. However, the failure mechanism is changed with the introduction of the web opening, as shown in Fig. 16. As shown in Fig.16, in stage - 01 and stage - 02, web crippling failure is initiated near to the web opening, and it proliferates towards the free edge of the web compared to another side. After that in stage - 03, it extends to another side of the web section due to the load increment. Beyond that point in the ultimate stage - 04, the web of the section is crippled. Due to above-mention reason, web crippling failure of unlipped channels with web openings under ETF load case should be investigated.

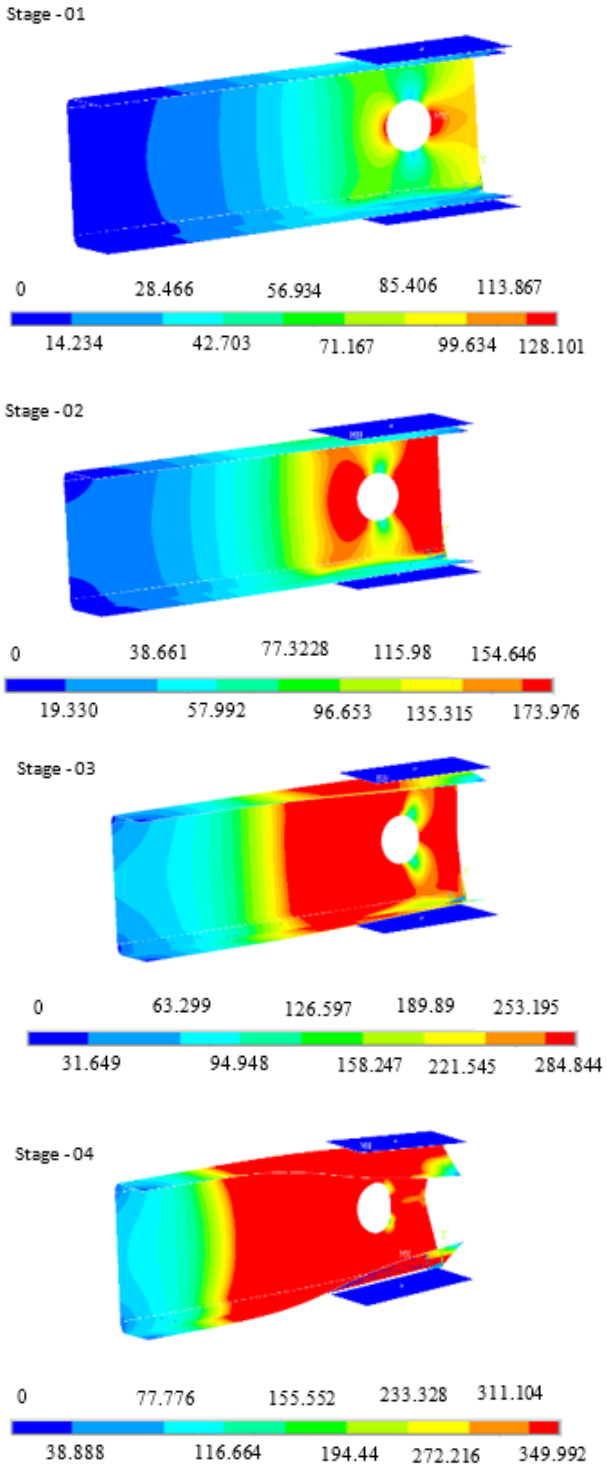

Fig. 16 Effect of web hole in the failure mechanism of unlipped channel section

Altogether, 186 and 540 numerical models of unlipped channels under ETF load case with two types of circular web openings such as (i) centred beneath and (ii) offset, respectively to investigate the effect of these openings on the web crippling capacity. The purpose of the study is also to identify the influencing parameters and to determine the reduction of web crippling capacity. The study indicated that two critical ratios such as (i) ratio of the diameter of the circular web opening to the height of the straight portion of the web (a/h) of unlipped channels and (ii) bearing length to the height of the straight portion of the web (N/h) of unlipped channels, dominated the reduction of web crippling of unlipped channels with centred beneath web openings. Similarly, another two critical ratios such as (i) the ratio of the nearest distance of the circular web opening to the edge of the bearing plate (x/h) and (ii) bearing length to the height of the straight portion of the web of unlipped channels (N/h) dominated the reduction of web crippling of unlipped channels with offset web openings. These observations are similar to past research outcomes. The effect of above-mentioned ratios on the web crippling capacity reduction of unlipped channels was investigated as discussed below.

The capacity reduction and its percentages of two unlipped channels such as 100×50×4 and 150×75×2, subjected to concentrated load via 100 and 150 mm bearing plates, respectively with varying ratio of the diameter of web opening to the height of straight web portion of the web of the channel (a/h) from 0 to 0.8 were investigated and reported in Table 6.

Table 6
Capacity reduction due to web hole

Bearing length N (mm)	a/h ratio	FEA value (kN)	Reduction %
	100×50×4, specimen length 300 mm		
100	0.0	30.0	-
100	0.2	27.1	9.7
100	0.4	23.6	21.3
100	0.6	20.4	32.0
100	0.8	17.5	41.7
	150×75×2, specimen length 450 mm		
150	0.0	6.1	-
150	0.2	5.6	8.2
150	0.4	4.9	19.7
150	0.6	4.2	31.1
150	0.8	3.6	40.1

As listed in Table 6, the capacity reduction of 100×50×4 unlipped channels due to web opening underneath the bearing plate subjected to the concentrated load via 100 mm bearing plate is 9.7, 21.3, 32.0 and 41.7 percentages with the variation of the ratio of the diameter of circular web opening to the height of the straight portion of the web of the section (a/h) from 0 to 0.8 in steps of 0.2. However, the observed reductions for 150×75×2 unlipped channels with circular web openings subjected to concentrated load via 150 mm are 8.2, 19.7, 31.1 and 40.1 percentages with the above (a/h) variation. The above observation showed the capacity reduction of web crippling depends on the bearing lengths in addition to different steel profiles. As discussed, although the reduction percentages varied for different steel profiles, the capacity reduction of web crippling for unlipped channels with circular centred beneath web opening almost linearly increases with the ratio of the diameter of circular web opening to the height of the straight portion of the web of unlipped channels as shown in Fig. 17. Fig. 17 showed that above mentioned a/h ratio is one of the critical parameters, dominates the web crippling reduction of unlipped channels with centred beneath web openings.

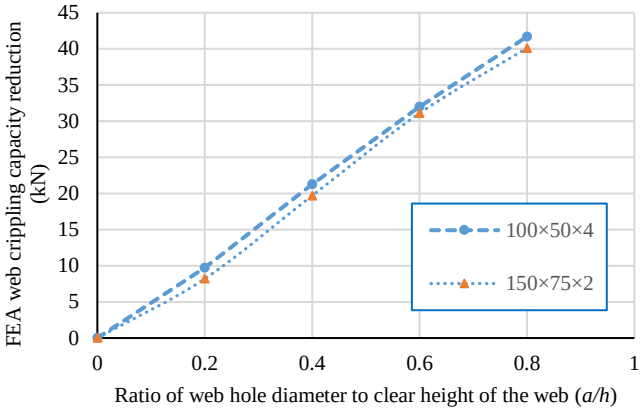

Fig. 17 Effect of web opening diameter to clear height of the web on web crippling capacity reduction

The effect of different bearing lengths on the web crippling capacity of unlipped channels with circular centred beneath web opening under ETF load case was investigated using two test samples such as (i) 100×50×4 mm unlipped channels concentrically loaded via bearing lengths of 50, 100 and 150 mm and (ii) 200×75×4 mm unlipped channels concentrically loaded via bearing lengths of 90, 120 and 150 mm. The effect of bearing plate lengths on web crippling capacity with increasing web opening diameter to height of the straight portion of the web (*a*/*h*) values for the section are shown in Fig. 18(a) and (b), respectively. As shown in Figs. 18(a) and 18(b), the ultimate capacities of unlipped channels with web openings under web crippling for ETF load case increases linearly with increasing bearing lengths for both considered sections. However, the increment percentage is different for both sections. The web crippling capacity increases by 24, 26, 30 and 34 percentages with the increasing a/h ratio values of 0.2, 0.4 and 0.6 for 100×50×4 mm unlipped channel subjected to concentrated load via 150 mm bearing plate compared to 100 mm bearing plate. Similarly, the web crippling capacity increases by 13% for all a/h values for 200×75×4 mm unlipped channel subjected to concentrated load via 150 mm compared to 120 mm. Fig. 18 displayed that the capacity reduction of unlipped channels depends on the bearing length also an addition to the ratio of the diameter of web opening to the height of the straight portion of the web of unlipped channels. Therefore, bearing length effect also must be included in the reduction factor. Therefore, the web crippling reduction factor for centred beneath web openings was developed using above mentioned two parameters such as (i) diameter of the circular web opening to the height of the straight portion of the web and (ii) bearing length to the height of the straight portion of the web.

This study also investigates the effects of circular web openings located away the concentrated loads (circular offset) on the capacity of unlipped channels under web crippling, and the observed results are displayed in Fig. 19. Fig. 19 portrayed the variation of web crippling capacity of unlipped channels with the increasing ratio of the near web opening distance from the edge of bearing plate to the height of the straight part of the web (*x*/*h*). The capacities of some unlipped channels under web crippling showed increment by 15%. In comparison, others showed 10% increment only with the variation of the ratio of the near web opening distance from the edge of bearing plate to the height of the straight part of the web (*x*/*h*) from 0 to 0.6. Based on the observation, another reduction factor should be proposed for offset circular web openings based on the ratios of the ratio of the near web opening distance from the bearing plate edge to the height of the straight web part (*x*/*h*) and diameter of circular web opening to the height of the straight web part (*a*/*h*).

6.4. Proposed strength reduction factor

The reduction due to web openings both located underneath and away from the bearing plate was determined by comparing the FE predicted capacity of unlipped channels with and without opening. Then the ratio of capacity reduction to the web crippling capacity of unlipped channels without web openings was determined, and this ratio was the capacity reduction factor. Based on conducted parametric study, the capacity reductions of unlipped channels with web openings underneath the bearing plates under ETF load case showed the linear variation trend for the two ratios such as: (i) the capacity reducing with the increasing ratio of the diameter of circular web opening to the height of straight part of the web (*a*/*h*) and (ii) the capacity increases with the ratio of the bearing length to the height of the straight part of the web (*N*/*h*). Based on the above observation and using all determined capacity reduction values from the parametric study, an equation for the reduction factor is developed using bivariate linear regression analysis in terms of above two ratios as shown in Equation 7a.

$$R_b = 0.95 - 0.6(a/h) + 0.06(N/h) \quad (7a)$$

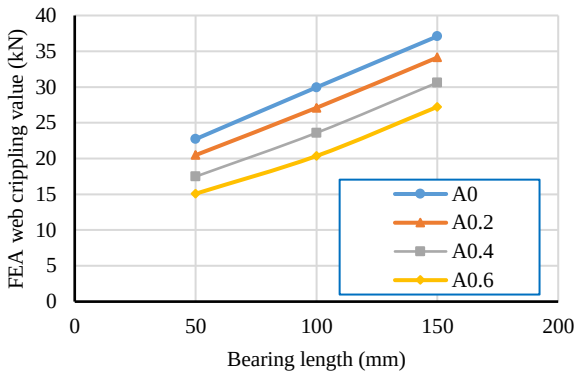

(a) 100×50×4 mm unlipped channel

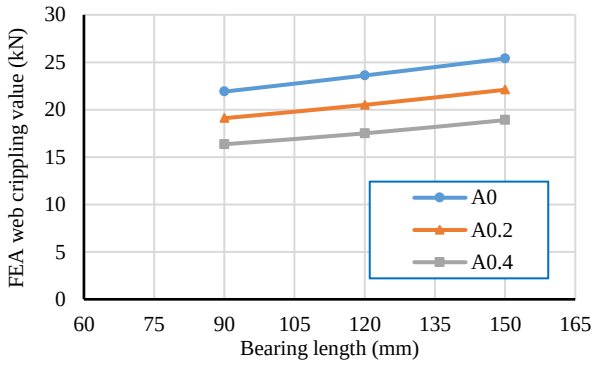

(b) 200×75×4 mm unlipped channel

Fig. 18 Effect of bearing length on web crippling capacity of unlipped channels

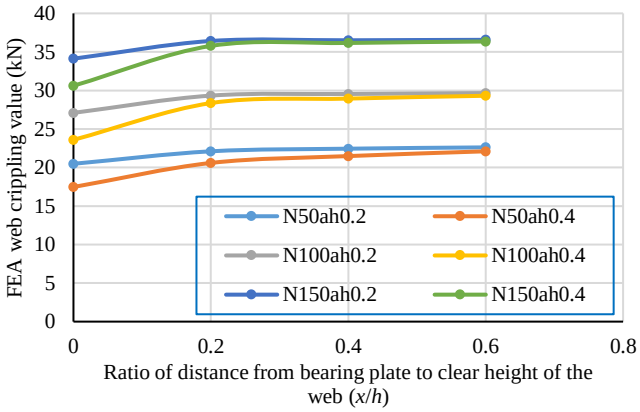

Fig. 19 Web crippling capacity variation with location of opening

Similarly, the capacity reductions of unlipped channels with web openings located away from the bearing plates (offset) showed a linear variation trend with two ratios such as (i) the capacity reducing with the increasing ratio of the diameter of circular web opening to the height of straight part of the web (*a*/*h*) and (ii) the capacity increases with the ratio of the near web opening distance from the edge of bearing plate to the height of the straight part of the web (*x*/*h*). Based on the above observation and using all determined capacity reduction values, an equation for the reduction factor is developed using bivariate linear regression analysis in terms of the above two ratios, as shown in Equation 7b.

$$R_b = 0.98 - 0.25(a/h) + 0.17(x/h) \quad (7b)$$

The limits for the reduction factor Equations 7a and 7b are $h/t_w \le 115$, $N/t_w \le 75$, $N/h \le 1.9$, $a/h \le 0.8$ and $\Theta = 90°$.

Figs. 20 and 21 compared the predictions of reduction factors determined using the above developed two equations for unlipped channels with circular centred beneath and offset web openings, respectively for ETF load case with calculated reduction factors using capacity values of unlipped channels with and without web openings. The mean value of the ratio of predicted reduction

factors using the proposed equation to reduction factors determined using FE capacities are 0.99 and 1.00 for centred beneath and offset web openings, respectively with the corresponding COV values of 0.05 and 0.11 for unlipped channels with unfastened supports for ETF load case. Therefore, the proposed capacity reduction factor equations with the unified design equation (Equation 1) can be used to predict the capacities of unlipped channels with web openings with unfastened supports under ETF load case.

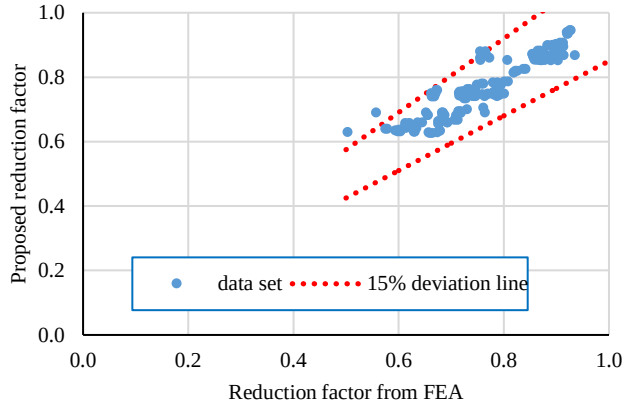

Fig. 20 Comparison of reduction factor obtained using proposed equation for centred beneath and FEA

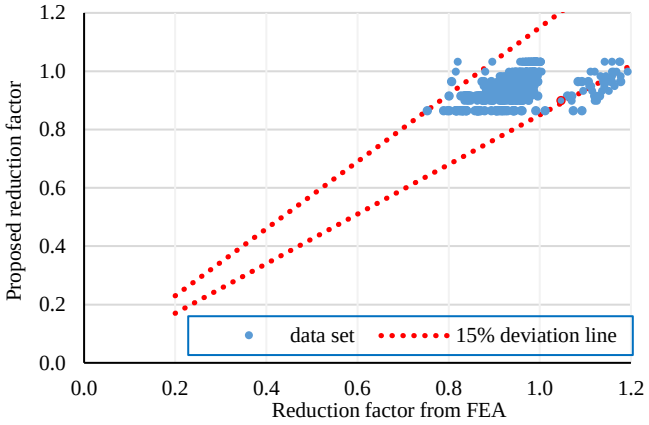

Fig. 21 Comparison of reduction factor obtained using proposed equation for offset and FEA

The capacity reduction factor is applied to adjust the prediction for safe design. The North American specification for the design of cold-formed steel structural members [20] recommends the following equation to calculate the capacity reduction factor (φ_w).

$$\phi_w = C M_m F_m P_m e^{-x} \tag{10}$$

$$x = \beta_0 \sqrt{V_M^2 + V_F^2 + C_P V_P^2 + V_Q^2} \tag{11}$$

In Eq. 10, C is equal to 1.521 from AISI S100. The statistical parameters are obtained from AISI S100 for web crippling strength, where Mm = 1.1, Fm = 1.0, VM = 0.1 and VF = 0.05. The parameters Pm and Vp are the mean and the coefficient of variation of the tested to predicted load ratio. The statistical parameter VQ is the coefficient of variation of load effects and depends on the dead load to live load ratio (D/L). It is given as 0.21 in AISI S100 [18]. The parameter Cp is a correction factor for the small number of tests and is given by ; n is the number of tests; m is the degree of freedom = n - 1. The values of Pm and Vp, in this case, are 0.990 and 0.049 for centred beneath and 1.00 and 0.11 for offset as well, which are based on the FEA/Proposed ratios. Using these values, Eq. 10 gives a capacity reduction (φ_w) of 0.90 and 0.87 for centred beneath and offset respectively for target reliability index of 2.5.

7. Conclusion

This article presented the details of numerical investigation of the effects of circular web openings on the web crippling performance of unfastened unlipped channels under ETF load case. The two types of web openings such as opening directly beneath the concentrated load (centred beneath) and an opening located away from the concentrated load (offset) were considered. Numerical models of lipped and unlipped channels without web openings were developed and validated in ANSYS software using existing five test data set in the literature to create more accurate FE model without errors due to practical differences. Based on the validated FE models, the behaviour of unlipped channels without web openings was first investigated and compared with predictions using available design equations. The capacity predictions of unlipped channels without web opening under ETF load case using unified design equation with current web crippling coefficients in AISI S100 and AS/NZS 4600 were unconservative while the suggested design equations by Young and Hancock [24] and Gunalan and Mahendran [25] were conservative and can be used. The improved coefficients were proposed to the current unified web crippling design equations to improve the capacity prediction accuracy of unfastened unlipped channels without web openings under ETF load case. The numerical models of unlipped channels with web circular openings underneath the bearing plate and away from the bearing plate were developed and validated using two existing test data. The validated numerical models were then used to investigate the capacity reduction of unfastened unlipped channels subjected to web crippling with circular web openings underneath and away from the concentrated loads for ETF load case. Each two ratios were identified as critical ratios for capacity reduction of unlipped channels with web openings underneath and away from the bearing plates such as (i) the diameter of circular web opening to the height of straight part of the web (*a*/*h*) and bearing length to the height of straight part of the web (*N*/*h*) for web openings directly underneath the load plates while (ii) the diameter of circular web opening to the height of straight part of the web (*a*/*h*) and the web opening near distance to the edge of the bearing plate to the height of the straight web part (*x*/*h*). Based on the parametric study, two separate reduction factor equations were developed for unlipped channels with web openings directly underneath and located away from the bearing plates, respectively based on above-identified two critical ratios under ETF load case. The proposed reduction factors can be used with the unified design equation (Equation 1) with proposed improved four coefficients from this study can be used to estimate failure loads of unlipped channels with both types of web openings under ETF load case.

References

[1] Hetrakul, N., and Yu, W.W. (1978), Structural behaviour of beam webs subjected to web crippling and a combination of web crippling and bending, Final Report, Civil Engineering Study 78-4, University of Missouri-Rolla, Rolla, Missouri, USA.

[2] Gerges, R.R. and Schuster, R.M. (1998), Web Crippling of single web cold-formed steel members subjected to end-one-flange loading, Proc. of Fourth International Specialty Conference on Cold-formed Steel Structures, St. Louis, Missouri, USA.

[3] Beshara, B. and Schuster, R.M. (2000), Web crippling of cold-formed steel C and Z sections, Proc. of 15th International Speciality Conference on Cold-Formed Steel Structures, St.Louis, Missouri, U.S.A.

[4] Macdonald, M., Heiyantuduwa, M.A., Koteko, M. and Rhodes, J. (2011), Web crippling behaviour of thin-walled lipped channel beams. Thin-Walled Structures, 49: 682–690.

[5] Sundarajah, L., Mahendran, M. and Keerthan, P. (2017), New design rules for lipped channel beams subject to web crippling under two-flange load cases, Thin-Walled Structures, 2017; 119: 421-437.

[6] Yu, W.W. and Davis, C.S., Cold-formed steel members with perforated elements, Journal of the Structural Division, 1973; 99: 2061-2077.

[7] Sivakumaran, K.S. and Zielonka, K.M., Web crippling strength of thin-walled steel members with web opening, Thin-Walled Structures, 1989; 8: 295-319.

[8] Langan, J.E., LaBoube, R.A. and Yu, W.W., Structural behavior of perforated web elements of cold-formed steel flexural members subjected to web crippling and a combination of web crippling and bending, Final report, Civil Engineering Study 94-3, Cold-Formed Steel Series, Rolla, MO: University of Missouri- Rolla; 1994.

[9] LaBoube, R.A., Yu, W., Deshmukh, S. and Uphoff, C.A. (1999), Crippling capacity of web elements with openings, Journal of Structural Engineering, 1999; 125(2): 137-141.

[10] Uzzaman, A., Lim, J.B.P., Nash, D., Rhodes, J. and Young, B., Web crippling behaviour of cold-formed steel channel sections with offset web holes subjected to interior-two-flange loading, Thin-Walled Structures, 2012; 50: 76-86.

[11] Uzzaman, A., Lim, J.B.P., Nash, D., Rhodes, J. and Young, B., Cold-formed steel sections with web openings subjected to web crippling under two-flange loading conditions-part I: Tests and finite element analysis. Thin-Walled Struct 2012;56:38-48.

[12] Uzzaman, A., Lim, J.B.P., Nash, D., Rhodes, J. and Young, B., Cold-formed steel sections with web openings subjected to web crippling under two-flange loading conditions-part II: Parametric study and proposed design equations, Thin-Walled Structures, 2012; 56: 79-87.

[13] Uzzaman, A., Lim, J.B.P., Nash, D., Rhodes, J. and Young, B., Effect of offset web holes on webcrippling strength of cold-formed steel achannel sections under end-two-flange loading condition, Thin-Walled Structures, 2013; 65: 34-48.

[14] Lian, Y., Uzzaman, A., Lim, J.B.P., Abdelal, G., Nash, D. and Young, B. (2016), Effect of web holes on web crippling strength of cold-formed steel channel sections under end-one-flange loading condition - Part I: Tests and finite element analysis, Thin-Walled Structures, 2016; 107: 443-452.

[15] Lian, Y., Uzzaman, A., Lim, J.B.P., Abdelal, G., Nash, D. and Young, B. (2016), Effect of web holes on web crippling strength of cold-formed steel channel sections under end-one-flange loading condition - Part II: Parametric study and proposed design equations, Thin-

Walled Structures, 2016; 107: 489-501.
[16] Lian, Y., Uzzaman, A., Lim, J.B.P., Abdelal, G., Nash, D. and Young, B. (2017), Web crippling behaviour of cold-formed steel channel sections with web holes subjected to interior-one-flange loading condition- Part I: Experimental and numerical investigation, Thin-Walled Structures, 2017; 111: 103-112.
[17] Lian, Y., Uzzaman, A., Lim, J.B.P., Abdelal, G., Nash, D. and Young, B. (2017), Web crippling behaviour of cold-formed steel channel sections with web holes subjected to interior-one-flange loading condition- Part II: Parametric study and proposed design equations. Thin-Walled Structures, 2017; 114: 92-106.
[18] American Iron and Steel Institute (AISI), Specifications for the cold-formed steel structural members, cold-formed steel design manual, AISI S100, Washington DC, USA, 2017.
[19] Standards Australia/Standards New Zealand (SA), Australia/New Zealand Standard AS/NZS 4600 Cold-formed steel structures, Sydney, Australia, 2018.
[20] Eurocode 3 Part 1.3 (ECS), Design of Steel Structures: Part 1.3: General Rules - Supplementary rules for cold-formed thin gauge members and sheeting, European Committee for Standardization, Brussels, Belgium, 2006.
[21] American Iron and Steel Institute, Standard test method for determining the web crippling strength of cold-formed steel beams, AISI S909, Washington DC, USA, 2017.
[22] Sivakumaran, K., Analysis of web crippling behaviour of cold-formed steel members, Comput. Struct. 32 (1989) 707–719.
[23] Winter, G. and Pian, R.H.J. (1946), Crushing Strength of Thin Steel Webs, Engineering Experiment, Bulletinno.35, Cornell University, New York, US
[24] Young, B. and Hancock, G., Design of cold-formed channels subjected to web crippling, Journal of Structural Engineering, 2001; 127: 1137-1144.
[25] Gunalan, S. and Mahendran, M. (2015), Web Crippling Tests of Cold-formed Unlipped Channel Sections under Two Flange Load Cases, Journal of Constructional Steel Research, Vol. 110, pp. 1-15
[26] Gunalan, S. and Mahendran, M. (2019), Experimental study of unlipped channel beams subject to web crippling under one flange load cases, Advanced Steel Construction, Vol. 15, pp. 165-172.
[27] Sundararajah, L. Web Crippling Studies of Cold-formed Steel Channel Beams- Experiments, Numerical Analyses and Design Rules (Ph.D. thesis), Queensland University of Technology, Brisbane, Australia, 2016.
[28] Janarthanan, B., Mahendran, M. and Gunalan, S., Bearing capacity of cold-formed unlipped channels with restrained flanges under EOF and IOF load cases, Steel Construction, 2015; 8: 146-154.
[29] Janarthanan, B., Mahendran, M. and Gunalan, S., Numerical modelling of web crippling failures in cold-formed steel unlipped channel sections, Journal of Constructional Steel Research, 2019; 158: 486-501.
[30] Janarthanan, B., Sundarajah, L., Mahendran, M., Keerthan, P. and Gunalan, S., Web crippling behaviour and design of cold-formed steel sections, Thin-Walled Structures, 2019; 140: 387-403.
[31] Janarthanan, B. and Mahendran, M., Numerical study of cold-formed steel channel sections under combined web crippling and bending action, Thin-walled Structures, 2020,152
[32] Ren, W.X., Fang, S.E. and Young, B., Finite-element simulation and design of cold-formed steel channels subjected to web crippling, Journal of Structural Engineering, 2006; 132: 1967-1975.
[33] Natario, P., Silvestre, N. and Camotim, D., Web crippling failure using quasi-static FE models, Thin-Walled Structures, 2014; 84: 34-49.
[34] Ellilarasi, K. and Janarthanan, B., effect of web holes on the web crippling capacity of cold-formed LiteSteel beams under End_Two-Flange load case, Structures, 2020; 25: 411-425.
[35] ANSYS Mechanical APDL Verification Manual, Release 15.0, 2013. MANUAL

Advanced Steel Construction – Vol. 16 No. 4 (2020) 321–327
DOI: 10.18057/IJASC.2020.16.4.4

BENDING CAPACITY OF BIAXIAL-HOLLOW RC SLAB WITH ASYMMETRIC STEEL BEAMS

Chao Gong [1], Zhao-Xin Hou [1], Guo-Zhong Cheng [2,*], Gang Wang [1] and Y. Frank Chen [2]

[1] *Central Research Institute of Building and Construction Co., Ltd, Beijing 100088, China.*
[2] *Key Laboratory of New Technology for Construction of Cities in Mountain Area (Chongqing University), Ministry of Education, Chongqing 400045, China*
** (Corresponding author: E-mail: chengguozhong@cqu.edu.cn)*

ABSTRACT

A new composite slim floor system with voided RC slab is proposed, where the precast RC slab is used as the structural component as well as the permanent formwork, with the large voids achieved by light-weight fillers introduced to reduce the slab weight. The overlapping rebars pass through the web openings of steel beam, thus enhancing the interaction between the RC slab and steel beam. As a pilot study of the proposed floor system, the bending behavior of the new composite slim beam was investigated experimentally on four specimens. The full interaction between the RC slab and steel beam is demonstrated by the test and finite element analysis results. In addition, a calculation method for bending capacity is proposed.

ARTICLE HISTORY

Received: 21 September 2019
Revised: 29 July 2020
Accepted: 10 August 2020

KEYWORDS

Composite slim floor;
Biaxial-hollow slab;
Asymmetric steel beam;
Bending capacity.

1. Introduction

A variety of composite floor systems have been proposed and used for buildings throughout the world [1-4]. Among them, the composite floor system with the H-shaped steel beam and reinforced concrete (RC) slab (Fig. 1(a)) has been commonly used in building structures [5,6]. The presence of RC slab increases the lateral stability and bending capacity of H-shaped beam and the profiled steel deck serves as the permanent formwork, resulting in a simpler construction process. However, such composite floor system has a larger depth than a typical RC beam as the steel deck needs to be set at the top flange of steel beam. Besides, it requires additional fire protection materials. To decrease the overall depth of floor systems in multi-story buildings, a composite slim floor system has been first developed in Scandinavia and then widely used in Europe and the United States [7,8]. In this system (Fig. 1(b)), an asymmetric steel beam with a wider bottom flange is used, where the deep steel deck is set at the bottom flange of the steel beam. As such, the steel beam is mostly contained within the depth of RC slab, resulting in a solid flat slab appearance similar to the RC construction that requires minimal fire protection [9,10]. Besides, the concrete surrounding the steel beam increases the bending capacity and local buckling strength of the steel beam. Therefore, the composite slim floor system is considered as a good alternative to the traditional floor system.

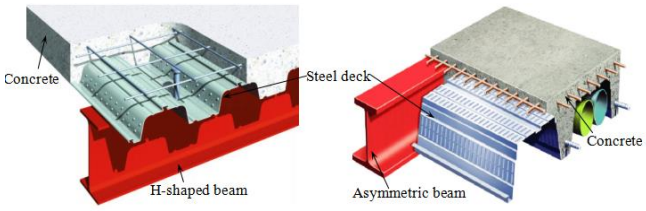

Fig. 1 Composite beams

The composite slim floor system had been studied somewhat extensively in terms of the integration of the composite beam and the connection between the composite slim floor and the column. Research on nine composite slim beams had been conducted at Helsinki University of Technology [11]. Additionally, a study on the behavior of composite beam-to-column connections had also been made at Helsinki University of Technology [12]. To investigate the influences of reinforcement ratio and load condition on the behavior of composite slim beams, experiments on eight specimens had been conducted at Trento University [13], in which the experimental results showed that the reinforcement ratio had a significant influence on the loading capacity of composite connections. The design of composite slim beams depends mainly on the shear transfer mechanism provided by the shear connectors between the RC slab and steel beam and a good number of studies on the behavior of shear connectors in such members had been conducted [14,15]. The available experimental results indicated that the interface slippage between the concrete slab and steel beam could be neglected. Besides the structural behavior, a holistic research had also been conducted on the fire resistance of composite slim floor systems [16,17]. In the composite slim floor system, deep decks are commonly used. Decks deeper than 200 mm may not be available in every place including China. Besides, the deeper decks need to be protected from corrosion, thus increasing the cost. Moreover, the traditional composite slim floor system is not suitable for moment resistance due to the semi-rigid connections between beams and columns. Therefore, the traditional composite slim floor system is not widely used in China. For improvement, a new composite floor system (Fig. 2) has been proposed by the researchers at Korea University, where the circular openings in the steel web enable the transverse reinforcements to pass through the beam, making the moment-resisting frame suitable. A number of spheres are introduced to reduce the weight of RC slab. The Glass Fiber Reinforced Plastic (GFRP) plate, which is attached to the bottom flange of the steel beam, acts as a structural reinforcement as well as a good heat insulator. A series of studies on the structural behavior of the new composite beam have been conducted at Korea University [18-20]. However, in this system the steel deck is only used as the permanent formwork, which requires additional supports; and it is time-consuming to place the numerous spheres in place.

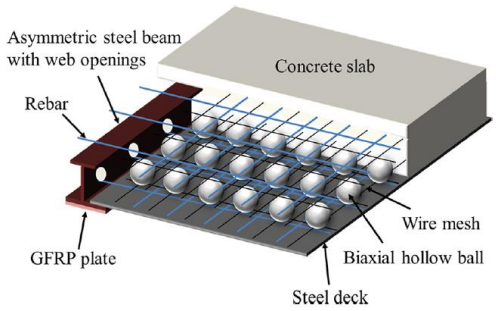

Fig. 2 The composite floor system proposed by Korea University

In this paper, a newer composite floor system, as shown in Fig. 3, is proposed to further improve the performance of existing composite slim floor systems. In this system, an asymmetric steel beam with web openings is used to reduce the depth of composite floor, similar to other composite slim floor systems. The overlapping rebars, which pass through the beam web openings, plus the shear studs enhance the integrity of composite floor. The stirrups are

used to transfer the shear force between the precast RC slab and cast-in-place concrete. The precast RC slab is used as the structural component as well as the permanent formwork, which is more cost-effective. The large voids achieved by light-weight fillers are introduced to reduce the weight of RC slab, which can be easily installed in place. The bottom flange of steel beam is covered by the concrete for fire protection. A practical project adopting the new composite floor system is shown Fig. 4, which is a prefabricated building in Tangshan City (China). To investigate the flexural performance of the proposed floor system, four composite slim beams were tested.

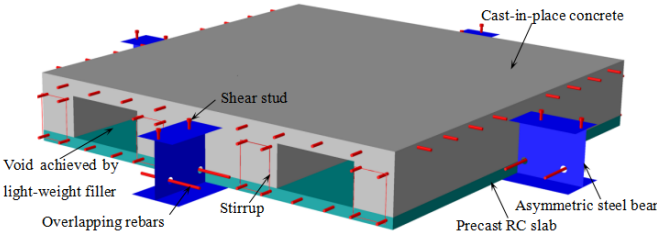

Fig. 3 Proposed composite floor system

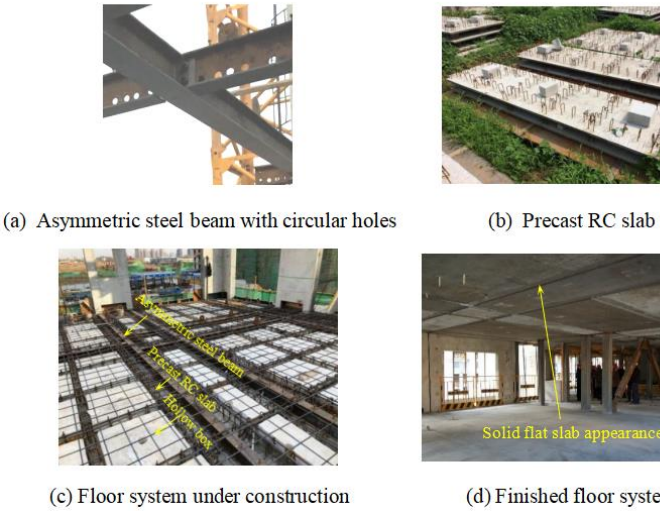

Fig. 4 A practical project using the new composite floor system

2. Experimental program

2.1. Description of specimens

Four full-scale specimens were designed and tested in this study. Each specimen consists of the asymmetric steel beam, precast concrete, fillers, cast-in-place (CIP) concrete, and rebars. The fillers are made of light-weight expanded polystyrene boards. Fig. 5 shows the specimen's cross-section and dimensions and Fig. 6 indicates the filler locations. As shown, the composite beam is typically 800 mm (width)×270 mm (height)×3900 mm (length). Two beam configurations were considered: Beam-T and Beam-C (Fig. 7). In Beam-T, each web trapezoidal opening acts as a shear connector, enhancing the interaction between the RC slab and steel beam. In Beam-C, both overlapping 14 mm-diameter rebars and 10 mm-diameter shear studs were used to transfer the shear force between the RC slab and steel beam, in which the overlapping rebars work as PBL (Perfo-Bond Leisten) shear connectors. In order to investigate the effect caused by the circular holes in Beam-C, the diameter of circular holes (d1) was taken as 36 mm for Specimen 3 and 60 mm for Specimen 4. Two different load conditions were considered: sagging moment and hogging moment (Fig. 8). The strength grade is C35 (compressive strength = 35 MPa) for the concrete, Q345B (yield stress = 345 MPa) for the steel, and HRB400 (yield stress = 400 MPa) for the rebars. The specimen details are specified in Table 1 and the material properties are listed in Tables 2 and 3.

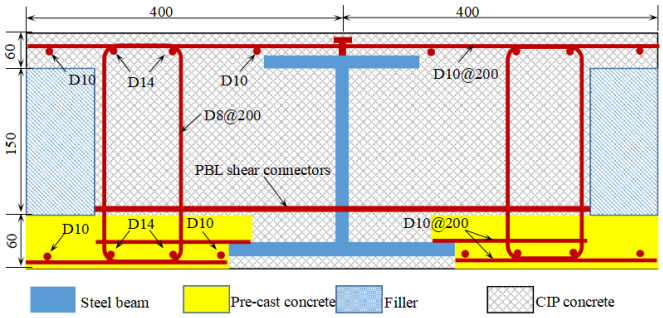

Fig. 5 Specimen cross-section and dimensions (in mm)

(Note: Dxx@yy denotes a bar with diameter xx and spacing yy, both in mm)

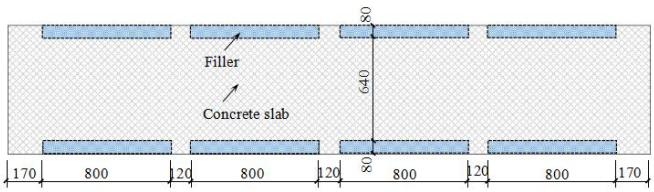

Fig. 6 Filler locations (dimensions in mm)

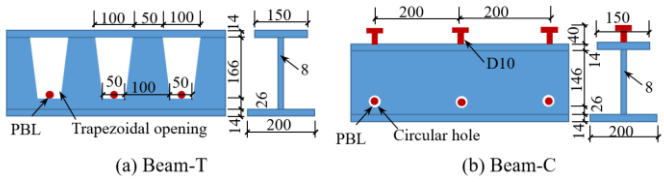

Fig. 7 Details of the asymmetric steel beam

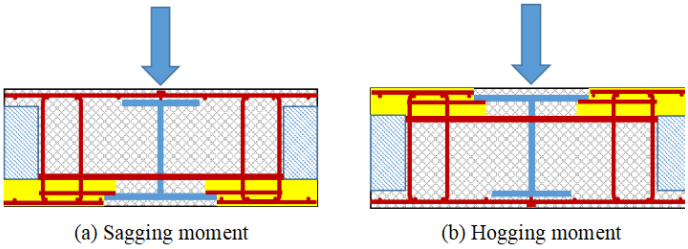

Fig. 8 Loading conditions

Table 1
Specimen details

Specimen label	Type of beam	Loading condition	Diameter of circular hole
Specimem-1	Beam-T	Sagging moment	/
Specimem-2	Beam-C	Sagging moment	d_1=36 mm
Specimem-3	Beam-C	Hogging moment	d_1=36 mm
Specimem-4	Beam-C	Hogging moment	d_1=60 mm

Table 2
The material properties of concrete

Material	$f_{cu,k}$ (N/mm^2)	f_c(N/mm^2)	E (10^3 N/mm^2)
Precast concrete	40	33	32.6
CIP concrete	28.1	24.5	29.1

Table 3
The material properties of steel and rebars

Material	Yield strength f_y (N/mm^2)	Ultimate strength f_u (N/mm^2)
T8	422	540
T14	358	510
D8	445	648
D10	483	669
D14	435	603

2.2. Test set-up

Each specimen was simply supported and equally loaded at one-third points through the use of a 1000-kN jack, as shown in Fig. 9. The distance between the two supports is 3800 mm. The specimens were set up to have a pure bending zone of 800 mm and a shear span to depth ratio of 5.6. The loading was applied using the load-controlled scheme with the loading rate of 5 kN/min for each load increment of 50 kN. Each load was retained for about 3 minutes to monitor the test data and to observe the cracks. When the load decreased to 85% of the peak load in the descending stage or when the crushing of concrete occurred, the specimen was considered a failure and the test was terminated.

The vertical load (P) was monitored by a load cell. All displacements were measured by linear variable differential transformers (LVDTs), as shown in Fig. 9. The deformations during the loading process were measured by LVDTs 1-3 and the support settlements were recorded by LVDTs 5-6 in order to determine the net deformation at mid-span (U_{mid}). The slippage between the RC slab and steel beam was monitored by LVDT 4. The strain gauges were arranged on the steel beam, rebars, and concrete surface at the mid-span section (Section A-A, Fig. 9(a)), as shown in Fig. 10.

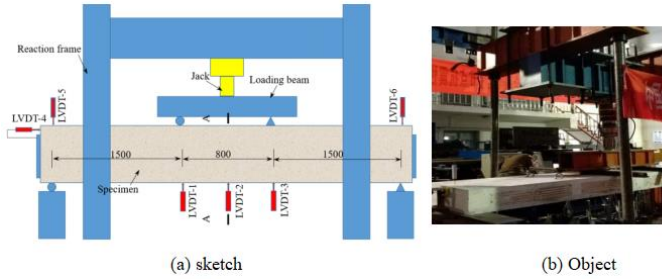

Fig. 9 Test set-up

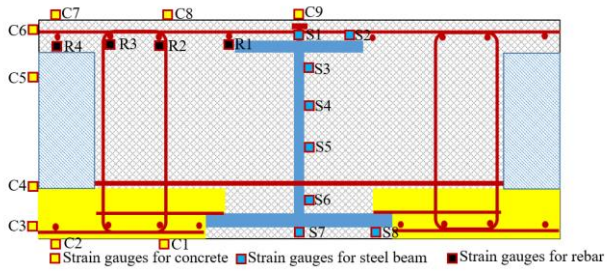

Fig. 10 Layout of the strain gauges at Section A-A (Fig. 9)

3. Test results

3.1. Failure progression

All four specimens displayed a flexural failure mode. Specimen 1 is chosen for detailed discussion hereafter. The initial crack on the bottom surface occurred at 30 kN. As the loading progressed, more cracks gradually developed. When P arrived at 165 kN, cracks spread to the filler with a slight sound heard. When P reached to 429 kN, the specimen yielded and a rapid growth of U_{mid} occurred. The crushing of concrete in the compressive zone was observed when U_{mid} was 88 mm. In all tested specimens, the slippage between the RC slab and steel beam was observed to be relatively small and no damage of PBL was observed after removing its surrounding concrete, which demonstrates the effectiveness of the shear connectors adopted in this study. Additionally, there was no crack or separation between the precast concrete and CIP concrete throughout the experiment. Typical failure modes are shown in Fig. 11.

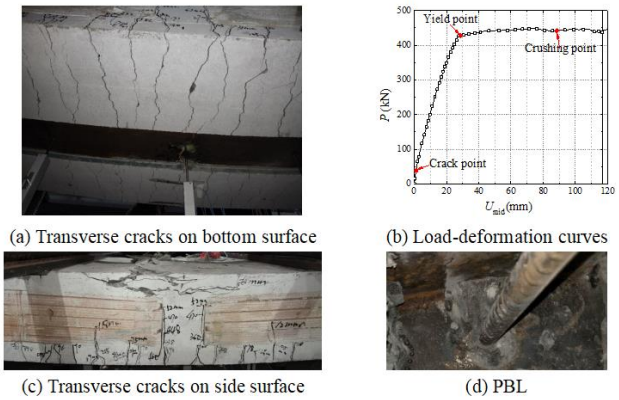

Fig. 11 Typical failure progression

3.2. Load-deformation curve

Fig. 12(a) shows the effect of shear connectors on the flexural behavior of the composite beam, indicating that the web openings can be an effective alternative to the shear studs. The effect of circular holes in Beam-C on the *P*-U_{mid} curves is shown in Fig. 12(b). The load versus deformation curves show little difference between Specimen 3 and Specimen 4, suggesting that the diameter of circular holes has little influence on the flexural behavior of the composite beam. Fig. 12(c) shows the effect of loading conditions on the *P*-U_{mid} curves, revealing that the composite beam under the sagging moment has a higher bending capacity and larger stiffness. This is mainly caused by the asymmetric steel beam.

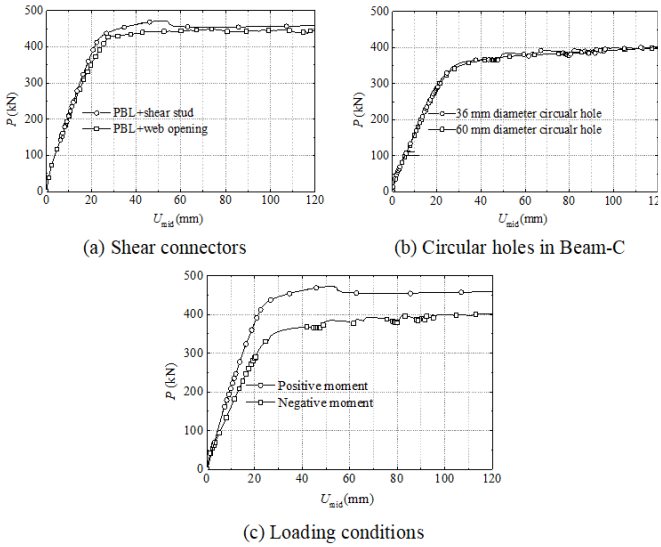

Fig. 12 Effects of experimental parameters on *P*-U_{mid} curves

3.3. Strain distributions

The load versus strain of steel beam is illustrated in Fig. 13. As shown, the yield load of specimen (P_y) was attained when the strain at bottom beam flange (S7 and S8) reached the yield strain. With an increase in load, the strain in the beam web (S3, S4, S5, and S6) entered into the yield condition. The peak load (Pu) was finally attained when the strain at top beam flange (S1 and S2) reached the yield strain. It can be stated that the plastic neutral axis of composite slim beam was near the top flange of steel beam. The strains along the beam height are approximately linearly distributed (Fig. 14), implying that Bernoulli's assumption of plane-remain-plane can be preserved. The load versus strain of rebars is shown in Fig. 15. The rebars at the top of beam (R1, R2, R3 and R4) consistently remained elastic before Pu was attained. The strains of rebars corresponding to 0.25P_y, 0.50P_y, and P_y are shown in Fig. 16, which shows evenly distributed strains across the beam width for a certain section. The load versus strain of concrete is given in Fig. 17. The strains of concrete linearly

increased before P_y was attained, beyond which there was a rapid growth of strains. The distribution of concrete strains along the beam height is shown in Fig. 14. The strains of concrete in the middle region consistently remained small during the entire test, as the continuity of concrete was disrupted by the fillers.

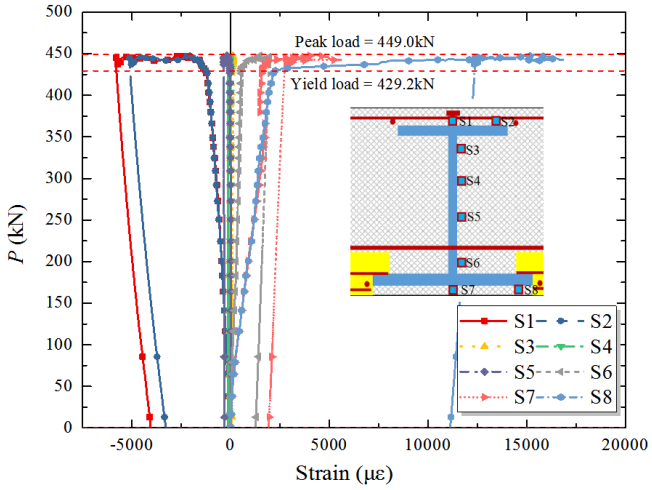

Fig. 13 Typical strains of steel beam

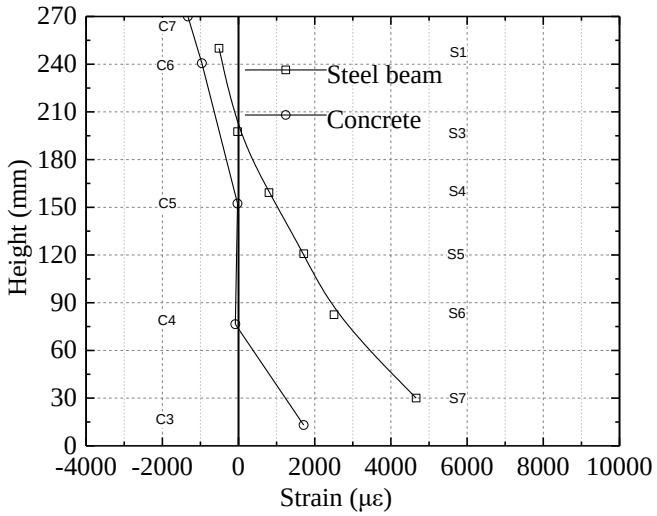

Fig. 14 Typical strain distributions along the beam height

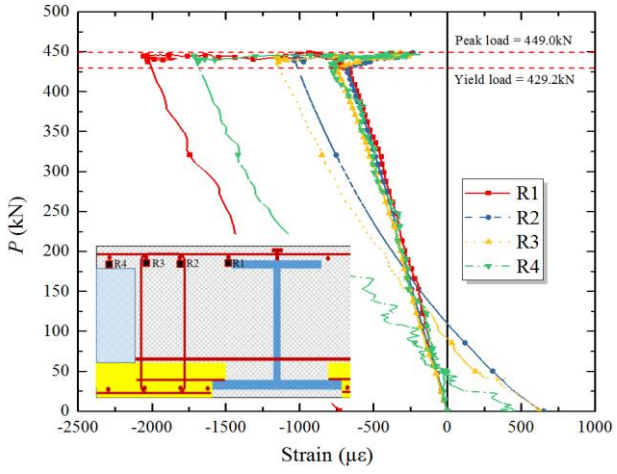

Fig. 15 Typical strains of rebars

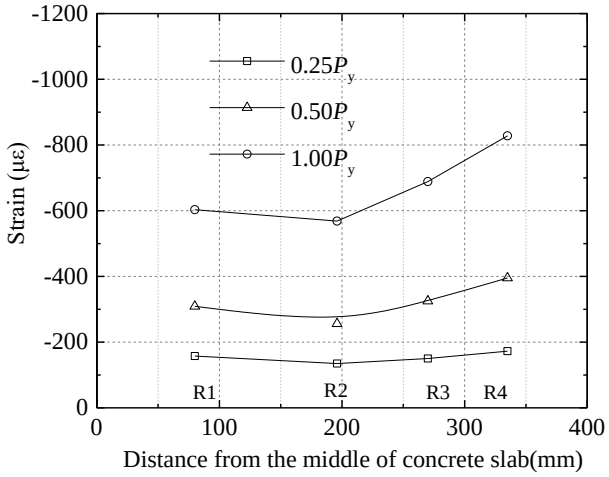

Fig. 16 Strains distributions of rebars along the beam width

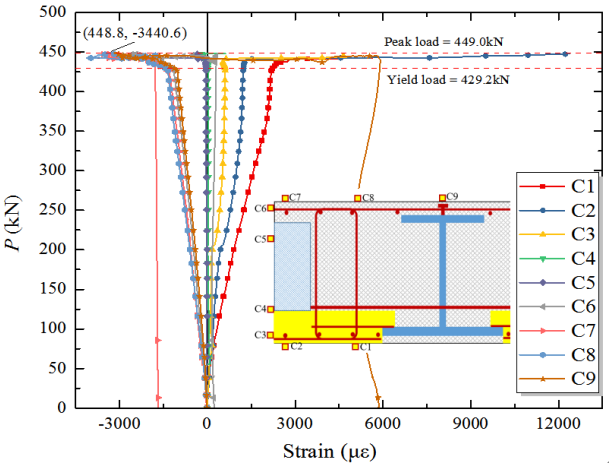

Fig. 17 Typical strains of concrete

4. Finite element analysis

A detailed finite element (FE) model was established using the FE program, ABAQUS [21], to investigate the flexural behavior of the composite beam.

4.1. Materials

4.1.1. Steel

For the steel beams and rebars, an elastic-perfectly plastic material was assumed in the FE model, in which the yield function $f(\sigma_{ij})$ of steel is expressed as

$$f(\sigma_{ij}) = \sqrt{3J_2(\sigma_{ij})} - f_s = 0 \tag{1}$$

where J_2 is the second deviatoric stress invariant, σ_{ij} is the tensor of stress, and f_s is the yield strength of steel.

4.1.2. Concrete

The concrete damaged plasticity model defined in ABAQUS was adopted for the concrete material. Considering that the plastic behavior of concrete core has little effect on the flexural behavior of the composite beam, the stress-strain relationship for concrete as specified in the GB 50010-2010 [22] was adopted. For the concrete in tension, the $\sigma(\varepsilon)$ is given as

$$\sigma(\varepsilon) = \begin{cases} \dfrac{n(\varepsilon/\varepsilon_{co})f_{co}}{n-1+(\varepsilon/\varepsilon_{co})^n} & (\varepsilon/\varepsilon_{co} \le 1) \\ \dfrac{(\varepsilon/\varepsilon_{co})f_{co}}{a_c(\varepsilon/\varepsilon_{co}-1)^2+\varepsilon/\varepsilon_{co}} & (\varepsilon/\varepsilon_{co} > 1) \end{cases} \tag{2}$$

where ε_{co} is the strain corresponding to the axial compressive strength of

concrete (f_{co}) and n and α_c are the corrective coefficients for different concrete grades. For the concrete in tension, the $\sigma(\varepsilon)$ is described by

$$\sigma(\varepsilon)=\begin{cases} E_c\varepsilon & \varepsilon\le\varepsilon_{ct} \\ f_{ct}-E_{ts}(\varepsilon-\varepsilon_{ct}) & \varepsilon_{ct}<\varepsilon \end{cases} \tag{3}$$

where $f_{ct}=0.1f_{co}$ and $\varepsilon_{ct}=f_{ct}/E_c$ with E_c being the elastic modulus of concrete. The softening modulus E_{ts} being dependent of the mesh size was used to handle the concrete localization issue, which is given as

$$E_{ts}=f_{ct}^2 l_c/(2G_f) \tag{4}$$

where l_c is the mesh size and G_f is the fracture energy calculated according to CEB-FIP MC90 [23]. The $\sigma(\varepsilon)$ for concrete in both compression and tension is shown in Fig. 18.

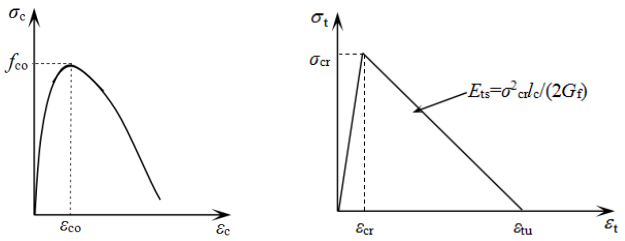

Fig. 18 Stress-strain curves of concrete

A detailed finite element (FE) model was established using ABAQUS [16] to investigate the flexural behavior of the composite beam. Typically, 4-noded shell elements with reduced integration (i.e., S4R elements) were used to represent the steel beam; 8-noded solid elements with reduced integration (i.e., C3D8R elements) were employed to simulate the concrete; and 2-noded truss elements (i.e., T3D2 elements) were used to represent the rebars. Both the steel beam and the rebars are assumed to be the elastic perfectly-plastic material in the FE model. Considering that the plastic behavior of concrete core has little effect on the flexural behavior of the composite beam, the stress-strain relationship for core concrete specified in the GB 50010-2010 [17] was adopted. The boundary conditions of FE model are depicted in Fig. 14. The rollers were simulated by the rigid body constraints tied to the surface of concrete slab.

4.2. Element types, interface, mesh, and boundary conditions

Solid elements were used to simulate the concrete. Shell elements and truss elements were employed to represent the steel beam and the rebars, respectively. The rebars were embedded in the concrete. Two extreme connection cases between the RC slab and steel beam were considered: fully-separated model (Model 1) and the complete-glued model (Model 2). In Model 1, the RC slab and steel beam were simulated separately, where the P-U_{mid} curves of RC slab and steel beam separately predicted by the FE model were simply added up. In Model 2, the steel beam was embedded in the concrete. A sensitivity study on the mesh size was performed, concluding the element mesh size of 60 mm which yields the predicted results with a relative error of 1% only. The boundary conditions of the FE model are depicted in Fig. 19, where the rollers were simulated using the rigid body constraints that are tied to the surface of concrete slab.

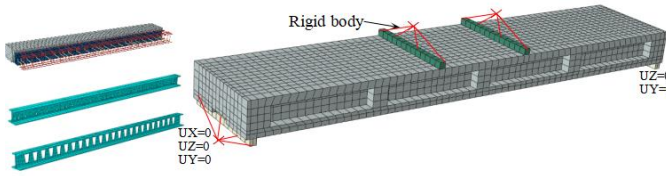

Fig. 19 Details for the FE model

4.3. FE analysis

Two extreme connection cases between the RC slab and steel beam were considered: fully-separated model (Model 1) and complete-glued model (Model 2). The P-U_{mid} curves predicted by the FE model are compared with the experimental ones, as shown in Fig. 20. As seen, the experimental results are generally in good agreement with the results predicted by Model 2, suggesting that the RC slab works well with the steel beam. Therefore, the full interaction between the RC slab and steel beam can be considered.

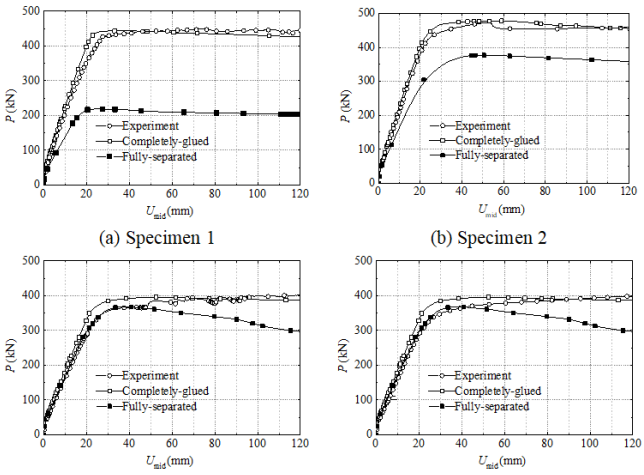

Fig. 20 Comparisons of P-U_{mid} curves

As a representative case, Specimen 1 is selected for further discussion. The failure modes of Specimen 1 predicted by the FE model are shown in Fig. 21. As seen, severe damage prevails in the pure bending zone, which is consistent with the experimental observation. The steel beam and rebars yield at the end of the test, indicating an adequately reinforced composite beam. All the PBL is consistently elastic, demonstrating a full interaction between the RC slab and steel beam.

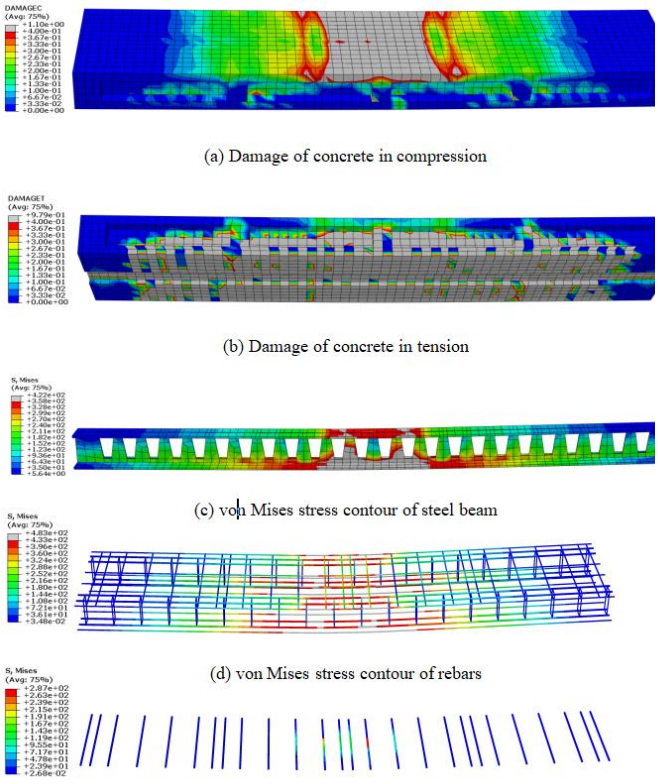

Fig. 21 Results predicted by the FE model

5. Proposed design method

The bending capacity of each specimen was determined according to the American Institute of Steel Construction Specification [2], which assumes that: (a) The distribution of strains along the section complies with the assumption of

plane-remain-plane and the compression strains are uniformly distributed across the cross-section at a specific level; (b) The stress of concrete in the tensile region is negligible; and (c) The concrete works well with the steel beam and longitudinal rebars. Note that these assumptions have been validated by tests. The strain and stress distributions under the full interaction condition are shown in Fig. 22. The plastic neutral axis (PNA) is likely to be located at one of the following positions: in the filler (PNA-1); between the filler and top steel beam flange (PNA-2); and in the top steel beam flange (PNA-3). As an example, PNA-2 is determined by

$$C_1 + T_2 + T_4 = T_1 + T_3 + T_5 \tag{5}$$

where C_1 is the compressive force in the concrete, T_1 is the tensile force in the steel beam flange, T_2 is the compressive force in the steel beam flange, T_3 is the tensile force of the longitudinal rebars, T_4 is the compressive force in the longitudinal rebars, and T_5 is the tensile force of the steel beam web. The notation in Fig. 22 is as follows: f_c is the axial compressive strength of concrete; f_s is the yield strength of steel beam; f_b is the yield strength of longitudinal rebars; A_{fb} is the cross-sectional area of the steel beam flange in tension; A_{sb} is the cross-sectional area of the longitudinal rebars in tension; A_{ft} is the cross-sectional area of the steel beam flange in compression; A_{st} is the cross-sectional area of the longitudinal rebars in compression; A_w is the cross-sectional area of the steel beam web in tension; b_c is the width of composite beam; h_1 is the distance between the extreme compression fiber and the centerline of top beam flange; and x is the distance between the extreme compression fiber and PNA. Due to the sectional properties of the composite beam, the PNA is generally near the top flange of steel beam. Since the thickness of beam flange is quite small, the PNA may be considered at the centerline of top beam flange for simplification (i.e., $x = h_1$). As such, the bending capacity M_{cal} can be calculated by

$$M_{cal} = T_1 \times y_1 + T_3 \times y_3 + T_5 \times y_5 + T_4 \times y_4 + 0.85 f_c b_c h_1 (h_1 - 0.85 h_1 / 2) \tag{6}$$

where y is the distance between the PNA and the centroid of the resultant force. The comparison between the calculated and measured bending capacities (M_{cal} and M_u) is given in Table. 4. As indicated, the proposed design method is acceptable.

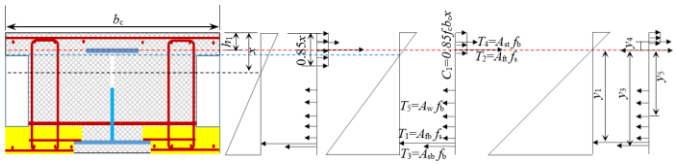

(a) PNA-1 (b) PNA-2 (c) PNA-3

Fig. 22 Strain and stress distributions under the full interaction condition

Table 4
Comparison between the calculated and measured bending capacities

Specimen label	M_{cal}(kN • m)	M_u(kN • m)	M_{cal}/M_u(kN • m)
Specimem-1	332	337	0.99
Specimem-2	360	354	1.02
Specimem-3	285	299	0.95
Specimem-4	283	295	0.96

6. Conclusions

This paper describes and discusses the bending behavior of a new composite slim floor system, based on an experimental study on four specimens. The following major findings are offered based on the results from this pilot study:

(1) The full interaction between the RC slab and steel beam can be achieved by the beam web openings as they act as effective shear connectors.

(2) The diameter of circular holes drilled on steel beam web has little influence on the flexural behavior of composite slim beam within the range of parameters considered in this study.

(3) Bernoulli's assumption of plane-remain-plane is maintained for the proposed composite slim beam. Due to the sectional properties of proposed composite slim beam, the plastic neutral axis is generally near the top flange of steel beam.

(4) The proposed design method for estimating the bending capacity of proposed composite slim beam is convenient and acceptable. Further studies on bending capacity and shear capacity are suggested for improving the design method, however.

Nomenclature

A_{fb}	cross-sectional area of the steel beam flange in tension
A_{ft}	cross-sectional area of the steel beam flange in compression
A_{sb}	cross-sectional area of the longitudinal rebars in tension
A_{st}	cross-sectional area of the longitudinal rebars in compression
A_w	cross-sectional area of the steel beam web in tension
b_c	width of composite beam
C_1	compressive force in the concrete
E_c	elastic modulus of concrete
E_{ts}	softening modulus
f_b	yield strength of longitudinal rebars
f_c	axial compressive strength of concrete
f_{co}	axial compressive strength of concrete
f_s	yield strength of steel beam
f_{ct}	tensile strength of concrete
G_f	fracture energy
h_1	distance between extreme compression fiber and centerline of top beam flange
J_2	second deviatoric stress invariant
l_c	mesh size
n	first corrective coefficient for different concrete grades
M_{cal}	calculated bending capacity
M_u	measured bending capacity
P	load applied on the loading beam
P_y	yield load applied on the loading beam
P_u	peak load applied on the loading beam
T_1	tensile force in the steel beam flange
T_2	compressive force in the steel beam flange
T_3	tensile force of the longitudinal rebars
T_4	compressive force in the longitudinal rebars
T_5	tensile force of the steel beam web
U_{mid}	displacement of the composite beam at mid-span
x	distance between the extreme compression fiber and the plastic neutral axis
y	distance between the plastic neutral axis and the centroid of resultant force
α_c	second corrective coefficient for different concrete grades
ε_{ct}	strain corresponding to the tensile strength of concrete
ε_{co}	strain corresponding to the axial compressive strength of concrete
$\sigma(\varepsilon)$	equivalent stress-strain relationship of concrete
σ_{ij}	tensor of stress

Acknowledgments

The authors greatly appreciate the financial support provided by the National Key R&D Program of China (No. 2016YFC0701201) and the National Natural Science Foundation of China (No. 51408620).

References

[1] An Q, Ren Q, Liu H, Yan XY, Chen ZH. Dynamic performance characteristics of an innovative cable supported beam structure–concrete slab composite floor system under human-induced loads[J]. Engineering Structures, 2016, 117: 40-57.
[2] Tian L M, Kou Y F, Hao J P, Zhao L W. Flexural performance of a lightweight composite floor comprising cold-formed steel trusses and a composite mortar slab[J]. Thin-Walled Structures, 2019, 144: 106361.
[3] de Seixas Leal L A A, de Miranda Batista E. Experimental investigation of composite floor system with thin-walled steel trussed beams and partially prefabricated concrete slab[J]. Journal of Constructional Steel Research, 2020, 172: 106172.
[4] Pang R, Zhang Y B, Dang L J, Liang S T. Experimental and numerical investigation on the vertical bearing behavior of discrete connected new-type precast reinforced concrete floor system[J]. Advances in Structural Engineering, 2020: 1369433220911141.
[5] Eurocode 4: Design of composite steel and concrete structures, Part 1.1, general rules and rules for Building. London: British Standards Institution; 2004 (BS EN 1994-1-1: 2004).
[6] ANSI/AISC 341-10. Seismic provisions for structural steel buildings. Chicago, Illinois, USA: American Institute of Steel Construction; 2010.
[7] Mullett D L. Slim floor design and construction[M]. UK: Steel Construction Institute, 1992.
[8] Lawson R M, Mullett D L, Rackham J W. Design of asymmetric slimflor beams using deep composite decking[M]. Berkshire: Steel Construction Institute, 1997.
[9] Bailey C G. The behaviour of asymmetric slim floor steel beams in fire[J]. Journal of Constructional Steel Research, 1999, 50(3): 235-257
[10] Ma Z, Mäkeläinen P. Behavior of composite slim floor structures in fire[J]. Journal of Structural Engineering, 2000, 126(7): 830-837.
[11] Lu X H, Makelainen P. Strength and stiffness of composite slim floor beams[C]. Proceedings of the 4st Pacific structural steel conference, 1995
[12] Malaska M. Behaviour of a semi-continuous beam-column connection for composite slim floors[M]. Helsinki University of Technology, 2000.
[13] Bernuzzi C, Gadotti F, Zandonini R. Semi-continuity in slim floor steel-concrete composite systems[C]//1st European Conference on Steel Structures, Athens, Greece. 1995.
[14] De Nardin S, El Debs A L H C. Study of partially encased composite beams with innovative

position of stud bolts[J]. Journal of Constructional Steel Research, 2009, 65(2): 342-350.
[15] Hosseinpour E, Baharom S, Badaruzzaman W H W, Al Zand A W. Push-out test on the web opening shear connector for a slim-floor steel beam: Experimental and analytical study[J]. Engineering Structures, 2018, 163: 137-152
[16] Maraveas C, Swailes T, Wang Y. A detailed methodology for the finite element analysis of asymmetric slim floor beams in fire[J]. Steel Construction, 2012, 5(3): 191-198.
[17]Ahn J K, Lee C H. Fire behavior and resistance of partially encased and slim-floor composite beams[J]. Journal of Constructional Steel Research, 2017, 129: 276-285.
[18] Ryu J, Ju Y K, Yoon S W, et al. Bending capacities of glass fibre reinforced plastic composite slab[J]. Materials Research Innovations, 2013, 17(sup2): s12-s18.
[19] Ryu J, Lee C H, Oh J, et al. Shear resistance of a biaxial hollow composite floor system with GFRP plates[J]. Journal of Structural Engineering, 2016, 143(2): 04016180.
[20] Ryu J, Lee C H, Oh J, Yoon S W, Ju Y K. Shear resistance of a biaxial hollow composite floor system with GFRP plates[J]. Journal of Structural Engineering, 2017, 143(2): 04016180.
[21] Hibbitt, Karlsson, Sorensen. ABAQUS/Standard User's Manual. Version 6.7.1, Hibbitt, Karlsson & Sorensen, Inc., 2007.
[22] GB 500010-2010. Code for design of concrete structures; 2010 [in Chinese].
[23] Design of concrete structures. CEB-FIP-Model-Code 1990. British Standard Institution, London, 1993.

Advanced Steel Construction – Vol. 16 No. 4 (2020) 328–336
DOI:10.18057/IJASC.2020.16.4.5

EXPERIMENTAL INVESTIGATION ON TEMPERATURE EVOLUTION OF STEEL BEAMS IN NATURAL FIRES

Er-Feng Du [1], Gan-Ping Shu [1, *], Yi-Qun Tang [1], Ying Qin [1], Xiao Lyu [2] and Zhong Zhou [1]

[1] *Key Laboratory of Concrete and Prestressed Concrete Structures of Ministry of Education, School of Civil Engineering, Southeast University, Nanjing, China*

[2] *School of Civil Engineering, Shandong Jianzhu University, Ji'nan, China*

** (Corresponding author: E-mail: shuganping@seu.edu.cn)*

ABSTRACT

This paper presents an experimental project of a 3D steel portal frame subjected to a natural fire to investigate the evolution of temperatures of the hot gas layer and the steel beams. Temperature evolution of the steel beams during the test was recorded and compared with those calculated by current design codes, i.e. Eurocode EN 1993-1-2 and Chinese Code CECS200. The experimental results revealed that the temperature of the hot gas gradually decreased with the distance from the fire source, and the temperature variations in the steel beams had obvious hysteresis compared to those of the hot gas. The results calculated according to the equations specified by EN 1993-1-2 and CECS200 were very similar. However, there were noticeable differences between the calculated data and the experimental results after the temperature of the steel beam was higher than 600°C. The calculation for the temperature of steel beams in the hot gas layer does not need additional consideration of the thermal radiation from the flame. Based on the experimental results, this paper improves the equations specified in EN 1993-1-2, using correction coefficients of convection and radiation. It is found that the modified method obtains calculation results in satisfactory agreement with the experimental results, thereby providing a reference for predicting the temperature of steel beams in natural fires.

ARTICLE HISTORY

Received: 3 June 2020
Revised: 5 September 2020
Accepted: 6 September 2020

KEYWORDS

Experimental study;
Steel beam;
Hot gas;
Temperature;
Natural fire

1. Introduction

Large-space steel structures are extensively utilized in public buildings, such as stadiums, airports, industrial plants, et al. Abundance research has been conducted on the structural performance and construction methods of these structures at ambient temperature [1-4]. In recent years, the fire resistance and the design method of large-space steel structures have become crucial issues concerned by researchers and engineers. Lu et al. [5] analysed the fire performance of a large exhibition centre in different fire scenarios and proposed recommendations on the fire-resistance design of large-space steel truss structures. Du et al. [6] proposed an analytical method to capture the transient tension force in a pre-tensioned steel cable subjected to localized fires. Woźniczka [7] investigated the effects of different factors on the fire resistance of long-span truss girders during the fire growth and decay phases, and the results showed that the fireproof insulation of the structure can be reduced. Liu et al. [8] explored the mechanical response of welded hollow spherical joints at elevated temperatures through experimental and numerical studies, and provided a simplified calculation formula to predict the bearing capacity of the joints at high temperatures. Jiang et al. [9] conducted fire tests on a full-scale roof structure having six main steel trusses in non-destructive and destructive manners, and obtained the failure modes and deformation curves in natural fires of the structure. Some scholars performed experimental studies and finite element analyses on the mechanical behaviours of different forms of steel portal frame structures under natural fires [10-14].

In general, fires occurring in large-space steel structures will localize rather than flashover. The temperature field of the whole building is not uniform, which is quite different from compartment fires. Thus, the traditional fire-resistance design method under standard fire conditions is unsuitable for large-space steel structures, and investigations on the performance-based design method should be conducted. The performance-based fire-resistance design method involves the consideration of a natural fire model based on the fire load, the geometrical size of the building, mechanic properties of steel at elevated temperatures, the temperature distribution in structural members and the response of the entire structural system under fires [15, 16].

To implement the performance-based fire-resistance design, a rational calculation method for the temperature evolution of structural members under natural fires is crucial. For large-space structures under natural fires, the space inside the building can be divided into three regions, including the flame region, the region of the hot gas layer, and the region under the hot gas layer. The heat-transfer mechanisms are different in these three regions, and thus the temperature development laws for structural members in these three regions are also different. According to the Chinese code CECS200 [17], the specified equation for the temperature rise of structural members is based on the standard fires. In terms of the European codes including EN 1991-1-2 [18] and EN 1993-1-2 [19], localized fire is specified, but its calculation method is inconvenient to use in practice since the temperature of the fire plume varies in the vertical direction.

Regarding the calculation methods for the temperature of structural members under natural fires, Latham et al. [20] experimentally investigated the temperature of steel members exposed to natural fires in a compartment. The test data were then used for estimating the structural response, by the equivalent time of fire exposure. Wong et al. [21] and Ghojel [22] studied the factors that may affect the temperature evolution of steel members under compartment fires, and proposed calculation models for the temperature rise of members, which took into account the absorption of flame radiation by the heat-transfer medium. Then the calculation models were experimentally verified. Wald et al. [23, 24] conducted compartment fire tests on buildings with full-scale steel frames. The temperature of the steel member was measured and compared with the results predicted by the calculation methods given in Eurocodes.

Based on the lumped differential formulation, Du and Li [25] presented a calculation method for the temperature rise of steel members under large-space fires, with consideration of the effect of flame radiation. They also proposed a limit value for the radiation shape factor based on the parametric analysis. By using the heat balance equation, Huang et al. [26] proposed a simplified calculation method for the temperature development of steel members in large-space fires. The influence of flame radiation was considered based on the parametric analysis. Meanwhile, a critical value of the building height was also suggested for the cases where the flame radiation effect was neglected. Zhang et al. [27] used the adiabatic surface temperature method to establish a simple heat transfer model of steel members under localized fires, and the results of the proposed model were close to those from the FDS (Fire Dynamics Simulator) simulation. Based on a point-source model, Zhang et al. [28] established a modified method for predicting the temperature rise of steel members, with consideration of the effect of flame radiation. An experimental study was performed on the temperature elevating process of a steel beam under a localized fire in a large space. The calculation results were found, by comparison, to be in satisfactory agreement with the experimental data.

In summary, the studies on the calculation methods for temperature evolution of steel members under natural fires are limited. Moreover, in the experiment conducted by Zhang et al. [28], the power of the fire source was small and the resulting temperatures of steel members were low. Additionally, the cooling period was not considered in the calculation methods proposed by the previous researches. Thus, it is necessary to perform more typical experiments in this research field.

To solve the aforementioned problems, a model of a portal frame building was designed and constructed in this study. A fire test was performed on the model to investigate the development of the natural fire, and the temperature distribution of the hot gas layer and the steel beams under the fire. Results obtained by the equations for the temperature evolution of steel beams specified by CECS200 and EN 1993-1-2 were compared to the experimental results, to validate the applicability of the equations under natural fires.

2. Experimental program

2.1. Introduction of the test model

The test model was a single compartment which covered an area of 6 by 12.5m as shown in Figs. 1 and 2. The columns were 2.25m high and the roof was inclined at 1/10. A total of six portal frames were spaced apart at an interval of 2.5m and the configuration of a representative frame is indicated in Fig. 3. The section of the beams and columns was H80×50×4.5×6.5mm. Roof purlins and wall purlins were bent from the galvanized steel sheet to form a section of C60×38×12×1.6mm. To ensure the safety of the beam-column connections before member failures, fully-welded connections at the beam ends were adopted and end-plate connections for the beam splices were applied at a distance of 0.8m from the column flange, as shown in Fig. 4.

Fig. 1 Steel portal frame building for the fire test

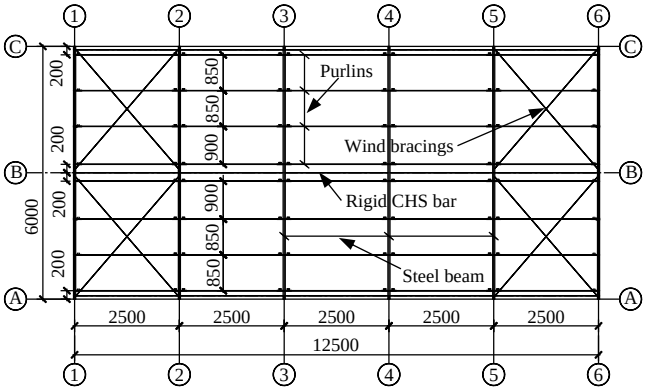

Fig. 2 Plan view of the roof structure (mm)

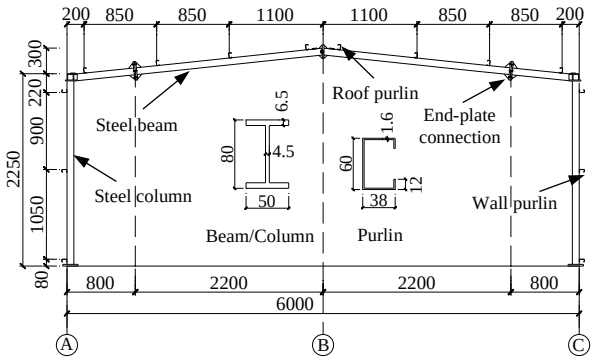

Fig. 3 Elevation view of the portal frame (mm)

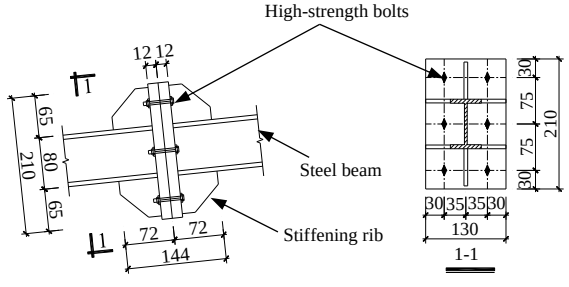

Fig. 4 End-plate connection for beam-to-beam joint (mm)

The purlins were connected to the beams and columns with M10 bolts, and knee braces of the roof purlins were used to prevent the out-of-plane buckling. Rigid bars (CHS42×3) were arranged between the ridges and the beam-column connections. Steel bars (Φ10) were employed as wind bracings in the outer spans. The roof cladding was made of 75mm thick composite panels with rock wool insulation, while the wall cladding was made of 0.5mm thick single-layered profiled steel sheets. The steel grade was Q235.

Each gable wall contained a 2.03m high and 1.2m wide door opening. Along Axis A, three window openings with a height of 0.9m were designed in the facade wall as plotted in Fig. 5. Cesium-potassium monolithic flameproof glass was installed in the middle window, while common glass was installed in the other two windows labelled with a, b. The flameproof glass was arranged for the convenience of observation during the test. Along Axis C, there were only two windows labelled with c and d in the wall, with common glass installed.

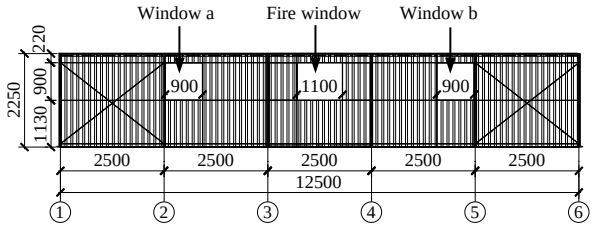

Fig. 5 Elevation view along Axis A (mm)

The concrete bases with a length of 0.7m, a width of 0.7m and a height of 0.6m supported the columns. The concrete grade was C25 and the columns of the main frames were designed to be pinned at the base with two anchor bolts (M20).

2.2. Fire source

A natural fire source was set up below the steel beam along Axis 3 as indicated in Fig. 6. The fire source consisted of six 0.7×0.7m oil pans each containing 11kg diesel. The amount of the fuel was designed to achieve a representative fire in an industrial building, based on the data from fire tests recorded in the literatures and simulation results from the software FDS [29]. To concentrate the heat on the rafters, the oil pans were raised to a height of 1.15m above the ground level by a supporting platform.

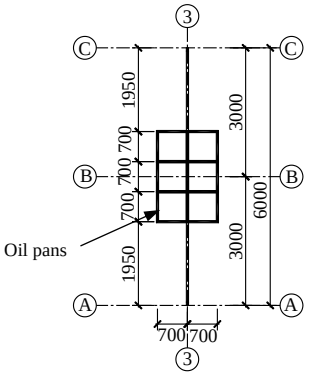

Fig. 6 Arrangement of the fire source (mm)

2.3. Setup of temperature measurement

Type-K thermocouples were adopted for measuring the temperatures of hot gas and steel members. The temperature data were collected by the data acquisition instrument TDS303. Fig. 7 shows positions of the thermocouples in the frame along Axis 3. The name of the thermocouple contains 3 parts, including “S” or “G”, the number of the axis and the number of the thermocouple, in which S and G represent the steel member and the hot gas, respectively. The thermocouples measuring the hot gas were arranged at a distance of 50mm from the member surface. To obtain the temperature distribution in the particular sections of the eaves and the ridge, the thermocouples were located at the top, mid-web and bottom flanges, as plotted in sections a and b.

For the other sections, each has only one thermocouple located at the mid-web.

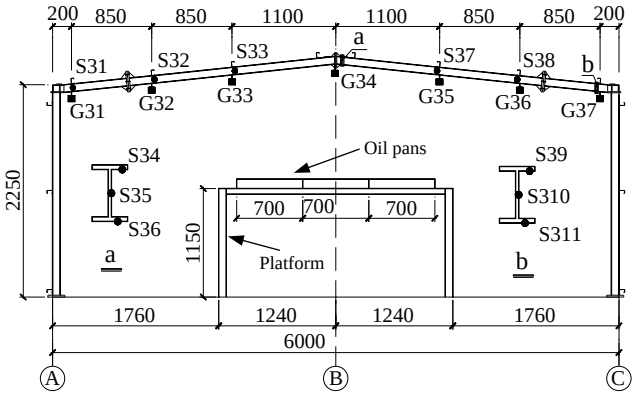

Fig. 7 Positions of thermocouples along Axis 3 (mm)

In terms of the other portal frames, the number of thermocouples was less than that along Axis 3. The setup of thermocouples at the eaves and the ridge was similar to Axis 3 except that only one thermocouple was located at the mid-web of the steel beam in the other portal frames, as plotted in Fig. 8. The number "0" in the plot means that no steel thermocouple was arranged for eaves along Axes 1 and 6.

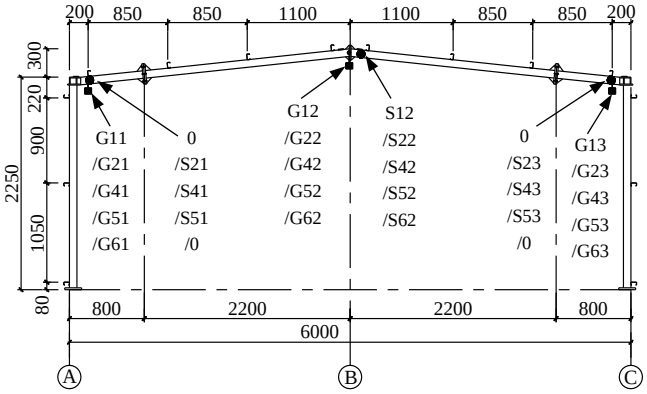

Fig. 8 Positions of thermocouples along Axes 1/2/4/5/6 (mm)

3. Experimental results

3.1. Visual observation and discussion

The middle two oil pans burned first following the ignition at the beginning of the test, and the other oil pans burned at 1min 25s after the ignition. A thick layer of smoke formed beneath the roof, with a large amount of smoke

Fig. 9 Test building in the fire (1min 25s)

Fig. 10 Test building in the fire (5min 56s)

Fig. 11 Test building in the fire (10min 19s)

Fig. 12 Test building in the fire (13min 20s)

emitting from the door openings, as shown in Fig. 9. Dark smoke spread out of the building at 2min 50s. At 5min 56s, the oil source blazed fiercely and the flame spread around the edge of oil pans, as plotted in Fig. 10. As shown in Fig. 11, the fire began to abate without flame spilling at 10min 19s. At 11min 20s, the smoke above the roof decreased greatly. At 13min 20s, fire in the middle oil pans almost extinguished, as plotted in Fig. 12. Then, the flame extinguished at 16min 58s. Moreover, at the initial stage of the test, a noise of "bang, bang" was heard sometimes. During the intermediate stage of the test, some flames emitted out of the roof through the sheet joints above the fire source.

(a) Window a

(b) Window b

(c) Window c

(d) Window d

Fig. 13 Windows with common glass after the fire test

Along Axis A, the corners of windows a and b cracked at 3min 16s and 3min 53s respectively after the ignition. At 4min 53s, the cracks in the corners of window a further expanded and some glass debris fell. A large crack occurred in window b and some glass debris fell at 5min 21s. At 6min 28s, most of the glass in window a dropped down and a sizable flame run out. The cracks in the corners of window c expanded seriously at 7min 50s. A great part of the glass in window b broke at 8min 55s. During the entire test, only tiny cracks appeared in window d. The windows with common glass after the test are shown in Fig. 13, while the fire-resistant glass was kept intact during the whole process of the fire test.

3.2. Temperature evolution and analysis

The temperature-time relationship of the hot gas below the steel beam along Axis 3 is plotted in Fig. 14. It can be seen that the temperature of the hot gas (G32-G36) above the fire source generally experienced three periods: a growth period, a fully developed period, and a decay period. The temperature rose fast during the first period, and then kept nearly constant or grew slowly in the second period. At the beginning of the third period, the temperature decreased rapidly. When the temperature dropped to 300ºC, it began to decline slowly. The highest gas temperature was found by the thermocouple G34 around the roof ridge right above the fire source, and its peak value was 1182.7ºC. The graph also indicates that the temperature of hot gas decreased from the roof ridge to the eaves. In general, the temperature distributed symmetrically on both sides of the roof ridge.

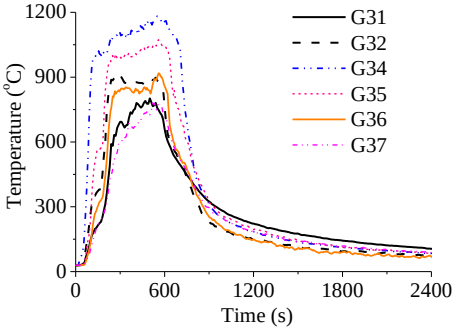

Fig. 14 Temperature of the gas near the beam along Axis 3

Figs. 15-17 show the temperature distribution of the hot gas near the ridge and the eaves along Axes A and C, respectively. It can be seen that the peak temperature declined from the span of Axis 3 to the other spans on both sides.

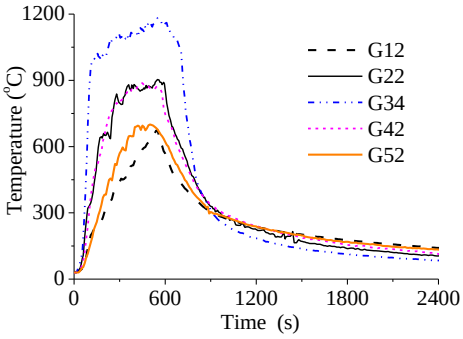

Fig. 15 Temperature of the gas near the ridge

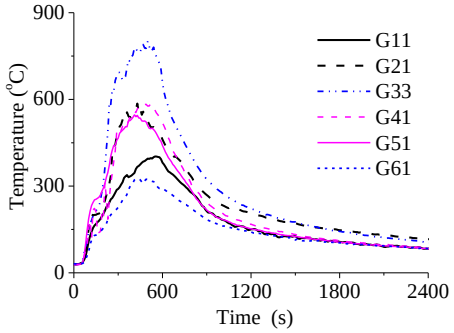

Fig. 16 Temperature of the gas near the eave along Axis A

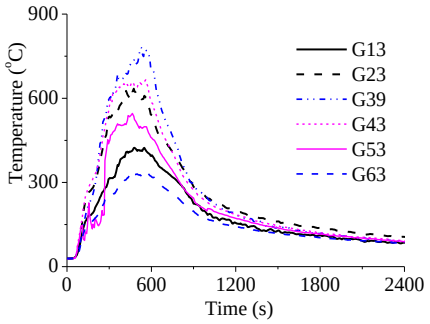

Fig. 17 Temperature of the gas near the eave along Axis C

The temperature-time curves for the top, mid-web and bottom flanges of the steel beam at the roof ridge (section a) along Axis 3 are shown in Fig. 18. It can be seen that the temperature distribution in the beam section was normally uniform, because the steel had sound conductivity and the beam section was entirely surrounded by the flame. During the heating period, the temperature of the beam was lower than that of the hot gas. The peak temperature of the steel beam reached 941ºC. During the cooling period, in turn, the temperature of the beam was much higher than that of the gas. Fig. 19 illustrates the temperature against time for the steel beams at the eave (section b) along Axis 3. The peak temperature reached about 600ºC and the temperature evolution law was similar to that in section a.

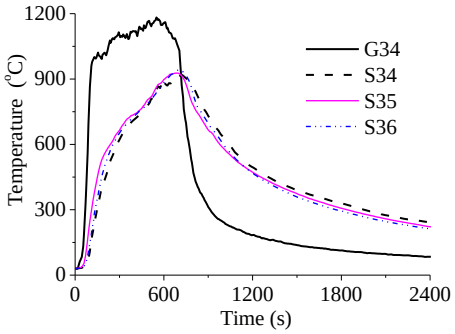

Fig. 18 Temperature histories for the ridge along Axis 3

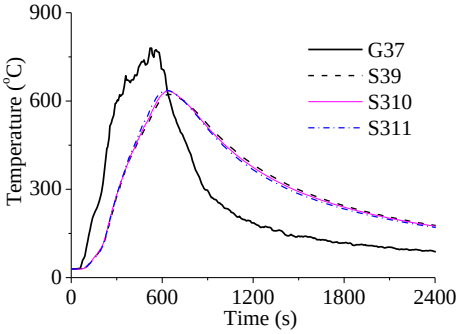

Fig. 19 Temperature histories for eaves along Axis 3

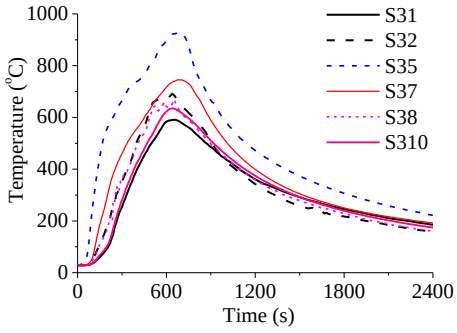

Fig. 20 Temperature of the beam along Axis 3

The temperature-time curves for the web of the steel beam along Axis 3 are plotted in Fig. 20. According to the measurement, the roof ridge had the highest temperature, and the temperature decreased gradually towards the two eaves.

Figs. 21-23 illustrate temperature-time curves for the webs of the beams at the roof ridge and the eaves along Axes A and C. As shown in Fig. 21, the peak temperature decreased from the span of Axis 3 to the other spans. Figs. 22-23 show that the peak temperature of the steel beam at the eave of Axis 4 was higher than that of Axis 2 since the position of Axis 4 was farther from the door opening than Axis 2. The peak temperature of the steel beam at the eave of Axis C was higher than that of Axis A because the window near Axis A was damaged greatly, leading to a great loss of heat. Due to the failure of thermocouples for measuring points G33, G62, S22 and S33, the corresponding temperature curves are not given here.

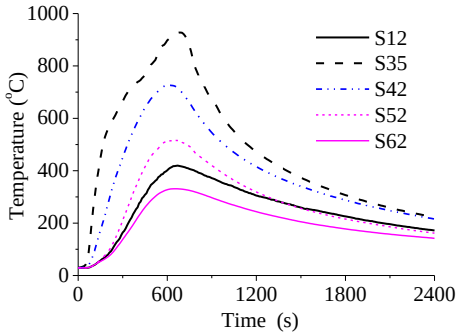

Fig. 21 Temperature of the beam at the ridge

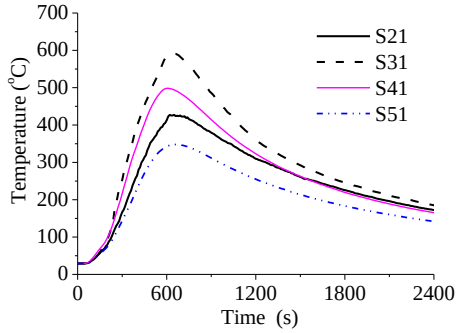

Fig. 22 Temperature of the beam at the eave along Axis A

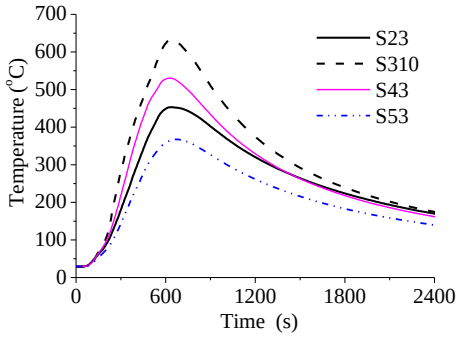

Fig. 23 Temperature of the beam at the eave along Axis C

4. Temperature calculation of steel beams

In this section, the equations for temperature variations of steel members under standard fires, specified by EN 1993-1-2 and CECS200, are assessed for the applicability in natural fires.

4.1. Calculation Method

4.1.1. EN 1993-1-2 Equation

The following equation for calculating the temperature of unprotected steel members under fires is provided by EN 1993-1-2:

$$\Delta T_a = k_{sh} \frac{A_m / V}{c_a \rho_a} h_{net} \Delta t \tag{1}$$

where ΔT_a is the temperature increment of a steel member [°C]; k_{sh} is the correction factor for the shadow effect; A_m/V is the section factor for the unprotected steel member [1/m], in which A_m is the surface area of the member per unit length [m^2/m] and V is the volume of the member per unit length [m^3/m]; ρ_a and c_a are the density and specific heat of steel, respectively, in which ρ_a=7850 kg/ m^3, and c_a=600 J/(kg·°C); h_{net} is the design value of net heat flux per unit area [W/m^2]; and Δt is the time interval and should not be more than 5 seconds.

h_{net} is determined by

$$h_{net} = h_{net,c} + h_{net,r} \tag{2}$$

where $h_{net,c}$, and $h_{net,r}$ are the net convective heat flux (W/m^2) and the net radiative heat flux (W/m^2) , respectively.

Moreover, $h_{net,c}$ is determined by

$$h_{net,c} = \alpha_c \left(T_g - T_a \right) \tag{3}$$

where α_c is the coefficient of convective heat transfer, which is taken as 25W/(m^2°C) here for the standard temperature-time curve; T_g is the gas temperature (°C); and T_a is the surface temperature of the steel member (°C).

Meanwhile, $h_{net,r}$ is given by

$$h_{net,r} = \Phi \varepsilon_m \varepsilon_f \sigma \left[\left(T_r + 273 \right)^4 - \left(T_a + 273 \right)^4 \right] \tag{4}$$

where, Φ is the configuration factor, which is usually 1.0; ε_m is the surface emissivity of the member, which is 0.7 for carbon steel; ε_f is the emissivity of gas, which is 1; σ is the Stefan-Boltzmann constant, which is 5.67×10^{-8} W/(m^2·°C); and T_r is the environment temperature, which is T_g in the case of fully surrounded members.

4.1.2. CECS200 Equation

The equation suggested by CECS200 is:

$$T_a \left(t + \Delta t \right) = \frac{B}{c_a \rho_a} \left[T_g \left(t \right) - T_a \left(t \right) \right] \Delta t + T_a \left(t \right) \tag{5}$$

where B is the comprehensive heat transfer coefficient [W/(m^3·°C)], given by

$$B = \left(\alpha_c + \alpha_r \right) \frac{A_m}{V} \tag{6}$$

where α_r is the radiation heat transfer coefficient [W/(m^2·°C)], given by

$$\alpha_r = \frac{2.041}{T_g - T_a} \left[\left(\frac{T_g + 273}{100} \right)^4 - \left(\frac{T_a + 273}{100} \right)^4 \right] \tag{7}$$

4.2. Temperature Calculation and Comparison

The temperature-time curves for steel beams obtained by Eqs. (1) and (5) are compared with the experimental curves. The parameters used in the equations adopt the values suitable for standard fires. For simplicity, this manuscript only provides temperature-time curves of some representative measuring points, as shown in Fig. 24. The letters “C” and “E” mean that the corresponding temperature-time curves of steel members are obtained by the equations in CECS200 and EN 1993-1-2, respectively. As mentioned in Section 2, “S” and “G” mean that the curves are derived from steel members and hot gas respectively in the fire test.

It can be seen from Fig. 24 that the curves given by the equations of the two codes are very close to each other. The curves plotted in Figs. 24(a)-(d)

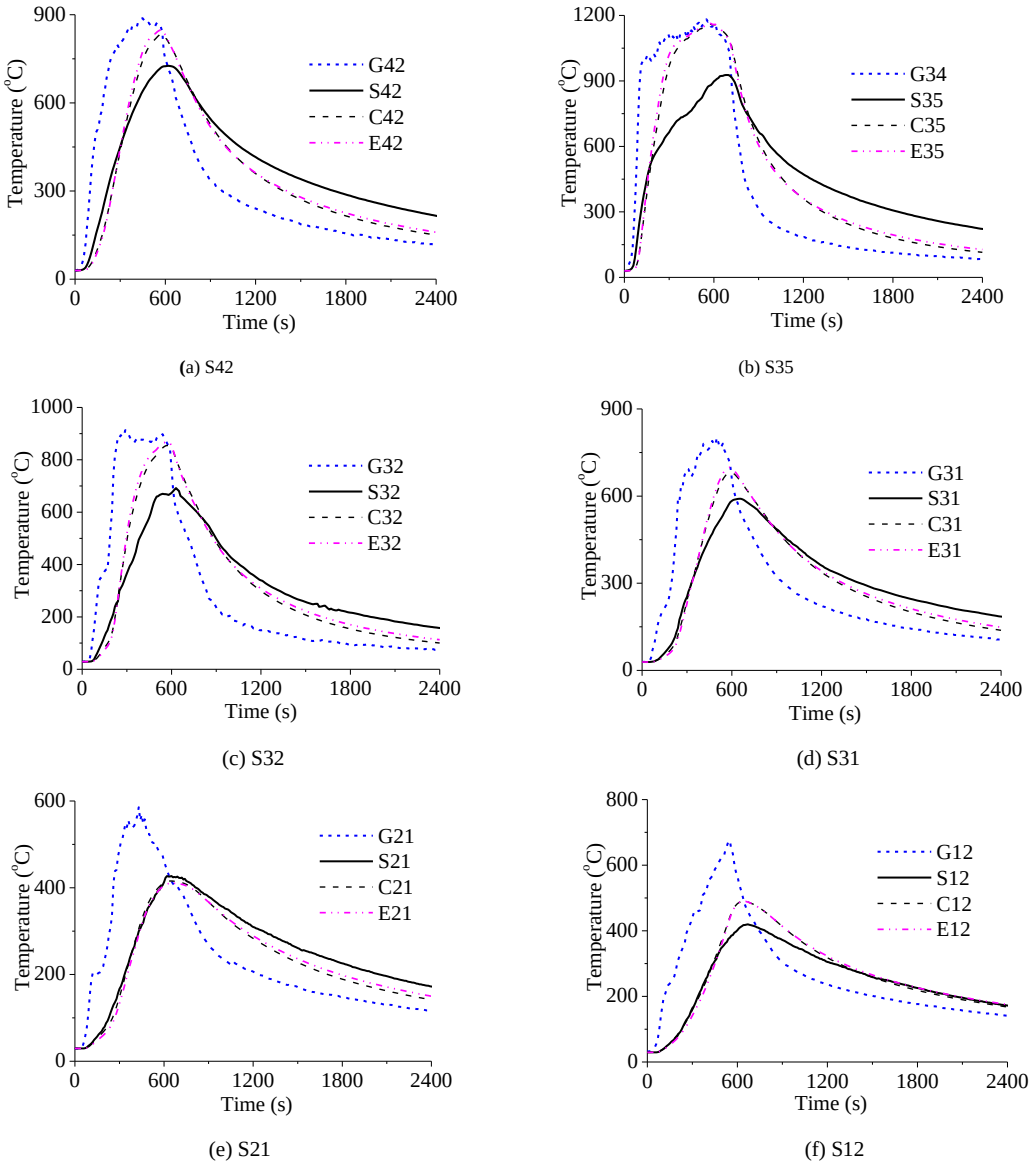

(a) S42 (b) S35

(c) S32 (d) S31

(e) S21 (f) S12

Fig. 24 Comparison of experimental and calculation curves

are obtained from measuring points in the flame or the high-temperature zone of the hot gas layer. The calculation results are in satisfactory agreement with the experimental results during the heating period. However, after the temperature is higher than 600ºC, the calculation results are higher than the experimental results, while the calculation results decrease faster than the experimental results during the cooling period.

Figs. 24(e)-(f) show results from measuring points in the slightly lower-temperature zone of the hot gas layer. The calculation and experimental curves of the measuring point S21 are very close to each other in the heating period, whereas the calculation curves have steeper downward slopes than the experimental curves during the cooling period. For the measuring point S12, the calculation results agree well with the experimental results during the heating period and the cooling period, but the calculation results are higher than the experimental results near the peak temperature.

Due to the fact that the calculation results from these representative measuring points are close to or higher than the experimental results during the heating period, the additional thermal radiation effect of the flame can be omitted in the calculation of the temperature of the steel beam within the hot gas layer. It also means that the thermal radiation heat from the flame is completely absorbed by the upper hot gas layer.

4.3. Modified Model and Calculation Comparison

To solve the problem of the difference between the calculation results from the equations and the experimental results, this manuscript proposes a modified equation based on the one specified by EN 1993-1-2. The coefficients of convection and radiation are modified through the regression analysis of the experimental data. The new form of the calculation equation for natural fires is described below:

$$T_a = k_{sh}\frac{A_m/V}{c_a\rho_a}\left\{\alpha_c\left(T_g - T_a\right) + \varepsilon_{mg}\sigma\left[\left(T_g+273\right)^4 - \left(T_a+273\right)^4\right]\right\}\Delta t \quad (8)$$

where ε_{mg} is the comprehensive radiation coefficient. During the heating period, α_c is 25W/(m²·ºC); ε_{mg} is 0.7 when $T_a \leq 600$ºC and 0.07 when $T_a > 600$ºC; and during the cooling period, α_c is 12.5W/(m²ºC) and ε_{mg} is 0.49.

The new results calculated by Eq. (8) are compared to those by the original equation specified by EN 1993-1-2 and to the experimental data, as plotted in Fig. 25. In these figures, the curves from the new equation with correction parameters are represented by the letter “N”. It can be seen from Figs. 25(a)-(e) that the new calculation results are very close to the experimental results. Table 1 shows the comparison of peak temperatures between calculation and experimental results, at the measuring points S42, S35, S32 and S31. The calculation errors from EN 1993-1-2 and the revised equation were 16.9%~25.6% and -2.4%~8.5%, respectively. Therefore, the calculation accuracy is evidently improved due to the correction parameters. In terms of the measuring point S12, as shown in Fig. 25(f), the calculation results from the proposed equation are slightly higher than the experimental results during the cooling period. The reason is that the calculation results have been higher than the experimental results before the beginning of temperature decline. However, they have the similar decline rates. On the whole, the proposed equation with the correction parameters can accurately predict the temperature variations of steel beams during the whole process of natural fires. Note that there is more work to be done to give equations that can be applied universally.

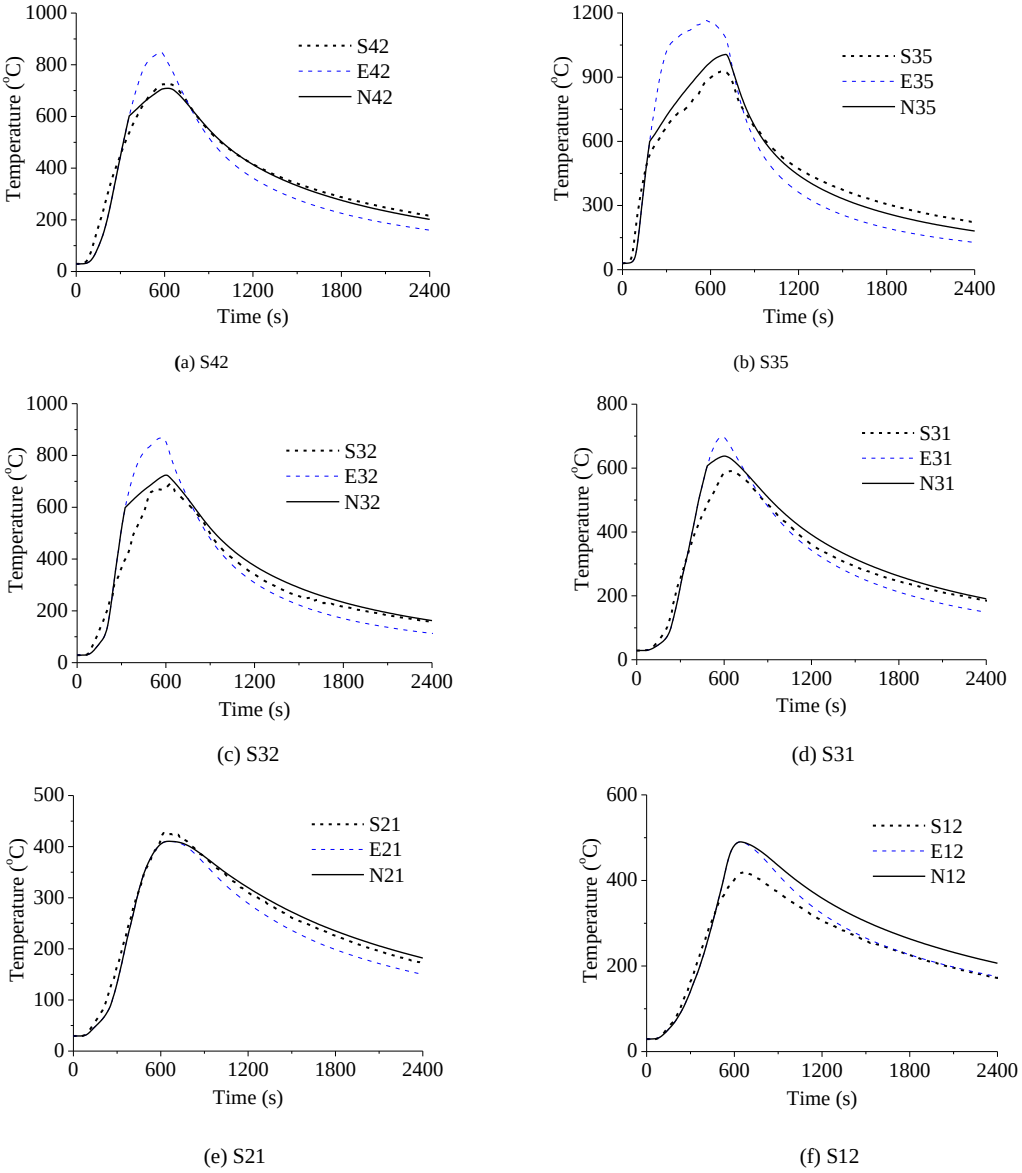

Fig. 25 New comparison of experimental and calculation curves

Table 1
Comparison of peak temperatures between calculation and experimental results

Measuring point	S/°C	E/°C	Error(E)	N/°C	Error(N)
S42	725.9	848.5	16.9%	708.8	-2.4%
S35	927.3	1164.5	25.6%	1006.4	8.5%
S32	692.1	867.3	25.3%	724	4.6%
S31	590.7	699	18.3%	637.4	7.9%

Notes: S is the experimental result of the peak temperature of the steel member; E and N are the calculation results of the peak temperature obtained by Eq. (1) and Eq. (8), respectively.

5. Conclusions

In this study, a model of a portal frame building was designed and constructed to perform a natural fire test. The temperature development of the hot gas layer and the steel beams inside the model was investigated. The equations specified by EN 1993-1-2 and CECS200 were adopted to calculate the temperature of the steel members. The calculation results were then compared to the experimental results. Meanwhile, some related parameters were modified to obtain more accurate calculation results based on the equation specified by EN 1993-1-2. The following conclusions can be drawn:

a) The temperature-time history of the hot gas above the fire source had three periods, including a growth period, a fully developed period, and a decay period. The peak temperature of the hot gas gradually decreased from the region directly above the fire source to the neighbouring regions. On the whole, the temperature symmetrically distributed along both sides of the roof ridge.

b) The entire temperature-time history of the steel beam showed apparent thermal hysteresis compared to that of the hot gas. Moreover, the temperature distribution of steel members was roughly uniform over the cross-section while non-uniform along the length direction. The experiment showed that the peak temperatures of the hot gas and steel beams were 1182.7°C and 941°C, respectively.

c) The calculation results for the temperature of steel beams given by the equations in EN 1993-1-2 and CECS200 were very similar. However, during the heating period, these calculation results were much higher than the experimental results after the temperature of the steel beam reached 600°C. Meanwhile, the predicted results had a higher decline rate than the experi-

mental results during the cooling period. Thus, the effect of thermal radiation from the flame can be ignored in the calculation of the temperature of the steel beam within the hot gas layer.

d) To accurately acquire the temperature-time curves of steel beams subjected to natural fires, the present study proposes a modified method based on EN 1993-1-2, through modifications to the coefficients of convection and radiation. It can be found that the proposed method leads to more accurate results than those obtained by EN 1993-1-2.

References

[1] Luo B., Sun Y., Guo Z.X. and Pan H.T., "Multiple random-error effect analysis of cable length and tension of cable-strut tensile structure", Advances in Structural Engineering, 19(8), 1289-1301, 2016.

[2] Tong G.S., Pi Y.L. and Gao W., "In-plane nonlinear analysis and buckling of shear-deformable circular arches", Advanced Steel Construction, 16(1), 55-64, 2020.

[3] Xue S.D., Lu J., Li X.Y. and Liu R.J., "Improved force iteration method based on rational shape design solving self-stress modes of cable-truss tensile structure", Advanced Steel Construction, 16(2), 170-180, 2020.

[4] Yan X.Y., Hu H., Chen Z.H. and Yang Y., "An improved mathematical calculation method for beam string structure based on static equilibrium principle", International Journal of Steel Structures, 20(4), 1241-1255, 2020.

[5] Lu L.M., Yuan G.L., Huang Z.H., Shu Q.J. and Li Q., "Performance-based analysis of large steel truss roof structure in fire", Fire Safety Journal, 93, 21-38, 2017.

[6] Du Y., Liew J.Y.R., Zhang H. and Li G.Q., "Pre-tensioned steel cables exposed to localised fires", Advanced Steel Construction, 14(2), 206-226, 2018.

[7] Woźniczka P., "Fire resistance assessment of the long-span steel truss girder", Archives of Civil Engineering, LXVI(2), 63-75, 2020.

[8] Liu H.B., Zhang Y.J., Wan L. and Chen Z.H., "Mechanical performance of welded hollow spherical joints at elevated temperatures", Advanced Steel Construction, 16(1), 1-12, 2020.

[9] Jiang S.C., Zhu S.J., Guo X.N. and Li Z.Y., "Full-scale fire tests on steel roof truss structures", Journal of Constructional Steel Research, 169, 1-13, 2020.

[10] Pyl L., Schueremans L., Dierckx W., and Georgieva I., "Fire safety analysis of a 3D frame structure based on a full-scale fire test", Thin-Walled Structures, 6, 204-212, 2012.

[11] Johnston R.P.D., Lim J.B.P., Lau H.H., Xu Y.X., Sonebi M., Armstrong C.G. and Mei C.C., "Finite-element investigation of cold-formed steel portal frames in fire", Structures and Buildings, 169(SB1), 3-9, 2015.

[12] Lou G.B., Wang C.H., Jiang J., Jiang Y.Q., Wang L.W. and Li G.Q., "Experimental and numerical study on thermal-structural behavior of steel portal frames in real fires", Fire Safety Journal, 98, 48-62, 2018.

[13] Lou G.B., Wang C.H., Jiang J., Jiang Y.Q., Wang L.W. and Li G.Q., "Fire tests on full-scale steel portal frames against progressive collapse", Journal of Constructional Steel Research, 145, 137-152, 2018.

[14] Roy K., Lim J.B.P., Lau H.H., Yong P.M., Clifton G.C., Johnston R.P.D., Wrzesien A. and Mei C.C., "Collapse behaviour of a fire engineering designed single-storey cold-formed steel building in severe fires", Thin-Walled Structures, 142, 340-357, 2019.

[15] Milke J.A., "Performance-based analysis methods to determine the fire resistance of structural members", Proceedings of the 2001 Structures Congress and Exposition, Washington, D.C., United States , 1-11, 2001.

[16] Shi Y.J., Bai Y. and Wang Y.Q., "Study on performance-based fire-resisting design and key technologies for large spatial steel structures", Engineering Mechanics, 23(Sup. II), 85-92, 2006.

[17] CECS200, Technical code for fire safety of steel structures in buildings, China Association for Engineering Construction Standardization, Beijing, China, 2006.

[18] EN1991-1-2, Eurocode1: Actions on structure. Part 1-2: General actions-Actions on structures exposed to fire, European Committee for Standardization, Brussels, Belgium, 2002.

[19] EN1993-1-2, Eurocode 3: Design of steel structures. Part 1-2: General rules-Structural fire design, European Committee for Standardization, Brussels, Belgium, 2005.

[20] Latham D.J., Kirby B.R. and Thomson G., "The temperatures attained by unprotected steelwork in experimental natural fires", Fire Safety Journal, 12, 139-152, 1987.

[21] Wong M.B., Ghojel J.I. and Grozier D.A., "Temperature-time analysis for steel structures under fire conditions", Structural Engineering and Mechanics, 6(3), 275-289, 1998.

[22] Ghojel J.I., "A new approach to modelling heat transfer in compartment fires", Fire Safety Journal, 31, 227-237, 1998.

[23] Wald F., Chladná M., Moore D., Santiago A. and Lennon T., "Temperature distribution in a full-scale steel framed building subject to a natural fire", Steel and Composite Structure, 6 (2), 159-182, 2006.

[24] Wald F., Chlouba J., Uhlír A., Kallerová P. and Štujberová M., "Temperatures during fire tests on structure and its prediction according to Eurocodes", Fire Safety Journal, 44, 135-146, 2009.

[25] Du Y. and Li G.Q., "Fire radiation effect on steel member at elevated temperature in large space fire", Fire Safety Science, 15(4), 189-199, 2006.

[26] Huang J.Q., Li G.Q., Du Y., Bao P.Q. and Liu K., "Influence of flame radiation on temperature rising of steel members in large space fire", Journal of Natural Disasters, 17(5), 87-94, 2008.

[27] Zhang C., Li G.Q. and Wang R.L., "Using adiabatic surface temperature for thermal calculation of steel members exposed to localized fires", International Journal of Steel Structures, 13(3), 547-556, 2013.

[28] Zhang G.W., Zhu G.Q. and Huang L.L., "Temperature development in steel members exposed to localized fire in large enclosure", Safety Science, 62(3), 319-325, 2014.

[29] McGrattan K., Hostikka S., Floyd J., McDermott R. and Vanella M., Fire Dynamics Simulator User's Guide (Version 6), National Institute of Standards and Technology (NIST), Maryland, 2015.

Acknowledgments

The research work described in this paper is sponsored by the Nation Science Foundation of China (Grant No. 51808117), the Fundamental Research Funds for the Central Universities (Grant No. 2242020K40088) and the National Key Research and Development Program of China (Grant No. 2018YFC0705502-4). Their financial support is highly appreciated.

Advanced Steel Construction – Vol. 16 No. 4 (2020) 337–345
DOI: 10.18057/IJASC.2020.16.4.6

STUDY ON MOMENT-ROTATION RELATIONSHIP OF STEEL SLEEVE BEAM-COLUMN JOINT WITH INTERFERENCE FIT

Wen-Tao Qiao [1, 2, *], Ren-Jie Zhu [1], Dong Wang [3], Jian Li [1, 4] and Jia-Wei Yuan [1]

[1] *School of Civil Engineering, Shi Jiazhuang Tiedao University, Shi Jiazhuang, China*
[2] *Cooperative Innovation Center of Disaster Prevention and Mitigation for Large Infrastructure in Hebei Province (Shi Jiazhuang Tiedao University), Shi Jiazhuang, China*
[3] *TRC Companies, Baton Rouge, United States of America*
[4] *School of Civil Engineering, Southwest Jiaotong University, Chengdu, China*
(Corresponding author: E-mail: tottyer@126.com)

ABSTRACT

The steel sleeve beam-column joint with interference fit (SSBCJ-IF) is a new steel structure beam-column joint based on interference fit in mechanical engineering. The refined finite element analysis (FEA) model is proposed by comparing analysis results with those of similarity test and theoretical calculations. The refined FEA model is used to perform variable parametric analyses on the moment-rotation relationship of SSBCJ-IF, including loading, material and geometry properties. Results show that the strength of concrete has little influence on both bearing capacity and initial stiffness of the joint, the strength of steel has obvious influence on flexural capacity of the joint but does not affect initial stiffness, both magnitude of interference and ratio of beam-column stiffness have some influence on the initial stiffness, the ratio of beam-column strength has some influence on both initial stiffness and bearing capacity, both initial stiffness and bearing capacity of the joint decrease significantly when the axial compression ratio exceeds 0.7. Finally, a simplified calculation method of the moment-rotation curve is proposed, and results calculated by this simplified method are in good agreement with those from the refined FEA.

ARTICLE HISTORY

Received: 23 July 2020
Revised: 13 August 2020
Accepted: 10 September 2020

KEYWORDS

Steel sleeve beam-column joint;
Interference fit;
Finite element analysis;
Parametric analysis;
Moment-rotation curve;

1. Introduction

Concrete-filled steel tubes (CFST) have become increasingly popular in construction and infrastructure projects because of the advantages of fast erection, high ductility of steel and high compressive strength of concrete. CFST has these advantages because the steel tube provides confinement for concrete which increase concrete stiffness and strength, while local and global buckling of the steel tube are inhibited by concrete.

Over the past several decades, researchers and structural engineers have proposed a wide variety of joints, including the joint with the external/internal diaphragm[1], joint with through diaphragm[2], joint with through web/flange/beam [3-5], joint with external stiffeners [6], joint using bolted connections[7-10] and so on.

The aforementioned joints need to be welded or bolted on site, and some of them require cutting on steel column. Based on the interference fit in mechanical engineering, a new joint design is proposed in this paper, namely steel sleeve beam-column joint with interference fit (SSBCJ-IF), to reduce construction difficulties. The new joint is composed of the sleeve and the cantilever short beam as illustrated in Fig.1. During construction, a connection between beams and columns can be achieved by pressing the sleeve onto the column, thus both on-site welding and column cutting are avoided.

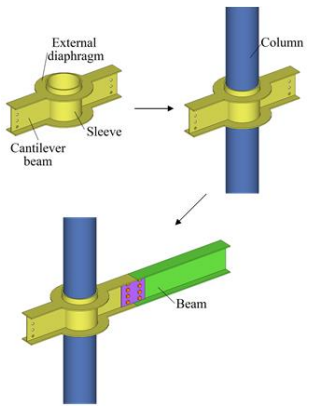

Fig. 1 Assembly process of the steel sleeve joint

In design practice, the connection between the beam and column is usually simplified as either rigid or pin connection. In reality, the ideal rigid or pin connection does not exist, and most of joints are semi-rigid connections. To clarify the influence of the beam-column angle change on the structure behavior and to represent the nonlinear behavior of the joint, the moment-rotation (M-θ) curve is usually used to describe the mechanical properties of the connection between beams and columns. Many calculation models for moment-rotation curve were proposed. Early studies use linear model to represent the connection characteristics for the whole loading process [11], but the linear model is only accurate for the elastic behavior of the connection. Frye et al. [12] proposed a polynomial model which can be easily used in structural analysis. The disadvantage of this model is that the polynomial has negative slope in some ranges which results in negative stiffness. B-spline model [13] can avoid the negative stiffness issue and give results in good agreement with those from test, however, more test data are needed to determine the B-spline model. Kishi and Chen [14] proposed a three-parameter power function model which requires much less data for function fitting than the data needed for the B-spline model. Also, the three-parameter power function model is applicable to the situation in which the bending moment-angle curve is flat at late levels of loading. Yee and Melchers [15] proposed the four-parameter exponential model. Although the moment-rotation curve given by the mathematical model is not as accurate as that obtained from experimental study or finite element analysis, the curves from the mathematical models are widely used due to the simplicity and convenience [16].

In this paper, a refined FEA model of SSBCJ-IF is established. The FEA results are compared with the results from test and theoretical calculation to verify the reliability of the FEA model. Then, variable parametric analyses are performed, with the parameters being categorized into three groups including loading, material and geometry properties. Finally, a simplified calculation method of moment-rotation relationship of SSBCJ-IF is proposed.

2. FEA modeling

As seen in Fig.2(a) is model dimension. The section size of steel column is 273 mm × 7 mm (diameter × wall thickness) filled with C40 concrete.The beam section size height, width, web thickness, flange thickness is 250 mm, 125 mm, 6 mm, 9 mm respectively. Fig.2(b) show sleeve joint details. The thickness of the diaphragm is the same as that of the beam flange. There are pinned about top and bottom of the column. The axial compressive ratio is 0.3. A pair of antisymmetric loads are applied at the beam ends.

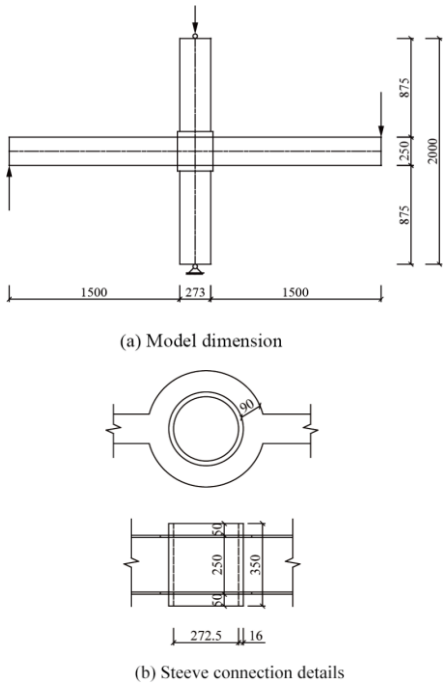

Fig. 2 Details of models (mm)

2.1. Material properties

In the model, Chinese grade Q235 was used for steel. The elastic modulus of steel *Es* is 206×10^3 N/mm^2 while Poisson ratio as 0.3 [17]. The constitutive model of steel suggested in reference [18] is adopted. The stress-strain curve is divided into four segments which are elastic segment, yield segment, strain-hardening segment and secondary yield segment. C40 concrete is used in the models. Concrete Young's modulus and Poisson ratio adopt corresponding values in [19]. The damaged plasticity of concrete (CDP) model in ABAQUS is used to simulate the mechanical properties of concrete. The stress-strain curve of concrete is calculated with the method introduced in reference [20]. The plastic-damage factor of concrete is determined with the method in reference.

2.2. Element type and meshing

The incompatible mode eight node brick element (C3D8I) is used for the steel column, concrete and steel sleeve. Four-node quadrilateral stress/displacement shell element (S4R) is used for the diaphragm and steel beams. To improve accuracy of the model, the mesh densities of the steel sleeve and steel column are unified to make the nodes at contact surface have one-to-one correspondence. Using the symmetry of the structure, a half model of the joint is created. Finer mesh is used for the core region of the joint and less fine mesh is used for other regions, so that both calculation accuracy and efficiency are considered.

2.3. Contact modeling and boundary condition

The "hard contact" is used to simulate the interference fit between the sleeve and the column [21]. The tangential direction is friction. Assume the friction conforms to the Coulomb friction criterion and the friction coefficient μ is 0.1. The "hard contact" is also used to simulate the interface between the steel tube and core concrete, while in the tangential direction the friction is considered with the Coulomb friction criterion and the friction coefficient μ is taken as 0.6 [20].

The column are pinned on top and bottom. while axial force is applied in y direction to simulate the axial pressure in the column. The forced displacement in y direction is applied to the reference points of the beam ends. The beams are laterally braced to avoid lateral instability of the beams. Since only half of the joint is created using symmetry of the structure, the symmetric boundary conditions are applied on the plane of symmetry.

The Newton-Raphson nonlinear solution method in ABAQUS/Standard is used. The automatic control for load increment in ABAQUS/Standard is selected.

3. Reliability of FEA modeling

To verify the reliability of FEA modeling of SSBCJ-IF, the following methods are used.

(1) Compared with the experimental study on similar beam-column joints to verify the simulation of contact connection between the steel sleeve and steel column.

(2) Compared with the experimental study on CFST columns to verify the simulation of contact connection between the steel column and concrete core.

(3) For interference fit, if the steel sleeve and steel column are in the elastic range, the connection structure behavior can be solved as an elastic plane-strain problem. The results from this solution are used to verify the assumption of nonlinear contact between steel sleeve and steel column in FEA model.

3.1. Beam-column joint

The separated sleeve joint proposed in reference [22] is similar to SSBCJ-IF. For both types of joints, the sleeve connectes the steel column and the steel beam. But the connection mechanisms of these two joints are different. For separated sleeve joint, the steel beam flange is welded to the sleeve and the beam web is welded directly to the steel column. In this paper, the specimen WTJ-2 from reference [22] is selected to verify the FEA modeling. The steel column section diameter, wall thickness is 219 mm, 10 mm respectively. The beam section width, web thickness and flange thickness is 200 mm, 100 mm, 5.5 mm and 8 mm respectively. The joint size is as shown in Fig.3.

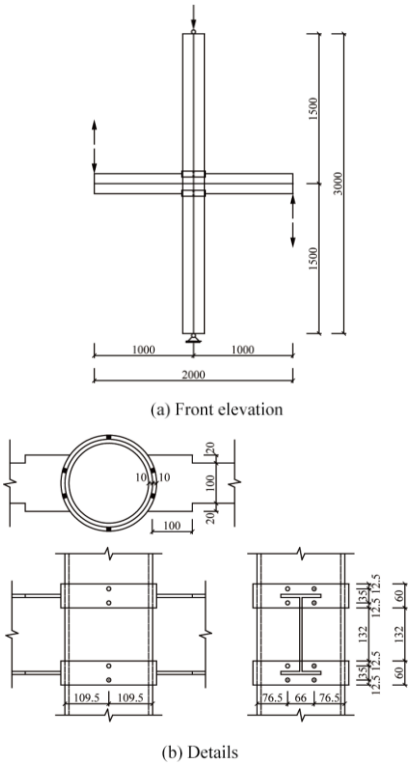

Fig. 3 Dimension of the specimen WTJ-2 (mm)

The FEA model is established in ABAQUS according to the settings described in Section 2. The boundary conditions are the same as those in experiments. The loading process in experiment is also simulated in FEA model. The Mises stress contour of the joint at the ultimate load state is shown in Fig.4. It is seen that the results from test and the finite element mode in Fig.5 are in good agreement,it shows that indicating that the finite element model established by the above method is reliable.

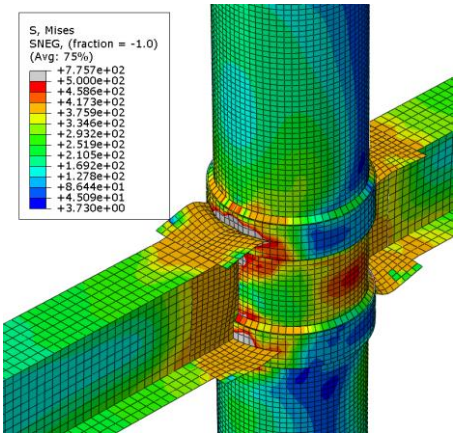

Fig. 4 WTJ-2 Mises stress contour

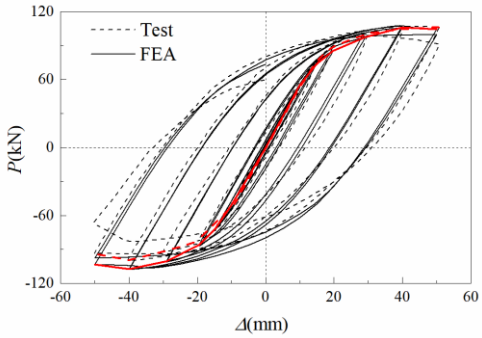

Fig. 5 Comparison of hysteresis curves between FEA calculation and test results for specimen WTJ-2

3.2. CFST Column

A series of experimental studies on CFST column under reversed load were performed in reference [22]. The specimen SC2-3 from reference [23] is selected in this paper to validate the FEA model. The column section is 114 mm × 3 mm and the column length is 1500 mm. The steel tube is filled with concrete. Both ends of the CFST column are pinned. At the end of the column, the axial force is applied. The reversed load is applied in the direction perpendicular to the column at midspan.

The FEA model is established in ABAQUS according to the settings in Section 2. The boundary conditions are the same as those in experiments. Fig.6 shows the failure model. The comparison of results from FEA and experiment study is shown in Fig.7, which for hysteresis curves the stiffness from FEA at late stage of unloading and reverse loading stage are slightly greater than those from test. The skeleton curves from FEA and test match well at loading stage. The skeleton curve from FEA at reverse loading stage is slightly smaller than that from test. In general, the results of FEA and experiment are in fairly good agreement.

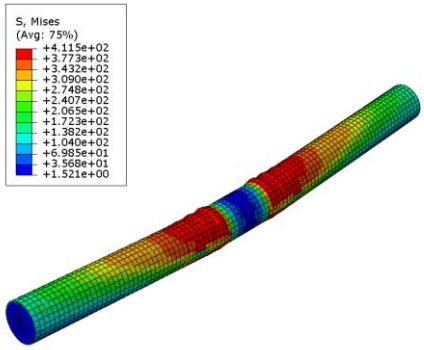

Fig.6. SC2-3 Mises stress contour plot.

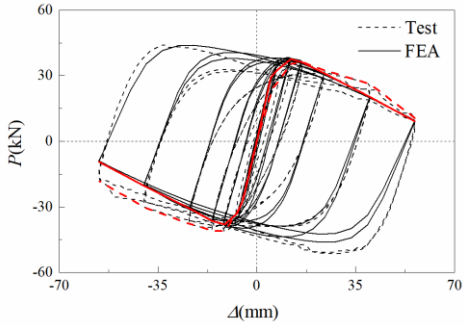

Fig. 7 Comparison of hysteresis curves from FEA and test for specimen SC2-3

3.3. Interference Fit

The magnitude of interference is the difference between the outer diameter of the steel column and the inner diameter of the sleeve. The mechanism of the interference fit is that each part is deformed to satisfy the compatibility of deformation. Thus, the contact pressure is generated. The steel sleeve and column can be analyzed as hollow thick-walled cylinders. If the interference fit is made before the concrete pouring and the sleeve and column do not reach plasticity stage during the interference fit, the interference fit connection structural behavior can be approximately simplified to axisymmetric plane-strain problem in elastic range.

The model described in Section 2 is selected for interference fit FEA simulation verification. The interference is 0.5 mm.

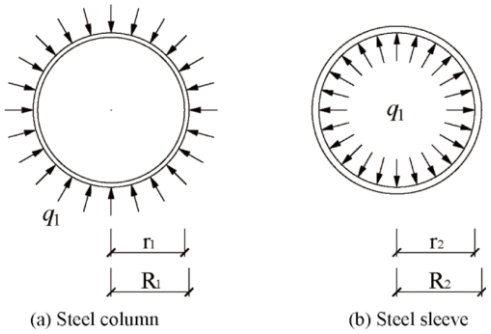

Fig. 8 Stress of each part after interference fit

As shown in Fig.8, assume that the pressure between steel column and sleeve is q_1.

For steel column, the stress field is:

$$\sigma_\rho = -\frac{1-\frac{r_1^2}{\rho^2}}{1-\frac{r_1^2}{R_1^2}}q_1 \qquad \sigma_\varphi = -\frac{1+\frac{r_1^2}{\rho^2}}{1-\frac{r_1^2}{R_1^2}}q_1 \tag{1}$$

Radial displacement is:

$$u_\rho = \frac{1+\mu}{E}\left[-\frac{r_1^2 R_1^2 q_1}{R_1^2 - r_1^2}\frac{1}{\rho} - (1-2\mu)\frac{R_1^2 q_1}{R_1^2 - r_1^2}\rho\right] \tag{2}$$

The radial stress is obtained as 13.89MPa, and the hoop stress is 264.16MPa.

For steel sleeve, the stress field is:

$$\sigma_\rho = -\frac{\frac{R_2^2}{\rho^2}-1}{\frac{R_2^2}{r_2^2}-1}q_1 \qquad \sigma_\varphi = \frac{\frac{R_2^2}{\rho^2}+1}{\frac{R_2^2}{r_2^2}-1}q_1 \tag{3}$$

Radial displacement is:

$$u_\rho = \frac{1+\mu}{E}\left[\frac{r_2^2 R_2^2 q_1}{R_2^2 - r_2^2}\frac{1}{\rho} + (1-2\mu)\frac{r_2^2 q_1}{R_2^2 - r_2^2}\rho\right] \quad (4)$$

The radial stress is obtained as 13.89MPa, and the hoop stress is -125.64MPa.

According to the settings in Section 2, a FEA model of steel sleeve joint is created in ABAQUS to simulate the interference fit assembly process specified in this section. The Mises stress contour of joint after interference fit is shown in Fig.9. Most regions of the components are in elastic stage. Fig.10, 11 show the comparison of both radial and hoop stresses from FEA model and theoretical analysis along the height of the column.

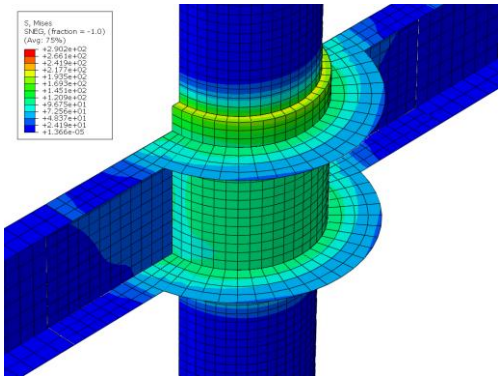

Fig. 3 Mises stress contour of joint after interference fit

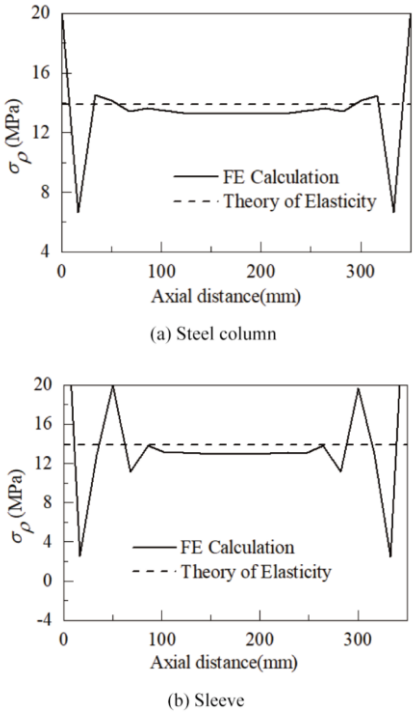

Fig. 4 Comparison of σ_ρ between elastic analysis and FE calculation

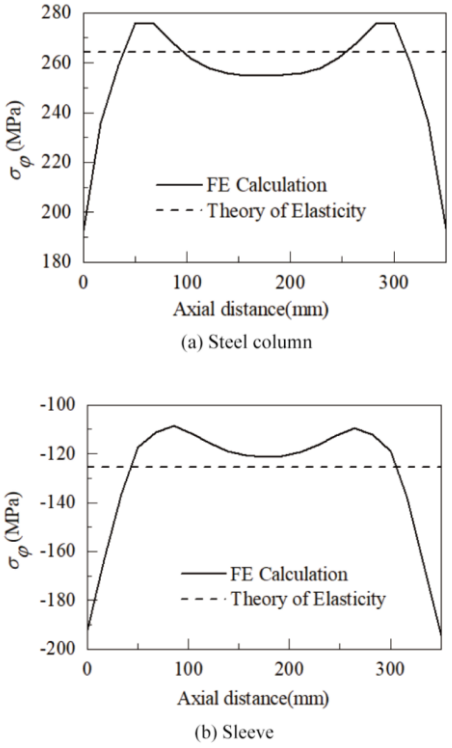

Fig. 5 Comparison of σ_φ between elastic analysis and FE calculation

It is seen from Fig.10 and 11 that the FEA results at both ends are different from the theoretical results due to the stress concentration. The stresses at height 50 mm and 300 mm are also different from the theoretical results due to the diaphragms. For the rest portion of the stress curves, the results of FEA and theoretical are in fairly good agreement..

The comparative studies in Section 3.1, 3.2 and 3.3 show that FEA model in ABAQUS matches closely with experimental study or theoretical calculation in terms of beam-column joint, CFST column as well as the interference fit. Therefore, the FEA model of SSBCJ-IF which is composed of the aforementioned three cases is highly reliable.

4. Parametric analysis of moment-rotation (M-θ) relationship

The parametric analyses of the SSBCJ-IF are performed from three aspects, material, geometry and load. The changing trend of the initial rigidity and capacity of the joint under each parameter is obtained. Also, a moment-rotation calculation model is established by using the results obtained from the parametric analyses. The location of the measuring point is shown in Fig.12.

4.1. M - θ relationship

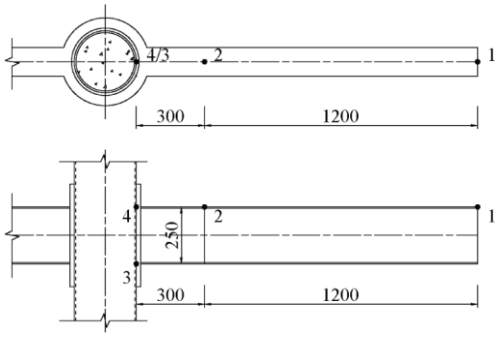

Fig. 6 Location of the measuring-point (mm)

The M - θ relationship of the joint is calculated by Eq. (5) and (6), where M is the moment and θ is the rotation of the joint [24].

$$M = PL_{load} \quad (5)$$

$$\theta=\theta_b-\theta_c \tag{6}$$

Where, P is the load (kN); L_{load} is the distance from the location of the loading to the edge of the column which equals to 1.5 m; θ_b is the rotation angles of the beam while θ_c is the rotation angles of the column (rad).

The beam rotation θ_b is given by Eq. (7) and (8):

$$\theta_b=\arctan\frac{\left|\delta_{\mathrm{DV1}}-\delta_{\mathrm{bel,DV1}}\right|-\left|\delta_{\mathrm{DV2}}-\delta_{\mathrm{bel,DV2}}\right|}{1200} \tag{7}$$

$$\delta_{\mathrm{bel,DV}i}=-\frac{P}{E_bI_b}\left(\frac{x^3_{\mathrm{DV}i}}{6}-\frac{L_{load}x^2_{\mathrm{DV}i}}{2}\right) \tag{8}$$

Where, $\delta_{\mathrm{DV}i}$ is the vertical displacement at measuring point i (mm); $\delta_{\mathrm{bel,DV}i}$ is the calculated elastic displacement of the beam at DVi (mm); E_b is the Young's modulus of the beam (MPa); I_b is the inertia moment of the steel beam section (mm^4); $x_{\mathrm{DV}i}$ is the distance from the measuring point i to the face of the column (mm).

The column rotation θ_c is given by Eq. (9):

$$\theta_c=\arctan\frac{\left|\delta_{\mathrm{DH3}}\right|+\left|\delta_{\mathrm{DH4}}\right|}{250} \tag{9}$$

Where, δ_{DHi} is the horizontal displacement of the measuring point i (mm).

The initial stiffness of K_i is taken as the secant rigidity corresponding to $0.2M_u$ [1].

$$K_i=\frac{0.2M_u}{\theta_{0.2}} \tag{10}$$

Where, $\theta_{0.2}$ is the rotation angle corresponding to $0.2M_u$ (rad); M_u is the ultimate flexural strength of the joint (kN·m).

4.2. Parametric studies

The basic configuration of the joint is set as follows: The section of the steel tube column is 273 × 7 (diameter × wall thickness in mm) filled with C40 concrete. The beam section height, width, web thickness and flange thickness is 250 mm, 125 mm, 6 mm and 9 mm, respectively. The thickness of the external diaphragm is 9 mm. The steel sleeve thickness is 16 mm. The sleeve height are 350 mm. The magnitude of interference is 0.5 mm. The axial compression ratio is 0.3. With this configuration, the parametric studies are performed for material parameter, geometric parameter as well as load parameter. Table 1 shows the values of parameter.

Table 1

Parameter detail Parameters

Material		Geometry				Load
C	Q	δ /mm	α	k	k_m	n
C40	Q235	0.1	0.077	0.257	0.418	0.1
C50	Q345	0.3	0.111	0.300	0.606	0.3
C60	Q390	0.5	0.164	0.375	0.764	0.5
C70	Q420	0.7	0.202	0.449	—	0.7
C80	Q460	0.9	0.242	0.529	—	0.9
—	—	—	0.283	0.599	—	—
—	—	—	—	0.691	—	—

Note: C – concrete grade; Q – steel grade; δ – magnitude of interference; α – steel ratio of the column section; k – beam-column linear stiffness ratio; k_m – beam-column strength ratio; n – axial compression ratio of the column.

(1) Concrete grade

Fig.13(a) shows that when concrete grade is within the range of C40 to C80 the flexural bearing capacity remains almost the same. This is because the failure mainly occurs at the beam flange and web near the column face while only small portion of the column section fails. The failure pattern of the joint satisfies the design principle of "strong column weak beam". Fig.13(b) shows that the initial rigidity increases slightly with the increase of the concrete grade. This is because there is an interrelation between concrete grade and concrete elastic modulus. Higher concrete grade usually corresponds to higher elastic modulus.

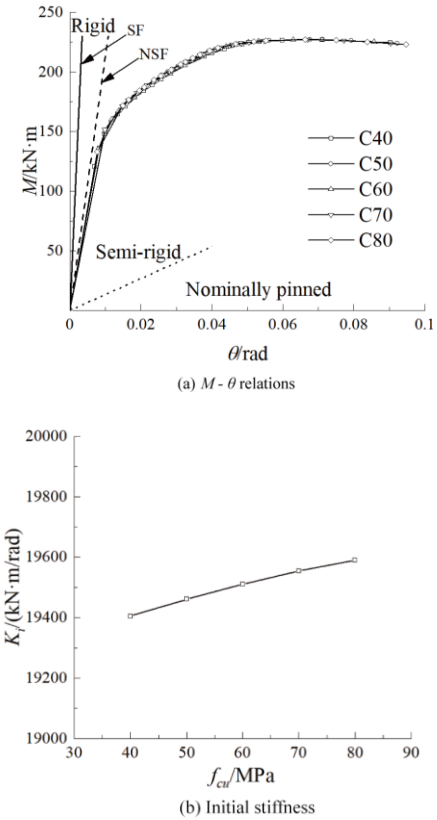

(a) M - θ relations

(b) Initial stiffness

Fig. 7 Influence of concrete strength

(2) Steel grade

Fig.14(a) shows that the flexural bearing capacity increases with the increase of the steel grade while the shape of the moment-rotation curves is similar with each other. The similar shape of the M-θ curves indicates the failure process is also similar. Fig.14(b) shows that the steel grade has without influence on the initial rigidity. This is because the elastic modulus of steel is not directly related to the steel grade.

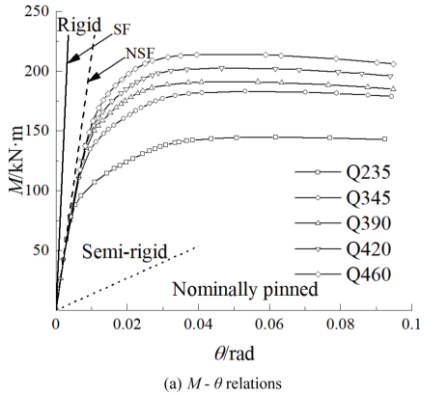

(a) M - θ relations

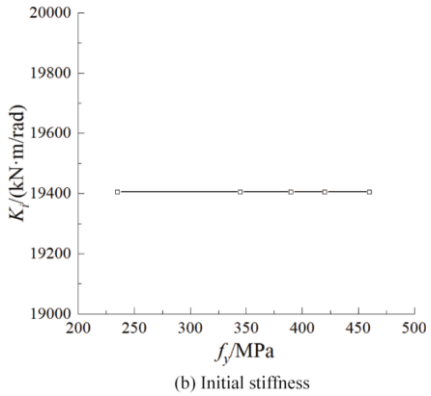

Fig. 8 Influence of steel strength.

(3) Magnitude of interference

Fig.15 shows that the flexural bearing capacity and the initial rigidity of joints increase with the increase of interference when the interference is less than 0.5 and decreases with the decrease of interference when the interference is more than 0.5. When the interference is low, the pre-tightening force between the steel tube and sleeve is small. In this case, the pre-tightening force will be lost under relatively small external load resulting in the stiffness decrease. When the magnitude of interference is high, the pre-tightening force between the steel tube and sleeve is large. In this case, the sleeve reaches plastic stage due to the excessive stress introduced by the large pre-tightening force resulting in the stiffness decrease.

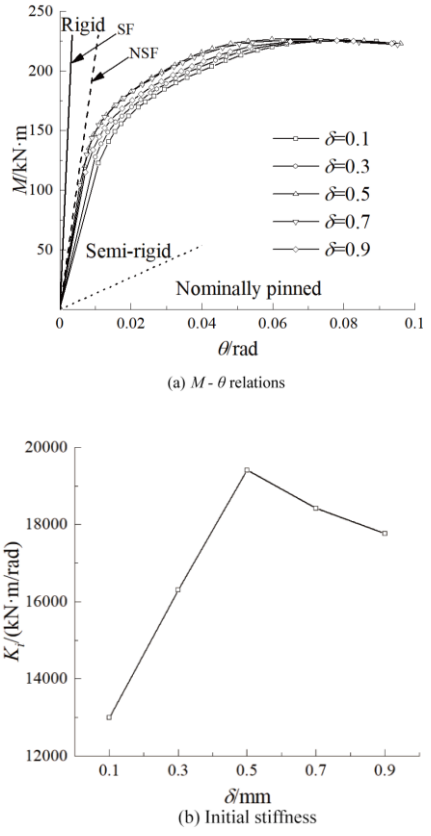

Fig. 9 Influence of magnitude of interference

(4) Steel ratio

The steel ratio $\alpha = A_s / A_c$, where A_s is the areas of steel tube, A_c is the areas of core concrete. Fig.16 shows that the initial rigidity and flexural capacity can be increased along with the increase of the steel ratio of column section. For specific performance: With the increase of the steel ratio, the restraint effect on the concrete is enhanced so that the bending rigidity of the column section is improved. Fig.16 shows that the steel ratio has a great influence on the initial rigidity. Because the major failure occurs at the beam sections near column face, the steel ratio only has relatively small influence on the bending capacity.

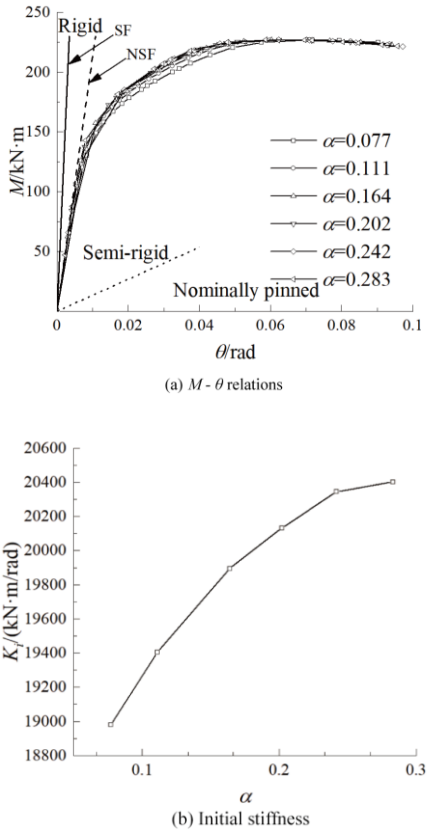

Fig. 10 Influence of steel ratio

(5) Beam-column linear stiffness ratio

The beam-column linear stiffness ratio is defined as:

$$k = \frac{(EI)_b H}{(EI)_c L}$$

where $(EI)_b$ is flexural rigidity of beam, $(EI)_c$ is flexural rigidity of CFST column, H is column height and L is beam span length.

The variation in beam-column linear stiffness ratio ranging from 0.257 to 0.691 is realized by changing the beam span length. Fig.17 shows that the variation of linear stiffness ratio has little influence on the capacity, but it has a significant influence on the initial stiffness. The maximum initial stiffness is reached when the beam-column linear stiffness ratio is about 0.5. To achieve the design goal and to improve the flexural rigidity of the joint, the linear stiffness ratio should not be too large. Thus, the optimum value of k is about 0.5.

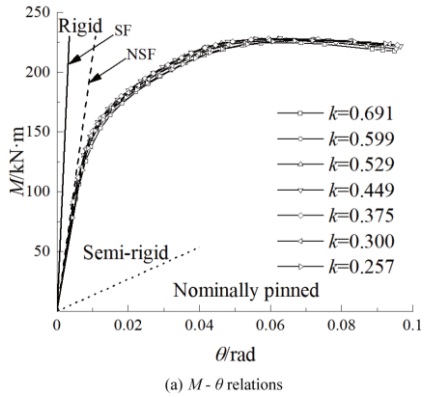

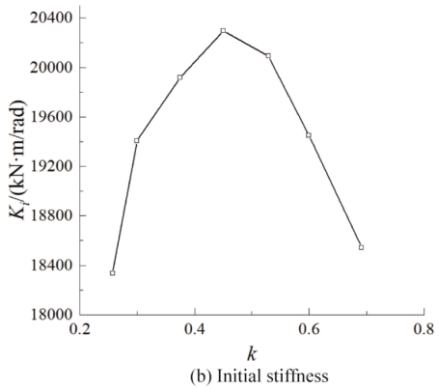

Fig. 11 Influence of beam-to-column linear stiffness ratio

(6) Beam-column strength ratio

The beam-column strength ratio is taken as $k_m = M_{ub} / M_{uc}$, where M_{ub}, M_{uc} is the bending strength of the steel beams and column, respectively. Fig.18(a) shows that the ratio k_m has a great effect on the M - θ curve. This is because the variation of k_m is realized by adjusting the beam section and the beam section with higher bending strength will give both a higher flexural bearing capacity and a higher initial stiffness.

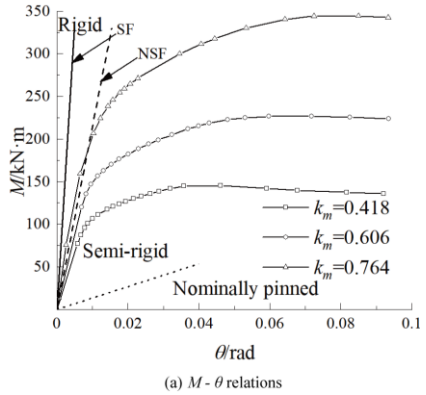

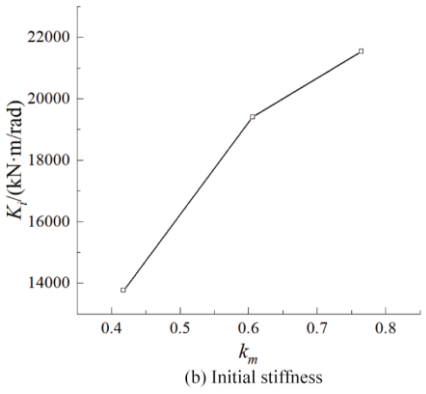

Fig. 12 Influence of strength ratio of beam to column

(7) Axial compression ratio of the column

Fig.19 shows the relationship between axial load ratio and moment-rotation curve. The axial load ratio ranges from 0.1 to 0.9. Both the flexural bearing capacity and initial rigidity of the joint remain the same when the axial compression ratio of column is between 0.1 and 0.7. They both decrease when the axial compression load ratio is above 0.7. This is because the large axial load ratio changes the failure pattern of the joint from beam failure to column compression-bending failure. This indicates that the failure of column prior to the beam failure should be avoided.

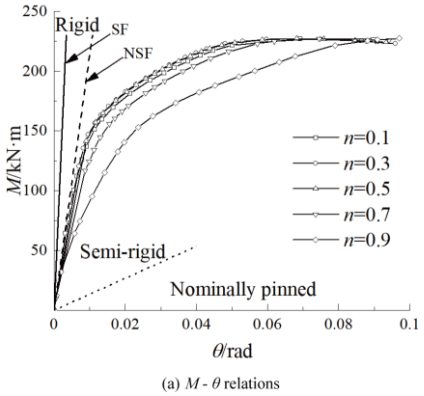

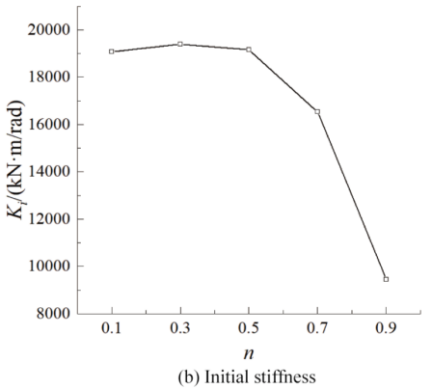

Fig. 19 Influence of axial compression ratio

4.3. Classification of joints

Using the classification method in European Standard (EC3-2005) [25], the joints are divided into three types based on the initial rotational rigidity. If the initial rigidity $S_{j,ini} \geqslant k_b EI_b/L_b$, the joint is rigid. If $S_{j,ini} \geqslant 0.5EI_b/L_b$, the joint is a nominally pinned joint. If $S_{j,ini}$ is between these two limits, the joint is semi-rigid. According to Fig.13-19, the SSBCJ-IF should be classified as a semi-rigid joint.

5. Simplified calculation of M-θ relationship

The three-parameter power model proposed by Kishi et al [14] is used to describe the moment-rotation relation of CFST beam-column joints.

$$\theta = \frac{M}{K_i} \frac{1}{\left[1-\left(M/M_u\right)^n\right]^{1/n}} \tag{11}$$

Where k_i is the initial rigidity (kN·m/rad); M_u is the ultimate flexural capacity (kN·m); n is the parameter related that affects the moment-rotation curve.

The three parameters in Eq. 11, K_i, M_u and n, are determined with numerical analysis as follows.

Initial stiffness k_i :

The parametric analyses indicate that the major factors affecting the initial rigidity are axial compression ratio n, steel ratio α, beam-column strength ratio k_m, linear stiffness ratio k and magnitude of interference δ.

The interference directly affects the radial contact pressure between the steel tube and the sleeve. The steel tube and the sleeve connection rely on the friction caused by the contact pressure to transfer and resist the load. The contact pressure can be calculate using linear elasticity method but solving system of equations is required in this method which is too complex. Here the contact pressure is obtained with the equation from mechanics of materials which is common in mechanical engineering as follows.

$$\delta = qd\left(\frac{C_1}{E_1} + \frac{C_2}{E_2}\right) \tag{12}$$

Where, q is the pressure on the interference-fitted surface (MPa); d is the diameter of the interference-fitted surface (mm); E_1 and E_2 are the Young's modulus of steel tube and sleeve, respectively (MPa); C_1 is the stiffness coefficient of the steel tube, $C_1 = (d^2+d_1^2) / (d^2-d_1^2) - \mu_1$; d_1 is the inner diameter of the steel tube; μ_1 is the Poisson's ratio of the steel tube; C_2 is the stiffness coefficient of the steel sleeve, $C_2 = (d_2^2+d^2) / (d_2^2-d^2) + \mu_2$; d_2 is the outer diameter of the steel sleeve (mm); μ_2 is the Poisson's ratio of the steel sleeve.

Using Eq. (12), the magnitude of interference can be converted into the corresponding contact pressure giving q=2.69~24.22 MPa. The ranges of other parameters are as follows: n=0.1～0.9, α=0.077～0.283, k_m=0.418～0.764, k=0.257～0.691. Based on these parameters, the equation for initial stiffness K_i is defined as follows.

$$K_i = R \cdot f(n) \cdot f(\alpha) \cdot f\left(k_m\right) \cdot f(k) \cdot f(q) \tag{13}$$

Where, R is a coefficient. $f(n)$, $f(\alpha)$, $f(k_m)$, $f(k)$ and $f(q)$ are the mathematical relations between K_i and n, a, k_m, k and q.

$$f(n) = (-2.13n^3 + 1.44n^2 - 0.11n + 1) \times 0.4 \tag{14}$$

$$f(\alpha) = 1.34\ln(3.12\alpha) + 4.8 \tag{15}$$

$$f(k_m) = 3.97k_m^{\ 2} + 2.25k_m + 13.04 \tag{16}$$

$$f(k) = -2.15k^2 + 2.05k + 0.32 \tag{17}$$

$$f(q) = \left(-q^2 + 37.18q + 432.11\right) \times 1.55 \tag{18}$$

Substituting Eq. (14) ~ (18) into Eq. (13), the initial stiffness of the joint K_i is given by:

$$\begin{aligned} K_i = & 0.62\left(-2.13n^3 + 1.44n^2 - 0.11n + 1\right) \\ & (1.34\ln(3.12\alpha) + 4.8)\left(3.97k_m^{\ 2} + 2.25k_m + 13.04\right) \\ & \left(-2.15k^2 + 2.05k + 0.32\right)\left(-q^2 + 37.18q + 432.11\right) \end{aligned} \tag{19}$$

Fig.20 shows the comparison between the initial stiffness from the proposed simplified calculation and that from the FEA modeling. It is seen that the two results are in good agreement with each other and the maximum error is less than 10%.

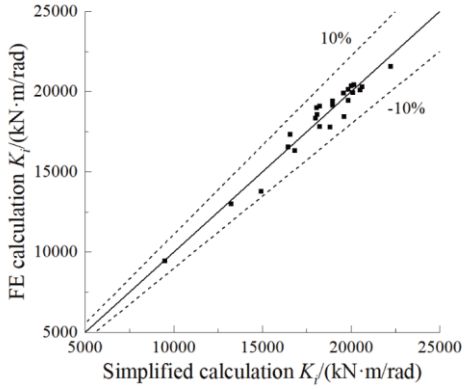

Fig. 13 Simplified calculation of initial stiffness compared with FEA calculation

Ultimate flexural capacity M_u:

Since the failure is ensured to occur at the beam section near column face, the ultimate flexural bearing capacity of the joint M_u is taken as the ultimate flexural bearing capacity of the beam.

$$M_u = W_{nx} f_u \tag{20}$$

Where, W_{nx} is the net cross-section flexural modulus of the beam (mm^3). f_u is the tensile strength of the beam (MPa).

Parameter n:

Substitute K_i and M_u into Eq. (11). After data fitting, the relation between n and θ_0 is given by:

$$n = 0.48\log_{10}\theta_0 + 2.5 \tag{21}$$

Where θ_0 is the reference rotation angle, $\theta_0 = M_u / K_i$.

Fig. 21 shows the comparisons between the M - θ curves from Eq. (11) and the curves from the FEA analysis. It is seen from the Fig.21 that the simplified calculation method can conservatively capture the nonlinear structural behavior of the joint.

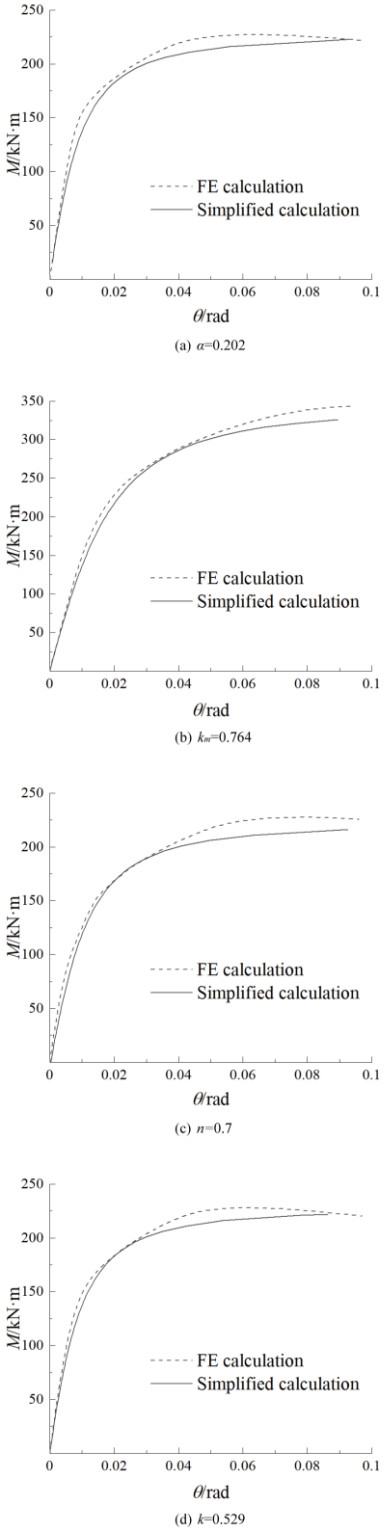

Fig. 21 Moment-rotation curves (simplified calculation method vs FEA calculation)

6. Conclusions

In this paper, the parametric analysis on the mechanical properties of SSBCJ-IF is performed. The influence of major parameters on the flexural bearing capacity and initial rigidity of the SSBCJ-IF are studied. One simplified calculation method for the moment-rotation curve is also proposed. The main conclusions are as follows.

(1) A FEA model of the SSBCJ-IF is proposed in this paper. The results from the FEA model are compared with the results from the experimental studies and theoretical calculation to verify the reliability of the FEA model.

(2) The parametric analysis is performed with three aspects, material, geometric and load. The results show that concrete strength increase had almost no influence on the flexural bearing capacity but has a small influence on the initial rigidity. The flexural capacity can be increases along with the increase of steel grade, and the steel grade has no effect on the initial stiffness. The stiffness of the joint reaches the peak when the magnitude of interference is 0.5 mm (corresponding to 13.45 MPa of pre-tightening force). The magnitude of interference has little influence on the joint flexural capacity. Increasing the steel ratio can slightly increases the initial stiffness of the joint. To satisfy the design goal of "strong column weak beam", the beam-column linear stiffness ratio should not be too large and the joint can reach the maximum stiffness when the linear stiffness ratio is about 0.5. Increasing the beam-column strength ratio through adjusting beam section can improve the initial stiffness and flexural bearing capacity of the joint significantly. When the axial load ratio is 0.7 or less, the change of column axial force has little influence on the joint. When the axial load ratio exceeds 0.7, the initial rigidity and the flexural bearing capacity both decrease significantly with the increase of the axial load ratio.

(3) The SSBCJ-IF is semi-rigid joint according to the classification method of European Standard (EC3) and it is similar with the rigid joint of braced frames.

(4) According to the results of the parametric analysis, a simplified calculation method for the M - θ relation is proposed by fitting the three-parameter power model. The M-θ curves obtained by the simplified calculation method are compared with the curves from the FEA method and the results match with each other very well.

Acknowledgement：

This research was funded by Science and Technology Research Key Project in Higher Institutions of Hebei Province (ZD2018250), Local Science and Technology Development Fund Project Guided by Central Government (206Z7601G) and Natural Science Foundation of Hebei Province (E2020210074).

References:

[1] Lin-Hai Han, Wei Li. Seismic performance of CFST column to steel beam joint with RC slab: Experiments[J]. Journal of Constructional Steel Research, 2010, 66(11): 1374-1386.
[2] Xi-Lin Liu, Yong Yu, Tanaka Kiyoshi. Experimental study on the seismic behavior in the connection between CFRT column and steel beam[J]. Structural Engineering and Mechanics, 2000, 9(4): 365-374.
[3] Jian-Guo Nie, Kai Qin, Rong Liu. Experimental study on seismic behavior of connections composed of concrete-filled square steel tubular columns and steel-concrete composite beams with interior diaphragms[J]. Journal of building structures, 2006, 27(4): 1-9.
[4] Ning Wang, Myung-Jae Lee. Structural behavior of beam-to-column connections of circular CFST columns by using mixed diaphragms[J]. International Journal of Steel Structures, 2015, 15(2): 347-364.
[5] Rui Li, Bijan Sanali, Zhong Tao, Md Kamrul Hassan. Cyclic behaviour of composite joints with reduced beam sections[J]. Engineering Structures, 2017, 136: 329-344.
[6] Yan-Xia Zhang, Quan-Gang Li, Wei-Zhen Huang, Kun Jiang, Yu Sun. Behavior of prefabricated beam-column connection with short strands in self-centering steel frame[J]. Advanced Steel Construction, 2019, 15(2): 203-214.
[7] Atorod Azizinamini, Stephen P. Schneider. Moment connections to circular concrete-filled steel tube columns[J]. Journal of structural Engineering, 2004, 130(2): 213-222.
[8] Kyung-Jae Shin, Young-Ju Kim, Young-Suk Oh, Tae-Sup Moon. Behavior of welded CFT column to H-beam connections with external stiffeners[J]. Engineering Structures, 2004, 26(13): 1877-1887.
[9] Shen Yan, Kim J.R. Rasmussen, Lu-Li Jiang, Chen Zhu, Hao Zhang. Experimental evaluation of the full-range behaviour of steel beam-to-column connections[J]. Advanced Steel Construction, 2020, 16(1): 77-84.
[10] Shan Gao, Man Xu, Lan-Hui Guo, Su-Mei Zhang. Behavior of CFST-column to steel-beam joints in the scenario of column loss. Advanced Steel Construction, 2019, 15(1): 47-54.
[11] Lightfoot E, Messuries A P L. Elastic analysis of frameworks with elastic connections. Journal of the Structural Division, 1974, 100(6): 1297-1309.
[12] Frye M.John, Morris Glenn. Analysis of flexibly connected steel frames[J]. Canadian journal of civil engineering, 1975, 2(3): 280-291.
[13] Jones Stephen W, Kirby Patrick A, Nethercot David A. Columns with semirigid joints[J]. Journal of the Structural Division, 1982, 108(2): 361-372.
[14] N. Kishi, Wai-Fah Chen. Moment-rotation relations of semirigid connections with angles[J]. Journal of Structural Engineering, 1990, 116(7): 1813-1834.
[15] Yee Yoke Leong, Melchers Robert E. Moment-rotation curves for bolted connections[J]. Journal of Structural Engineering, 1986, 112(3): 615-635.
[16] Gang Shi, Xue-Sen Chen. Moment-rotation curves of ultra-large capacity end-plate joints based on component method[J]. Journal of Constructional Steel Research, 2017, 128: 451-461.
[17] G.C. Li, C.Y. Di, L. Tian, C. Fang. Nonlinear finite element analysis on long columuns of high-strength concrete-filled square steel tube with inner cfrq circular tube under axial load[J]. Advanced Steel Construction, 2013, 9(2): 124-138.
[18] Yong-Jiu Shi, Meng wang, Yuan-Qing Wang. Study on constitutive model of structural steel under cyclic loading[J]. Engineering Mechanics, 2012, 29(9): 92-98+105.
[19] GB/T 50081-2002 Chinese standard for test method of mechanical properties on ordinary concrete. Beijing: China Construction Industry Press,2002 .
[20] Lin-Hai Han, Guo-Huang Yao, Zhong Tao. Performance of concrete-filled thin-walled steel tubes under pure torsion[J]. Thin-Walled Structures, 2007, 45(1): 24-36.
[21] CORP D S S. ABAQU 6.14 Analysis user's guide volume V: Prescribed Conditions, Constraints & Interactions [M]. USA: ABAQUS, Inc, Dassault Systemes, 2014.
[22] Ming-Lie Yan, Jun-Ping Wang, Zhang-Tao Li, Si-Mao Ren. Experimental study on sleeve joints of round steel tubes[J]. Building Structure, 2019, 49(06): 66-68.
[23] Lin-Hai Han, You-Fu Yang. Cyclic performance of concrete-filled steel CHS columns under flexural loading[J]. Journal of Constructional Steel Research, 2005, 61(4): 423-452.
[24] Xu-Hong Qiang, Nian-Du Wu, Yong-Feng Luo, Xiao Liu, Xu Jiang. Performance test and Finite element Analysis of overhanging End-plate joints in high strength steel[J]. Journal of Hunan University (Natural Science edition), 2018, 45(07): 1-9.
[25] CEN E. Eurocode 3: Design of steel structures Part 1–8: Design of joints[S]. 2005.

Advanced Steel Construction – Vol. 16 No. 4 (2020) 346–353
DOI:10.18057/IJASC.2020.16.4.7

MECHANICAL BEHAVIORS OF SIDE-PLATE JOINT BETWEEN WALLED CONCRETE-FILLED STEEL TUBULAR COLUMN AND H-SHAPED STEEL BEAM

Yu-Qi Huang [1, *], Ji-Ping Hao [1], Rui Bai [2], Chun-Lei Fan [1] and Qiang Xue [1]

[1] *School of Civil Engineering, Xi'an University of Architecture & Technology, Xi'an, China*
[2] *Department of Civil and Environmental Engineering, The Hong Kong Polytechnic University, Hong Kong, China*
(Corresponding author: E-mail: huangyuqi_1989@163.com)

ABSTRACT

The mechanical behaviors of an innovative joint, the side-plate joint, that connects a walled concrete-filled steel tubular column and an H-shaped steel beam, were analytically and experimentally investigated. The mechanical characteristics of the joint panel zone under shear were studied. A three-stage shear-yield model was established for describing the relation between shear force and shear deformation of the joint panel zone. Three failure modes and the corresponding evaluating criteria were proposed for design practices based on the shear-yield model and internal force transfer mechanism. To verify the reliability of the proposed method, three full-scale walled concrete-filled steel tubular column joints were tested under cyclic loads. Moreover, the hysteresis curve, skeleton curve, ductility, energy dissipation capacity, stiffness degradation, and strain of the joint were evaluated based on the experimental results. The predicted failure mode and ultimate bearing capacity predicted by the proposed method show good agreement with the test results; the hysteresis loop of the specimen is relatively full and shuttle-shaped without discernible pinching, which indicates the side-plate joint exhibits preferable deformation performance and possesses an energy dissipation capacity.

ARTICLE HISTORY

Received: 28 February 2020
Revised: 25 August 2020
Accepted: 10 September 2020

KEYWORDS

Walled concrete-filled steel tubular column;
Side-plate joint;
Panel zone;
Failure mode;
Full-scale specimen;
Hysteresis behavior

1. Introduction

A concrete-filled steel tube (CFST) column is the vertical bearing member formed by pouring core concrete into a steel tube. Core concrete can increase the stiffness and vertical bearing capacity of the column and restrain the local buckling of the steel tube. The external hollow steel tube in turn can be used as the pouring formwork of the core concrete, and it can provide constraints on the core concrete, thereby keeping the concrete in a three-way compression state and improving its tensile and compressive strengths. CFST columns are widely used in construction engineering owing to their characteristics such as large bearing capacity and stiffness, excellent economy, and ease of processing and construction [1–3].

Typically, CFST columns and beams are combined to form a reliable steel moment frame system. The beam-to-column joints are the key segments for transmitting forces. The design of the joints is an important part of structural design. Research on the failure mode and mechanical performance of the joints is a prerequisite to ensure the normal operation of a structure. In engineering applications, the CFST columns are commonly shaped as circular and rectangular sections. According to the Technical Code for Concrete-Filled Steel Tubular Structures (GB 50936-2014) [4], internal diaphragm and outer reinforced-ring-plate are recommended for use in the joints between CFST columns and steel beams.

To ensure that the core concrete in the internal diaphragm joint is poured smoothly, the diameter of a pouring hole, which is not less than 200 mm, must be opened in the internal diaphragm. If the column section is too small to meet the pouring requirements, the outer reinforced-ring-plate joint can be adopted. An internal diaphragm does not exist in the outer reinforced-ring-plate joint, and the beam flange axial force is transmitted through the ring plate. The width of the plate should not be less than 0.7 times the flange width of the steel beam [4]. In engineering practices, the column width may be the same as the thickness of the infill wall to avoid column exposure inside the room and increase the usable space, which leads to a small column section. Therefore, the internal diaphragm joint cannot be adopted in such CFST columns. Similarly, the outer ring plate joint, which has a wider boundary, protrudes from the beam-column members and affects the architectural beauty and decoration layout, and should be avoided in engineering applications as well.

To avoid the exposure of columns inside a room, Hao et al. [5, 6] proposed a walled concrete-filled steel tube (WCFT) column with a large aspect ratio and thickness equal to that of the infilled wall in multi-story steel structure buildings. Fig. 1 shows a typical section of a WCFT column. Due to the small width of this column, the internal diaphragm joint cannot be used, and the outer-ring-plate joint could possibly influence the indoor beauty and practicality. Therefore, the authors propose a new type of side-plate joint suitable for a WCFT column. Based on the components of the side-plate joint, this paper presents a theoretical study on the force-transfer mechanism and failure mode at the panel zone and beam end. Quasi-static tests of three full-scale joint specimens were used to verify the theoretical research, and demonstrate the hysteretic performance, failure mode, deformation capacity, and bearing capacity of the side-plate joint. The work offers guidance for the mechanical property analysis and design of the side-plate joint.

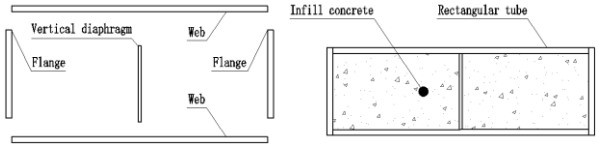

Fig. 1 Walled concrete-filled steel tubular (WCFT) column

2. Theoretical analysis

The components of the side-plate joint in this study are shown in Fig. 2. The embedded side plate is set along the web of the WCFT column. The cantilever segment of the side plate extend outward along the steel beam aims to transmit the bending moment at the beam end to the joint panel directly. The height of the extended part can be determined according the moment. Details of the joint configuration can be found in sections 2.1 to 2.3. The end of the beam is welded to the WCFT column flange. The moment at the beam end is mainly transmitted through the side plate and column flange, and the shear force is transmitted through the weld between the beam web and column flange.

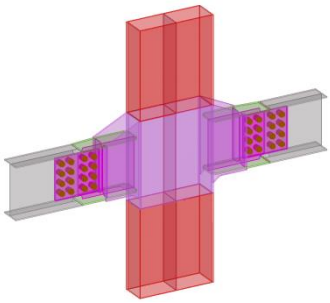

(a) Integrated schematic view of side-plate joint

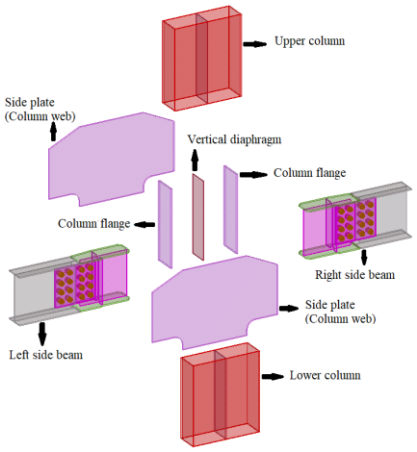

(b) Exploded schematic view of side-plate joint

Fig. 2 Typical side-plate joint of a WCFT column–H-shaped beam

2.1. Shear mechanism of the joint panel zone

The design of panel zone of the beam–column joint is a critical part in the seismic design process, where a reasonable force-transmission mechanism describing the performance of the joint panel zone under horizontal earthquakes must be established. Fig. 3 shows the bending moment distribution at the column and beam ends of the frame and the stress on the joint under horizontal seismic forces. The moments at the beam ends on both sides of the intermediate column are anti-symmetric. If the moment at the end of the steel beam reaches the full-section plastic moment M_{bp}, the pair of force couples that decomposes in the panel zone is defined as follows:

$$T = C = M_{bp} / (h_b - t_{bf}) \tag{1}$$

where T and C respectively represent the tension and pressure after the beam end moment is decomposed, h_b is the height of the steel beam, and t_{bf} is the thickness of the beam flange.

The beam–column joint panel zone in the middle floor of the frame system is considered as a part of the column. The position of the inflection point of the column is assumed to be located at the half story. As shown in Fig. 3b, the force couple T/C that is decomposed from the beam moment causes a sudden change in the shear force at the panel zone. According to the moment balance, the column shear force can be obtained as follows:

$$V_c = 2M_{bp} / H \tag{2}$$

where V_c is the shear force at the inflection point of the column, and H is the distance between the upper and lower inflection points, i.e., the story height.

The shear force at the panel zone (V_n) is calculated as

$$V_n = \frac{2M_{bp}}{h_b - t_{bf}} - \frac{2M_{bp}}{H} = \frac{2M_{bp}}{H} \times \frac{H - (h_b - t_{bf})}{h_b - t_{bf}} \tag{3}$$

$$\frac{V_n}{V_c} = \frac{H - (h_b - t_{bf})}{h_b - t_{bf}} \tag{4}$$

Assuming that the heights of the steel beam and story are 0.4 to 0.6 m and 3 to 3.6 m, respectively, the horizontal shear force V_n at the joint panel zone is 4 to 8 times the shear force, V_c.

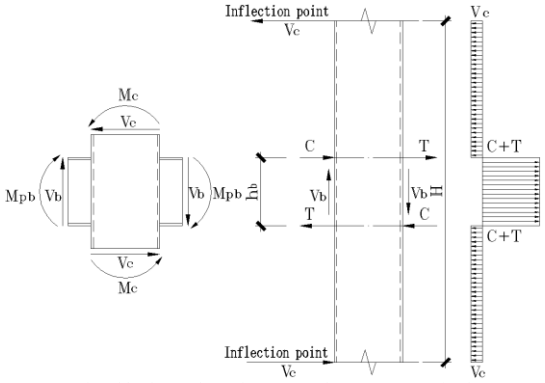

(a) Isolated body (b) Column (panel zone as part of column)

Fig. 3 Internal force analysis of joint under horizontal seismic effect

Considering the abrupt change in the shear force of the joint panel zone, the analysis of its shear bearing capacity is a prerequisite to satisfy the requirement of strong joints and weak members. Many scholars have theoretically analyzed and experimentally demonstrated the shear capacity of conventional CFST column joints [7–11]. Most researchers analyzed the shear contribution of each part based on the stress and deformation mechanisms, and then used the principle of superposition to obtain the total shear capacity of the joint panel zone [12]. The stress and deformation mechanisms of the core concrete adopt the "inclined beam–truss mechanism" proposed by Park and Paulay [13, 14] for concrete beam–column joints. For the side-slab joints of the WCFT column examined in this study, an internal diaphragm was not set in the joints, and thus the concrete in the panel zone will not show the shear mechanism of an inclined beam–truss. There are two ways for the axial force of the beam flange in the side-plate joint to be transmitted to the panel zone. First, the force is directly transmitted to the column web through the weld of the side-plate extension and beam flange. The force is also transmitted to the column flange through the weld between the beam flange and column flange.

Based on the mechanical characteristics of the side-plate joint of the WCFT column, the shear force development of the joint panel zone can be divided into the following three stages and is plotted in Fig. 4:

First stage: The end of the steel beam begins to bend, and the moment at the beam end is transmitted to the column web and column flange through the two above-mentioned paths. Owing to the bond stress between the column web and core concrete [15, 16], the core concrete and column web deform compatibly before reaching their ultimate bond strength. At this stage, the column web is subjected to shear deformation, the column flange is under bending, and the bond stress causes continuous strain to the column web and core concrete. The core concrete in turn provides shear capacity in the plane shear mode with large shear stiffness.

Second stage: As the bending moment at the beam end gradually increases, the bond stress between the core concrete and column web reaches a critical value or the stress on the core concrete reaches the ultimate shear strength (point A); the core concrete cannot further sustain the shear force. The column web and flange contribute the shear resistance of the joint panel zone, and with the moment increase, the column web yields (point B). At this stage, the shear stiffness of the panel zone comprises the shear stiffness of the column web and the bending stiffness of the column flange. Compared with that in the first stage, the shear stiffness is significantly reduced.

Third stage: After shear yielding at the column web (point B), the column flange contributes toward shear resistance due to bending deformation until the column flange side enters the yield state (point C), at which point the joint panel zone also reaches the yield state. In this stage, research has shown that the strain on the column web does not increase sharply [17], indicating that the core concrete can effectively restrain the buckling of the column web.

The three stages representing the shear mechanism of the WCFT column joint panel zone are shown in Fig. 4. The corresponding shear force and deformation of turning points (A, B, and C) must be determined to describe the shear performance of the panel zone.

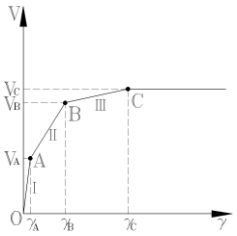

Fig. 4 Shear force–shear deformation model for side-plate joint panel

2.2. Shear force–shear deformation model for panel zone

As described in Section 2.1, the column web, column flange, and core concrete contribute to the shear resistance of the joint panel zone. The shear stiffness and bearing capacity of the core area of the node can be obtained by the superposition principle [12]. The axial force transmitted from the beam flange generates a shear force on the panel zone, resulting in shear deformation at the column web and bending deformation at the column flange, as shown in Fig. 5.

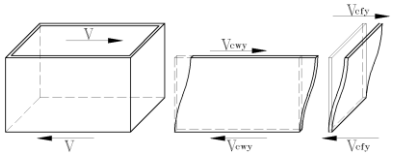

(a) Panel zone (b) Web (c) Flange

Fig. 5 Schematic of the deformation of steel tube at the panel zone

The shear stiffness of the column flange (K_{cf}) due to the bending deformation is formulated as

$$K_{cf}=2\times\frac{3E_sI_{cf}\times 2^2}{\left(h_b-t_{bf}\right)^2}=\frac{2E_s(b_{cf}-2t_{cw})t_{cf}^3}{\left(h_b-t_{bf}\right)^2} \tag{5}$$

where E_s is the elastic modulus of steel, I_{cf} is the bending stiffness of the column flange, h_b is the height of the steel beam, t_{bf} is the thickness of the steel beam flange, b_{cf} is the width of the column flange, t_{cw} is the thickness of column web in the joint panel zone, and t_{cf} is the thickness of column flange in the joint panel zone.

The shear stiffness of the column web (K_{cw}) due to shear deformation is formulated as

$$K_{cw}=2G_sA_{cw}=2G_sh_{cw}t_{cw} \tag{6}$$

where G_s is the shear modulus of steel, A_{cw} is the area of the single web side of the panel zone, and h_{cw} is the section height on the side of column web.

The core concrete of the panel zone is subject to plane shear stress, and its shear stiffness (K_{cc}) is formulated as

$$K_{cc}=G_cA_{cc}=G_c\left(h_{cw}-2t_{cf}\right)\left(b_{cf}-2t_{cw}\right) \tag{7}$$

where G_c is the shear modulus of the core concrete and A_{cc} is the area of the core concrete. As the thickness of the vertical diaphragm in the joint is very thin, its influence on the stiffness and shear capacity is ignored.

Equations (5) to (7) show the shear-stiffness contribution by each part of the joint. To determine the positions of the three turning points in Fig. 4, the shear force of these points must be determined.

First, the yield shear force of the column flange (V_{cfy}) can be calculated by the principle of virtual work:

$$V_{cfy}=\frac{4M_{cfy}}{h_b-t_{bf}}=\frac{2f_y(b_{cf}-2t_{cw})t_{cf}^2}{3\left(h_b-t_{bf}\right)} \tag{8}$$

where M_{cfy} is the yield moment at the column flange in the joint panel zone and f_y is the yield strength of the steel. The shear deformation value in the panel zone is generally small, and the influence of the axial force on yield shear force V_{cfy} is ignored.

It is assumed that the longitudinal strains of the steel tube and infill concrete in the joint panel zone are continuous under the axial force, and the axial stress σ_{sN} of the steel tube is defined as

$$\sigma_{sN}=\frac{N_cE_s}{E_sA_{cs}+E_cA_{cc}}$$

$$\sigma_{sN}=\frac{N_cE_s}{E_s\left[2h_{cw}t_{cw}+2t_{cf}\left(b_{cw}-2t_{cf}\right)\right]+E_c\left(h_{cw}-2t_{cf}\right)\left(b_{cf}-2t_{cw}\right)} \tag{9a}$$

where N_c is the column's axial force, E_c is the elastic modulus of the infill concrete, and A_{cs} is the area of the steel tube that lies inside the panel zone.

According to the Von Mises yield criterion, when the column web in the panel zone is subjected to simultaneous shear and compression, the shear yield stress τ_{cwy} is formulated as

$$\tau_{cwy}=\sqrt{f_y^2-\sigma_{sN}^2}/\sqrt{3} \tag{9b}$$

The shear stress in the joint panel zone is assumed to be uniformly distributed along the web side of the column, and therefore the shear yield force V_{cwy} of the column web in the joint panel zone is given as

$$V_{cwy}=\frac{2h_{cw}t_{cw}\sqrt{f_y^2-\sigma_{sN}^2}}{\sqrt{3}} \tag{9c}$$

Bond stress is mainly generated by the friction between the column web and core concrete. The average bond strength of the CFST sections is 0.2 to 1.0 MPa according to Zhong et al. [18]. The adhesion force F_μ between the column web and core concrete in the joint panel zone is calculated as

$$F_\mu=V_{cc1}=2f_\mu\left(h_{cw}-2t_{cf}\right)\left(h_b-t_{bf}\right) \tag{10a}$$

where V_{cc1} is the maximum shear bearing capacity that the core concrete in the joint panel zone can provide due to the bonding stress, and f_μ is the bonding stress between the column web and core concrete.

Considering the confinement effect on the shear strength of the filled concrete, the ultimate shear strength of core concrete is taken as $2f_t$ [19], and the ultimate shear force of the core concrete is calculated as

$$V_{cc2}=\frac{2f_t\left(h_{cw}-2t_{cf}\right)\left(b_{cf}-2t_{cw}\right)}{\kappa} \tag{10b}$$

where V_{cc2} is the ultimate shear force that the core concrete in the joint panel can reach, f_t is the axial tensile strength of ordinary concrete, and κ is the nonuniformity coefficient of shear stress; it can be taken as 1.2 for a rectangular concrete cross section [13].

$$V_{cc}=\min\left(V_{cc1},V_{cc2}\right) \tag{10c}$$

where V_{cc} is the ultimate shear force of core concrete in the joint panel zone.

The shear strain γ_A and shear value V_A at the end of the first stage (point A) are formulated as

$$\gamma_A=\frac{\min\left(V_{cc1},V_{cc2}\right)}{G_c\left(h_{cw}-2t_{cf}\right)\left(b_{cf}-2t_{cw}\right)} \tag{11}$$

$$V_A=V_{cc}+(K_{cf}+K_{cw})\gamma_A$$

$$V_A=\min\left(V_{cc1},V_{cc2}\right)+\left[\frac{2E_s(b_{cf}-2t_{cw})t_{cf}^3}{\left(h_b-t_{bf}\right)^2}+2G_sh_{cw}t_{cw}\right]\gamma_A \tag{12}$$

Furthermore, the shear strain γ_B and shear value V_B at the end of second stage (point B) are formulated as

$$\gamma_B=\frac{V_{cwy}}{K_{cw}}=\frac{\sqrt{f_y^2-\sigma_{sN}^2}}{\sqrt{3}G_s} \tag{13}$$

$$V_B=V_{cc}+V_{cwy}+K_{cf}\gamma_B$$

$$V_B=\min\left(V_{cc1},V_{cc2}\right)+\frac{2h_{cw}t_{cw}\sqrt{f_y^2-\sigma_{sN}^2}}{\sqrt{3}}+\frac{2E_s(b_{cf}-2t_{cw})t_{cf}^3\sqrt{f_y^2-\sigma_{sN}^2}}{\sqrt{3}G_s\left(h_b-t_{bf}\right)^2} \tag{14}$$

Finally, the shear strain γ_C and shear value V_C at the end of the third

stage (point C) are formulated as

$$\gamma_C = \frac{V_{cfy}}{K_{cf}} = \frac{f_y\left(h_b - t_{bf}\right)}{3E_s t_{cf}} \tag{15}$$
$$V_C = V_{cc} + V_{cwy} + V_{cfy}$$

$$V_C = \min\left(V_{cc1}, V_{cc2}\right) + \frac{2h_{cw}t_{cw}\sqrt{f_y^2 - \sigma_{sN}^2}}{\sqrt{3}} + \frac{2f_y(b_{cf} - 2t_{cw})t_{cf}^2}{3\left(h_b - t_{bf}\right)} \tag{16}$$

The shear force–shear deformation mode of the panel zone of the side-plate joint can be obtained according to equations (11) to (16), as shown in Fig. 4.

2.3. Failure-mode analysis of the side-plate joint

Under the loading conditions, where the horizontal load plays a controlling role, the bending moment directions of the beam ends on both sides of the joint are consistent. Assuming that the beam end moment is the full-section plastic bending moment, M_{pb}, it can be converted into the force couple T_p/C_p acting on the beam flange, as shown in Fig. 6. The axial force of the beam flange in the side-plate joint is transmitted by the column flange, column web, and core concrete. Part of the shear force at the beam end is transmitted through the weld between the beam flange and column flange to the column flange, the remaining shear force is transmitted through the weld between beam flange and side plate to the column web and core concrete. The side-plate joint (excluding the joint panel zone) has three failure modes: (mode I) horizontal weld failure between the beam flange and side plate; (mode II) flexural failure of the side plate at the column flange position; and (mode III) significant damage or buckling at the beam beyond the side plate.

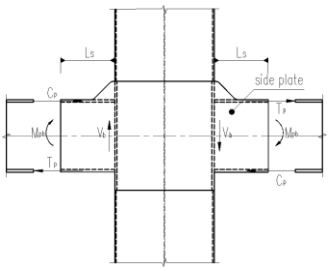

(a) Internal force diagram of beam end

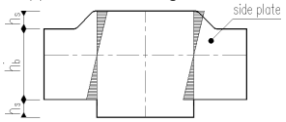

(b) Stress diagram of side plate in the column flange

Fig. 6 Internal force diagram of side-plate joint

According to equations (11) to (16), the value of the moment M_{bf} transferred from the flange at the beam end is given as

$$M_{bf} = \frac{V_{cfy}}{2} \times \left(h_b - t_{bf}\right) = f_y(b_{cf} - 2t_{cw})t_{cf}^2 \tag{17}$$

The proportion of the bending moment transmitted by the column flange is assumed to be $\theta = M_{bf}/M_{pb}$; then, the moment transmitted by the side plate (M_{bs}) is formulated as

$$M_{bs} = M_{bp} - M_{bf} = (1-\theta)M_{bp} \tag{18}$$

The horizontal strength of side plate is determined as follows:

$$\frac{2f_{yw}(L_s - 2t_{bf})t_{bf}}{\sqrt{3}} \le \frac{M_{bs}}{h_b - t_{bf}} = \frac{(1-\theta)M_{bp}}{h_b - t_{bf}} \tag{19a}$$

$$F_{\mathrm{I}} = \frac{2f_{yw}(L_s - 2t_{bf})t_{bf}}{\sqrt{3}(1-\theta)} \le \frac{M_{bp}}{h_b - t_{bf}} \tag{19b}$$

Further, the vertical flexural strength of the side plate is formulated as

$$f_y\left(h_b + h_s\right)t_{cw} \le \frac{2M_{bs}}{h_b + h_s} = \frac{2(1-\theta)M_{bp}}{h_b + h_s} \tag{20a}$$

$$F_{\mathrm{II}} = \frac{f_y\left(h_b + h_s\right)^2 t_{cw}}{2(1-\theta)\left(h_b - t_{bf}\right)} \le \frac{M_{bp}}{h_b - t_{bf}} \tag{20b}$$

$$F_{\mathrm{II}} = \frac{f_{yw}\left(h_b + h_s - 2t_{cw}\right)^2 t_{cw}}{2(1-\theta)\left(h_b - t_{bf}\right)} \le \frac{M_{bp}}{h_b - t_{bf}} \tag{20c}$$

The strength of the steel beam flange is formulated as

$$F_{\mathrm{III}} = \frac{M_{bp}}{h_b - t_{bf}} \le \min\left(F_{\mathrm{I}}, F_{\mathrm{II}}\right) \tag{21}$$

where L_s is the external length of the side plate beyond the column flange. Considering the defect at the beginning and ending of the weld, the base metal thickness will be reduced two-fold when calculating the weld length. h_s is the height of the side plate beyond the upper beam flange, b_{bf} is the width of beam flange, and f_{yw} is the tensile strength of the butt weld. Equation (20b) is applicable to the joint with the column web and the side plate processed into a complete plate in the panel zone. Equation (20c) is applicable to the joint with the column web and side plate broken by the column flange and connected with the column flange through groove welding.

When $F_{\mathrm{III}} / \min(F_{\mathrm{I}}, F_{\mathrm{II}}) \le 100\%$, failure mode I occurs due to damage or buckling at the beam beyond the side plate. $F_{\mathrm{II}} / F_{\mathrm{III}} \le 100\%$ indicates that vertical flexure strength of the side plate at the column flange is insufficient, resulting in failure mode II. $F_{\mathrm{I}} / F_{\mathrm{III}} \le 100\%$ indicates that the horizontal weld strength of the extended side plate is insufficient, resulting in failure mode III.

3. Experimental study

3.1. Specimen design and loading system

In order to verify the proposed equations for evaluating the joint failure modes and bearing capacity, three full-scale middle column WCFT joints were manufactured. The specimens possessed double-cavity WCFT columns and H-shaped welded composite beams. The WCFT column can meet the requirements of the stronger based on the AISC Seismic Provision recommendations [20]. The material property of steel was Q235B, and C25 grade of infill concrete was used in all specimens.

In addition to the conditions of the laboratory equipment, the column axial pressure ratio of all specimens was retained at 0.3 during the test. The axial compression ratios of the specimens were experimentally obtained as per the following relationship: $n = N / \left(f_{cm}A_c + f_{ym}A_s\right)$, where N is the constant vertical load applied to the top of the column, f_{cm} is the average test measurement of the axial compression strength of concrete, A_c is the area of the infill concrete, and A_s is the area of the steel tube.

The average values of different steel plates of the test pieces are listed in Table 1, and the cross-sections and detailed dimensions of the specimens are listed in Table 2. A 150-mm cube (standard test block) was obtained when the infill concrete of the specimens was poured. The average compressive strength of the concrete cube measured after curing for 28 days under the same conditions as the specimens was 32.25 MPa. The modulus of elasticity of concrete was determined based on the compressive strength and $E_c = 10^5 / (2.2 + 34.7 / f_{cu})$ [17], where the shear modulus G_c was taken as 0.4 times the elastic modulus, E_c [21]. Fig. 7 shows the schematic of the specimen and test equipment.

Table 1
Steel properties

Plate specification	f_y/MPa	f_u/MPa	δ	E_s/MPa	f_u/f_y
Steel tube (8 mm)	371.67	520.00	24.97%	188667	1.40
Steel tube (12 mm)	375.00	493.33	30.59%	217000	1.32
Beam flange	383.33	535.00	30.18%	210667	1.40
Beam web	380.40	513.70	24.67%	175700	1.35

δ is the steel elongation.

Table 2
Section size of test specimens

Specimen number	WCFT column/mm	H-shaped beam/mm	Column web in panel zone/mm	Column flange in panel zone/mm	Extension length of side plate/mm	Column height /mm
JD-1	550 × 180 × 8	H400 × 180 × 8 × 14	550 × 600 × 12	156 × 600 × 12	300 × 500 × 12	2900
JD-2	550 × 180 × 8	H400 × 180 × 8 × 14	526 × 600 × 12	180 × 600 × 12	300 × 500 × 12	2900
JD-3	550 × 180 × 8	H400 × 180 × 8 × 14	550 × 600 × 12	156 × 600 × 12	240 × 500 × 12	2900

1. The joint configuration of the JD-1 specimen implies that the column web in the panel zone and extended side plate are processed into a complete plate; the column web and side plate of the JD-2 specimen are separate and connected to the column flange through groove welding. 2. The column height is the distance from the top of the column to the center of the bottom pin shaft.

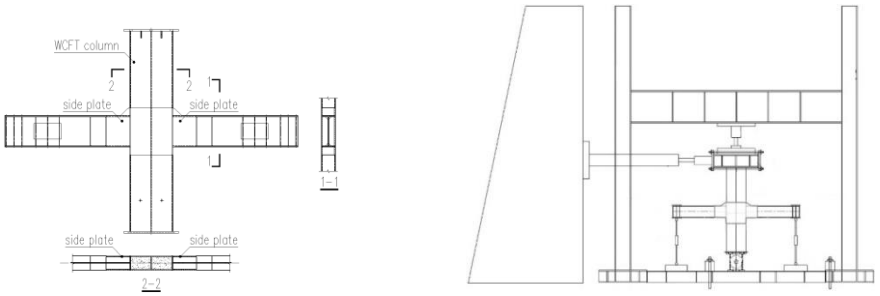

(a) Schematic of specimen (b) Schematic of test equipment

Fig. 7 Schematic of test specimens and test equipment

During the specimen-loading process, a predetermined constant vertical load was first applied to the top of the column, followed by a low-period horizontal cyclic load. The horizontal loading scheme followed the load–displacement hybrid method [22], i.e., the load control and displacement control before and after the yield of specimens, respectively. In the displacement control, a same displacement is repeated three times at each load stage until the test specimen is broken. The test specimen loading scheme is shown in Fig. 8.

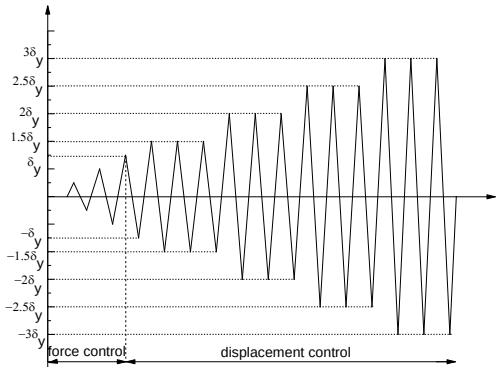

Fig. 8 Schematic of loading system

3.2. Test phenomenon and failure mode

As the JD-1 specimen loading reached a reciprocating load of 36 mm, the strain-data acquisition box showed that the steel beam flange had reached the yield strain at many points, and the load–displacement curve showed a slight inflection point, indicating that the JD-1 specimen had entered plasticity at this moment. When a reciprocating load of $2.5\delta_y$ (90 mm) was applied on the JD-1 specimen, the web of the east beam slightly deformed and buckled; furthermore, during the reciprocating load of $3.5\delta_y$, the upper and lower flanges of the steel beam outside the east side appeared to buckle, and the web bulging was evident. During first round of application of a reciprocating load of $4\delta_y$ (144 mm) on the JD-1 specimen, the beam web and flanges on both sides of the column buckled, and the bearing capacity decreased by 0.8 times the ultimate bearing capacity. At this moment, the test was stopped; the failure mode of the JD-1 specimen is shown in Fig. 9. Owing to the existence of the side plate at the beam end, the position of the plastic hinge of JD-1 was shifted from the panel zone; this effectively protected the panel zone of the joint. A plastic hinge was formed at approximately 0.8 to 1.0 times the beam height from the column flange that effectively protected the panel zone of the joint.

(a) Final failure state (b) Buckling of flange

Fig. 9 Final failure mode of JD-1 (mode I)

As the JD-2 specimen loading reached a reciprocating load of 40 mm, a slight inflection point appeared in the load–displacement curve, and the JD-2 specimen was observed to enter the plastic state. During the test cycle of $1.5\delta_y$ (60 mm), when the first circle was pulled to 60 mm, no obvious deformation phenomenon was observed on the flange and web of the beam; however, the weld at the joint between the lower flange of the southwest beam and column flange cracked. As the second circle was pushed to 60 mm, the weld connecting the column flange and southeast-side plate cracked, and the crack developed rapidly to 15 cm. The test was stopped at this time; the test failure mode of the JD-2 test piece is shown in Fig. 10.

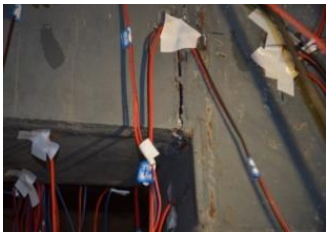

Fig. 10 Final failure mode of JD-2 (mode II)

As the JD-3 specimen loading reached the yield load, a reciprocating load of 36 mm was applied on it. During the test cycle of $1.5\delta_y$ (54 mm), no obvious deformation phenomenon occurred in the column and side plate; however, the weld at the joint connecting the lower flange of the southwest beam and upper flange of the northeast beam with the side plate cracked, and the crack quickly developed. Furthermore, the horizontal load at the top of the column could not be maintained, and the test was stopped. The test failure mode of the JD-3 specimen is shown in Fig. 11.

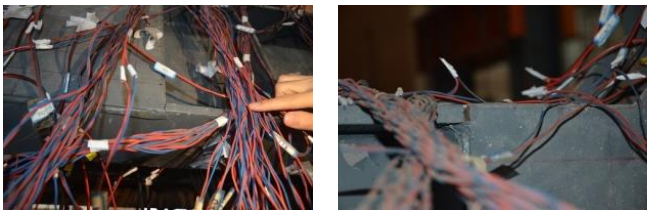

(a) Cracking on the east-side beam (b) Cracking on the west-side beam

Fig. 11 Final failure mode of JD-3 (mode III)

After all specimens were tested, the core web and column flange plates were cut open. The integrity of the core concrete in the panel zone of all specimens was good, and no horizontal or oblique cracks were visible on the surface, as shown in Fig. 12.

(a) Column flange side (b) Column web side

Fig. 12 Final status of core concrete

4. Test results and analysis

4.1. Hysteresis curve

The hysteresis curve can reflect many indexes of the seismic performance of the joint. By monitoring the displacement and load at the top of the column during the test, the load–displacement hysteresis curves of the three specimens were obtained, as shown in Fig. 13.

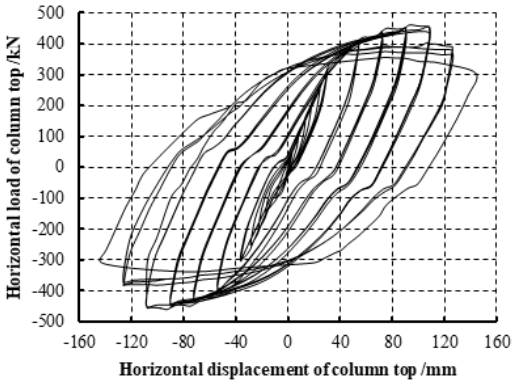

(a) Hysteresis curve of JD-1

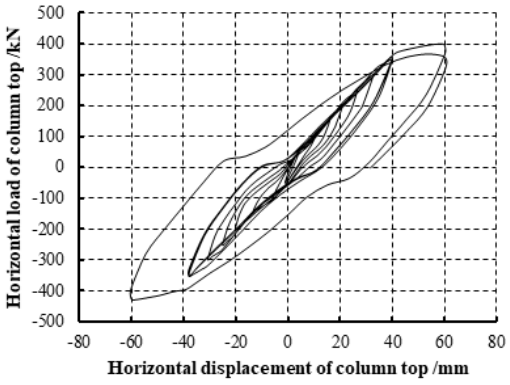

(b) Hysteresis curve of JD-2

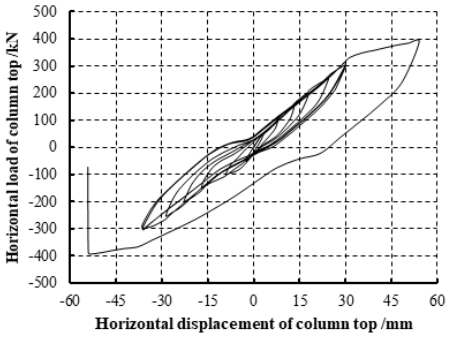

(c) Hysteresis curve of JD-3

Fig. 13 Cyclic lateral load versus lateral displacement hysteresis curves

1) Before the specimens enter the yield state, the area of all the hysteresis loops are small, and the shape of the hysteresis curve is a sharp shuttle. After the JD-1 specimen yields, the hysteresis loop area expands continuously with the increase of plastic deformation. The steel beam gradually enters plasticity to form a plastic hinge. Under ultimate load, the whole hysteresis loop is full and shuttle-shaped without any evident pinching phenomenon.

2) Compared with JD-1 and JD-3, the shape of the hysteresis curve of the JD-2 specimen in the elastic stage is similar to that of the JD-1 specimen, and it shows a sharp shuttle shape. In the first cycle of the displacement loading stage, cracks appeared in the weld between the side plate and column flange, resulting in a break in the hysteresis curve. The hysteresis curve of the JD-2 specimen reflects the joint configuration has less plastic deformation ability.

3) In the JD-1 and JD-3 specimens, the column web in the panel zone and the extended side plate are processed into one complete plate. The difference is that the length of extended side plate of JD-3 is 80% that of JD-1. The hysteresis curves of these specimens before yielding are coincident. During the first cycle of the displacement loading stage, the weld between the tensile flange at the end of the JD-3 test specimen and the extended side plate cracks, resulting in an interruption in the hysteresis curve without the formation of a closed hysteresis loop after yield.

4.2. Skeleton curve

Fig. 14 shows the horizontal load–displacement skeleton curves of the specimens at the top of the column. The "universal bending-yield method" was adopted to determine yield load P_y and yield displacement $\triangle_y$ [23]. The corresponding displacement when the skeleton curve load drops to 85% of peak load P_p is considered the ultimate displacement, $\triangle_u$ [26]. The story drift ratio θ_u is defined as the ratio of horizontal limit displacement $\triangle_u$ to the column height. During the loading process, the difference between the loads in the two directions, i.e., push and pull, is small. The displacement and load at the characteristic point were obtained from the average value of both loads. The displacements, loads, and story drift ratio at the characteristic points of the three specimens are shown in Table 3.

According to Fig. 14 and Table 3, the following results can be derived.

1) The growth of the skeleton curves of all joint specimens are similar at the early stage, and the slopes of the skeleton curves of all three specimens at this stage are very close; this shows that the extended length of the side plate have a small effect on the initial stiffness of the side plate joint.

2) The ultimate loads of the JD-2 and JD-3 specimens are larger than the yield loads of the JD-1 specimen; i.e., 91.3% and 96.4% of the ultimate loads of the JD-1 specimen, respectively. This indicates that the JD-2 and JD-3 specimens also enter the yield stage of the joints, while the strain-hardening potential of steel material is not effectively developed.

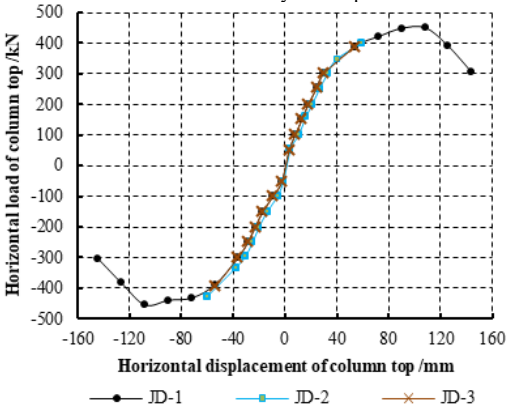

Fig. 14 Skeleton curves of specimens

Table 3
Main test results

Specimen number	P_y/kN	Δ_y/mm	P_p/kN	Δ_u/mm	θ_u/rad
JD-1	369.10	44.02	452.60	132.73	0.045
JD-2	/	/	413.19	59.71	0.020
JD-3	/	/	391.05	53.67	0.018

The JD-2 and JD-3 specimens reached their failure modes shortly after they entered plasticity, and the yield load could not be determined according to the universal bending yield method. The values of P_p, Δ_u, and θ_u were obtained from the end point data of the skeleton curve.

4.3. Shear and strain in the joint panel zone

To study the stress distribution in the joint panel zone, the strains at the center points of the column webs of the three test pieces were extracted. The strains of the JD-2 and JD-3 specimens were similar to the early stage of the JD-1 specimen. Fig. 15 shows the relation between the shear strain at the center point of the web in the panel zone and horizon load at the column top of the JD-1 specimen. The maximum strain value of the center point of the web was 2.32×10^{-3}, which did not reach the shear yield strain of the specimen web. The concrete in the joint panel zone of the specimen, as presented in Fig. 12, did not show cracks or crushing. This indicates that when the ultimate load of the specimen was reached, the panel zone was still in the elastic stage without shear failure, which is suitable for a ductile moment frame [24, 25].

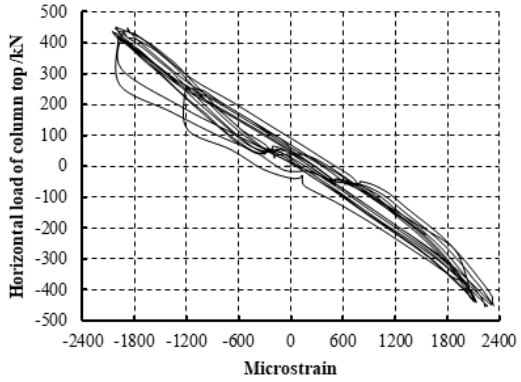

Fig. 15 Shear strain curve of JD-1 column web versus lateral load

The horizontal shear forces and shear deformation of the joint panel zone at the yield points of the JD-1 specimen calculated from equations (5) to (16) are presented in Table 4. Under the ultimate load, the maximum shear strain of the web was between γ_A and γ_B. This shows that the panel zone is at the second stage of the shearing model, as shown in Fig. 4. By substituting the shear strain of the web recorded by the strain gauge into equations (5) to (16) and by using Fig. 4, the maximum shear force value V_{n1} of the panel zone was found to be 2709 kN. Then, based on the principle of static equilibrium, the ultimate horizontal shear force V_{n2} of the panel zone was calculated as 2948 kN, by substituting the ultimate load of the column in the test into equations (2) to (4).

The maximum horizontal shear force V_{n1} in the joint panel zone obtained by equations (5) to (16) and Fig. 4 was 91.9% of V_{n2} by the principle of static equilibrium. This may be because equations (10a) to (10c) underestimate the shear contribution of core concrete in the specimen.

Table 4
Turning point parameters of the shear model in the panel zone

Specimen number	V_{cc1}/kN	V_{cc2}/kN	V_A/kN	γ_A (10^{-4})
JD-1	81 to 406	286	81.2 to 286	0.8 to 2.8
Specimen number	γ_B(10^{-4})	V_B/kN	γ_C(10^{-4})	V_C/kN
JD-1	27.2	2924 to 3129	204.5	2937 to 3142

4.4. Deformation capacity and energy-consumption performance

The AISC Seismic Provision [20] recommends that the story shift angle of the beam–column joints in the special moment frames should not be less than 0.04 rad. According to the data in Table 3, the story shift angle corresponding to the ultimate displacement of JD-1 is 0.045 rad, which exceeds the specified limit value.

In this study, the displacement ductility coefficient Δ_u/Δ_y was adopted as an important index to measure the deformation ability of the specimens [27]. The JD-2 and JD-3 specimens were damaged quickly and lost their ability to continue to bear load after they entered the plastic phase, thus showing the characteristics of brittle failure. According to the data in Table 5, the displacement ductility coefficients of the JD-1 specimen were 3.02 and 3.01 in two loading directions. This indicates that the reasonably designed side-plate joint specimen has preferable ductility.

The equivalent viscous damping coefficient, h_e, was adopted to evaluate the energy dissipation capacity of the joint specimen [28]. Fig. 16 shows the equivalent viscous damping coefficient curve of the JD-1 specimen. According to Fig. 16, the equivalent viscosity coefficient, h_e, gradually increases with the increase in the cyclic loading level. At the time of specimen failure, the h_e of the JD-1 specimen was 0.47, indicating that the specimen has a large energy-consumption capacity.

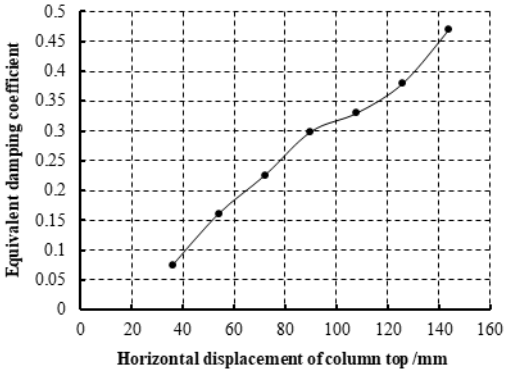

Fig. 16 Equivalent viscous damping coefficient

Table 5
Ductility factor of the JD-1 specimen

Specimen number	Loading direction	Yield displacement /mm	Ultimate displacement /mm	Ductility coefficient
JD-1	+	43.73	108.21	3.02
	−	44.32	108.13	3.01

4.5. Stiffness degradation

To further study the change pattern of the load–displacement curve of the side-plate joint, the peak stiffness K_i, calculated using equation (22), was adopted to analyze the stiffness degradation of the structure under the influence of cumulative damage. The degradation curve of the peak stiffness for each cycle stage of the JD-1 specimen is shown in Fig. 17, where the horizontal axis is the displacement of each cycle's loading stage, and the vertical axis represents K_i/K_0, where K_0 is the initial stiffness of the specimen. As shown in Fig. 17, the stiffness degradation of the JD-1 specimen is relatively uniform and gentle, and no obvious sharp drops are evident in the stiffness; this indicates that the energy-consumption capacity of the JD-1 specimen is relatively stable.

$$K_i = \frac{|-F_i| + |+F_i|}{|-X_i| + |+X_i|} \tag{22}$$

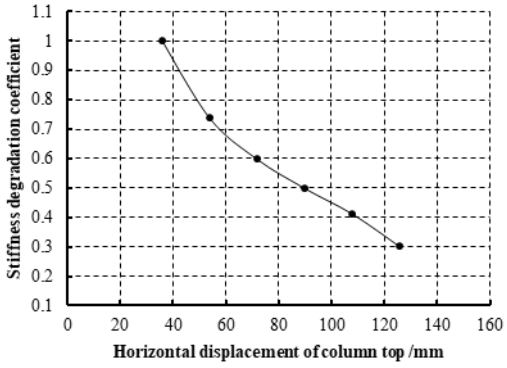

Fig. 17 Stiffness degradation coefficient

4.6. Verification of the ultimate bearing capacity calculation method

Table 6 lists the strength ratios and predicted failure modes of the three specimens according to the theoretical formulae in (18) to (21). A comparison among the test phenomena of the three specimens shows that the predicted failure modes agree well with those obtained in the tests, as shown in Table 6. In addition, when the bending moment at the end of the steel beam reached the full-section plastic moment, M_{bp}, the theoretical ultimate load of the three joints was calculated according to equation (2) as 457.42 kN. Table 7 shows the ultimate load of the three specimens. The ultimate load of the JD-1 specimen is very similar to its theoretical value, showing that the plastic hinge is formed at the beam end of the specimen. As shown, the theoretically calculated strength ratios in Table 6 are in good agreement with the ultimate load ratios obtained from three specimens listed in Table 7.

Table 6
Strength ratio of specimens and expected failure mode

Specimen number	$F_{\mathrm{I}} / F_{\mathrm{III}}$(%)	$F_{\mathrm{II}} / F_{\mathrm{III}}$(%)	Predicted failure mode
JD-1	110	121	Mode I
JD-2	110	88	Mode II
JD-3	85	121	Mode III

Table 7
Ultimate load index at the top of column

Specimen number	JD-1		JD-2		JD-3	
Loading direction	+	−	+	−	+	−
Ultimate load /kN	461.2	−460.6	429.0	−399.9	389.1	−393.0
Ratio (%)	100.8	100.7	93.8	87.4	85.1	85.9

The ratio is the ultimate load of the specimens divided by the theoretically calculated ultimate load.

5. Conclusions

This paper presented a new side-plate column–beam joint for WCFT columns. The force-transfer mechanism and failure mode of the joint were theoretically studied. Three full-scale joints were tested to demonstrate the reliability of the proposed design method for different failure modes. Additionally, the mechanical properties of the joints were experimentally analyzed. The following conclusions were obtained.

1) Based on the analysis of the deformation characteristics of the panel zone of the side-plate joint of the WCFT column, the shear mechanisms of the joint was simplified as a three-stage model, which could be used to describe the force–deformation relation of the panel zone under shear.

2) The paper proposes three failure modes for the side-plate joints by examining the transfer mechanism of the internal force at the beam end. Mode I failure occurs due to the plastic hinge at the beam end beyond the side plate; mode II indicates the flexure failure of the side plate that occurs at the column flange; and mode III is the horizontal weld failure that occurs between the beam flange and side plate. The corresponding formulas of these failure modes are derived in this paper.

3) Three full-scale specimens of the WCFT column side-plate joint were designed for experimental demonstration. The theoretical failure modes and the predicted ultimate load were found to be in good agreement with the test results.

4) In the JD-1 specimen, where failure mode I occurred, typical beam end plastic hinges were formed at the section located 0.8 to 1.0 times the beam height from the column flange. The panel zone was in the elastic stage, the displacement ductility coefficient was more than 3, the elastic–plastic story displacement shift angle was 0.045 rad, and the equivalent viscous damping coefficient was 0.47. Thus, the joint specimen with failure mode I showed good deformation ability and energy dissipation performance.

5) Moreover, the joint specimens with failure modes II and III failed under the first-stage cyclic displacement load after yielding. In addition, plastic deformation did not occur, and the cumulative area of the hysteresis loop was small. Thus, the specimens with failure modes II and III presented the characteristics of brittle failure. During the design process, it should be ensured that both F_I/F_{III} and F_{II}/F_{III} are greater than 100% to avoid the brittle failure of modes II and III, thereby forming a plastic hinge at the beam end.

6) Based on the comprehensive analysis of the failure modes, hysteresis curve, skeleton curve, deformation capacity, and energy dissipation capacity of the side plate joints, the innovative joint that is used to connect a WCFT column and steel beam can achieve an ideal seismic performance through reasonable design.

References

[1] Nakashima, M., Roeder C.W. and Maruoka. Y., “Steel Moment Frames for Earthquakes in United States and Japan”, Journal of Structural Engineering, 126(8), 861-868, 2000.
[2] Sherman, D.R., “Designing with Structural Tubing”, Engineering Journal, 33(3), 101-109, 1996.
[3] Mirghaderi, S.R., Torabian, S. and Keshavarzi, F., “I-beam to Box–column Connection by a Vertical Plate Passing through the Column”, Engineering Structures, 32(8), 2034-2048, 2010.
[4] GB 50936-2014 Technical Code for Concrete Filled Steel Tubular Structures, China Architecture & Building Press, Beijing, China, 2014. (in Chinese)
[5] Hao, J.P., Sun, X.L., Xue, Q. and Fan, C.L., “Research and Application of Fabricated Steel Structure Building System”, Engineering Mechanics, 34(1), 1-13, 2017. (in Chinese)
[6] Sun, X.L., Hao, J.P., Xue, Q., Fan, C.L., Liu, H. and He, M.N., “Experimental Study on Seismic Behavior of Walled Concrete-filled Steel Tubular Columns”, Journal of Building Structures, 39(6), pp. 92-101, 2018. (in Chinese)
[7] Sasaki, S., Teraoka, M. and Fujiwara, T., “Structural Behavior of Concrete-filled Square Column with Partial-penetration Weld corner Seam to Steel H-beam Connections”, Pergamon Press, Singapore, 2, 33-40, 1995.
[8] Shim, J.S., Han, D.J. and Kim, K.S., “An Experimental Study on the Structural Behaviors of H-shaped Steel Beam-to-concrete Filled Steel Square Tubular Column Connections”, Pergamon Press, Singapore, 2, 41-48, 1995.
[9] Lu, X.L., Yu, Y., Kiyoshi, T. and Satoshi, S., “Experimental Study on the Seismic Behavior in the Connection Between CFRT Column and Steel Beam”, Structural Engineering and Mechanics, 9(4), 365-374, 2000.
[10] Cheng, C.T. and Chung, L.L., “Seismic Performance of Steel Beams to Concrete-filled Steel Tubular Column Connections”, Journal of Constructional Steel Research, 59(3), 405-426, 2003.
[11] Fukumoto, T. and Morita, K., “Elasto-plastic Behavior of Panel Zone in Steel Beam-to-concrete Filled Steel Tube Column Moment Connections”, Journal of Structural Engineering, 131(12), 1841-1853, 2005.
[12] Furlong, R.W., “Design of Steel-encased Concrete Beam-column”, Journal of Structural Division, 94(ST1), 267-281, 1968.
[13] Park, R. and Paulay, T., “Reinforced Concrete Structures”, Chongqing University Press, Chongqing, China, 1985. (in Chinese))
[14] Paulay, T. and Priestley, M.J.N., “Seismic Design of Reinforced Concrete and Masonry Buildings”, China Architecture & Building Press, Beijing, China, 1999. (in Chinese)
[15] Morishita, Y., Tomii, M. and Yoshimura, K., “Experimental Studies on Bond Strength in Concrete Filled Square and Octagonal Steel Tubular Columns Subjected to Axial Loads”, Transactions of Japan Concrete Institute, 1, 359-366, 1979.
[16] Morishita, Y., Tomii, M., “Experimental Studies on Bond Strength between Square Steel Tube and Encased Concrete Core under Cyclic Shearing Force and Constant Axial Force”, Transactions of Japan Concrete Institute, 4, 363-370, 1982.
[17] Xu, L.H., Fan, H. and Li, Q.S., “Experimental Studies on Seismic Behavior of Connection between Concrete-filled Steel Square Tubular Column and Steel Beam”, Engineering Mechanics, 25(2), 122-131, 2008. (in Chinese)
[18] Zhong, T., T.Y. Song, Brian Uy. and Han, L.H., “Bond Behavior in Concrete-filled Steel Tubes”, Journal of Constructional Steel Research, 120, 81-93, 2016.
[19] Xiao, C.Z., Cai, S.H. and Xu C.L., “Experimental Study on Shear Performance of Concrete Filled Steel Tube Columns”, China Civil Engineering Journal, 4, 5-11, 2005. (in Chinese)
[20] ANSI/AISC 341-16 Seismic Provisions for Structural Steel Buildings, American Institute of Steel Construction, Chicago (IL), 2016.
[21] Zia, P. “Torsional strength of prestressed concrete members”, Journal Proceedings, 57(4), 1337-1360, 1961.
[22] JGJ101—96 Specification of Testing Methods for Earthquake Resistant building, China Architecture & Building Press, Beijing, China, 1997. (in Chinese)
[23] Wang, W.D., Han, L.H., Uy B., “Experimental Behaviour of Steel Reduced Beam Section to Concrete-filled Circular Hollow Section Column Connections”, Journal of Constructional Steel Research, 64(5), 493-504, 2008.
[24] FEMA-355D State of the Art Report on Connection Performance, Federal Emergency Management Agency, Washington (DC), 2000.
[25] Roeder, C.W., “General Issues Influencing Connection Performance”, Journal of Structural Engineering, 128(4), 420-428, 2002.
[26] Chen, J., Chan, T.M., Su, R.K.L. and Castro, J.M., “Experimental Assessment of the Cyclic Behaviour of Concrete-filled Steel Tubular Beam-columns with Octagonal Sections”, Engineering Structures, 180, 544-560, 2019.
[27] EN 12390-3:2009 Testing Hardened Concrete. Part 3: Compressive Strength of Test Specimens, CEN (European Committee for Standardization), 2009.
[28] Wang, Y.H., Lu, G.B. and Zhou, X. H., “Experimental Study of the Cyclic Behavior of Concrete-filled Double Skin Steel Tube Columns Subjected to Pure Torsion”, Thin-Walled Structures, 122, 425-438, 2018.

Advanced Steel Construction – Vol. 16 No. 4 (2020) 354–362
DOI:10.18057/IJASC.2020.16.4.8

SECOND-ORDER ANALYSIS OF STEEL SHEET PILES BY PILE ELEMENT CONSIDERING NONLINEAR SOIL-STRUCTURE INTERACTIONS

Wei-Hang Ouyang [1], Yi Yang [2, *], Jian-Hong Wan [1] and Si-Wei Liu [3]

[1]*School of Civil Engineering, Sun Yat-Sen University, Zhuhai, P.R. China*
[2] *Department of Civil Engineering, Chu Hai College of Higher Education, Hong Kong, China*
[3]*Department of Civil and Environmental Engineering, The Hong Kong Polytechnic University, Hong Kong, China*
** (Corresponding author: E-mail: yyang@chuhai.edu.hk)*

ABSTRACT

Comparing to other supporting pile walls, steel sheet piles with a lower flexural rigidity have a more obvious and significant second-order effect with the large deformation. Also, the nonlinear Soil-Structure Interaction (SSI) can highly influence the efficiency and accuracy of the deformation and buckling of the steel sheet pile. Currently, some empirical methods with linear assumptions and the discrete spring element method are always used for the design of steel sheet piles in practical engineering. However, these methods are normally inaccurate or inefficient in considering the nonlinear SSI and the second-order effect. In this paper, a new line element, named pile element, is applied to analyze the structural behaviors of the steel sheet pile. In this new element, the soil resistance and pressure surrounding the pile as well as the pile shaft resistance are all integrated into the element formulation to simulate the nonlinear SSI. The Gauss-Legendre method is innovatively introduced to elaborate the realistic soil pressure distribution. For reducing the nonlinear iterations and numerical errors from the buckling behavior, the proposed numerical method and Updated-Lagrangian method will be integrated within a Newton-Raphson typed approach. Finally, several examples are given for validating the accuracy and efficiency of the developed pile element with the consideration of the realistic soil pressures. It can be found that the developed pile element has a significant advantage in simulating steel sheet piles.

ARTICLE HISTORY

Received: 27 October 2020
Revised: 11 November 2020
Accepted: 12 November 2020

KEYWORDS

Steel sheet pile;
Finite element method;
Soil-structure interactions;
Lateral earth pressure;
Pile deflection;
Second-order effect

1. Introduction

Steel sheet piles are widely used to support the excavation in urban areas. Many single sheet piles through interlocks to generate steel sheet pile wall as shown in Fig.1 (a). Normally, the installation method for the steel sheet pile is vibratory driving, which is a straightforward technique and usually used in the supporting projects [1, 2]. Comparing with the installation of the steel sheet pile, however, its design is much more difficult.

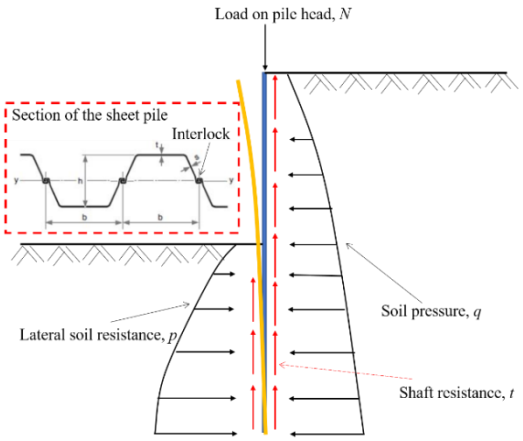

(a) Schematic of the steel sheet pile

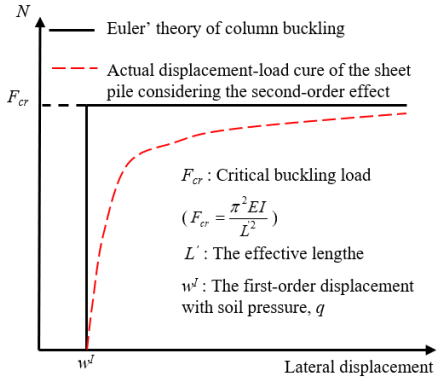

(b) Displacement-load curve of the steel sheet pile

Fig. 1 Design framework of the steel sheet pile

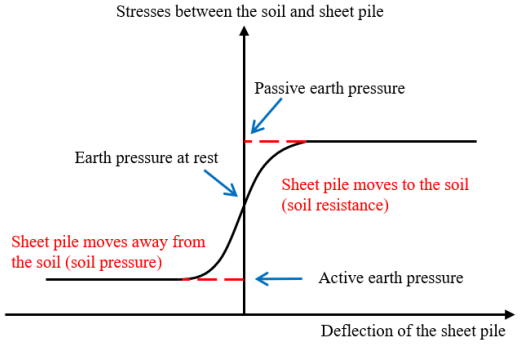

(a) The relationship between the earth pressure and the lateral deflection of the sheet pile

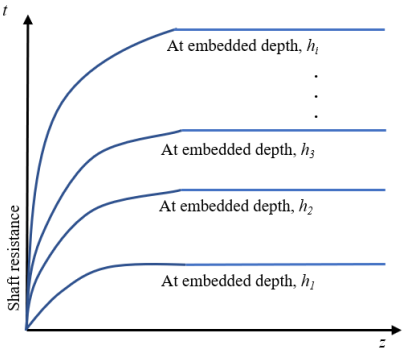

(b) The relationship between the shaft resistance and the vertical deflection of the sheet pile

Fig. 2 The Soil-Structure Interaction (SSI) relationships of the sheet pile

Steel sheet pile can be easily transported and installed. However, its bearing capacity is lower than other supporting types. As a flexible supporting structure, the ultimate capacity of the steel sheet pile cross-section and maximum deformation should be carefully considered in the design procedure [3]. Also, its second-order effect is significant because of the large deformation.(Fig.1 (b)) [4, 5]. Thus, how to accurately describe the buckling behavior of steel sheet piles is really important.[6]. Comparing to the complicity of the structural behavior, the highly nonlinear Soil-Structure Interaction (SSI) [7-9] in steel sheet pile is also essential for the steel pile deformation and much more complicated. As the lateral pressure and resistance (as shown in Fig.2 (a)) can highly influence the structural behaviors of steel sheet piles [10, 11],

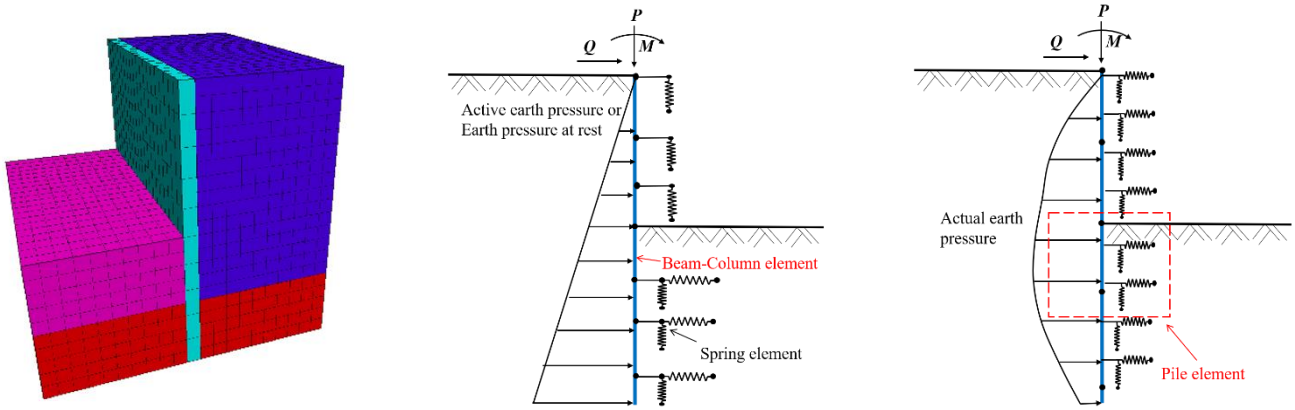

(a) Three-dimension solid (b) Discrete spring element (c) Pile element

Fig. 3 Different finite element models for the sheet pile

different researches have been carried out [12-17]. Rankine and Coulomb theories are two most common theories in the study of retaining walls [12]. Many researchers have developed these two classical theories to consider other factors [13, 14]. Although these lateral earth-pressure theories have clear physical meanings and are easy to be applied, their shortcomings are obvious, where soil pressure, especially the passive pressure in front of the steel sheet pile, is only mobilized on a large displacement. In practical projects, the allowed displacement is normally smaller than the limit deformation in classical theories, where the lateral pressure distribution is nonlinear [15, 16]. For this reason, Duncan et al. [17] introduced the initial soil stiffness and other parameters into the hyperbolic relationship and built the relationship between the soil resistances in front of the pile (p) and the lateral pile deflection (y) for considering the resistance-deflection behavior. Additionally, the SSI also includes the relationship between pile shaft resistance (t) and its vertical displacement (z) [18](as shown in Fig.2 (b)), which should also be properly measured into the design of the steel sheet pile, especially considering its second-order effect.

For accurately describing the SSI and second-order effect, finite difference and finite element method are usually considered. In the finite difference method, the nonlinear SSI cannot be accurately captured [19]. Hence, the finite element with the capacity of simulating an accurate and nonlinear SSI is usually selected for solving steel sheet pile problems. In the finite element method, there are two main approaches: one is used three-dimension solid element [20] (Fig. 3 (a)); the other one is used the discrete spring element [21] (Fig. 3 (b)). The three-dimension solid element method can be directly used to build a realistic model of steel sheet pile wall and surrounding soils, where the realistic SSI can be considered. However, the modeling procedure is rather complicated and time-consuming. These factors restrain the three-dimension solid element method mainly in the research area. Thus, the most common finite element model used in practical engineering is the discrete spring element method based on the Winkler foundation beam method. In the discrete spring element method, the complicated structural behaviors of the sheet pile wall can be described by a large number of elements which will decline the efficiency of design. Another shortcoming is that the lateral pressure behind the steel sheet pile is assumed as constantly active or at rest, which is different with reality. Although the increase in the number of elements can solve the complex mechanical behavior of the steel sheet pile, the numerical modeling procedure and calculation will be much more complicated and time-consuming.

In practical engineering, many empirical with linear assumptions are widely introduced to describe the structural behaviors of the steel sheet pile with only considering a constant soil stiffness [22]. Besides, the effective length method based on Euler's theory of column buckling (Fig.1 (b)), which identifies the buckling behavior of steel sheet pile by different safety factors under different boundary conditions, is still the most common solution, like Eurocode 3 [23]. However, these simplifications cannot accurately consider the nonlinear SSI and the second-order effect of steel sheet piles to evaluate their complicated structural behaviors.

To overcome these limitations in numerical and practical design methods, recently, Liu et al. [24] proposed a new line element based on Euler-Bernoulli beam-column theory, named pile element, as shown in Fig. 3 (c). This new proposed pile element has a high computational efficiency, where the soil response is directly incorporated into the beam element. This pile element is not required to consider the soil spring elements and can accurately evaluate the nonlinear SSI. Li et al. [25] extended this pile element to study the pile with nonlinearly varying soil stiffness under different boundary conditions with reasonable results. In the present paper, the pile element will be developed to directly include soil springs in front of the pile in the analysis of steel sheet piles. Meanwhile, the realistic distribution of soil pressure behind the pile can be considered and evaluated.

In this paper, the detailed derivation of the developed pile element can be seen in the second part. Then, the selected lateral and axial shape functions will be introduced to derive the total potential energy formula. Using the Gauss-Legendre method, p-y, t-z relationships, and the soil pressure behind the pile can be directly described. A semi-analytical solution of the stiffness matrix and secant relations will be obtained and incorporated with the Newton-Raphson incremental-iterative numerical procedure through the variation of the total potential energy, where the computational errors of the nonlinear iteration and large deformation can be eliminated. Finally, three benchmark examples are present to verify the accuracy and efficiency of the developed pile element. Comparison studies include the analytical method and the discrete spring method. In addition, the lateral pressure on the behind of the pile is explored to consider the active, at rest, and realistic distributions.

2. Assumptions in pile element formulation

The assumptions in the pile element formulation are made in here:
a. warping and shear deformations will be ignored;
b. loads on the element are conservative;
c. the material of the pile is isotropic, homogeneous and linear elastic, which means Hooke's material law [26] can be introduced;
d. the Euler-Bernoulli assumption is introduced in element formulation;
e. strains are small, meanwhile, displacement can be moderately large.

3. Pile element formulations

3.1. Shape functions of pile-element

For describing the deformation along the element, the axial and lateral deflection of the element are given as:

$$u(x)=(-\frac{x}{L}+1)u_1+\frac{x}{L}u_2 \tag{1}$$

$$\begin{aligned} v(x)=&[2(\frac{x}{L})^3-3(\frac{x}{L})^2+1]v_1+[-(\frac{x}{L})^2-2\frac{x}{L}+1]x\theta_1 \\ &+[-2(\frac{x}{L})^3+3(\frac{x}{L})^2]v_2+[(\frac{x}{L})^2-\frac{x}{L}]x\theta_2 \end{aligned} \tag{2}$$

where u and v are the value of the axial and the lateral deflections along the element, respectively; and u_1, u_2, v_1, v_2, θ_1 and θ_2 are the displacement at two different sides of the element, which are all plotted in Fig. 4.

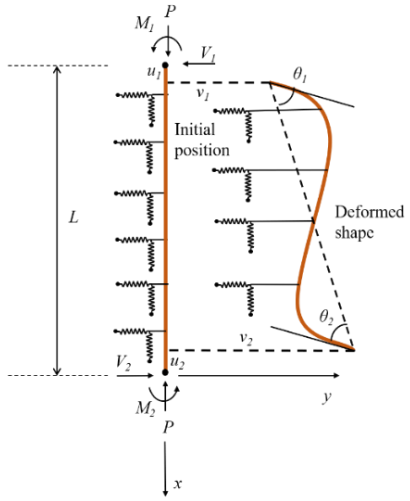

Fig. 4 Element forces and displacements

3.2. Total energy function of the element

To getting the tangent stiffness matrix and the secant relations of the element, the total energy of the element, Π, is given as:

$$\Pi = U_E + U_S + W_P + W_S \tag{3}$$

where U_E and U_s are the energy accumulating in the pile and the surrounding medium, respectively; W_P and W_s are the work done by the force at the nodes of the elements and the distributed soil pressure behind the steel sheet pile, respectively.

The strain energy of the pile can be given as:

$$U_E = \frac{1}{2}\int_V (\sigma_x \varepsilon_x + \tau_{xy}\varepsilon_{xy})dV \tag{4}$$

By introducing Green-Lagrangian strain theory and Hooke's material law [26] into Eq.4 when ignoring the high order terms, U_E can be rewritten as:

$$\begin{aligned} U_E = {} & \frac{1}{2}\int_0^L [EA(\frac{\partial u(x)}{\partial x})^2 + EA(\frac{\partial v^2(x)}{\partial x^2})^2]dx \\ & + \frac{1}{2}\int_0^L P(\frac{\partial v(x)}{\partial x})^2 dx - \int_0^L \frac{V}{A}(\frac{\partial u(x)}{\partial x}\frac{\partial v(x)}{\partial x})dv \end{aligned} \tag{5}$$

The energy absorbed by soil can be separated into two parts, which are:

$$U_S = U_{SP} + U_{S\tau} \tag{6}$$

where U_{SP} and $U_{S\tau}$ are the energy consumed by the lateral soil resistance and shaft resistance, respectively. And their expression can be given as:

$$U_{SP} = \int_0^L \int_0^v p(v)dvdx \tag{7}$$

$$U_{S\tau} = \int_0^L \int_0^u t(u)dudx \tag{8}$$

where p and t are the lateral and shaft resistance per unit along the element, which can be given according to p-y and t-z curve, respectively. However, due to the complex expression of p-y and t-z curve of the sheet pile, the analytical solutions of the Eqs.7 ~ 8 are difficult to be given. For this reason, the Gauss-Legendre method is adopted for simplified the expressions of U_{SP} and $U_{S\tau}$. Thus, the energy absorbed by soil can be rewritten as:

$$U_{SP} \approx \frac{1}{2}\sum_{i=1}^{n} H_i k_p(v_i) v_i^2 \tag{9}$$

$$U_{S\tau} \approx \frac{1}{2}\sum_{i=1}^{n} H_i k_t(u_i) u_i^2 \tag{10}$$

where $k_p(v)$ and $k_t(u)$ are the tangential values of p-y and t-z curve at some specified deflections; n is number of Gaussian points, respectively; v_i and u_i are the lateral and axial deflection at the i^{th} Gaussian point, respectively; H_i is weight of the i^{th} Gaussian point.

The work done by the force at the nodes of the element can be written as:

$$W_P = Pu_1 + M_1\theta_1 + V_1 v_1 - Pu_2 + M_2\theta_2 + V_2 v_2 \tag{11}$$

And the work done by the distributed soil pressure can be given as:

$$W_S = \int_0^L \int_0^v q(v)dvdx \tag{12}$$

where q is the lateral pressure per unit along the element, which is varied with x and v. Similarly, using the Gauss-Legendre method, W_S can be simplified as:

$$W_S \approx \frac{1}{2}\sum_{i=1}^{n} H_i k_q(v_i) v_i^2 \tag{13}$$

where $k_q(v)$ is the tangential value of the function of soil pressure.

3.3. Tangent stiffness matrix of the element

For describing the deformation process of the element, the tangent stiffness matrix is given by using the second-order variation of the total energy function, Π:

$$\delta\Pi = \frac{\partial^2 \Pi_i}{\partial u_i \partial u_j}\delta u_i \delta u_j \tag{14}$$

Thus, the stiffness matrix of the element can be divided into four parts as:

$$[k]_E = [k]_L + [k]_G + [k]_{SR} + [k]_{Sq} \tag{15}$$

where $[k]_E$ is the tangent stiffness matrix of the whole pile element; $[k]_L$ is the linear stiffness matrix; $[k]_G$ is the geometric stiffness matrix; $[k]_{SR}$ is the soil resistance stiffness matrix; and $[k]_{Sq}$ is the soil pressure stiffness matrix.

The linear stiffness matrix, $[k]_E$, can be written as:

$$[k]_L = \begin{bmatrix} \frac{EA}{L} & 0 & 0 & -\frac{EA}{L} & 0 & 0 \\ 0 & 12\frac{i}{L^2} & 6\frac{i}{L} & 0 & -12\frac{i}{L^2} & 6\frac{i}{L} \\ 0 & 6\frac{i}{L} & 4i & 0 & -6\frac{i}{L} & 2i \\ -\frac{EA}{L} & 0 & 0 & \frac{EA}{L} & 0 & 0 \\ 0 & -12\frac{i}{L^2} & 6\frac{i}{L} & 0 & 12\frac{i}{L^2} & -6\frac{i}{L} \\ 0 & -6\frac{i}{L} & 2i & 0 & -6\frac{i}{L} & 4i \end{bmatrix} \tag{16}$$

Where

$$i = \frac{EI}{L} \tag{17}$$

The geometric stiffness matrix, $[k]_G$, can be written as:

Table 1
Coefficients A_{ji} and B_{ji} in the stiffness matrix

Gaussian points	1	2	3	4	5	6	7	8	9
Location	0.01592	0.08198	0.19331	0.33787	0.50000	0.66213	0.80669	0.91802	0.98408
A_{1i}	0.03935	0.07612	0.08480	0.06847	0.04128	0.01783	0.00487	0.00061	0.00001
A_{2i}	0.00064	0.00680	0.02032	0.03494	0.04128	0.03494	0.02032	0.00680	0.00064
A_{3i}	0.00001	0.00061	0.00487	0.01783	0.04128	0.06847	0.08480	0.07612	0.03935
B_{1i}	0.04058	0.08691	0.10610	0.08429	0.04128	0.01099	0.00124	0.00003	0.00000
B_{2i}	0.00063	0.00602	0.01309	0.00814	-0.01032	-0.02093	-0.01298	-0.00265	-0.00006
B_{3i}	0.00003	0.00169	0.01148	0.03044	0.04128	0.03044	0.01148	0.00169	0.00003
B_{4i}	0.00001	0.00064	0.00524	0.01752	0.03096	0.03020	0.01496	0.00278	0.00006
B_{5i}	0.00001	0.00042	0.00162	0.00079	0.00258	0.03983	0.13550	0.21453	0.14759
B_{6i}	0.00000	0.00012	0.00142	0.00294	-0.01032	-0.05794	-0.11990	-0.13655	-0.07739
B_{7i}	0.00000	0.00004	0.00065	0.00169	-0.00774	-0.05747	-0.15622	-0.22501	-0.14880
B_{8i}	0.00000	0.00000	0.00000	0.00000	0.00000	0.00025	0.00239	0.00416	0.00089
B_{9i}	0.00000	0.00001	0.00057	0.00633	0.03096	0.08361	0.13824	0.14322	0.07802
B_{10i}	0.00000	0.00000	0.00026	0.00364	0.02322	0.08293	0.18011	0.23600	0.15003

$$[k]_G=\begin{bmatrix} \frac{P}{L} & -\frac{M_1+M_2}{L^2} & 0 & -\frac{P}{L} & \frac{M_1+M_2}{L^2} & 0 \\ -\frac{M_1+M_2}{L^2} & \frac{6P}{5L} & \frac{P}{10} & \frac{M_1+M_2}{L^2} & -\frac{6P}{5L} & \frac{P}{10} \\ 0 & \frac{P}{10} & \frac{2PL}{15} & 0 & -\frac{P}{10} & -\frac{PL}{30} \\ -\frac{P}{L} & \frac{M_1+M_2}{L^2} & 0 & \frac{P}{L} & -\frac{M_1+M_2}{L^2} & 0 \\ \frac{M_1+M_2}{L^2} & -\frac{6P}{5L} & -\frac{P}{10} & -\frac{M_1+M_2}{L^2} & \frac{6P}{5L} & -\frac{P}{10} \\ 0 & \frac{P}{10} & -\frac{PL}{30} & 0 & -\frac{P}{10} & \frac{2PL}{15} \end{bmatrix} \tag{18}$$

The soil resistance stiffness matrix, $[k]_{SR}$, can be written as:

$$[k]_{SR}=\begin{bmatrix} \sum_{i=1}^{n}A_{1i}k_{ti}L & 0 & 0 & \sum_{i=1}^{n}A_{2i}k_{ti}L & 0 & 0 \\ 0 & \sum_{i=1}^{n}B_{1i}k_{pi}L & \sum_{i=1}^{n}B_{2i}k_{pi}L^2 & 0 & \sum_{i=1}^{n}B_{3i}k_{pi}L & \sum_{i=1}^{n}B_{4i}k_{pi}L^2 \\ 0 & \sum_{i=1}^{n}B_{2i}k_{pi}L^2 & \sum_{i=1}^{n}B_{5i}k_{pi}L^3 & 0 & \sum_{i=1}^{n}B_{6i}k_{pi}L^2 & \sum_{i=1}^{n}B_{7i}k_{pi}L^3 \\ \sum_{i=1}^{n}A_{2i}k_{ti}L & 0 & 0 & \sum_{i=1}^{n}A_{3i}k_{ti}L & 0 & 0 \\ 0 & \sum_{i=1}^{n}B_{3i}k_{pi}L & \sum_{i=1}^{n}B_{6i}k_{pi}L^2 & 0 & \sum_{i=1}^{n}B_{8i}k_{pi}L & \sum_{i=1}^{n}B_{9i}k_{pi}L^2 \\ 0 & \sum_{i=1}^{n}B_{4i}k_{pi}L^2 & \sum_{i=1}^{n}B_{7i}k_{pi}L^3 & 0 & \sum_{i=1}^{n}B_{9i}k_{pi}L^2 & \sum_{i=1}^{n}B_{10i}k_{pi}L^3 \end{bmatrix} \tag{19}$$

where k_{ti} and k_{pi} denote $k_p(v_i)$ and $k_t(u_i)$, respectively; and A_{ji} and B_{ji} are the corresponding coefficients, which are given in Table 1.

Accordingly, the soil pressure stiffness matrix, $[k]_{Sq}$, can be given as:

$$[k]_{Sq}=\begin{bmatrix} 0 & 0 & 0 & 0 & 0 & 0 \\ 0 & \sum_{i=1}^{n}B_{1i}k_{qi}L & \sum_{i=1}^{n}B_{2i}k_{qi}L^2 & 0 & \sum_{i=1}^{n}B_{3i}k_{qi}L & \sum_{i=1}^{n}B_{4i}k_{qi}L^2 \\ 0 & \sum_{i=1}^{n}B_{2i}k_{qi}L^2 & \sum_{i=1}^{n}B_{5i}k_{qi}L^3 & 0 & \sum_{i=1}^{n}B_{6i}k_{qi}L^2 & \sum_{i=1}^{n}B_{7i}k_{qi}L^3 \\ 0 & 0 & 0 & 0 & 0 & 0 \\ 0 & \sum_{i=1}^{n}B_{3i}k_{qi}L & \sum_{i=1}^{n}B_{6i}k_{qi}L^2 & 0 & \sum_{i=1}^{n}B_{8i}k_{qi}L & \sum_{i=1}^{n}B_{9i}k_{qi}L^2 \\ 0 & \sum_{i=1}^{n}B_{4i}k_{qi}L^2 & \sum_{i=1}^{n}B_{7i}k_{qi}L^3 & 0 & \sum_{i=1}^{n}B_{9i}k_{qi}L^2 & \sum_{i=1}^{n}B_{10i}k_{qi}L^3 \end{bmatrix} \tag{20}$$

where k_{qi} denotes $k_q(v_i)$.

3.4. Secant relations of the element

For eliminating the error accumulating in the iterative procedure, the secant relations of the element are elicited by the minimum potential energy method as:

$$\frac{\partial \Pi}{\partial u_i}=0 \tag{21}$$

And the resisting force on the element can be divided into two parts: the force from the element deformation and the SSIs of the sheet pile. Thus, the total resisting force vector, $\{F_T\}$, can be expressed as:

$$\{F_T\}=\begin{Bmatrix} F_{Ex1} \\ F_{Ey1} \\ M_{E1} \\ F_{Ex2} \\ F_{Ey2} \\ M_{E2} \end{Bmatrix}+\begin{Bmatrix} F_{Sx1} \\ F_{Sy1} \\ M_{S1} \\ F_{Sx2} \\ F_{Sy2} \\ M_{S2} \end{Bmatrix} \tag{22}$$

where F_{x1} and F_{x2} are the forces along the *x*-axis at the two sides of the pile element; F_{y1} and F_{y2} are the forces along the *y*-axis at the two sides of the pile element; M_1 and M_2 are the bending moments at the two sides of the pile element; and the subscripts $_E$ and $_S$ denote the resisting forces from the element deformation and the SSIs relationships.

The first part of $\{F_T\}$ can be given as:

$$F_{Ex1}=\frac{EA}{L}(u_1-u_2)+\frac{(M_{1E}+M_{2E})}{L^2}(-v_1+v_2) \tag{23}$$

$$F_{Ex2}=\frac{EA}{L}(-u_1+u_2)+\frac{(M_{1E}+M_{2E})}{L^2}(v_1-v_2) \tag{24}$$

$$F_{Ey1}=\frac{(M_{1E}+M_{2E})}{L^2}(-u_1+u_2)+\frac{12EI}{L^3}(v_1-v_2)+\frac{6EI}{L^2}(\theta_1+\theta_2)+\frac{6P}{5L}(v_1-v_2)+\frac{P}{10}(\theta_1-\theta_2) \tag{25}$$

$$F_{Ey2}=\frac{(M_{1E}+M_{2E})}{L^2}(u_1-u_2)+\frac{12EI}{L^3}(-v_1+v_2)+\frac{6EI}{L^2}(-\theta_1-\theta_2)+\frac{6P}{5L}(-v_1+v_2)+\frac{P}{10}(-\theta_1-\theta_2) \tag{26}$$

$$M_{E1}=\frac{6EI}{L^2}(v_1-v_2)+\frac{2EI}{L}(2\theta_1+\theta_2)+\frac{P}{10}(v_1-v_2)+\frac{LP}{30}(4\theta_1-\theta_2) \tag{27}$$

$$M_{E2}=\frac{6EI}{L^2}(v_1-v_2)+\frac{2EI}{L}(\theta_1+2\theta_2)+\frac{P}{10}(v_1-v_2)+\frac{LP}{30}(-\theta_1+4\theta_2) \tag{28}$$

Table 2
Coefficients C_{ji}, D_{ji} and O_{ji} in the secant relations

Gaussian points	1	2	3	4	5	6	7	8	9
Location	0.01592	0.08198	0.19331	0.33787	0.50000	0.66213	0.80669	0.91802	0.98408
C_{1i}	0.03999	0.08292	0.10512	0.10341	0.08256	0.05277	0.02519	0.00741	0.00065
C_{2i}	0.00065	0.00741	0.02519	0.05277	0.08256	0.10341	0.10512	0.08292	0.03999
D_{1i}	0.04061	0.08860	0.11758	0.11474	0.08256	0.04144	0.01273	0.00172	0.00003
D_{2i}	0.00003	0.00172	0.01273	0.04144	0.08256	0.11474	0.11758	0.08860	0.04061
O_{1i}	0.00063	0.00624	0.01639	0.02313	0.02064	0.01180	0.00393	0.00056	0.00001
O_{2i}	0.00001	0.00056	0.00393	0.01180	0.02064	0.02313	0.01639	0.00624	0.00063

By using the Gauss-Legendre method, the second parts of $\{F_T\}$ can be simplified and written as:

$$F_{sx1} = \int_L \left(1-\frac{x}{L}\right) t(x)\,dx \approx L\sum_{i=1}^{n} C_{1i}\, t(x_i) \tag{29}$$

$$F_{Sx2} = \int_L \frac{x}{L} t(x)\,dx \approx L\sum_{i=1}^{n} C_{2i}\, t(x_i) \tag{30}$$

$$F_{S1y} = \int_0^L \left(\frac{3x}{L}+\frac{L-x}{L}\right)\left(1-\frac{x}{L}\right)^2 [p(x)+q(x)]dx \approx L\sum_{i=1}^{n} D_{1i}[p(x_i)+q(x_i)] \tag{31}$$

$$F_{S2y} = -\int_0^L \left[\frac{x}{L}+\frac{3(L-x)}{L}\right]\left(\frac{x}{L}\right)^2 [p(x)+q(x)]dx \approx -L\sum_{i=1}^{n} D_{2i}[p(x_i)+q(x_i)] \tag{32}$$

$$M_{S1} = \int_0^L x\left(1-\frac{x}{L}\right)^2 [p(x)+q(x)]dx \approx L^2\sum_{i=1}^{n} O_{1i}[p(x_i)+q(x_i)] \tag{33}$$

$$M_{S2} = -\int_0^L \frac{x^2}{L^2}(L-x)[p(x)+q(x)]dx \approx -L^2\sum_{i=1}^{n} O_{2i}[p(x_i)+q(x_i)] \tag{34}$$

where C_{ji}, D_{ji} and O_{ji} are the corresponding coefficients which are all given in Table 2.

4. Newton-raphson typed numercial procedure for pile element

For describing the large deformation process,[27], Updated- Lagrangian (UL) method [28, 29] have been adopted in the numerical procedure. By using UL method, the equilibrium condition can be established according to the last-known element location in the iterative procedure (as shown in Fig. 5).

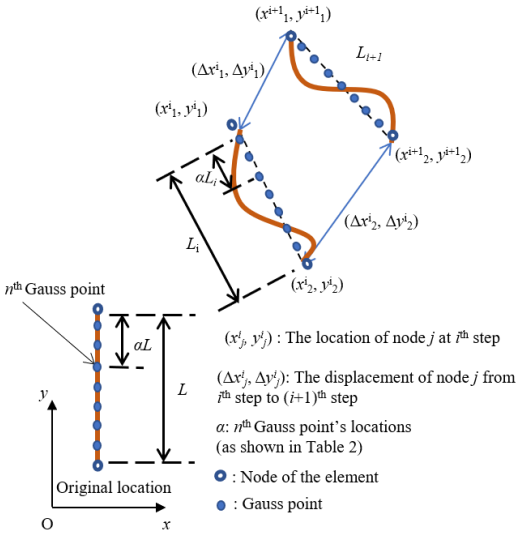

Fig. 5 Schematic of Updated- Lagrangian method for pile element

Therefore, the element stiffness matrix can be converted accordingly before assembling it into the global stiffness matrix, [k], which can be given as:

$$[k] = \sum_{i=1}^{N} [\gamma]_i [k]_E [\gamma]_i^T \tag{35}$$

where $[\gamma]_i$ is the transformation matrix for describing the initial position of the pile element during the i^{th} step; and N is the total number of the pile elements.

For eliminating the error accumulating in the nonlinear calculation, a new incremental-iterative procedure is proposed based on Newton-Raphson procedure [30] to integrated UL method and element formulation. And the flowchart is plotted in Fig. 6. Also the displacements and unbalanced forces are selected as the converge criterion in this paper to obtain an accurate result. Meanwhile, UL method and Newton-Raphson incremental-iterative procedure have been widely adopted in structural analysis and their robustness have been proven [24, 31-33].

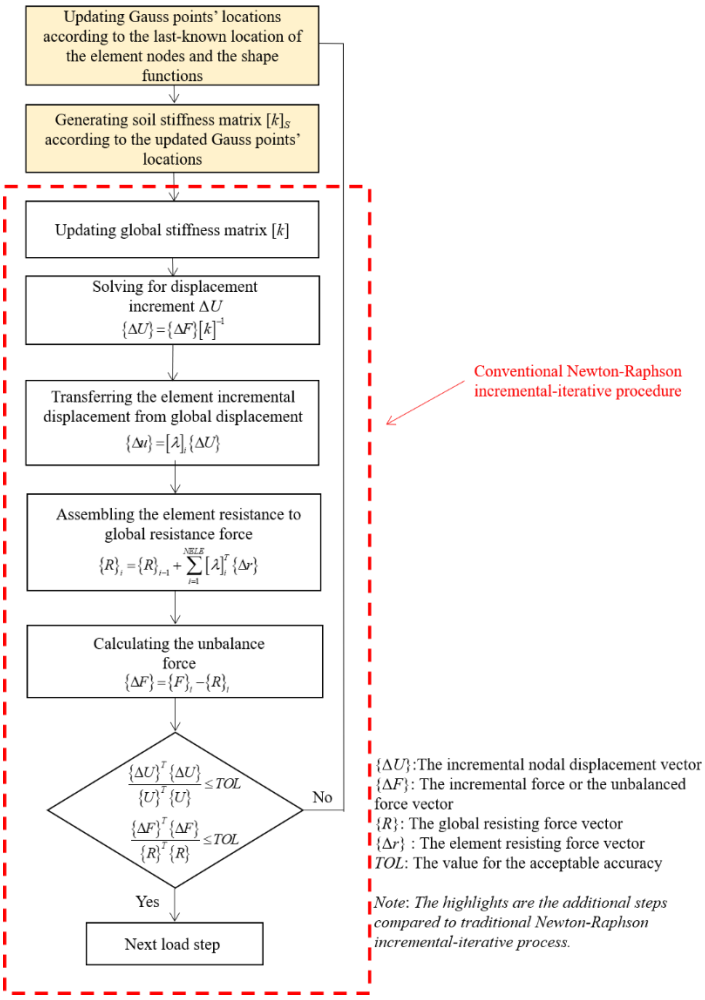

Fig. 6 Flowchart of the Newton-Raphson typed incremental-iterative procedure

5. Verification examples

In this section, three examples are presented to verify the accuracy and efficiency of the developed pile element.

5.1. Example 1 -The buckling behaviour of steel sheet pile in elastic medium

Steel sheet piles are easily to be installed but with a lower strength. Their failure behaviors are usually determined by the buckling strength, F_{cr}, which has been evaluated by some analytical and semi-analytical methods with the linear assumption. Assuming the pile top and toe are pinned, only the vertical load is applied on the pile top, where the shaft resistance is ignored, the analytical solution of F_{cr} can be seen as follow:

$$F_{cr}=\frac{\pi^2 EI}{L^2}+k\frac{L^2}{\pi^2} \tag{36}$$

where F_{cr} is the critical buckling load; EI and L are the flexural rigidity and the length of the sheet pile, respectively; and k is the lateral stiffness of the soil.

In order to consider the horizontal loads and the bending moment, Vincent [34] proposed a semi-analytical solution to consider the buckling behavior of the steel sheet pile wall. Details can be seen:

$$F_{cr}=\frac{\frac{w^{II}}{w^{I}}+\delta}{\frac{w^{II}}{w^{I}}-1}N \tag{37}$$

where N is the vertical load on the pile top; w^I and w^{II} are the first-order and second-order lateral displacements at the middle of the pile, respectively; and δ is an empirical coefficient which can be found in [34].

In this example, the cross section AZ18-700 of the steel sheet pile is selected to verify the developed pile element with analytical and semi-analytical methods. The steel sheet pile is 10 m long with a unit cross section 1.392 x 10^{-2} m^{-2} and an inertia moment 3.780 x 10^{-4} m^{-4}. Detailed load and boundary conditions can be seen in Fig. 7 and Fig. 8.

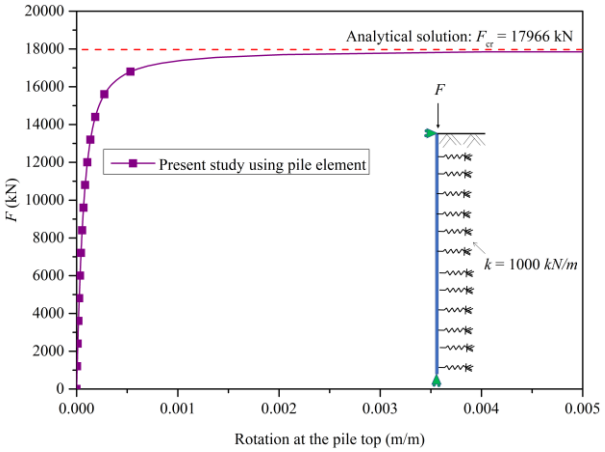

Fig. 7 Comparison of the result with the analytical solution and pile element

It can be found that the analytical solution can match well with the developed pile element. However, there still exists a difference with the semi-analytical method when the horizontal loads and bending moment are considered. This may be induced by the pile compression is ignored by the semi-analytical method. This difference also hints that the bucking behavior of steel sheet pile is extremely complicated even within the linear elastic condition. Hence, it is necessary to introduce the advanced finite element to simulate the structural buckling behavior.

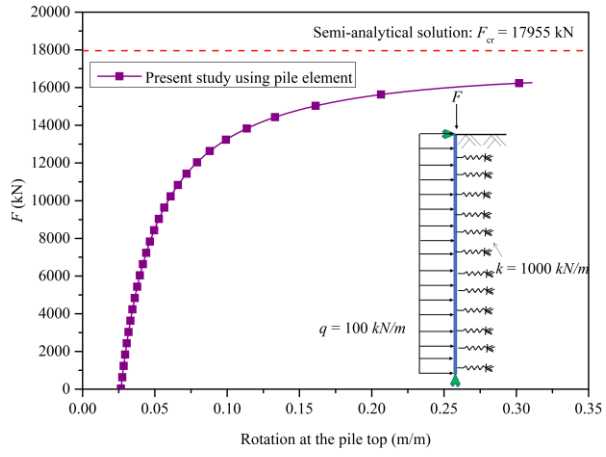

(a) Comparison of the result with the semi-analytical solution and pile element under load condition A

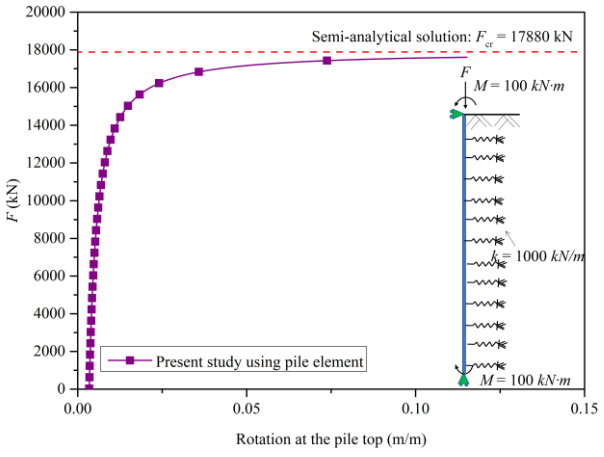

(b) Comparison of the result with the semi-analytical solution and pile element under load condition B

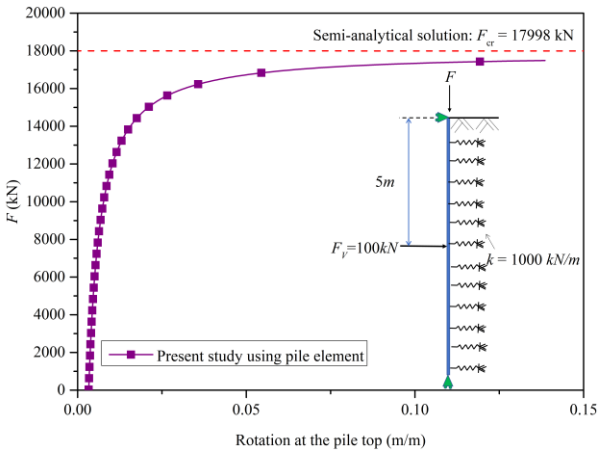

(c) Comparison of the result with the semi-analytical solution and pile element under load condition C

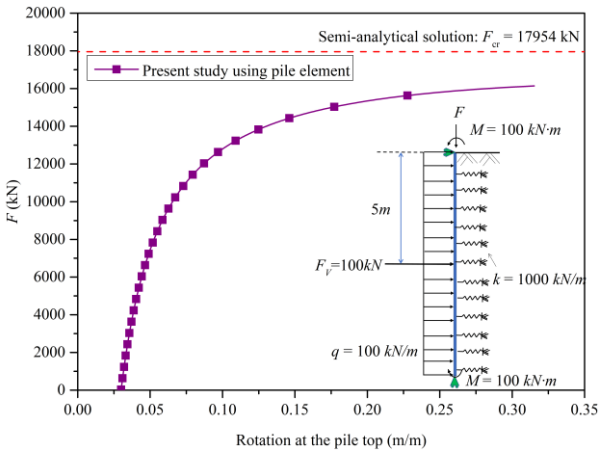

(d) Comparison of the result with the semi-analytical solution and pile element under load condition D

Fig. 8 Comparison of the result with the semi-analytical solution and pile element under different load conditions

5.2. Example 2-The deformation and buckling of the steel sheet pile considering nonlinear SSI

In practical engineering, the soil surrounding the steel sheet pile is always assumed with a constant stiffness in the analysis of the pile's second-order effect[22]. However, soil as a natural discrete material its stiffness can be highly influenced by the depth and the relative displacement between pile and soil. For accurately considering the nonlinear SSI, the *p-y* curve is incorporated the linear elastic spring model by many investigations [18, 21]. In this example, the developed pile element is considered to compare with the discrete spring element to verify its accuracy and efficiency with the consideration of nonlinear SSI. Similar as Example 1, the steel sheet pile AZ18-700 is selected to study the deformation and buckling process with the pile cap load and lateral active pressure. The steel sheet pile is 10 m long, with a unit pile soil contact area 2.574 m^2, a unit cross section 1.392x10^{-2} m^2 and an inertial moment 3.780x10^{-4} m^4. The elastic modulus of the pile is 2.06 x10^8 kPa. Soil properties and loading conditions can be seen in Fig. 9. Meanwhile, the related *p-y* curve and *t-z* curve will be followed by previous studies [17, 18] and plotted in Fig. 10.

It can be found in Fig. 11 that the developed pile element model with 10 elements can obtain a similar result with the conventional discrete spring element with 50 beam elements and 75 soil spring elements. That means the discrete spring element will require more than 5 times of the proposed element to obtain a nearly accurate solution. As known, the element number can dramatically increase the modelling procedure and time. Hence, the present pile element with high accuracy and efficiency has a huge potential in the practical design of the steel sheet pile wall.

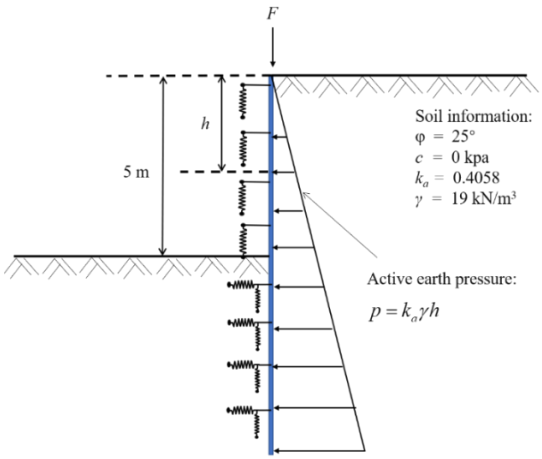

Fig. 9 Schematic of the sheet pile in Example 2

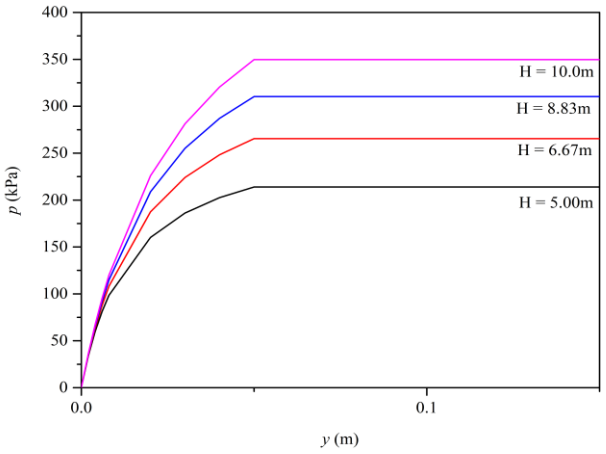

(a) *p-y* curve of the sheet pile in Example 2

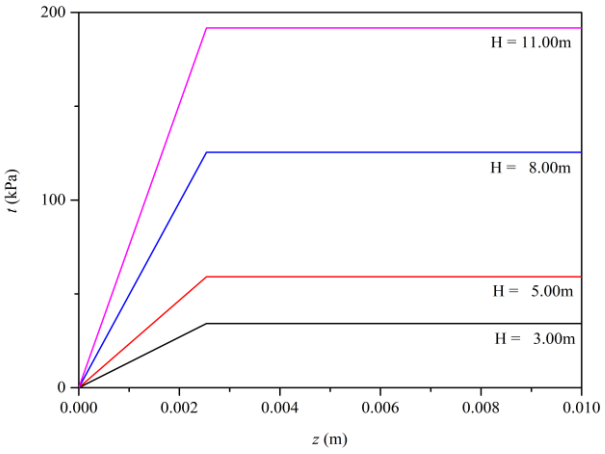

(b) *t-z* curve of the sheet pile in Example 2

Fig. 10 *p-y* and *t-z* curves of the sheet piles in Example 2

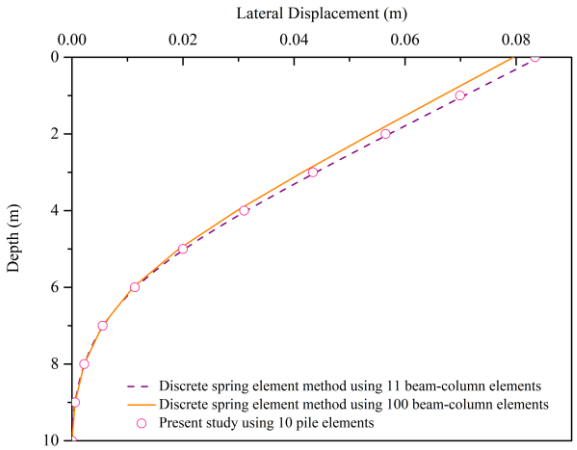

(a) The lateral deflection of the sheet pile when F = 450 kN

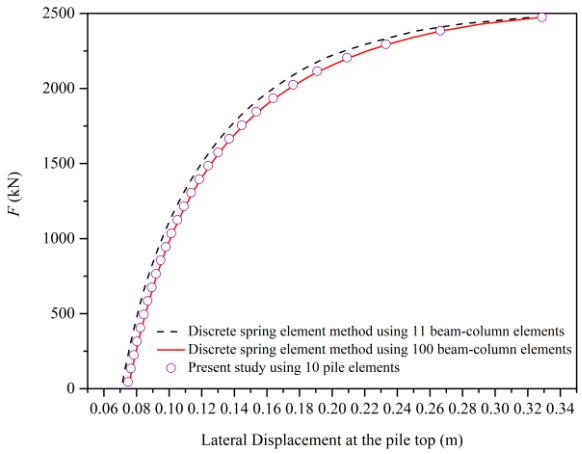

(b) The lateral displacement at the pile top under different load at the pile's top

Fig. 11 Comparison of different finite element models when simulating the deformation and buckling of the sheet pile

5.3. Example 3-The deformation and bearing capacity of the steel sheet pile wall with the consideration of the realistic soil pressure distribution

The passive and active lateral pressures are unbalanced in front of and behind the steel sheet pile. The soil resistance in front of the steel sheet pile can be described by the *p-y* curve, which can be introduced into the discrete element method to simulate the lateral pressure from the rest to passive [21]. However, for the soil pressure behind the pile, it usually adopts the factor of safety to combine with the rest or active lateral pressure, where the realistic variation of the active lateral pressure is ignored. This will induce a large numerical error.

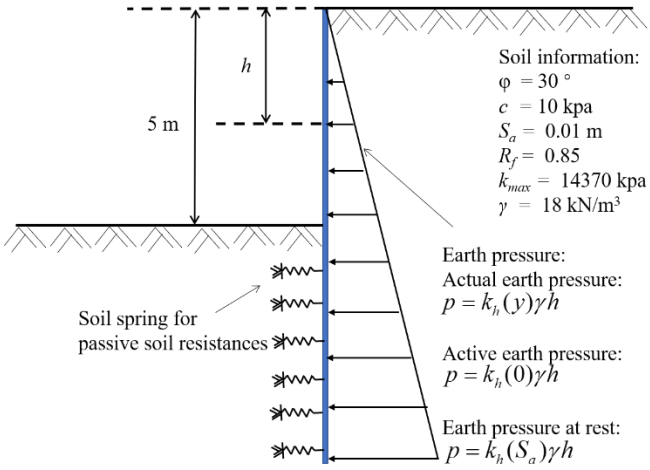

Fig. 12 Schematic of the steel sheet pile in Example 3

In this example, the present pile element will be used to mimic the realistic variation of lateral pressure behind the pile. Comparisons are carried out with the rest and active lateral pressures. Also the selected steel sheet pile AZ28-700 is 10 m long, with a unit inertial moment 6.362 x 10^{-4} m^4 and a cross section 2.002 x 10^{-2} m^2. The elastic modulus of the steel sheet pile is 2.100 x 10^8 GPa. Soil properties can be found in Fig. 12. In this example, the variation of lateral pressure with the deformation is selected from previous studies [17, 35].

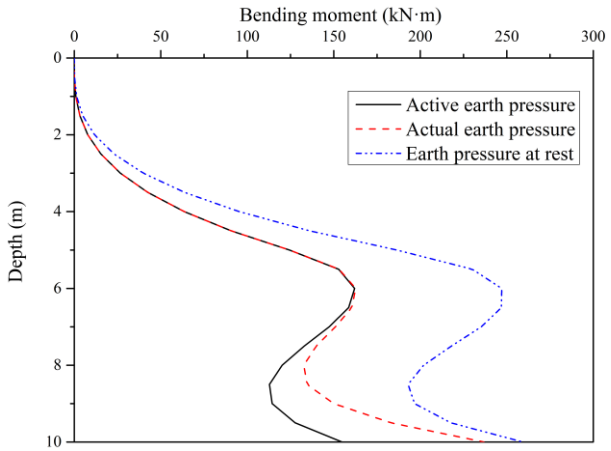

(a) The bending moment along the sheet pile under different earth pressure

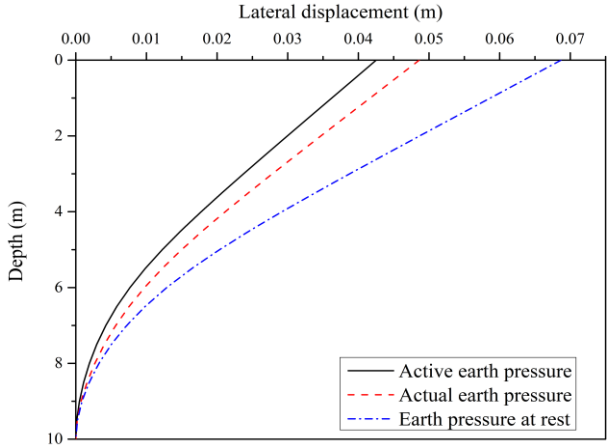

(b) The lateral displacement along the sheet pile under different earth pressure

Fig. 13 Comparison of the influence from different consideration of the earth pressure behind the sheet pile

It can be found that the maximum bending moment along the steel sheet pile has a clear difference from the rest and active lateral pressure to the actual lateral pressure in Fig. 13. The comparison values are 31.4% and 9.8%, which mean overestimate and underestimate. Meanwhile, the relative errors of the lateral displacement at the pile top are 12.5% and 41.3%. It can also be seen that the curves of the bending moment on the upper pile under the active and actual earth pressure are similar because the earth pressure is nearly fully mobilized into active. Regarding the lower pile, however, the difference is dramatically increased. Hence the developed pile element incorporated the

actual lateral pressure distribution can effectively capture the realistic bearing capacity.

6. Conclusions

Steel sheet piles, as a common supporting structure in the excavation projects, are often used in urban areas. The second-order effect and nonlinear SSI can highly influence the failure behaviour of the steel sheet pile. However, they cannot be accurately and efficiently reflected in the design. In this paper, a developed pile element is proposed to consider the realistic nonlinear SSI and second-order effect. Finally, three examples are selected to verify the accuracy and efficiency of the pile element. It can be found the nonlinear bucking can be accurately captured and compared with the analytical and semi-analytical methods. The pile element is much more efficient than the discrete spring element with increasing more than five times. With the consideration of the actual lateral pressure, the proposed element is strong in practical engineering.

Acknowledgements

The work described in this paper was partially supported by a grant from the Research Grants Council of the Hong Kong Special Administrative Regain, China (Project No. UGC/FDS13/E06/18). The third author would like to acknowledge Sun- Yat- Sen University for providing the “2019 Laboratory Open Fund Project of Sun Yat-sen University” (201902146), as well as the “Innovation Training Program for College Students” from School of Civil Engieering, Sun- Yat- Sen University. The last author wants to thank the support by the National Natural Science Foundation of China (No. 52008410).

References

[1] Denisov G. V., Lalin, V. V. and Abramov D. S., "Preservation of Lock Joints in Steel Sheet Piling During Vibratory Driving.", Soil Mechanics and Foundation Engineering, 51(1), 29-35, 2014.
[2] Lee S. H., Kim B. I. and Han J. T., "Prediction of penetration rate of sheet pile installed in sand by vibratory pile driver.", *KSCE J. Civ. Eng.*, 16(3), 316-324, 2012.
[3] Yan Q. Z., Rao J. and Xie Z. Q., "Research and Use of the Steel Sheet Pile Supporting Structure in the Yellow River Delta.", Advanced Materials Research, 243-249, 2684-2689, 2011.
[4] Du Z. L., Liu Y. P. and Chan S. L., "A second-order flexibility-based beam-column element with member imperfection.", Engineering Structures, 143, 410-426, 2017.
[5] Yang C., Yu Z. X., Sun Y. P., Zhao L. and Zhao H., "Axial residual capacity of circular concrete-filled steel tube stub columns considering local buckling.", Advanced Steel Construction, 14(3), 496-513, 2018
[6] Sobala D., and Jarosław R., "Steel sheet piles-applications and elementary design issues.", IOP Conference Series-Materials Science and Engineering, 245, 1-10, 2017.
[7] Huo T., Tong L. and Zhang Y., "Dynamic response analysis of wind turbine tubular towers under long-period ground motions with the consideration of soil-structure interaction.", Advanced Steel Construction, 14(2), 227-250, 2018.
[8] Tapia-Hernandez E., De Jesus-Martinez Y. and Fernandez Sola L., "Dynamic soil-structure interaction of ductile steel frames in soft soils.", Advanced Steel Construction, 13(4), 361-377, 2017.
[9] Chen Z., Yang J. and Liu Z., “Experimental and numerical investigation on upheaval buckling of free-span submarine pipeline.”, Advanced Steel Construction, 15(4): p. 323-328, 2019.
[10] Fang Y. S., Chen T. J. and Wu B. F., "Passive earth pressures with various wall movements.", Journal of Geotechnical Engineering, 120(8), 1307-1323, 1994.
[11] Fang Y. S., Ho Y. C. and Chen T. J., "Passive earth pressure with critical state concept.", Journal of Geotechnical and Geoenvironmental Engineering, 128(8), 651-659, 2002.
[12] Lambe, T. W., and Whitman, R. V., Soil mechanics, John Wiley & Sons, 1991.
[13] Rowe P., and Peaker K. J. G., "Passive earth pressure measurements." Geotechnique, 1965, 15(1): 57-78.
[14] Han S, Gong J and Zhang Y. “Earth pressure of layered soil on retaining structures”, Soil Dynamics and Earthquake Engineering, 83: 33-52, 2016.
[15] Sherif M. A., Fang Y. S. and Sherif R. I., “KA and K o Behind Rotating and Non-Yielding Walls”, Journal of Geotechnical Engineering, 110(1): 41-56, 1984.
[16] Fang Y. S. and Ishibashi I., “Static earth pressures with various wall movements”, Journal of Geotechnical Engineering, 112(3): 317-333, 1986.
[17] Duncan J. M. and Mokwa R. L., “Passive earth pressures: theories and tests”, Journal of Geotechnical and Geoenvironmental Engineering, 127(3): 248-257, 2001.
[18] Recommended practice for planning, designing and constructing fixed offshore platforms—Working stress design, American Petroleum Institute, Washington DC, USA, 2000.
[19] Phanikanth V. S., Choudhury D. and Reddy G. R., “Response of single pile under lateral loads in cohesionless soils”, Electronic Journal of Geotechnical Engineering, 15(10), 813-830, 2010.
[20] Lee F., Hong S., Gu Q. and Zhao P., “Application of large three-dimensional finite-element analyses to practical problems.”, International Journal of Geomechanics, 11(6), 529-539, 2011.
[21] Wang S. T., L. Vasquez and X. Daqing, “Application of Soil-Structure Interaction (SSI) in The Analysis of Flexible Retaining Walls.”, International Conference on Geotechnical & Earthquake Engineering 2013, 567-577, 2013.
[22] Technical specification for retaining and protection of building foundation excavations, Ministry of Housing and Urban-Rural Development, PRC, 2012.
[23] Design of plated structures: Eurocode 3: Design of steel structures, part 1-5: Design of plated structures., British Standards Institution, London, UK, 2012.
[24] Liu S. W., Wan J. H., Zhou C. Y., Liu Z. and Yang X., "Efficient Beam-Column Finite-Element Method for Stability Design of Slender Single Pile in Soft Ground Mediums.", International Journal of Geomechanics, 20(1), 2020.
[25] Li X., Wan J., Liu S. and Zhang L., "Numerical formulation and implementation of Euler-Bernoulli pile elements considering soil-structure-interaction responses.", International Journal for Numerical and Analytical Methods in Geomechanics, 44(14), 1903-1925, 2020.
[26] Timoshenko, S. P. and Gere, J. M., General theory of elastic stability, Courier Corporation, 1973.
[27] Lee K. S. and Han S. E., "Semi-rigid elasto-plastic post buckling analysis of a space frame with finite rotation.", Advanced Steel Construction, 7(3), 274-301, 2011.
[28] Tang Y. Q., Liu Y. P. and Chan S. L., "A co-rotational framework for quadrilateral shell elements based on the pure deformational method.", Advanced Steel Construction, 14(1), 90-114, 2018.
[29] Iu C. K. and Bradford M. A., "Higher-order non-linear analysis of steel structures, part i: elastic second-order formulation.", Advanced Steel Construction, 8(2), 168-182, 2012.
[30] Huang Z. F., and Tan K. H., "FE simulation of space steel frames in fire with warping effect.", Advanced Steel Construction, 3(3), 16, 2007.
[31] Liu S. W., Liu Y. P. and Chan S. L., "Advanced analysis of hybrid steel and concrete frames Part 2: Refined plastic hinge and advanced analysis.", Journal of Constructional Steel Research, 70, 337-349. 2012.
[32] Liu S. W., Liu Y. P. and Chan S. L., "Direct analysis by an arbitrarily-located-plastic-hinge element - Part 1: Planar analysis.", Journal of Constructional Steel Research, 103, 303-315, 2014.
[33] Liu S. W., Bai R., Chan S. L. and Liu Y. P., "Second-Order Direct Analysis of Domelike Structures Consisting of Tapered Members with I-Sections.", Journal of Structural Engineering, 142(5), 2016.
[34] Vincent van D., "Global buckling mechanism of sheet piles: The influence of soil to the global buckling behaviour of sheet piles.", Delft University of Technology, 2020.
[35] Ni P., Mangalathu S., Song L., Mei G. and Zhao Y., "Displacement-Dependent Lateral Earth Pressure Models.", Journal of Engineering Mechanics, 144(6), 2018.

Advanced Steel Construction - Vol. 16 No. 4 (2020) 363-369
DOI:10.18057/IJASC.2020.16.4.9

INFLUENCE OF A ROOFING SYSTEM ON THE STATIC STABILITY OF RETICULATED SHELLS

Wen-Liang Li [1, 2], Xu-Dong Zhi [1, 2 *], Duo-Zhi Wang [3], Feng Fan [1, 2] and Shi-Zhao Shen [1, 2]

[1] *Key Lab of Structure Dynamic Behaviour and Control of the Ministry of Education, Harbin Institute of Technology, Harbin, China*
[2] *Key Lab of Smart Prevention and Mitigation of Civil Engineering Disasters of Ministry of Industry and Information Technology, Harbin Institute of Technology, Harbin, China*
[3] *Key Laboratory of Earthquake Engineering and Engineering Vibration, Institute of Engineering Mechanics, China Earthquake Administration, Harbin, China*
** (Corresponding author: E-mail: zhixudong@hit.edu.cn)*

ABSTRACT

According to the existing experimental results, the roofing systems considerably influence the bearing capacity and plastic development of reticulated shell substructure models; however, the mechanism of this influence of the roofing system on the static stability of reticulated shell structures remains unclear. In this paper, based on experimental studies, the finite element model of reticulated shell structures with different roofing systems are established, and the influence of various factors of the reticulated shell structures (rise span ratio, roof load, initial imperfection amplitude and mode) and roofing system (pillar and purlin joint) are analysed. Furthermore, the influence ranges of the roofing system on the static bearing capacity of the shells are recommended.

ARTICLE HISTORY

Received: 19 February 2020
Revised: 12 September 2020
Accepted: 18 September 2020

KEYWORDS

Reticulated shells;
Roofing systems;
Static load;
Influences of different factors;

1. Introduction

With the continuous growth in society, the demand for large-span space buildings for production and recreational purposes is increasing. Architects often employ single-layer reticulated shell structures, owing to their low weight and reasonable force bearing capacity. An example of classical engineering is the Spectacle Roof of the MGM GRAND in Macau, which is the world's largest single-layer reticulated shell structure, providing people with a comfortable and extensive leisure and entertainment space. In recent years, scholars have systematically performed the analysis and design of reticulated shell structures. Shen Shizhao and Chen Xi [1] examined the elastic stability of single-layer shells and proposed design methods for different kinds of single-layer shell structures. Fan Feng et al. [2-3] studied the elastic-plastic stability of reticulated shell structures and established a modified design method. Zhi Xudong [4-5] studied the dynamic response and failure mechanism of single-layer reticulated shell structures. M. Fong, Y.P. Liu and S.L. Chan [6] employed a second-order analysis method to study the buckling load and failure mode of a shell with semi-rigid joints and initial imperfections, and the method was verified experimentally. Kato et al. [7-8] and Ma Huihuan [9-10] analysed the static stability of reticulated shell structures with different joint rigidities. Si-Wei Liu [11] used curved tapered-three-hinge beam column elements (TTH) to simulate a tapered member with I-sections in dome-like structures, the method exhibited a high calculation efficiency and accuracy and could be used to analyse practical engineering structures with tapered members. Furthermore, Rui Bai and Si-Wei Liu [12] proposed an efficient method using non-prismatic elements to analyse the dynamic response of frame structures with tapered sections members. As an innovative approach, Y.P. Liu and S.L. Chan [13-14] applied the second-order direct analysis (SODA) method and TTH method to the design and construction of the MGM Spectacle Roof in Macau, the construction and offload processes of the Spectral Roof were monitored and compared with the analysis results of the SODA method, thereby ensuring the safety and accuracy of the construction process, the practicability of the analysis method was also verified in this manner. Xie Xiangyang [15] analysed the key design and analysis technologies of reticulated shells with prism joints in the construction of the MGM Spectacle Roof.

The aforementioned studies provided valuable guidance for the analysis of single-layer reticulated shell structures under static and seismic loads. However, the influence of a roofing system on the reticulated shell structures was not considered in most of the existing studies, and this simplification may induce deviations in the research findings of reticulated shell structures. In the current steel structure design codes [16-19], the influence of roofing systems on the bearing capacity of the main structure are not clearly specified, even though these elements are considered as the safety reserve of the structures, the influence characteristics of the roofing systems on reticulated shell structures has not been clarified. Several scholars attempted to examine the influence of the roofing systems on the static and seismic performances of long-span space structures. He Yongjun [20] analysed the influence of concrete roof panels on the static stability of grid structures and established a simplified finite element analysis method pertaining to the concrete panels in grid structures. Zhang Yigang [21] analysed the influence of metal-faced roofing panels on the frequency response of cylindrical reticulated shells, by performing a shaking table test. Maria Koliou [22-23] analysed the seismic performance of long-span structures with roof and wall panels and observed that the roof and wall panels could improve the seismic performance of the main structures. Zhi Xudong and Li Wenliang [24-26] conducted static loading experiments using single-layer reticulated shell substructure models, considering different types of roofing systems, as shown in Fig. 1, the static and dynamic characteristics of a reticulated shell with a roofing system were preliminarily analysed.

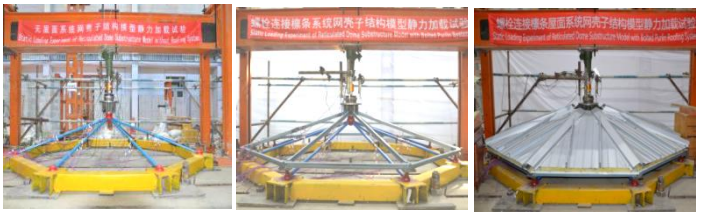

(a) Substructure model without roofing system
(b) Substructure model with only purlin system
(c) Substructure model with complete roofing system

Fig. 1 Finite element model of the roofing system

According to the aforementioned studies, roofing systems notably influence the static and dynamic characteristics of long-span space structures. However, there are still some important issues to be addressed: (1) mechanism of the effect of roofing systems on the static stability of reticulated shells and (2) the characteristics of different roofing systems influences on different reticulated shell structures static bearing capacity need to be further studied, and the influence range should also be obtained.

2. Finite element model of the reticulated shell structure with a roofing system

The shell members and roofing system components in the structures are designed according to the relevant requirements in the current Chinese specifications [16,19]. All the roof panels in the finite element models (FEMs) are simulated according to the commonly implemented installation processes

for roof panels in China, as shown in Fig. 2(a). The bottom panels in the reticulated shell are shallow profiled steel sheets fixed on purlins through self-tapping screws. Subsequently, the insulating layers are laid on the bottom panels and secondary purlins, as shown in Fig. 2(b). Finally, the profiled metal-faced panels are compacted onto the supports, which are fixed on the secondary purlins, as shown in Fig. 2(c). When using the current installation technologies for roofing systems, the insulation layer, faced panels and secondary purlins do not notably affect the static stability of the shells and are thus not considered in the following analysis.

(a) Installation process of the roof panel in an actual engineering application

(b) Procedure of laying the insulating glass cotton

(c) Procedure of laying the faced panels

Fig. 2 Process of installing the roof panels

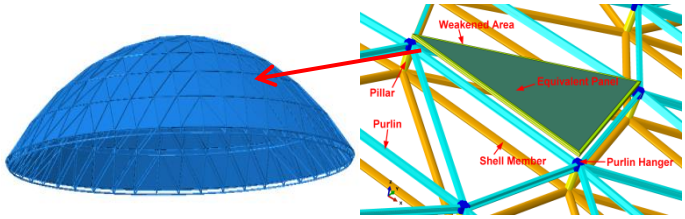

Fig 3 Finite element model of the roofing system

Fig. 3 shows that the FEM includes the purlin system, purlin hangers, equivalent orthotropic panel, weakened areas, pillars and reticulated shell. Specifically, the connections between the panel and purlins are simulated as the weakened areas, and the orthotropic panel is used to simulate the shallow profiled steel sheet for the roof panel. The mechanical properties are researched according to the experimental results and finite element analysis (FEA) according to Ref [24]. In practical engineering applications, bolted or welded connections are widely used in purlin joints, the mechanical properties of which are different from those of hinge or fixed joints. Xie Xiangyang [27] analysed semi-rigid joints with six degrees of freedom and applied such joints in steel tubular scaffolds with couplers. In general, the method of simulating semi-rigid joints is highly reliable, and which can be used to model the purlin joints for the shells with a roofing system, taking into account the rigidity and plastic development of the purlin joints. The constitutive models for the FEM are ideal elastic-plastic models, and the elastic modulus and yield strength of the shell members, purlin, and pillars are 206 GPa and 235 MPa, respectively..

3. The reticulated shell finite element analysis with roofing system

According to the modelling method described in Section 2, the effects of the roofing system on the static stability of the reticulated shell structures are analysed.

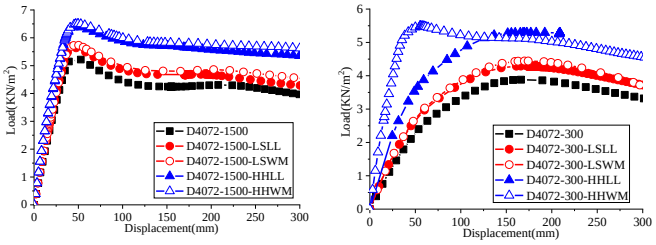

(a)D4072-1500 (b)D4072-1500

Fig. 4 Load-displacement curves of D4072

Fig. 4 shows that the bolted purlin system increases the static bearing capacity of the reticulated shell with the L/1500 initial imperfection by 8.27%, the complete bolted purlin roofing system increases the static bearing capacity by 10.1%. When the purlin joints are used as welded connections, the bearing capacity is increased by 22.1%, and after the addition of the roof panels, the bearing capacity is increased by 24.8%. Fig. 5 shows that because of the roofing system, the plastic shell members gradually develop towards the outer rings of the shell, the shell bearing capacity is respectively increased by 10.1% and 14.9% owing to the bolted purlin system and the complete bolted purlin roofing system for the shell with an L/300 initial imperfection. The influences of the welded purlin system on the static bearing capacity are more significant; specifically, this system increases the bearing capacity by 36%, moreover, the complete welded purlin roofing systems increase the static bearing capacity by 41.4%.

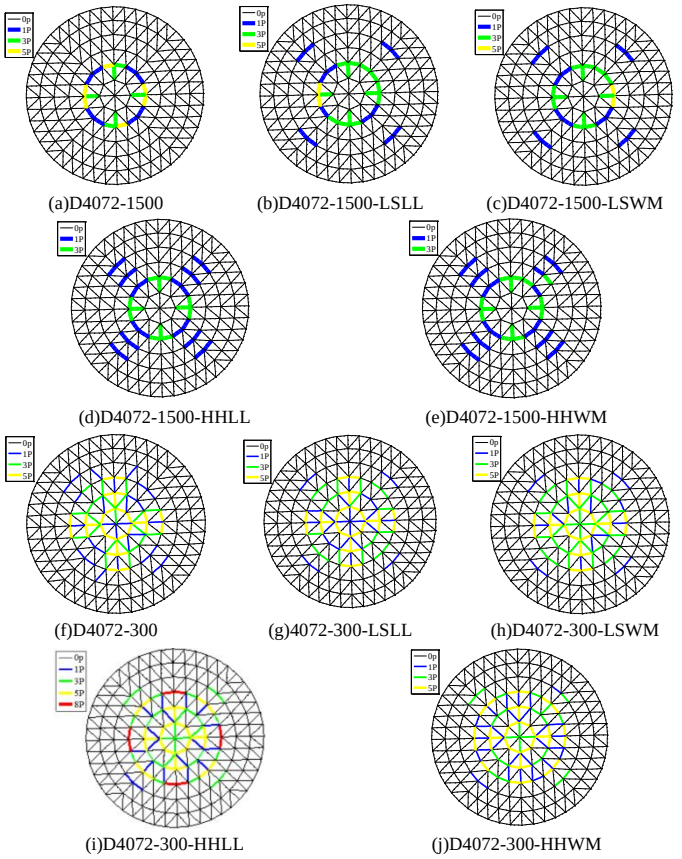

(a)D4072-1500 (b)D4072-1500-LSLL (c)D4072-1500-LSWM

(d)D4072-1500-HHLL (e)D4072-1500-HHWM

(f)D4072-300 (g)4072-300-LSLL (h)D4072-300-LSWM

(i)D4072-300-HHLL (j)D4072-300-HHWM

Fig. 5 Distribution of plastic members in D4072

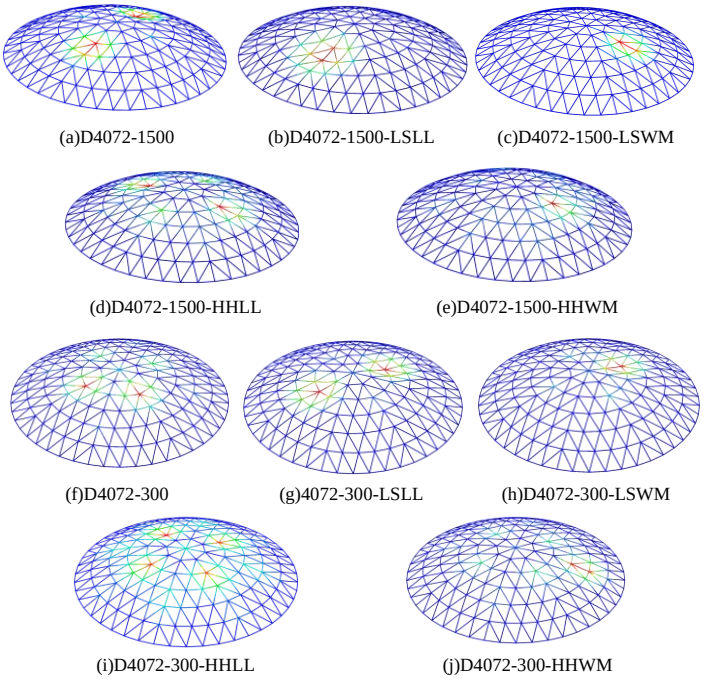

(a)D4072-1500 (b)D4072-1500-LSLL (c)D4072-1500-LSWM

(d)D4072-1500-HHLL (e)D4072-1500-HHWM

(f)D4072-300 (g)4072-300-LSLL (h)D4072-300-LSWM

(i)D4072-300-HHLL (j)D4072-300-HHWM

Fig. 6 Deformation in D4072

Fig. 6 indicates that roofing system changed the failure mode of the reticulated shell structure. The failure mode of the reticulated shell

(D4072-1500) without a roofing system is symmetrical, and notable depressions develop continuously and collapse on the two vertices of the secondary ring around the centre vertex. After installing the roofing system, the reticulated shell structure exhibits a notable unilateral depression, and the local damage of the reticulated shell structure becomes more significant, as shown in Figs. 6(c) and 6(e). Moreover, Figs. 6(f) and. 6(j) show that the location of damage in the shell changes owing to the welded roofing system, and the local damage phenomena become more significant. The static bearing capacity of the single-layer spherical reticulated shell structure primarily depends on the bending and membrane rigidity around the vertices on the main rib rings of the reticulated shell structures. When the purlin system and roof panels are installed, all these members act as composite beams to bear an external load along with the shell members. In the scenario, the bending and membrane rigidity of the shell increase, and the bearing capacity of the reticulated shell structures with the roofing system increases significantly. In general, the static bearing capacity is closely related to many factors such as the initial imperfection amplitude and mode, axial load-displacement and bending moment rotation relationships of the purlin joint, and pillar height, the influence of these factors should be further analysed.

(a) Deformation of the purlin and shell members

(b) Plastic deformation at the location of the bolted hole

Fig. 7 Deformation of the shell members and bolted purlin in the experimental models

In general, the effect of the bolted purlin roofing system on the static stability of a shell is not as significant as that of the welded roofing system, because premature yielding occurs at the locations of the bolted holes, while there is no plastic deformation occurs in the purlin members. The same phenomenon is also observed in the experimental studies, as shown in Fig. 7, even at the end of the experiments, the deformations at most of the purlins are not notable, while significant plastic deformation can be observed near the bolted hole of the bolted purlin connections. In the case of the bolted and welded purlin roofing systems, when D4072-1500 exhibits the highest static bearing capacity, 70.2% and 72.4% of the purlin joints yield in the axial restraint direction, respectively, and 12.7% and 2.2% of the purlin joints yield in the out-of-surface moment directions, respectively. In the bolted and welded roofing systems, when D4072-300 exhibits the highest bearing capacity, 44.6% and 56% of the purlin joints yield in the axial restraint direction, respectively, and 45% and 18.64% of the purlin joints yield in the out-of-surface moment directions, respectively. The torsional moment and the moment in the surface of the purlin joints are nearly still in elastic stages. The out-of-surface and axial constraints of the purlin joints are the main factors facilitating the increase in the shell bearing capacity owing to the roofing system.

4. Influence of different factors on the static stability of reticulated shell structures with roofing systems

The aforementioned analysis results show that the roofing system's influences on the shell's static stability are obvious, and further analysis should be carried out according to different influence factors in the reticulated shell and the roofing system, as shown in Table 1.

In this study, except when analysing the influence of the imperfection modes, the 1st order buckling mode of the reticulated shells is considered as the initial imperfection mode for the calculations.

4.1. Influence of the rise span ratios

The effect of the span on the static stability of the shells with roofing systems was analysed in Ref [24]. In this section, the influence of the roofing systems on the static stability of the shells, corresponding to rise span ratios of 1/3, 1/5 and 1/7 are analysed.

Table 1
Parameter analysis

Rise span ratios	1/3, 1/5, 1/7
Initial imperfection amplitude	0, L/1500, L/300
Initial imperfection modes	The 1st-order buckling mode, the consistent imperfection mode (1), the consistent imperfection mode (2), the 1st-order frequency mode
The purlin joint's rigidity	0.2, 1.0, 2.0
Height of the pillar (m)	0.2, 0.6, 1.0
Roof load (kg/m^2)	35/50, 95/50, 155/50

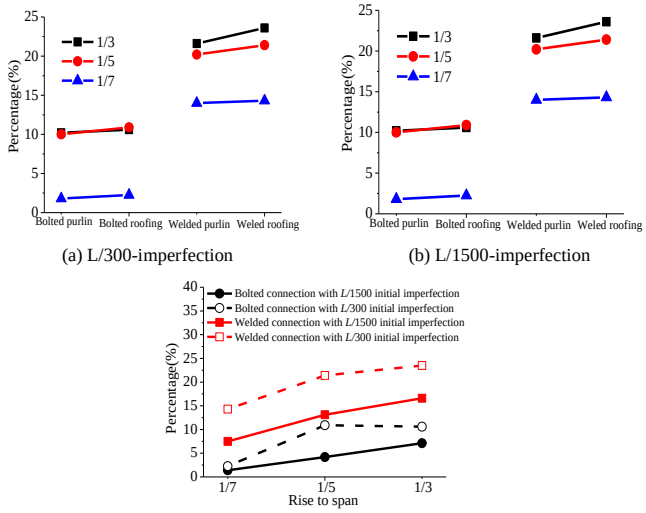

(a) L/300-imperfection

(b) L/1500-imperfection

(c) Percentage improvement with the rise span

Fig. 8 Percentage improvement in the bearing capacity of the shells with different rise span ratios

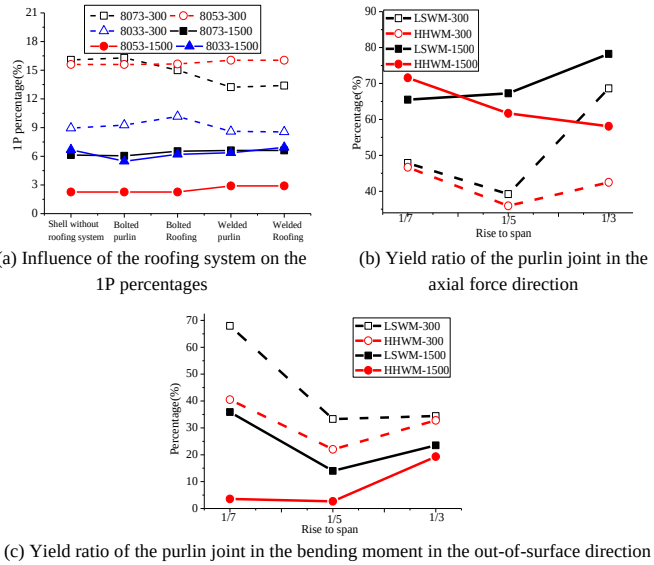

(a) Influence of the roofing system on the 1P percentages

(b) Yield ratio of the purlin joint in the axial force direction

(c) Yield ratio of the purlin joint in the bending moment in the out-of-surface direction

Fig. 9 Influence of the roofing system on the plastic member and plastic purlin joint percentage

The effects of the roofing system on the static stability of the shell are different under different rise span ratios. Fig. 8 shows that as the rise span ratios increase, the effect of the roofing system on the static bearing capacity becomes more notable. Fig. 9(a) shows that the roofing systems do not significantly influence the proportion of the plastic members in the reticulated shells under the three rise span ratios (changes within 3%). No plastic deformation occurs in the purlin members and roof panels; however, a large number of axial constraints and out-of-surface bending moment constraints in

the purlin joints exhibited yielding, as shown in Figs. 9 (b) and (c). As the rise span ratio increases in the shell with the L/1500 initial imperfection, the yield ratio of the axial constraints and out-of-surface moment constraints of the welded purlin joints decreases and increases, respectively. The yield ratio of the axial restraint for both kinds of purlin joints is significantly higher than that of the out-of-surface bending moment constraints, thereby indicating that the axial restraint of the purlin joint more notably influences the increase in the bearing capacity of a shell with a smaller initial imperfection (L/1500). The yield ratio of the out-of-surface bending moment constraint significantly increases in the case of the reticulated shell structures with an initial imperfection of L/300, and the out-of-surface moment constraints are more notably factors to influence the the static bearing capacity of a shell with a roofing system with a smaller rise span ratio (1/7).

4.2. Influence of the initial geometric imperfections

The initial geometric imperfections influence the static stability of the reticulated shell structures; therefore, the cases in which both the roofing systems and reticulated shells contain initial imperfections need further analysis. The amplitudes of the initial imperfection are L/1500, L/900 and L/300. The 1st-order buckling modes of the reticulated shells are used as the initial imperfection modes, and the influences of the roofing systems on the reticulated shells under three kinds of spans and rise span ratios are analysed.

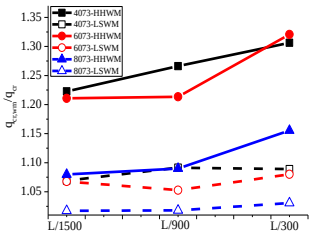

(a) Ratio of the bearing capacity of shells with different spans

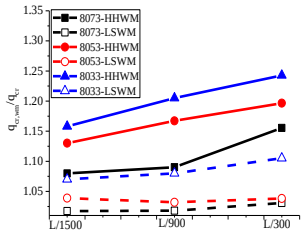

(b) Ratio of the bearing capacity of shells with different rise spans

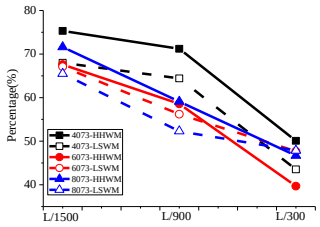

(c) Axial constraint yield ratio in shells with different spans

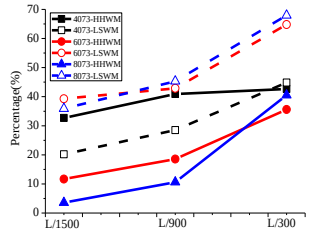

(d) Bending moment out-of-surface yield ratios in shells with different spans

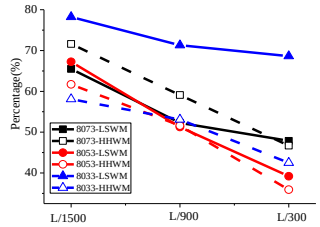

(e) Axial constraint yield ratio in shells with different rise spans

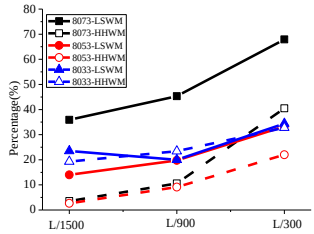

(f) Bending moment out-of-surface yield ratio in shells with different rise spans

Fig. 10 Influence of the amplitudes of the initial imperfections on the bearing capacity and purlin joint yield ratio of shells with a roofing system

According to the aforementioned analysis, the roofing system considerably influences the shells with different initial imperfection amplitudes, and the influence of the roofing system on the static bearing capacity tends to increase with an increase in these amplitudes, as shown in Figs. 10 (a) and (b). The increase in the static stability of the reticulated shells owing to the welded purlin roofing system is higher under a smaller span and larger imperfection amplitude. The increase in the static bearing capacity of the shell is not as notably influenced by the initial imperfection amplitudes in the case of the bolted purlin roofing system as that in the case of the welded purlin roofing system (the fluctuation amplitude is within 3%).

Figs. 10(c)-(f) show that as the amplitude of the initial geometric imperfection increases, the yield proportion of the axial constraints and out-of-surface bending moment constraints in the purlin joints gradually decreases and increases, respectively. This phenomenon occurs because the mechanism of the membrane stress in the reticulated shell with a smaller initial imperfection is more significant, and more axial direction constraints act on the bearing external load as well as on the reticulated shell, owing to which, a larger number of axial direction constraints enter the plastic stage. Additionally, when the initial imperfection amplitude are larger, the reticulated shell exhibits a continuous depression around the locations of the initial imperfections, owing to which the shell stops effectively transmitting the membrane force earlier, and more out-of-surface bending moment constraints in the purlin joints yield around the concave position.

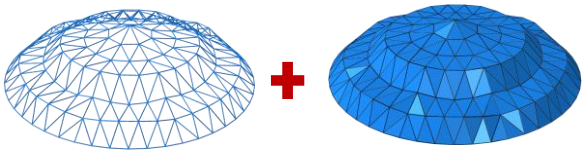

(a) The 1 st-order buckling mode (shell)+the 1 st-order buckling mode (roofing system) (BB)

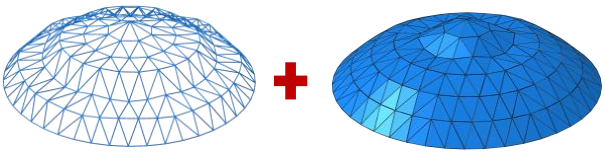

(b) The 1st-order buckling mode (shell)+the consistent imperfection mode (1) (roofing system) (B1)

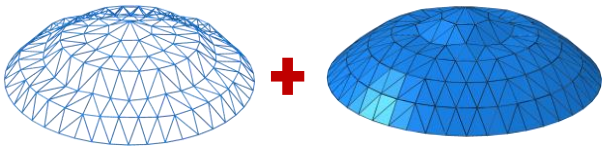

(c) The 1 st-order buckling mode (shell)+the consistent imperfection mode (2) (roofing system) (B2)

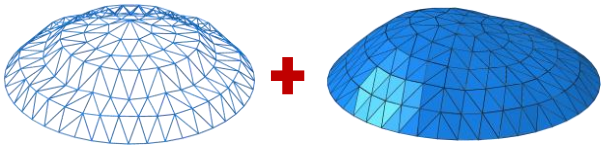

(d) The 1 st-order buckling mode (shell)+the 1 st-order frequency mode (roofing system) (BF)

Fig. 11 The combination of different initial imperfection modes (L/30)

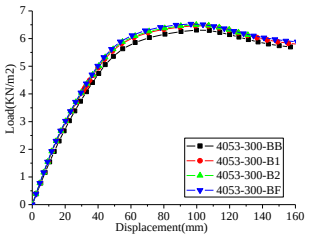

(a) Bolted purlin roofing systems

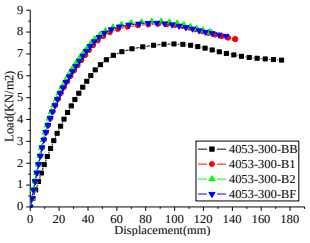

(b) Welded purlin roofing systems

Fig. 12 Load-displacement curves of shells under different combinations of the initial imperfection modes

The above analysis were obtained for the case in which the initial imperfection modes for the reticulated shell structure and roofing system are equivalent. Nevertheless, further analyses are required for the case in which the imperfection modes of the shell and roofing system are different. Therefore, four kinds of initial imperfection modes are analysed in this paper, as indicated in Table 1. The 1st-order buckling mode of the reticulated shells is used as the initial imperfection modes of the reticulated shells, and the initial imperfections for the roofing system are set as follows: 1st-order buckling mode, consistent imperfection mode (1), consistent imperfection mode (2) and the 1st order frequency mode of the reticulated shell, as shown in Fig. 11. In consistent imperfection mode (1), the calculations are performed using the Riks method in ABAQUS, the differences in the displacement of the vertices in the reticulated shell between the step ((i-1)th step) before the peak value of the static bearing capacity occurs (ith step) and the step ((i+1)th) after the peak value are estimated. In consistent imperfection mode (2), the

calculations are performed using the General method in ABAQUS; specifically, the differences in the displacement of the vertices in the reticulated shell between the (i-1)th step before the peak value and the instant of the peak value (ith step) are estimated.

Fig. 12 shows that the influence of the different initial imperfection modes on the shell bearing capacity is smaller in the case of the bolted purlin roofing system (fluctuations within 3.5%) than in the case of the welded purlin roofing system (13.6%). When the imperfection modes of the reticulated shell and roofing system are equivalent, the adverse effects of the initial imperfections are more notable.

4.3. Influence of the purlin joint

According to the analysis in Section 3, the rigidity and strength of the purlin joints are key factors influencing the increase in the structural bearing capacity owing to the roofing system, and their role should be further analysed.

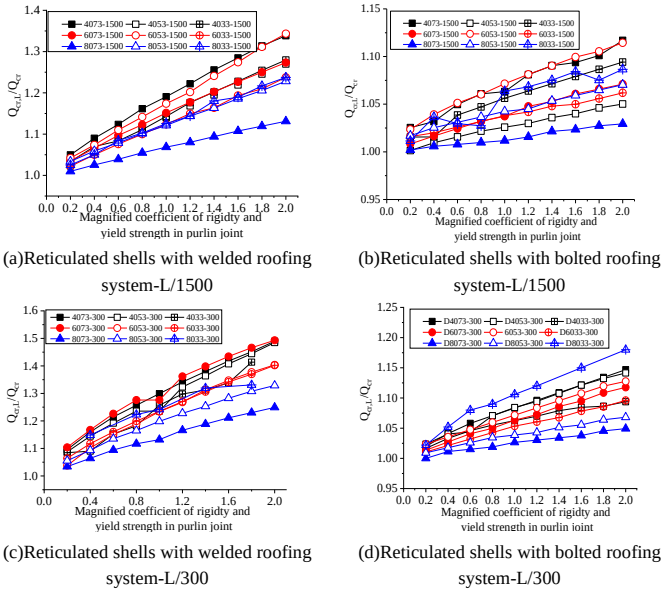

(a)Reticulated shells with welded roofing system-L/1500

(b)Reticulated shells with bolted roofing system-L/1500

(c)Reticulated shells with welded roofing system-L/300

(d)Reticulated shells with bolted roofing system-L/300

Fig. 13 Ratio of peak load to magnified coefficient of rigidity and yield strength in joints

Fig. 13 shows that the static bearing capacity of the reticulated shell increases with an increase in the axial rigidity, rotational rigidity and yield strength in the purlin joints. As the purlin joint rigidity and yield strength increase from 0.2 to 2.0 times those of the original purlin joint, the effect of the welded and bolted purlin roofing systems on the bearing capacity of the reticulated shells increases by 1-34% and 1-11.7% under the initial imperfection of L/1500, respectively. Under the initial imperfection of L/.300, the influence of the welded and bolted purlin roofing systems on the bearing capacity increases from 3.4% to 49.3% and 0% to 18%, respectively. When the rise span ratio of the reticulated shell is 1/7 and the span is 80 m, the amplitude of the bearing capacity increases as the rigidity and yield strength of the purlin joints are lower than those under the other conditions, and the amplitude tends to decrease as the span increases. A similar phenomenon can be observed in the shell with a rise span ratio and initial imperfection of 1/5 and L/300, respectively.

4.4. Influence of the pillar height

Pillars are critical load-bearing members and assist the roofing system in improving the static stability of the shells. The influences of the pillar height (0.2 m, 0.6 m and 1.0 m) on the static stability of reticulated shells with different spans and rise span ratios are analysed. The initial imperfection amplitude of the reticulated shell structure is L/300.

As shown in Fig. 14, the pillar height significantly influences the static stability of the shell structures. With an increase in the pillar height, the static bearing capacity and structural rigidity of the shell increase significantly. When the pillar height is 0.2 m in the D8073-300 shell, the static bearing capacity of the shell with the bolted purlin and welded roofing systems increases by 3.2% and 15.6%, respectively. When the pillar height is 1.0 m, the static bearing capacity of the shell of the bolted and welded roofing systems increases by 20.3% and 60%, respectively. The rigidity of the vertex with the largest displacement in the reticulated shell is 1.26 and 1.65 times higher when the pillar height is 1.0 m than that when the height is 0.2 m. Similar phenomena can also be observed in the shells with other spans and rise span ratios.

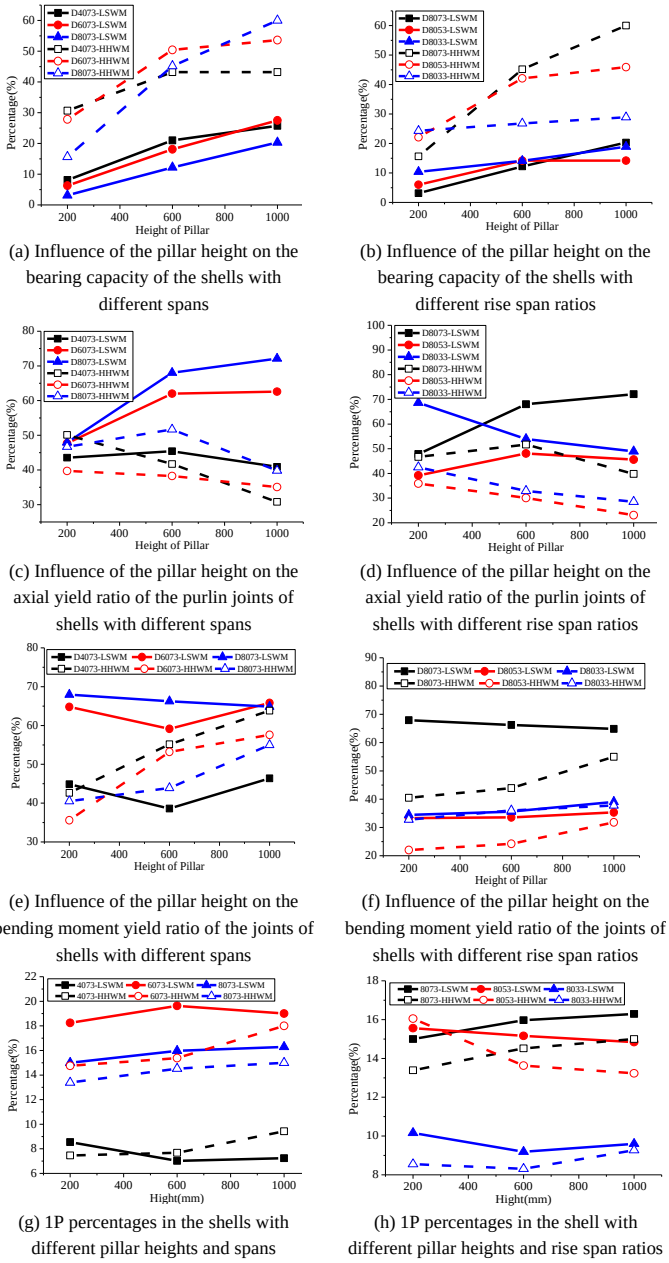

(a) Influence of the pillar height on the bearing capacity of the shells with different spans

(b) Influence of the pillar height on the bearing capacity of the shells with different rise span ratios

(c) Influence of the pillar height on the axial yield ratio of the purlin joints of shells with different spans

(d) Influence of the pillar height on the axial yield ratio of the purlin joints of shells with different rise span ratios

(e) Influence of the pillar height on the bending moment yield ratio of the joints of shells with different spans

(f) Influence of the pillar height on the bending moment yield ratio of the joints of shells with different rise span ratios

(g) 1P percentages in the shells with different pillar heights and spans

(h) 1P percentages in the shell with different pillar heights and rise span ratios

Fig. 14 Influence of the pillar height on the bearing capacity, yield ratio of purlin joints and 1P percentages of the shell members

When the rise span ratio is 1/7, at the peak value of the static bearing capacity of the shell with the welded purlin roofing system, the proportion of the 1P plastic shell members increases as the pillar height increases, this trend is not significant in the case of the shell with the bolted purlin roofing system. Due to the weak constraint of the bolted purlin joints when the reticulated shell bears a larger static load, the bolted purlin joints aggravate the local instability more notably, and the proportion of the plastic shell members decreases slightly. The cross-sections of the shell members, purlins and roof panels are similar to the composite section beams, considering the fully transmitted load for the purlins joints, as the distance between the section centroids of the purlin and shell members increases, the rigidity and bearing capacity of the reticulated shell structure is significantly improved. Figs. 14 (e) and (f) show that when the purlin joints have a welded connection, the axial constraints of the welded joints are sufficiently strong to transmit the axial load, and the yield proportion of the out-of-surface bending moment constraint in the purlin joints increases as the pillar height increases. When the purlin joints are bolted connections, with weaker axial constraints, more purlin joints enter the plastic stage earlier, and the pillar height does not notably influence the yield proportion of the bolt purlin joints.

According to above analysis results, when the pillar height is small, the rigidity of the reticulated shell membrane can be increased by the roofing system, and the increase in the purlin section and axial constraint of the purlin joints can enhance the increase in the shell static stability owing to the roofing system. When the pillar height is large, the purlins bear a larger bending moment, and the purlin joints need provide sufficient bending moment constraints for the influence of the roofing system to be notable.

4.5. Influence of the roof load

The effect of the roof load on the static stability of the reticulated shells with different spans, rise span ratios and imperfection amplitudes is analysed.

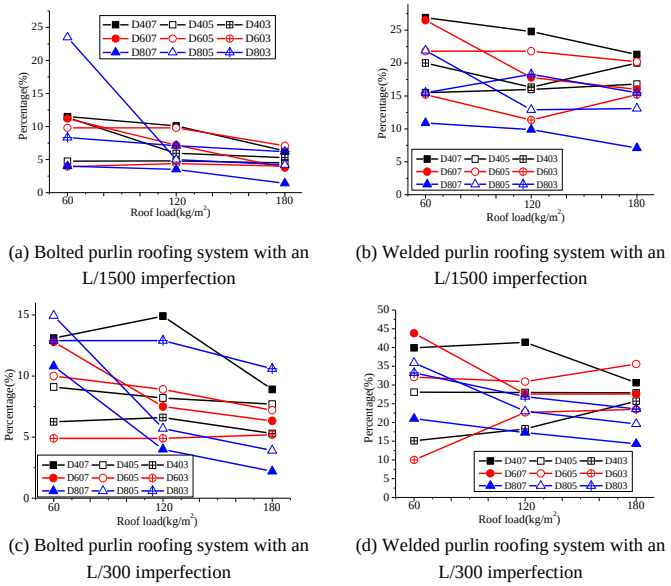

(a) Bolted purlin roofing system with an L/1500 imperfection

(b) Welded purlin roofing system with an L/1500 imperfection

(c) Bolted purlin roofing system with an L/300 imperfection

(d) Welded purlin roofing system with an L/300 imperfection

Fig. 15 Effect of the roof loads on the shell bearing capacity

Fig. 15 shows that the effect of the bolted purlin roofing system on the static bearing capacity of the shell decreases with increasing roof load. The bolted purlin roofing system does not notably influence the static bearing capacity of a shell with a large span, small rise span ratio and large roof load; nevertheless, its effect is notable in the case of a shell with a small span, large rise span ratio and a lighter roof load. When the rise span ratios are 1/5 and 1/7, the effect of the welded purlin roofing system on the shell bearing capacity decreases with an increasing roof load. When the shell span is 80 m and the roof load is larger (120 kg/m2 and 180 kg/m2), the influence of the roofing system on the shell increases as the rise span ratio of the shell increases.

4.6. Statistical results of the effect of the roofing system on the static bearing capacity

The statistical analysis of the effect of the roofing systems on the static bearing capacity of the reticulated shell structures with different roof loads, spans, rise span ratios and imperfection amplitudes indicates that the influence is in accordance with the normal distribution, with the coefficient of confidence being 95%, as shown in Fig. 16. The effect of the roofing systems on the static bearing capacity and the effect of the skin of the roof panels on the bearing capacity of a shell with only purlin systems are also indicated in Table 2.

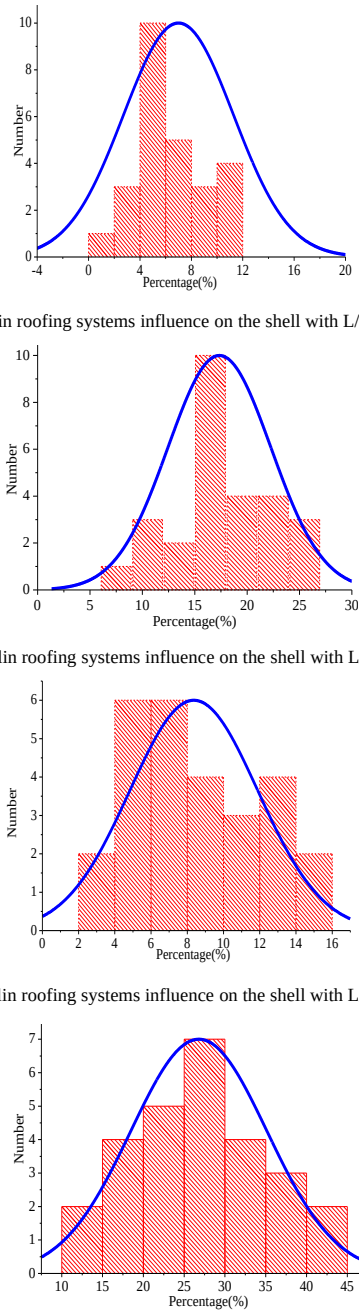

(a) Bolted purlin roofing systems influence on the shell with L/1500 imperfection

(b) Welded purlin roofing systems influence on the shell with L/1500 imperfection

(c) Bolted purlin roofing systems influence on the shell with L/300 imperfection

(d) Welded purlin roofing systems influence on the shell with L/300 imperfection

Fig. 16 Histogram of the effect of the roofing systems on the bearing capacity of the reticulated shell

Table 1
Statistics of the effect of the roofing systems on the static bearing capacity of the reticulated shell

Roofing system	Initial imperfection amplitude	Effect of the roofing system (%)				Effect of the roof panels (%)	
		Expected value	Standard deviation	Maximum	Minimum	Maximum	Minimum
Bolted purlin roofing system	L/1500	7.00	4.28	23.50	1.40	3.13	0.39
	L/300	8.36	3.50	14.94	2.20	5.22	0.26
Welded purlin roofing system	L/1500	17.36	4.92	26.90	7.10	6.6	0.37
	L/300	26.80	8.36	43.80	10.00	7.10	0.27

5. Conclusion

The FEAs of the reticulated shell structures with different roofing systems were performed based on experimental analyses, and the results indicated that the roofing systems notably influence the static stability of reticulated shell structures. The following conclusions were derived:

(1). Roofing systems can significantly increase the static bearing capacity of reticulated shell structures and intensify the shell members' plastic development around the location of the initial imperfection at the peak bearing capacity. The influence of the roofing systems should be considered in the design and analysis of the reticulated shell structures, in terms of the static stability, the roofing systems notably affect the nonlinear whole-process failure mode of the reticulated shell structures under a static load.

(2). The roofing system considerably affects the static bearing capacity of different reticulated shell structures and exhibits certain characteristics. The influence of the roofing systems on the bearing capacity of a shell with an 80 m span (roof load of 120 kg/m2 or 180 kg/m2) increases with an increase in the rise span ratios. Furthermore, this influence increases with an increase in the imperfection amplitude, and the trends related to the welded purlin roofing systems are more notable. When the initial imperfection modes of the roofing systems and reticulated shell structures are equivalent, the initial imperfection is detrimental to the shell bearing capacity.

(3). In roofing systems, the purlin systems are the key factors to increase the static bearing capacity of the reticulated shell structures, and the purlin joints help intensify the effect of the purlin systems on the reticulated shell structures. In most cases, even when the shell is subjected to the highest static load, no plastic deformation occurs in any of the roofing system components. The axial constraints and out-of-surface bending moment constraints of the purlin joints are critical factors. In the design and analysis of reticulated shell structures, when considering the effect of the roofing system on the bearing capacity of reticulated shells, sufficient strength and rigidity of the purlin joints must be ensured during construction.

(4). The influences of the roofing systems' components on the reticulated shell structures' static stability are analysed. The pillars are important force transmission components, and the roofing systems' influences on reticulated shells' static bearing capacity increase with increasing pillar height. The roofing system's influences on the reticulated shell structures' static bearing capacity increases with increasing axial rigidity, rotational rigidity and yield strength in the purlin joints, the trend is more significant in the welded purlin roofing system. The roof panels' skin effects on the reticulated shells structures' static bearing capacity with L/1500 initial imperfection are 0.39%-3.13% and 0.37%-6.6% for shells with bolted and welded purlin systems respectively. The roof panels' skin effects on the reticulated shell structures' static bearing capacity with L/300 initial imperfection are 0.26%-5.22% and 0.27%-7.1% for shells with bolted and welded purlin systems respectively.

(5). The effect of the roofing systems on the bearing capacity of the reticulated shell structures with different factors is in agreement with the normal distribution, and the numerical values of these characteristics are listed in Table 2. The results can provide a reference for the design and analysis of reticulated shell structures.

Acknowledgements

This study was supported by the National Key Research and Development Program of China (2018YFC1504304), the National Nature Science Foundation of China (No. 51778183) and the National Science Foundation for Distinguished Young Scholars of China (No. 51525802). The authors extend their sincere gratitude for the support.

References

[1] Shizhao S. and Xi C., Stability of Reticulated Shells, Science Press, Beijing, 1999.
[2] Fan F, Cao Z.G., and Shen S.Z., "Elasto-plastic stability of single-layer reticulated shells", Thin Walled Struct, 48, 827-836, 2010.
[3] Feng F, Zhenggang C, Huihuan M, and Jiachuan Y., Elasto-plastic Stability of Reticulated Shells. Science Press, Beijing, 2015.
[4] Zhi X.D., Fan F., and Shen S.Z., "Elasto-plastic instability of single-layer reticulated shells under dynamic actions", Thin Walled Struct, 48, 837-845, 2010.
[5] Zhi X.D., Fan F., and Shen S.Z., "Failure of the single layer reticular dome under earthquake", China Civil Engineering Journal, 38, 11-20, 2005.
[6] M. Fong, Y.P. Liu, and S.L. Chan, "Second-Order Analysis and Experiments of Semi-Rigid and Imperfect Domes", Advances in Structural Engineering, 15(9), 1537-1546, 2012.
[7] S.Kato, I. Mutoh and M. Shomura, "Effect of joint rigidity on buckling strength of single layer lattice domes", Bulletin of the International Association for Shell and Spatial Structures, Madrid, Spain, 35, 101-109, 1994.
[8] Kato S., Mutoh I. and Shomura M., "Collapse of semi-rigidly jointed reticulated domes with initial geometric imperfections", J Construct Steel Res, 48, 145-68, 1998.
[9] Huihuan M., Feng F., Peng W., Zhang H. and Shen S.Z., "Experimental and numerical studies on a single-layer cylindrical reticulated shell with semi-rigid joints", Thin Walled Struct, 86, 1-9, 2015.
[10] Ma Huihuan, Ma Yueyang, Yu Zhiwei and Fan Feng, "Experimental and numerical research on gear-bolt joint for free-form grid spatial structures", Engineering Structures, 148, 522-540, 2017.
[11] Si Wei Liu, Rui Bai, Siu-Lai Chan and Yao-Peng Liu, "Second-Order Direct Analysis of Dome-like Structures Consisting of Tapered Members with I-Sections", Journal of Structural Engineering, 142(5), 04016009-1-11, 2016.
[12] Rui Bai, Si-Wei Liu and Siu-Lai Chan, "Modal and Elastic Time-History Analysis of Frames with Tapered Sections by Non-Prismatic Elements", International Journal of Structural Stability and Dynamics, 18(9), 1850106-1-34, 2018.
[13] Yao-Peng Liu, Siu-Lai Chan, Zuo-Lei Du and Jian-Wei He, "Second-order direct analysis of long-span roof structures", EUROSTEEL, 3930-3939, 2017.
[14] Y. P. Liu, S. J. Pan, Simon W. K. Leung and S. L. Chan, "Design and construction of long-span single-layer dome structures by direct analysis", HKIE TRANSACTIONS, 25(1), 29-43, 2018.
[15] Xie Xiangyang, Chen Guo and Yin Lei, "Key Technology in Design and Construction of Single-layer Reticulated Shell of H-section Units in MGM resorts Development LCC，Macau", Construction Technology, 45(21), 61-65, 2016.
[16] Code for design of steel structures (GB50017-2017), China Planning Press, China, 2017.
[17] Eurocode 3 Design of steel structures Part 1-6: Strength and Stability of Shell Structures, European Committee For Standardization, the European Union Per Regulation, 2007.
[18] Eurocode 3 Design of steel structures Part 1-3: General rules-Supplementary rules for cold-formed members and sheeting, European Committee For Standardization, the European Union Per Regulation, 2011.
[19] Technical Specification for Space Frame Structures (JGJ 7-2010), China Architecture & Building Press, China, 2010.
[20] Yongjun He and Xuhong Zhou, "Research on load bearing of the reinforced concrete roof board cooperative with grid structure", J Harbin Inst Technol, 39, 188-91, 2007.
[21] Yizhe Z., "Shaking table test and performance study of single-layer reticulated cylindrical shell with skin diaphragm", Beijing university of technology, Beijing, 2012.
[22] Maria Koliou and Andre Filiatrault, "Buildings with Rigid Walls and Flexible Roof Diaphragms. I: Evaluation of Current U.S. Seismic Provisions", Journal of Structural Engineering, 142(3), 04015166, 1-13, 2016.
[23] Maria Koliou and Andre Filiatrault, "Buildings with Rigid Walls and Flexible Roof Diaphragms. II: Evaluation of a New Seismic Design Approach Based on Distributed Diaphragm Yielding. Journal of Structural Engineering", 142(3), 04015167, 1-9, 2016.
[24] Li Wenliang, Zhi Xudong, Wang Duozhi, Fan Feng and Shen Shizhao, "Static stability analysis of a reticulated shell with a roofing system", Engineering Structures, 185, 315-331, 2019.
[25] Xudong Z., Zhang T., Wenliang L. and Feng F., "Effect of roofing system on elasto-plastic stability and seismic performance of single-layer reticulated shells", China Civil Engineering Journal, 50, 19-26, 2017.
[26] Duozhi W., Wenliang L., and Xudong Z., "Static stability analysis of reticulated shell with purlin roofing system", Eng Mech, 34 (Suppl), 71-77, 2017.
[27] Xie Xiangyang, Chen Guo and Yin Lei, "Multi-parameter simulation method of semi-rigid node of steel tubular scaffold with coulpers", Journal of Civil and Environmental Engineering, 41(4), 92-103, 2019.

Advanced Steel Construction - Vol. 16 No. 4 (2020) 370-379
DOI:10.18057/IJASC.2020.16.4.10

BUCKLING BEHAVIOR OF EQUAL ANGLE RESTRAINED BY WELD SEAM AT BOTH ENDS: NUMERICAL ANALYSIS

Zhong-Wei Zhao [1, 2, *], Xiong-Tao Fan [1], Xiang-Yang Jian [1], Bing Liang [3] and Hai-Qing Liu [1]

1 School of Civil Engineering, Liaoning Technical University, Fuxin 123000, China;
2 School of Civil Engineering, Southeast University, Nanjing, Jiangsu, 211189, China;
3 School of Mechanics and Engineering, Liaoning Technical University, Fuxin 123000, China
** (Corresponding author: E-mail: zhaozhongwei@lntu.edu.cn)*

ABSTRACT

Welding the reinforced component on the surface of a steel structure is a common method for reinforcing steel structures in practical engineering. Intermittent weld has been recognized as an efficient method for reducing the amount of field welding work and the cost of reinforcing work. The angles welded by intermittent weld have been widely utilized in practical engineering, such as the strengthening of steel column presented in this work. However, the mechanical behavior of angles welded by intermittent weld has not been clearly clarified. The buckling behavior of angles with weld limbs (AWL) is systematically investigated in this work to determine their loading capacity. The buckling factor and slenderness of AWLs are derived through a numerical analysis. The influences of weld length (Lw), yield strength (fy), residual stress, and initial geometrical imperfection on the buckling factor (φcr) are also investigated. The results indicate that material strength can be fully played out when applying intermittent weld. The results derived in this paper can provide reference for the design of angles welded by intermittent weld.

ARTICLE HISTORY

Received: 8 March 2020
Revised: 12 September 2020
Accepted: 18 September 2020

KEYWORDS

Angles with weld limbs;
Buckling factor;
Compression–flexure member;
Bearing capacity;
Finite element analysis

1. Introduction

Reinforcing steel columns has become an increasingly common practice in practical engineering due to the changes in their structural use, corrosion, and structural damage caused by incidental load, such as fire or seismic action [1-2]. Rectangular steel columns have been widely used in actual projects due to their ease of connection to the beam. Therefore, an efficient method for strengthening rectangular steel columns must be developed.

Steel columns are mainly strengthened by increasing their number of member sections, which in turn can be achieved by welding additional members to the original members and by welding steel angles to the steel columns. Steel angles are traditionally welded through a continuous weld, but this method is time consuming, expensive, and requires large-scale fieldwork. In addition, field welding is a labor-intensive task that does not guarantee a high weld quality. All these factors significantly increase the cost of reinforcement projects. The extent of field welding work also affects the reinforcement progress. Therefore, the continuous weld method must be replaced with intermittent weld or other efficient welding methods.

Intermittent weld can be used to replace continuous weld and to reduce the amount of weld workload in construction sites without changing the reinforcement effect as shown in [3-4]. However, the buckling behavior of angles that are welded via intermittent weld has not been thoroughly investigated in the literature. The force transferring mechanism between the angle and steel column also greatly differs from that of RC column reinforcement [5-8]. The buckling of steel members has always been a hot topic among researchers and engineers, and many mature research findings have been obtained in recent years [9-13]. For instance, Hussain [14-15] proposed an effective stress-strain relationship representing the typical failure modes and initial imperfections and this effective stress-strain relationship can be used for the direct analysis of steel structures made of angle sections without use of the effective length method. Ban et al. [16] investigated the overall buckling behavior of high-strength steel welded section columns. Li et al. [17-18] employed numerical and experimental methods to investigate 12 Q690 HS steel welded box and I-section columns. Nie et al. [19] performed an experiment on eight box columns with varying cross sections, slenderness, and eccentricities. Previous studies on buckling have mainly focused on members that are subjected to axial load, while only few studies have examined the buckling of compression–flexure members. Although the mechanical behavior of angles has been widely investigated in the literature [14-17], such behavior greatly varies when applied for strengthening steel columns. The failure mode of angle welded by intermittent weld seam (tested by the authors) is shown in Fig. 1. It can be seen that the failure mode of angle welded by intermittent weld is different with that welded by continuous weld. The load capacity of angles welded by intermittent weld has not been revealed. This work investigates the axial loading capacity of angles that are welded by an intermittent weld seam, which forms the premise for investigating the force transferring mechanism between angles and steel columns

(a) Schematic (b) Practical project (c) Parameters of the reinforced scheme

Fig. 1 Steel column reinforcement method

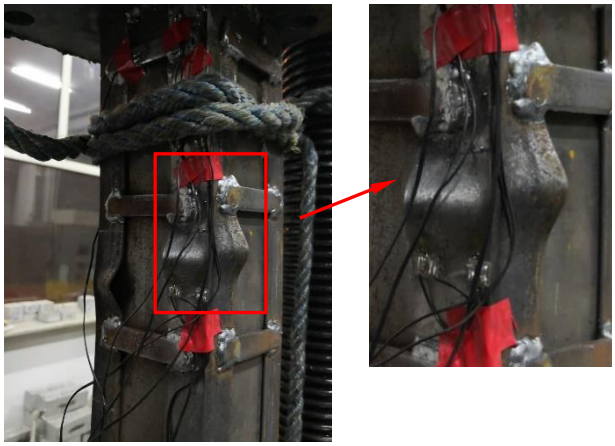

Fig. 2 Failure mode of angle welded by intermittent weld seam

2. Detailed description of angles with weld limbs (AWL)

When steel angles are used to strengthen box steel columns, both limbs are welded to the columns. The steel angles are subjected to eccentric loading when the column is subjected to axial load. The characteristics of an AWL that is subjected to both axial force and moment (Fig. 3) may greatly differ from those of angles that are only subjected to axial force. The appearance of moment will reduce the loading capacity for load in the axial direction. The influence of moment is considered in designing a compression–flexure member in GB50017[24] by using Eq. 1, which can also be used to assess the reliability of a member. However, the buckling capacity of a specified compression–flexure member, such as AWL, cannot be easily calculated.

$$\frac{N}{\varphi_x Af}+\frac{\beta_{mx}M_x}{\gamma_x W_{1x}(1-0.8N/N'_{Ex})}\le 1, \tag{1}$$

where N is the design value of axial force, φ_x is the buckling factor in the plane of the bending moment, M_x is the maximum moment along the member, β_{mx} is the equivalent moment factor, W_{1x} is the gross section modulus, and $N'_{Ex}=\pi^2EA/(1.1\lambda^2)$.

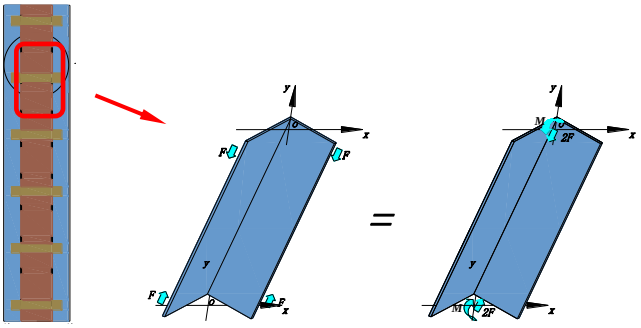

Fig. 3 Schematic of AWL

The detailed dimensional size of AWL is shown in Fig. 4, where L denotes the overall length of AWL, L_w denotes the length of the weld seam at both ends of the AWL, and t and w denote the thickness and width of the AWL, respectively.

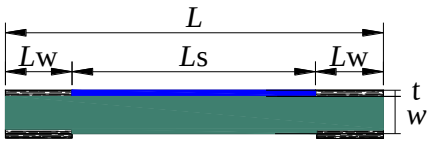

Fig. 4 Dimensional size of AWL

This work aimed to propose a simplified method for computing the axial bearing capacity of AWLs. The buckling factor φ_{cf} of AWL in this work indicated the ratio of axial bearing capacity (f_u) and Af_y. Given that the value of φ_{cf} automatically considers the influence of bending moment, the loading capacity of AWLs with a specified section can be easily derived when the buckling factor is known. The relationship between φ_{cf} and λ_n was also systematically investigated in this work. λ_n denotes the slenderness ratio λ normalized by the yield strength f_y of steel as shown in Eq. (2).

$$\lambda_n=\frac{\lambda}{\pi}\sqrt{\frac{f_y}{E}}, \tag{2}$$

Given that the rotation of both ends of the AWL was restrained by the weld seam, the AWL was assumed to be in the fixed-fixed condition. Therefore, the computational length factor was set to 0.5. The slenderness of AWL can be derived as i_x where denotes the gyration radius about the x-axis.

$$\lambda=\frac{L-2L_w}{2i_x}=\frac{L_s}{2i_x}, \tag{3}$$

3. Finite element model

Finite element analysis was conducted with the finite element code ANSYS to investigate the relationship between φ_{cf} and λ_n. All components were modeled with the SOLID45 element. The mesh at the weld seam was refined to obtain accurate results. The ideal elastic–plastic model was adopted in the numerical analysis. The constitutive relationship of steel is presented in Fig. 5. The weld seam was not considered in the FE model for simplification and under the premise that the weld cannot encounter failure before the buckling of AWL. Vertical displacement was applied at the weld zone (Fig. 6.), and the translational degrees of the weld zone were fixed.

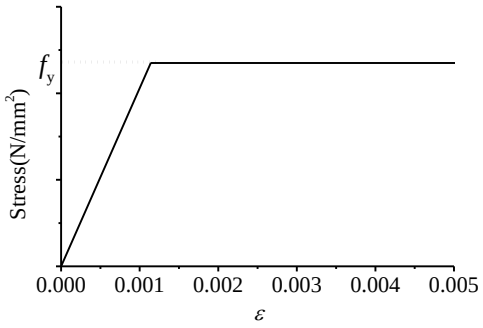

Fig. 5 Constitutive relationship of steel

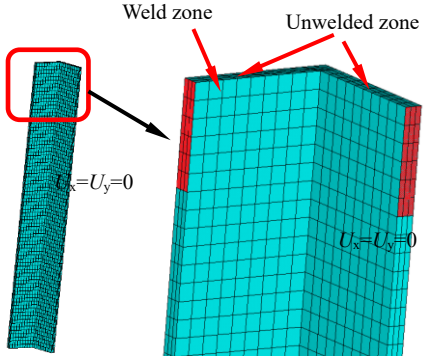

Fig. 6 Restraint condition at the end of AWL

4. Validation of numerical model

The experiment was conducted to validate the reliability of FE model. The section of AWL was *L*30×3 and the length were set to 200, 400 and 500 mm. The detailed information about test specimen was shown in Tab. 1. A total of 9 specimens were tested and the load was applied in displacement controlling method with a rate equaling to 0.1 mm/s. The meaning of each symbol was shown in Fig. 4. The composition of test specimens was shown in Fig. 7. The experiment was conducted by utilizing universal testing machine with measuring range of 300 kN, as shown in Fig. 8. The compression force was applied and the deformation of one specimen was shown in Fig. 9. The load-displacement curves of each specimen were shown in Fig. 10. The ultimate load of each specimen derived in the experiment was shown in Tab. 2. It can be seen form the results that the ultimate load is obviously affected by the L_w and L.

The expected failure mode was the symmetric bending failure which was shown in Fig. 9. The failure mode of each specimen derived in experiment was shown in Fig. 11. It can be seen that the failure mode of SJ-200-60 was local buckling of AWL. The SJ-400-60 and SJ-500-60 failed by the fracture of weld and local buckling of AWL. The failure modes of SJ-400-60 and SJ-500-60 was not consistent with the actual condition. This failure mode can be avoided due to the existence of steel column.

The standard tension test was conducted to determine the ultimate load which was the most important parameter in present work. The test coupon was taken from the AWL and the standard tension test was performed three times and the mean value was extracted, as shown in Fig. 12 and Fig. 13. The standard tension test indicated that the ultimate load of test specimen was 108 kN. Then the buckling factor of each specimen was computed and compared with that derived in FEA. The comparison was shown in Fig. 14. It can be seen that the buckling factor derived in numerical analysis agreed well with the experiment and the reliability of FE model can be validated

Table 1
Detailed information about test specimens

Specimen number	Section (mm)	L (mm)	L_w (mm)	L_s (mm)	Normalized slenderness λ_n	Computational buckling factorφ
SJ-200-40	*L*30×3	200	40	120	0.1105	0.7904
SJ-400-40	*L*30×3	400	40	320	0.2946	0.7801
SJ-500-60	*L*30×3	500	40	420	0.3866	0.7728
SJ-200-20	L30×3	200	20	160	0.1473	0.4758
SJ-400-20	L30×3	400	20	360	0.3314	0.4393
SJ-500-20	L30×3	500	20	460	0.4235	0.4191
SJ-200-60	L30×3	200	60	120	0.0736	0.9808
SJ-400-60	L30×3	400	60	320	0.2577	0.9776
SJ-500-60	L30×3	500	60	420	0.3498	0.9742

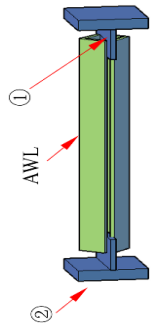

Fig. 7 Composition of test specimen

Fig. 8 Loading device

Fig. 9 Deformation of SJ-500-20

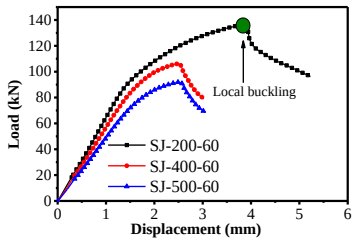

a) L_w=60 mm

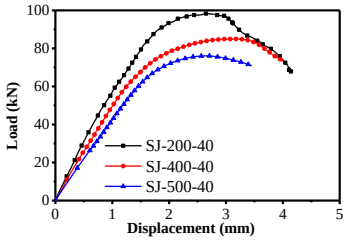

b) L_w=40 mm

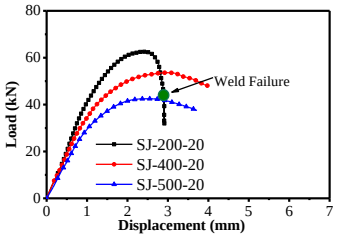

c) L_w=20 mm

Fig. 10 Load-displacement curves of test specimens

Table 2
Ultimate load of each specimen

Specimen number	Ultimate load (kN)	Specimen number	Ultimate load (kN)
SJ-200-60	135.056	SJ-400-20	53.595
SJ-200-40	90.991	SJ-500-60	85.05
SJ-200-20	62.532	SJ-500-40	76.005
SJ-400-60	103.950	SJ-500-20	42.39
SJ-400-40	97.875		

Fig. 11 Failure mode of each specimen

Fig. 12 Specimen in standard tension test

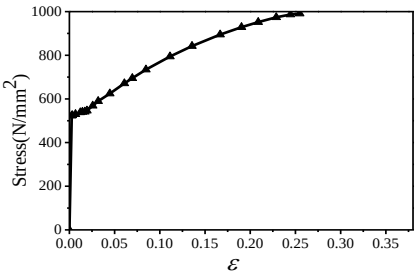

Fig. 13 The stress-strain curve

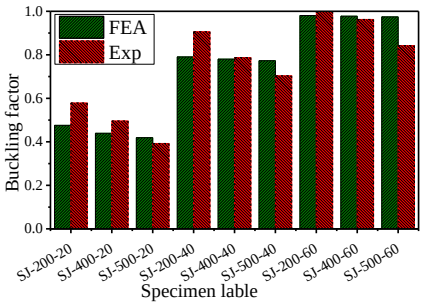

Fig. 14 Comparison of buckling factor

5. Effects of initial geometric imperfections

The AWL with a typical sectional scale that is often used in actual projects was analyzed in this paper. Tab. 3 presents detailed information on the specimens used in the numerical analysis. The yield strength of steel was varied to investigate its influence on φ_{cf} .

The effect of initial geometrical imperfection was investigated in this section. Linear buckling analysis was conducted and an initial imperfection was applied according to the buckling model. The buckling mode of $L45\times5$ angle corresponding to L_w=90 mm is shown in Fig. 16. It can be observed that the first buckling mode is not suitable as it is not consistent with the failure mode shown in Fig. 2. The failure mode indicated by the first buckling mode cannot happened due to the existence of steel column. So, the geometrical imperfection is applied according to the fourth buckling mode. The amplitude of the initial imperfection was set to 1‰ of the column height. Static analysis was conducted afterward. The large deformation effect was considered by 'nlgeom,1' command. The Newton-Raphson option was specified to solve the nonlinear problems. The initial substep number was set to 1000 and the max substep number was set to 2000. The influence of geometrical imperfections is shown in Fig. 15. The buckling factor φ_{cf} was almost not influenced by geometrical imperfection when the amplitude was set to 1‰ of the column height. This factor greatly differed from the axially compressed bar. Given that the influence of initial imperfection can be neglected, the influence of initial geometrical imperfection was not considered in the analysis.

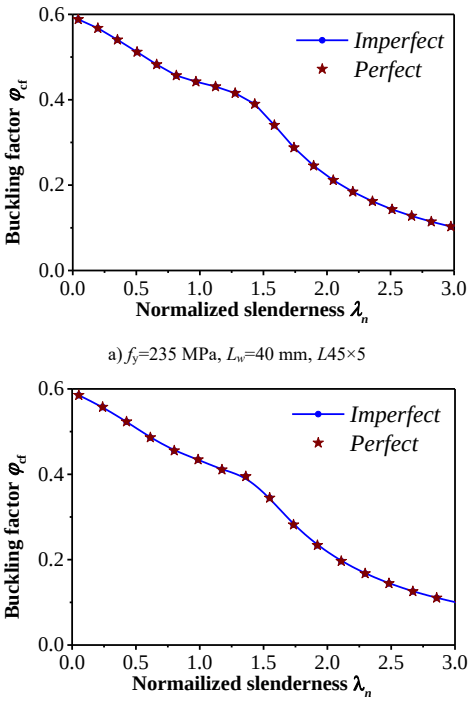

Fig. 15 Influence of geometric imperfection on buckling factor

Table 3
Detailed information on the specimens

Number	Section	f_y (MPa)	A (cm^2)	i_y (cm)	F_y (kN)
1	*L*50×5	235	4.80	0.98	112.8
2	*L*56×5	235	5.41	1.1	127.1
3	*L*63×5	235	6.14	1.25	144.3
4	*L*45×5	235	4.29	0.88	100.8
5	*L*45×5	345	4.29	0.88	148.0
6	*L*45×5	610	4.29	0.88	261.7
7	*L*70×5	235	6.87	1.39	161.4
8	*L*70×5	345	6.87	1.39	237.0
9	*L*70×5	420	6.87	1.39	288.5
10	*L*70×5	610	6.87	1.39	419.1
11	*L*40×5	235	3.79	0.78	89.1
12	*L*36×5	235	3.38	0.7	79.4
13	*L*56×8	235	8.37	1.09	196.7
14	*L*63×8	235	9.51	1.23	223.5
15	*L*70×8	235	10.7	1.37	251.5
16	*L*75×8	235	11.5	1.47	270.3
17	*L*75×8	345	11.5	1.47	396.7
18	*L*75×8	420	11.5	1.47	483.0
19	*L*75×8	610	11.5	1.47	701.5
20	*L*200×20	235	76.5	3.93	1797.8

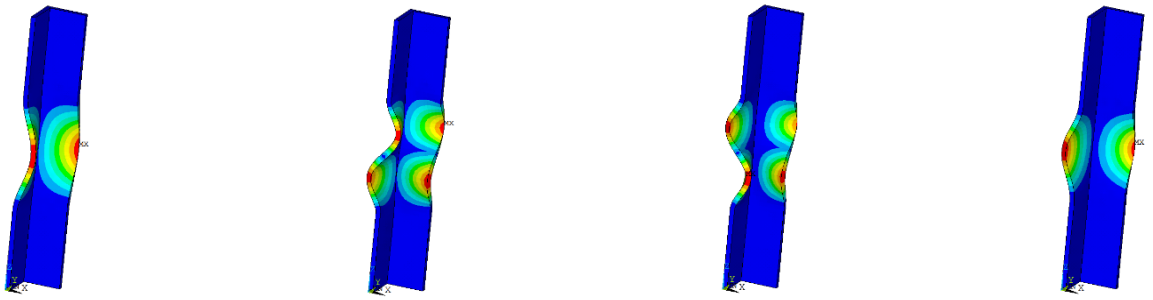

a) The first buckling mode b) The second buckling mode c) The third buckling mode d) The fourth buckling mode

Fig. 16 The first four buckling modes

6. Influence of residual stress

The influence of residual stress on the buckling capacity of the angle was systematically investigated in this section. The distribution mode of residual stress in the length direction is illustrated in Fig. 17, where "+" denotes the tensioning stress, while "-" denotes the compression stress. The residual stress was applied through initial stress in general finite element code ANSYS. The values of β were set to 0, 0.3, 0.5, and 0.7. The contour of residual stress is illustrated in Fig. 18. Although some errors were observed between the actual and target values of residual stress, these errors were very small and could be ignored.

The curves of the buckling factor along with λ_n under the influence of residual stress are shown in Fig. 19. The yield strength of the adopted steel was set to 235, 345 and 610 MPa to determine the influence of welding residual stress on angles with different yield strengths. The residual stress can reduce the buckling factor of short AWLs but can increase the buckling factor of AWLs with large slenderness ratios. The influence of residual stress on buckling factor increased along with the residual stress magnitude (i.e., the value of β). However, the change in the buckling factor between $0.3f_y$ and $0.7f_y$ was very small. Therefore, only β=0.7 was considered in the latter analysis. The results in Fig. 19 indicate that the influence of residual stress on AWLs with large slenderness ratios can be ignored for safety. Given that residual stress has a small influence on the buckling factor of AWLs with small slenderness ratios and that the value of β in actual conditions is less than 0.7, the influence of residual stress was ignored in this study for simplicity.

The failure modes (λ_n=0.07) corresponding to different values of σ_r are presented in Fig. 20. The residual stress magnitude directly influences the stress distribution at the failure state. The tensioning stress at the middle part of the AWL decreased along with an increasing σ_r, thereby suggesting that the strength of the material at this location cannot be fully played out. In this case, the buckling capacity of the AWL is reduced.

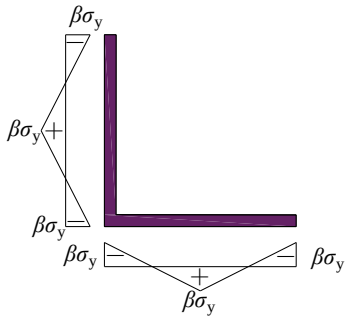

Fig. 17 Typical distribution mode of residual stress

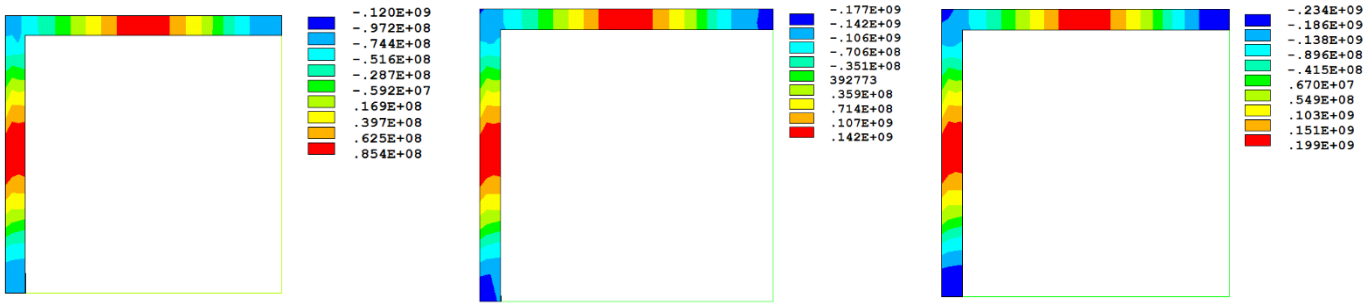

a) σ_r=0.3f_y b) σ_r=0.5f_y c) σ_r=0.7f_y

Fig. 18 Distribution of residual stress (f_y=345 MPa)

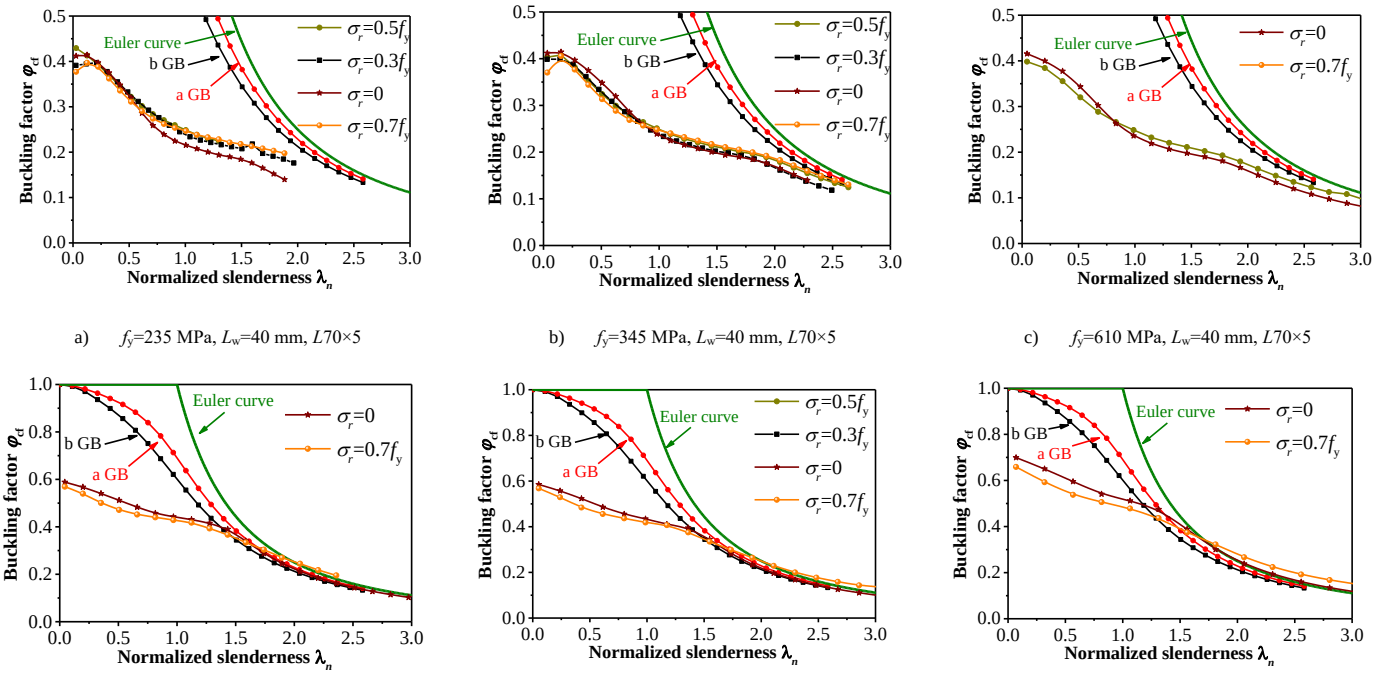

a) f_y=235 MPa, L_w=40 mm, L70×5 b) f_y=345 MPa, L_w=40 mm, L70×5 c) f_y=610 MPa, L_w=40 mm, L70×5

d) f_y=235 MPa, L_w=40 mm, L45×5 e) f_y=345 MPa, L_w=40 mm, L45×5 f) f_y=610 MPa, L_w=40 mm, L45×5

Fig. 19 Influence of residual stress on buckling factor

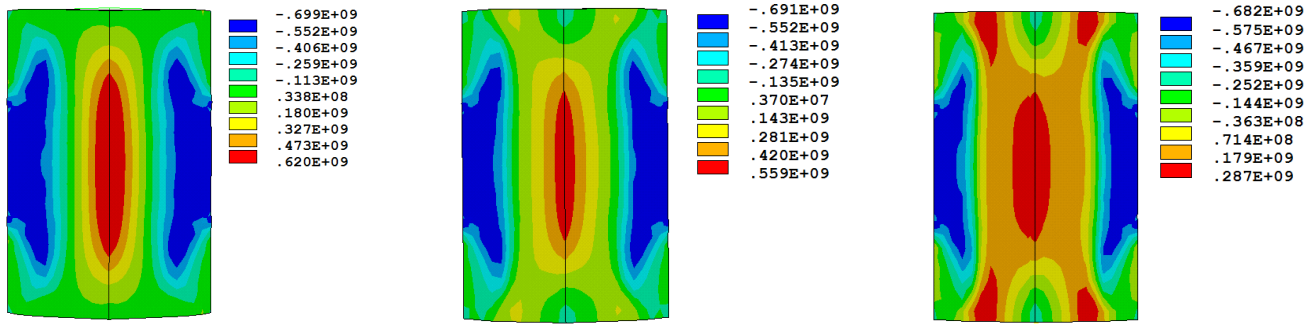

a) σ_r=0 b) σ_r=0.5f_y c) σ_r=0.7f_y

Fig. 20 Failure modes corresponding to different values of σ_r (f_y=610 MPa)

7. Influence of weld length on buckling capacity

7.1. Effect of L_w on buckling factor

The weld length at both ends of an AWL can directly determine the constraint strength. The influence of weld length on the buckling capacity of AWLs was investigated in this section. The curves of buckling factor and λ_n corresponding to different values of L_w are compared in Fig. 21 a, which was derived based on section L45×5. The maximum buckling factor was equal to 0.36, 0.58, 0.80, and 1.0 when the values of L_w were 20, 40, 60, and 80 mm, respectively. The AWL was welded to the surface of the steel column, and the translational degree of weld is equal to 0. Therefore, the constraint condition changed along with the values of L_w, while the constraint induced by the weld was strengthened along with an increasing L_w. The AWL was subjected to axial force when the value of L_w reached 200 mm. The steel grade nearly had no influence on the buckling factor. Fig. 21 d shows that the buckling factor changes almost linearly along with L_w for L70×5, while the AWL with section L70×5 is subjected to axial force when the value of L_w is twice larger than that of w. In other words, the AWL can be seen as an axial compression bar when the length of the weld is twice larger than the value of w.

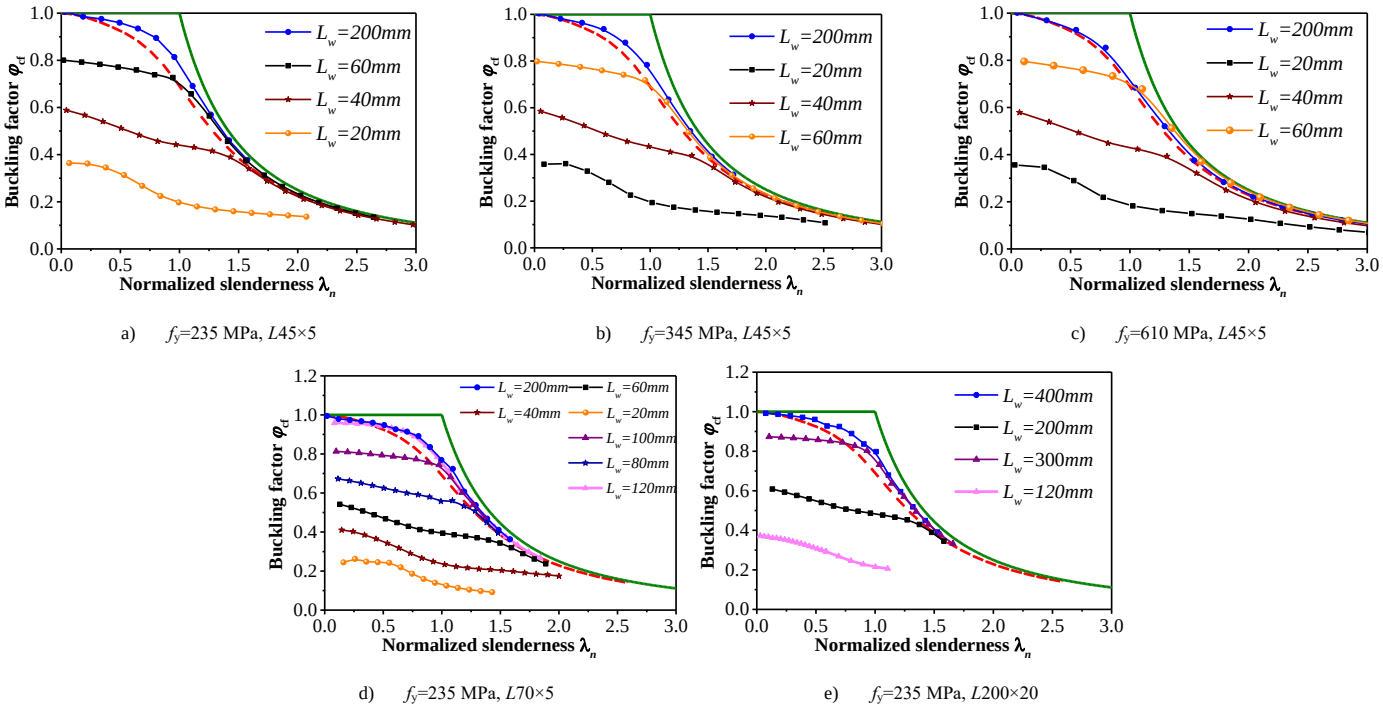

a) f_y=235 MPa, L45×5 b) f_y=345 MPa, L45×5 c) f_y=610 MPa, L45×5

d) f_y=235 MPa, L70×5 e) f_y=235 MPa, L200×20

Fig. 21 Influence of L_w on buckling factor

7.2. Effect of constraint condition on buckling factor

Only the translational degree of the weld was constrained in the above analysis. The translational degrees of the unwelded zone at the top and bottom of the AWL were not constrained because this zone was not directly connected to the steel column as shown in Fig. 6. However, the translational degree of the unwelded zone could be constrained by the steel column in a certain degree. Therefore, the translation degree of the unwelded zone was constrained to investigate its influence on the buckling factor of AWLs. The symbols "C" and "F" denote that the translational degrees of the unwelded zone are restrained and not restrained, respectively. The results are presented in Fig. 22, where the symbols "C" and "F" denote that the translation degree of the unwelded zone is fixed and not constrained, respectively. Given that the translational degree does not have any influence on the buckling factor of AWLs, this influence can be neglected.

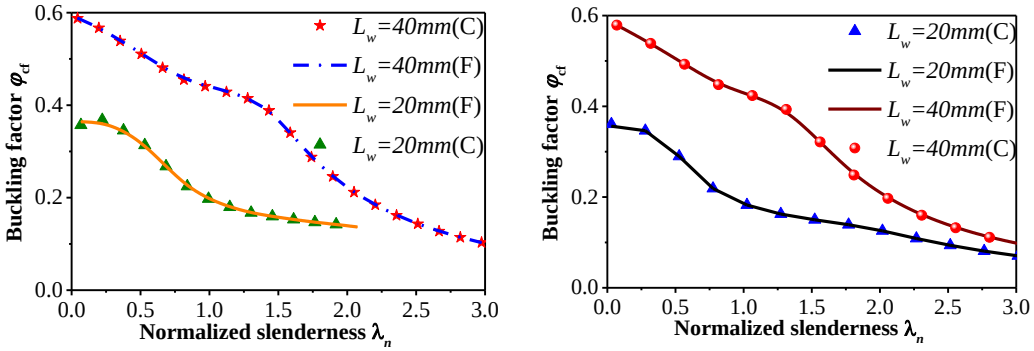

a) f_y=235 MPa, L45×5 b) f_y=610 MPa, L45×5

Fig. 22 Influence of constraint condition on buckling factor

7.3. Effect of L_w on failure mode

The effect of L_w on the failure mode of angle was systematically investigated in this section. The overall length of AWL (L) was set to 0.6 m, while the length of the weld zone (L_w) was set to different values. The thicknesses of AWL (T) were set to 3 mm and 8 mm. The restraint conditions of the top and bottom of the angle were set to pined-pinned (the translational degree of the unwelded zone was not restrained) and fixed-fixed (the translational degree of the unwelded zone was fixed), respectively, to investigate the influence of the constraint condition on the mechanical behavior of the angle. The load–displacement curves of AWLs with different L_w are presented in Fig. 23 and Fig. 24. The loading capacity of AWL increased along with the value of L_w. Material strength can be fully played out when the L_w exceeds 100 mm. The AWL seemed to be an axially compressed bar when L_w was sufficiently large. A rigid loading region could also be formed at two sides of the AWL when the L_w was sufficiently large to ensure that the ultimate loading capacity could be reached. The loading capacity of the AWL also linearly decreased along with thickness (T) in the two constraint conditions.

The von Mises stress of AWL is presented in Fig. 25 and Fig. 26. The stress level at the middle part of the AWL was very low when L_w was equal to 10 mm. Meanwhile, the stress level at the low stress zone increased along with L_w. The size of the low stress zone also decreased along with increasing L_w. A rigid loading region could be formed at two sides of the AWL when L_w was sufficiently large. The stress was uniformly distributed at the middle part of the AWL.

The results derived in these two constraint conditions are compared in Fig. 27. The constraint condition almost had no influence on loading capacity when L_w exceeded 100 mm. The constraint condition could be seen as fixed-fixed when L_w exceeded 100 mm. The constraint condition also had a slight influence on loading capacity when L_w was equal to 10 mm and 15 mm. Therefore, the constraint conditions had minimal influence on axial loading capacity when L_w was not sufficiently large.

The development of stress in the length direction during the loading process is illustrated in Fig. 28. The value of L_w was set to 200 mm in this analysis. The strength of the material between welded zones can be fully played out. Given that the buckling of limb can occur after the full section is yielded, the material strength can be fully played out by using intermittent weld.

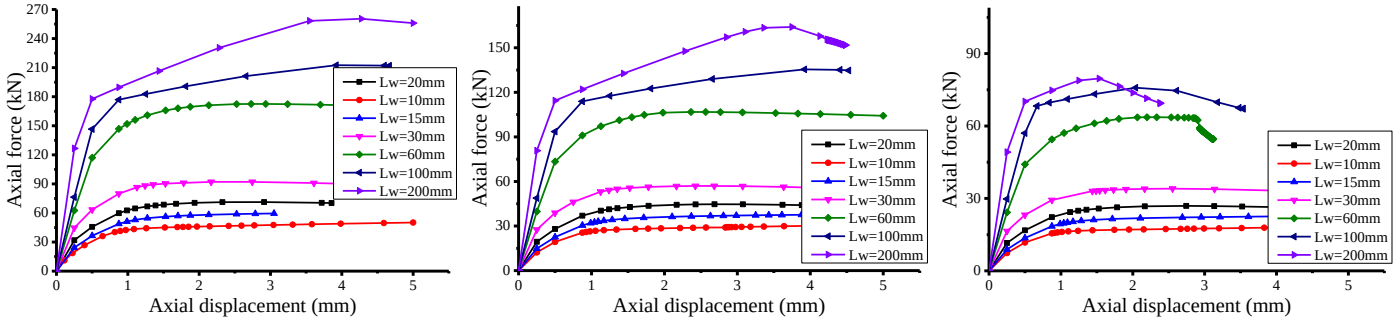

a) T=8 mm, L=0.6 m b) T=5 mm, L=0.6 m c) T=3 mm, L=0.6 m

Fig. 23 Influence of weld length on loading capacity (pined-pinned condition)

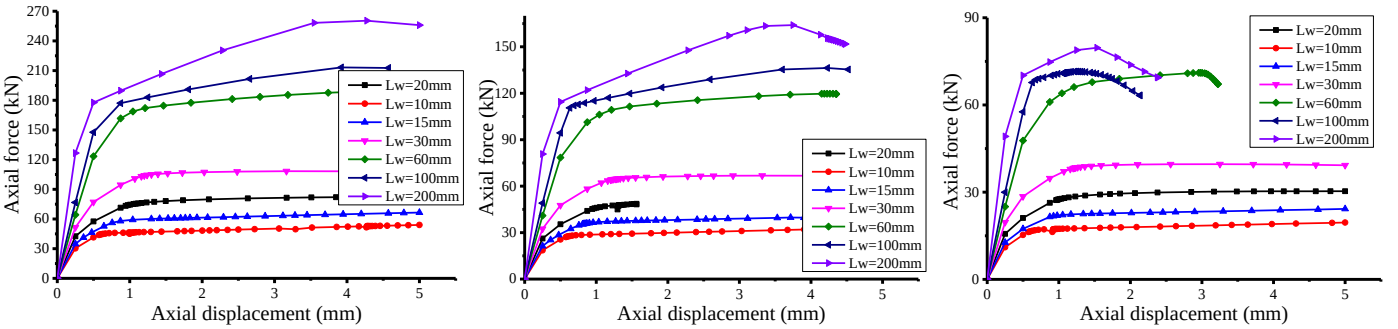

a) T=8 mm, L=0.6 m b) T=5 mm, L=0.6 m c) T=3 mm, L=0.6 m

Fig. 24 Influence of weld length on loading capacity (fix-fixed condition)

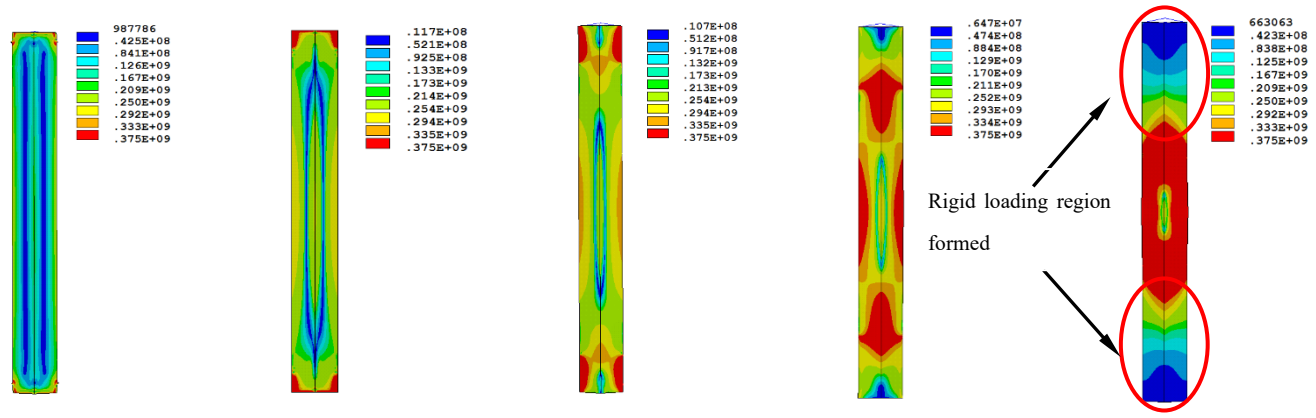

a) L_w=10 mm b) L_w=30 mm c) L_w=60 mm d) L_w=100 mm e) L_w=200 mm

Fig. 25 Failure modes of angles with different weld lengths (T=8 mm, L=0.6 m)

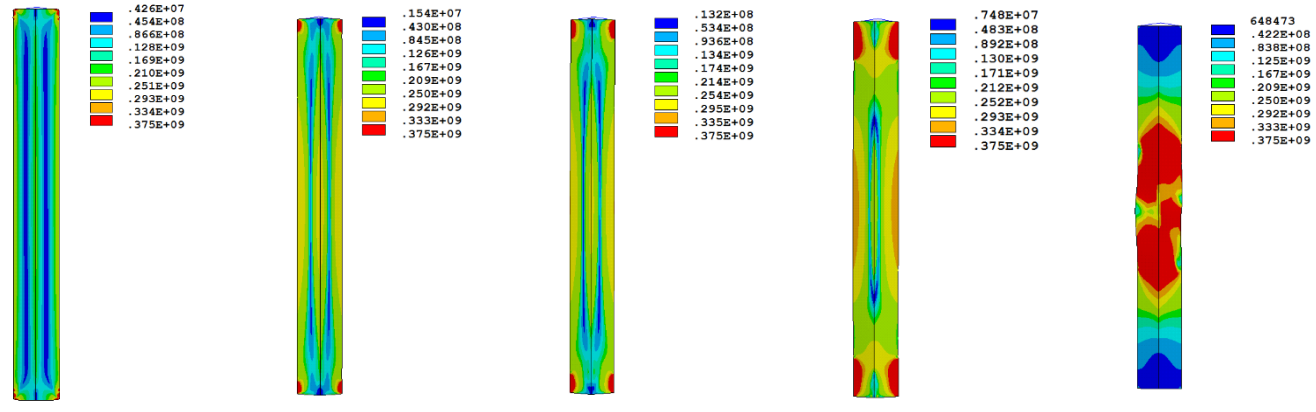

a) L_w=10 mm b) L_w=20 mm c) L_w=30 mm d) L_w=60 mm e) L_w=200 mm

Fig. 26 Failure modes of angles with different weld lengths (T=3 mm, L=0.6 m)

8. Influence of sectional dimension and steel grade

8.1. Effects of sectional dimension on buckling capacity

The aforementioned results indicated that the sectional dimension could significantly influence the buckling factor of AWL. The yield strength f_y was set to 235 MPa. The section typically adopted in actual projects was systematically investigated. Fig. 29 shows that the buckling factor significantly decreases along with an increasing w. This finding can be attributed to the fact that the additional moment caused by the bias of load increases along with w. The curves of buckling factor and λ_n approached the Euler curve as λ_n continued to increase, thereby indicating that the failure mode was transformed from strength failure to buckling failure after λ_n reached a certain value. The bias of load could be neglected at that time and the AWL seemed to be subjected to axial force. AWL with different thicknesses are compared in Fig. 29 c. Given that the shear stiffness of the welded zone increased along with t, the buckling factor of AWL increased along with t when the value of w was kept constant.

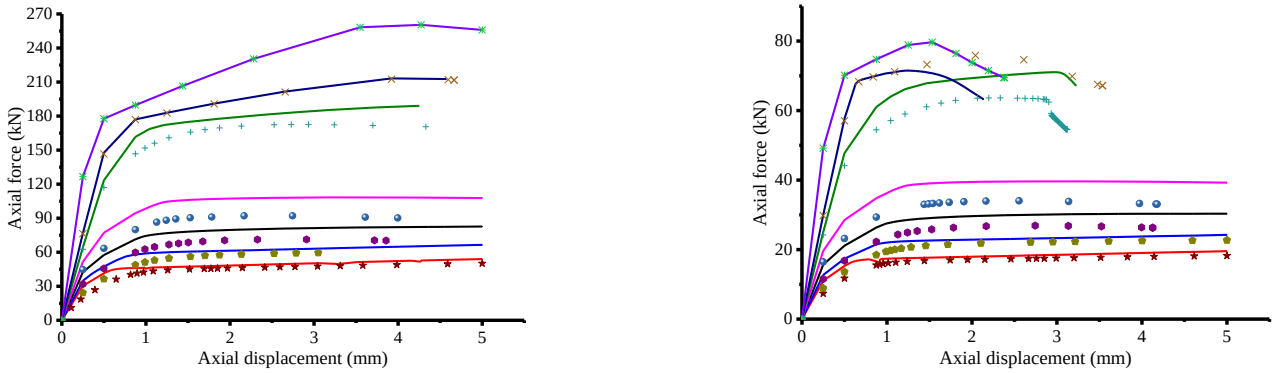

a) T=8 mm, L=0.6 m b) T=3 mm, L=0.6 m

Fig. 27 Comparison of the results derived in different constraint conditions

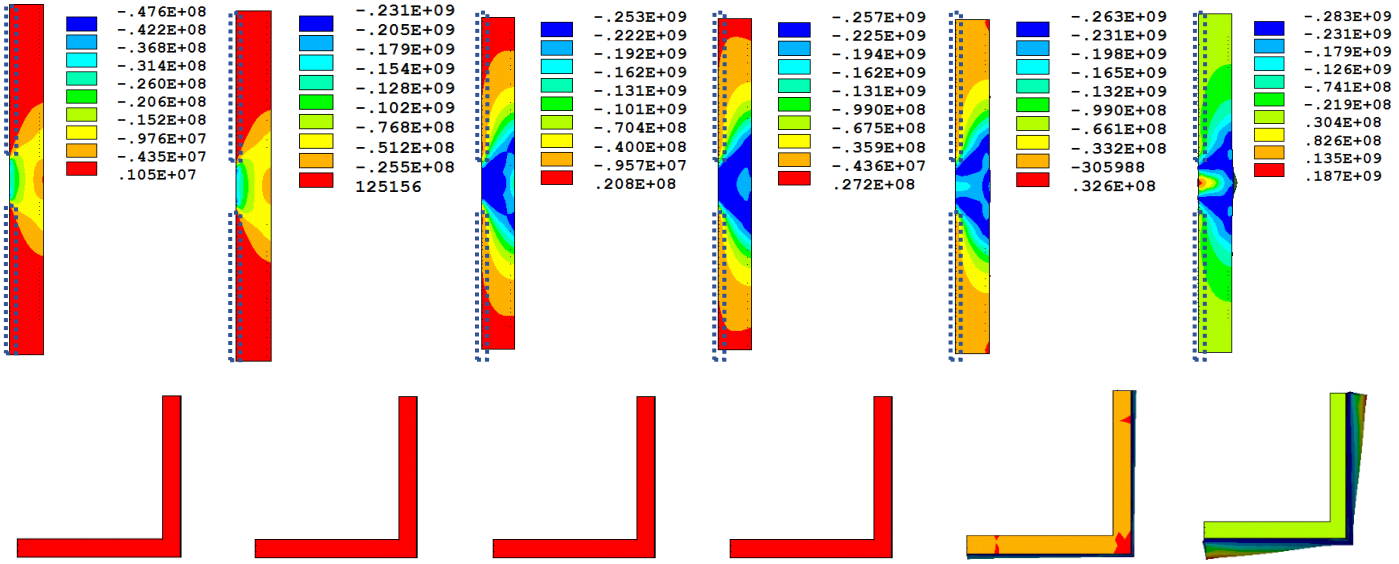

Fig. 28 Development of vertical stress during the loading process (Unit: Pa)

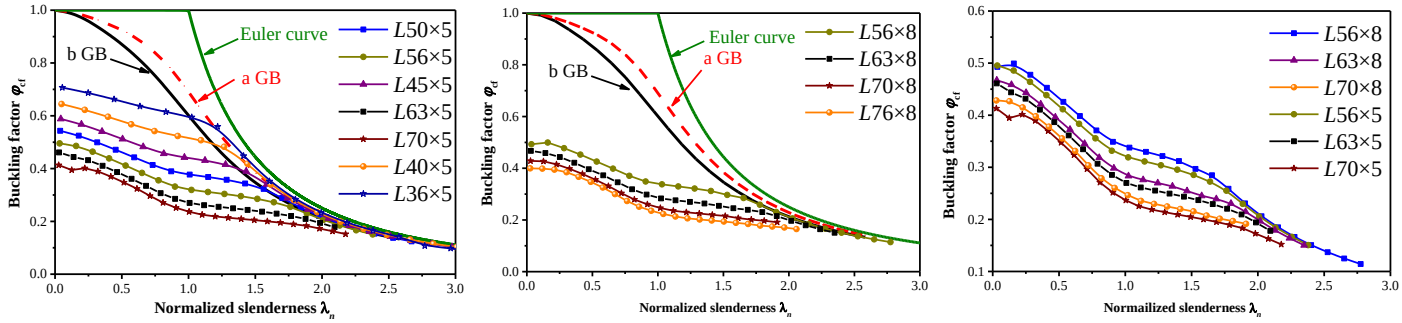

a) f_y=235 MPa, L_w=40 mm, t=5 mm b) f_y=235 MPa, L_w=40 mm, t=8 mm c) Comparison of AWL with different sections

Fig. 29 The influence of w/t ratios on buckling capacity

8.2. Effects of steel grades (f_y) on buckling capacity

High-strength steel has been widely utilized along with the advancements in material science. The possible influence of yield strength f_y on buckling factor was investigated in this section. The sectional dimensions were set to $L70\times5$ and $L75\times8$, while the values of f_y were set to 235, 345, 410, and 610 MPa. The curves of the buckling factor along with λ_n are shown in Fig. 30.

The yield strength f_y has a very slight influence on the buckling factor of AWL, especially for $L70\times5$ and $L75\times8$. Therefore, the influence of f_y on the buckling factor of AWL can be neglected.

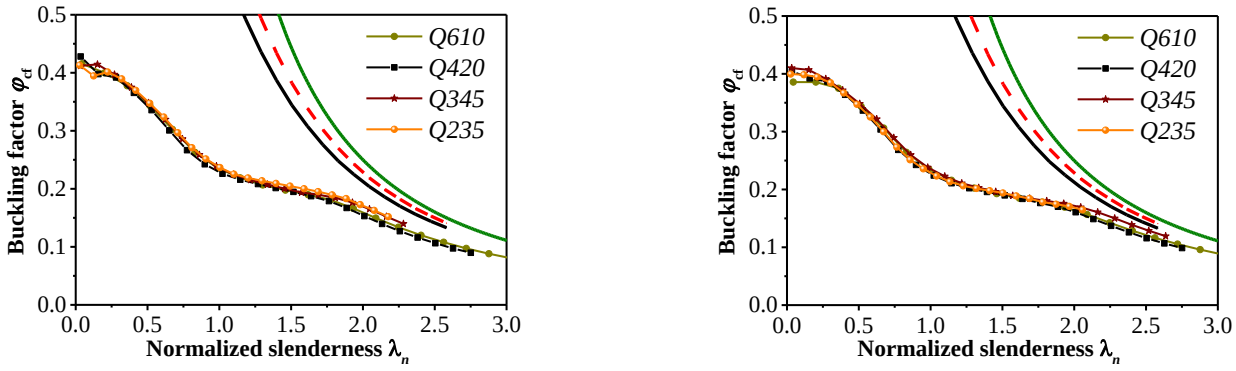

a) t=5 mm, L_w=40 mm, L70×5 b) t=8 mm, L_w=40 mm, L75×8

Fig. 30 Influence of f_y on buckling factor

9. Conclusions

The angles welded by intermittent weld have been widely utilized in pratical engineering, such as the strengthening of steel column presented in this work. However, the mechanical behavior of angles welded by intermittent weld has not been clearly clarified. There is no guidance for the design of angles welded by intermittent weld, such as the weld length (L_w) and the intermintent distance. The work presented is performed based on this background. The mechanical behavior of AWLs that are used for strengthening steel box columns was investigated in this paper and their buckling factor was systematically computed. The influence of L_w, f_y, residual stress, and initial geometrical imperfection was also studied. The conclusions are summarized as follows:

1) The influence of initial geometrical imperfection on the buckling factor of AWLs can be neglected, and residual stress has a slight influence on buckling factor. However, residual stress has different effects on AWLs with small and large slenderness.

2) The AWL seems to be an axial compression bar when the value of L_w is twice larger than the width of AWL. The buckling factor can be obtained through curve a in GB 50017-2003 for safety.

3) The constraint condition at both ends of the AWL has a minimal influence on axial loading capacity when the value of L_w is not sufficiently large. This finding can be ascribed to the fact that the constraint from the weld is not strong enough when L_w has a small value.

4) The comparison among AWLs with different thicknesses reveals that the buckling factor of AWL increases along with t while the value of w is kept constant.

5) The curves of the buckling factor and λ_n approach the Euler curve as λ_n continues to increase. This finding indicates that the failure mode changes from strength failure to buckling failure after λ_n reaches a certain value. The bias of load can be neglected and the AWL seems to be subjected to axial force.

Acknowledgements

The work described in this paper was financially supported by the State Key Research Development Program of China (Grant Nos. 2016YFC0801404 and 2016YFC0600704) and Basic Research Project of Education Department of Liaoning Province (LJ2020JCL036).

References

[1] H.Fukuyama; S.Sugano. Japanese seismic rehabilitation of concrete buildings after the hyogoken-nanbu earthquake. Cement and Concrete Composites, 2000, 22(1): 59–79.
[2] Garzón-Roca, Julio;Ruiz-Pinilla, Joaquín;Adam, Jose M.; Calderón, Pedro A. An experimental study on steel-caged RC columns subjected to axial force and bending moment. Engineering Structures, 2011, 33(2): 580–590.
[3] Yang Yuan, Chen Zhihua, Zhao Zhongwei, Liu Xiaoke. Axial compression performance of steel box columns with different strengthening schemes. International journal of steel structures, 2017, 17(2): 367-378.
[4] Zhongwei Zhao, Haiqing Liu, Bing Liang. Mechanical behavior of angle used in strengthening of rectangular column[J]. Structures and Buildings, 2019. (DOI: 10.1680/jstbu.18.00076)
[5] G. Campione; A. Monaco(1); M. Papia. Simplified analytical model for moment–axial force domain in the presence of shear in R.C. members externally strengthened with steel cages. Materials and Structures, 2016, 49(8): 3143-3157.
[6] Campione G. Analytical model for high strength concrete columns with square cross-section. Structural engineering and mechanics, 2008, 28(3): 295-316.
[7] Adam JM; Ivorra S; Gimenez E; Moragues JJ; Miguel P; MirAgall C; Calderon PA. Behaviour of axially loaded RC columns strengthened by steel angles and strips. Steel and composite structures, 2007, 7(5): 405-19.
[8] Adam JM; Giménez E; Calderón PA; Pallarés FJ; Ivorra S. Experimental study of beam-column joints in axially loaded RC columns strengthened by steel angles and strips. Steel and composite structures, 2008, 8(4): 329-42.
[9] R.C. Spoorenberg, H.H. Snijder, L.G. Cajot, N. Popa, Buckling curves for heavy wide flange QST columns based on statistical evaluation, J. Constr. Steel Res. 101 (2014) 280–289.
[10] J. Jönsson, T.C. Stan, European column buckling curves and finite elementmodelling including high strength steels, J. Constr. Steel Res. 128 (2017) 136–151.
[11] D. Chen, J. Yang, S. Kitipornchaia. Buckling and bending analyses of a novel functionally graded porous plate using Chebyshev-Ritz method. Archives of Civil and Mechanical Engineering, 19(1): 157-170.
[12] M. Bodaghi, A.R. Damanpack, G.F. Hu, W.H. Liao. Large deformations of soft metamaterials fabricated by 3D printing. Materials & Design, 2017, 131: 81-91.
[13] Marian Antoni Giżejowski, Radosław Szczerba, Marcin Daniel Gajewski, Zbigniew Stachura. Buckling resistance assessment of steel I-section beam-columns not susceptible to LT-buckling. Archives of Civil and Mechanical Engineering, 2017, 17(2): 205-221.
[14] A. Hussain, Zuo-Lei Du, Yao-Peng Liu and Siu-Lai Chan, Stability design of single angle member using effective stress-strain method. Structures, 2019 (20): p. 298-308.
[15] A. Hussain, Yao-Peng Liu and Siu-Lai Chan, Stability design of single angle member using effective stress-strain method. Advances in Structural Engineering, 2020, Vol. 23(10) 2121–2135.
[16] H. Ban, G. Shi, Overall buckling behaviour and design of high-strength steel welded section columns, J. Constr. Steel Res. 143 (2018) 180–195. doi:10.1016/j.jcsr.2017.12.026.
[17] T.J. Li, G.Q. Li, S.L. Chan, Y.B. Wang, Behavior of Q690 high-strength steel columns: part 1: experimental investigation, J. Constr. Steel Res. 123 (2016) 18–30.
[18] T.J. Li, S.W. Liu, G.Q. Li, S.L. Chan, Y.B. Wang, Behavior of Q690 high-strength steel columns: part 2: parametric study and design recommendations, J. Constr. Steel Res. 122 (2016) 379–394.
[19] S.D. Nie, S.B. Kang, L. Shen, B. Yang, Experimental and numerical study on global buckling of Q460GJ steel box columns under eccentric compression, Eng. Struct. 142 (2017) 211–222.
[20] Katalin Oszvald, Pál Tomka, László Dunai. The remaining load-bearing capacity of corroded steel angle compression members. Journal of Constructional Steel Research, 2016, 120: 188-198.
[21] Kulatung M.P., Macdonald M., Rhodes J., Harrison D.K.. Load capacity of cold-formed column members of lipped channel cross-section with perforations subjected to compression loading – Part I: FE simulation and test results. Thin-Walled Structures, 2014, 80: 1-12.
[22] Lip H. Teh, and Benoit P. Gilbert. Net Section Tension Capacity of Cold-Reduced Sheet Steel Angle Braces Bolted at One Leg. Journal of Structural Engineering, 2013, 139(3): 328-337.
[23] Maia W.F., Vieira Jr. L.C.M., Schafer B.W., Malite M.. Experimental and numerical investigation of cold-formed steel double angle members under compression. Journal of Constructional Steel Research, 2016, 121: 398-412.
[24] GB 50017-2017, Code for Design of Steel Structures, China Architecture & Building Press, Beijing, 2006.
[25] N.S. Trahair, M.A. Bradford, D.A. Nethercot, L. Gardner, The Behaviour and Design of Steel Structures to EC3, 4th edn Spon Press, London, 2008